EPFL

Thèse n° 8282

Cavity Quantum Electrodynamics with strongly correlated fermions

Présentée le 28 janvier 2022

Faculté des sciences de base
Chaire Fondation Sandoz en physique des gaz quantiques
Programme doctoral en physique

pour l'obtention du grade de Docteur ès Sciences

par

Kevin Etienne Robert ROUX

Acceptée sur proposition du jury

Prof. F. Mila, président du jury
Prof. J.-Ph. Brantut, directeur de thèse
Prof. J. H. Thywissen, rapporteur
Prof. J. Reichel, rapporteur
Prof. G. Pupillo, rapporteur
Prof. P. Scarlino, rapporteur

École polytechnique fédérale de Lausanne

2022

KEVIN ROUX
Cavity Quantum Electro Dynamics with strongly correlated fermions,
Diss. EPFL No. 8282 © October 2021

A mon grand-père.

ABSTRACT

This thesis presents the first cavity quantum electrodynamics experiments performed with a degenerate gas of ^{6}Li with strong atom-atom interactions. In the first part of this manuscript, I describe the design and building of the apparatus, which was specifically developed to bring together a high-finesse optical cavity and a strongly interacting Fermi gas. I describe how the cavity and all the laser-cooling procedure can be integrated into the same vacuum chamber, thus speeding up the production cycle of the degenerate Fermi gas.

This new experimental apparatus is the first of its kind combining these two fields of quantum physics. Placing a quantum gas of fermions within an optical resonator gives important technical advantages, allowing for the fast, all-optical production of a degenerate gas of ^{6}Li. We apply a technique modifying the longitudinal structure of the cavity trap to cancel its lattice structure. It increases phase space density after evaporative cooling, leading to an ultracold gas at temperature lower than ten percent of the Fermi temperature. I describe how magnetic fields allow us to tune the interatomic interactions, making use of the broad Feshbach resonance of ^{6}Li at 832 G and how we characterize the thermodynamic properties of the ultracold Fermi gas. The direct observation of phase separation for a spin-imbalanced Fermi gas, between a fully paired region at the cloud center and a spin-polarized shell surrounding it, experimentally proves the emergence of superfluidity at low enough temperatures.

The first experiment showing the strong coupling between cavity photons and a strongly interacting Fermi gas is shown in this manuscript. The large avoided-crossings observed during cavity transmission spectroscopy are the experimental smoking gun of the strong light-matter coupling regime. We observe the expected scaling of the light-matter coupling strength with the number of atoms in the gas, proving the coherent coupling of the atoms with the cavity field.

The third part of this manuscript presents the first cavity quantum electrodynamics experiments in which pairs of atoms couple to cavity photons, forming a new dressed state: the pair-polariton. This dressed state inherits from its atomic part the characteristics of the many-body physics of the strongly interacting Fermi gas. We confirm experimentally that the properties of the short-range two-body correlation function, known as Tan's contact, can directly be measured optically, on the pair-polariton transmission spectrum. We observe the coherent coupling of the ground state fermion pairs with the cavity photons and use the pair-polariton to perform single shot, real-time, weakly destructive measurements of the short range two body correlation function. This new measurement of Tan's contact allows to follow in time the evolution of a single system, in contrast with existing techniques.

The last part of this thesis shows experiments carried out far in the dispersive regime, where both the cavity resonance and the probe laser frequency are far detuned from the atomic resonance. I discuss how we can, in this regime, measure the atom number evolution in time, with a weak destructivity. I show that an optical non-linearity emerges, which depends on the atom-atom interaction strength. Lastly, I present the implementation

of a pump not aligned with the cavity axis, that allows for the creation of long-range interactions between atoms.

Keywords: Cavity QED, quantum gases, strongly correlated Fermions, photoassociation, pair-polaritons, Tan's contact, quantum sensing

RÉSUMÉ

Cette thèse présente les premières expériences d'électrodynamique quantique en cavité réalisées avec un gaz dégénéré de ^{6}Li en présence d'interactions fortes entre atomes.

La première partie de ce manuscrit décrit la conception et la construction du dispositif expérimental, qui a été développé spécifiquement pour combiner une cavité optique de haute finesse et un gaz de Fermi en interaction forte. Je décris comment la cavité et le dispositif de refroidissement laser des atomes peuvent être intégrés dans la même chambre à vide, accélérant ainsi le cycle de production du gaz de Fermi dégénéré. Ce nouveau dispositif expérimental est le premier du genre à combiner ces deux domaines de la physique quantique. Mettre un gaz quantique de fermions à l'intérieur d'un résonateur optique présente des avantages techniques importants et permet une production rapide, toute optique, d'un gaz dégénéré de ^{6}Li. Nous utilisons une technique de modification de la structure longitudinale du piège en cavité afin d'annuler sa structure en réseau. Cela augmente la densité dans l'espace des phases après refroidissement évaporatif, réalisant un gaz ultra-froid à des températures inférieures à 10% de la température de Fermi. Je décris comment les champs magnétiques nous permettent de contrôler les interactions inter-atomiques en utilisant la large résonance de Feshbach du ^{6}Li à 832 G, et comment nous caractérisons les propriétés thermodynamiques du gaz de Fermi ultra-froid. L'observation directe de la séparation de phase dans un gaz de Fermi déséquilibré en spin, entre une région intégralement appairée au centre du nuage et une enveloppe polarisée autour, prouve expérimentalement l'apparition de la superfluidité aux températures suffisamment basses.

La première expérience démontrant le couplage fort entre des photons en cavité et un gaz de Fermi en interaction forte est décrite dans ce manuscrit. Les importants anti-croisements observés lors de la spectroscopie en transmission de la cavité constitue une preuve éclatante du régime de couplage fort entre lumière et matière. Nous observons le comportement attendu de la force de couplage lumière-matière en fonction du nombre d'atomes, ce qui montre le couplage cohérent des atomes au champ de cavité.

La troisième partie de ce manuscrit présente les premières expériences d'électrodynamique quantique en cavité où des paires atomiques sont couplées aux photons en cavité, réalisant ainsi un nouvel état habillé : le polariton de paire. Cet état habillé hérite de sa composante atomique les caractéristiques à N-corps du gaz de Fermi en interaction forte. Nous confirmons par l'expérience que les propriétés de la fonction de corrélation à deux corps à courte portée, appelée contact de Tan, peuvent être mesurées directement par détection optique, sur le spectre de transmission du polariton de paire. Nous observons le couplage cohérent des paires de fermions dans l'état fondamental avec les photons en cavité et utilisons le polariton de paire pour réaliser une mesure faiblement destructive, en temps réel et en une seule acquisition de la fonction de corrélation à deux corps et à courte portée. Cette nouvelle mesure du contact de Tan permet de suivre l'évolution temporelle d'un système unique contrairement aux autres méthodes existantes. La dernière partie de ce manuscrit présente des expériences menées dans le régime fortement dispersif, où la résonance de la cavité comme la fréquence

du laser de sonde sont largement désaccordées de la résonance atomique. Je discute la façon dont nous pouvons suivre, dans ce régime, l'évolution au cours du temps du nombre d'atomes de manière faiblement destructive. Je démontre l'émergence d'une non-linéarité optique qui dépend de la force de l'interaction entre atomes. En dernier lieu, je décris l'introduction d'une pompe non parallèle à l'axe de la cavité, qui permet de faire apparaître des interactions à longue portée entre les atomes.

Keywords: Electrodynamique quantique en cavité, gaz quantique, Fermions fortement corrélés, photoassociation, pair-polaritons, contact de Tan, mesure quantique

CONTENTS

Detailed tables of contents can be found at the beginning of each chapter.

1 INTRODUCTION

Cavity quantum electrodynamics (QED) is a cornerstone of quantum science, from quantum simulation [1] to quantum information [2] and quantum sensing [3–5]. Condensed matter physics has provided experimental platforms where the strong coupling between individual systems in cavity or circuit QED [6, 7], such as Josephson junctions[8–11], nanophotonics structures [12] or quantum dots [13–17], constitute now the building blocks for the architecture of quantum computers [18–22]. In parallel, more fundamental aspects of strongly correlated materials [23] interacting with light have been explored [24, 25], and interest has grown to use these systems for the next generation of quantum technologies, hoping for the ability to control superconductivity with light [26–29]. However, these strongly correlated systems are so far restricted to the weak coupling regime.

In the last decades, the field of cavity QED in atomic physics has also shown impressive progresses [1], making it possible to control the interaction between light and atoms at the level of a single quanta [30–32]. These breakthroughs lead to the simulation of new phases of matter [33–35], to use atoms as quantum network memories [36, 37], and to perform quantum measurements of both atomic and electromagnetic field properties [38–40], reaching the quantum limit [41]. While the study of single atoms or thermal ensembles coupled to cavities is studied for more than twenty years [42], combining ultracold and degenerate quantum gases and cavity QED is more recent, with the first quantum gas of bosons reaching the strong light-matter coupling regime in 2007 [43, 44]. The study of these systems has allowed to create new type of interactions between atoms [45–47], to perform extremely sensitive measurement using spin-squeezing [38, 39], to create atomic clocks [48] and to simulate new phases of matter [33, 34, 49, 50] such as supersolidity [35, 51–53].

Among all these different systems, almost all of them are weakly interacting gases, making it possible to calculate their ground state and compare it with the results of the experiment. Only one example of a strongly-correlated system strongly coupled to light has been studied so far, the bosonic Mott insulator [33, 34]. In this system, the atom-atom interactions between bosons are made dominant by placing the gas in a three-dimensional deep optical lattice. Moreover the coupling between light and matter has only been studied in the context of single atom optical or microwave transitions. Despite theoretical and experimental interests [54–57], the strong coupling to molecular transitions has never been observed experimentally with cold atoms, while the optical addressing of molecular transitions in quantum gases is becoming an important topic with the emergence of ultracold and degenerate molecular gases [58]. Cavity QED with molecular transitions could help in the preparation of ground state molecules [59–61] or to perform coherent quantum chemistry [62–67]

The work presented in this manuscripts brings a new strongly correlated system to the cavity QED field [68]. We couple a strongly interacting Fermi gas to the electromagnetic field of an optical cavity, giving us a simultaneous

and independent control of both the strong atom-atom and atom-photon interactions. Our atomic system displays very rich properties in its ground state due to the large short-range interactions, such as pairing and superfluidity [69, 70]. Applying an external magnetic field allows us to tune the interactions [71], creating at will a gas of interacting bosonic molecules, a fermionic gas of Cooper pairs or a strongly interacting Fermi gas with unitary-limited interactions [69]. In addition, taking advantage of the pre-existent pair correlations in the ground state, we address molecular transitions to excited molecular states [72] and reach the strong light-matter coupling regime, creating for the first time dressed-states mixing pairs of atoms and cavity photons.

Our hybrid system of photons and strongly correlated fermions opens up a variety of applications, ranging from quantum sensing to quantum simulation of strongly correlated fermionic systems. The dressing of molecular transitions captures the properties of the ground state of the many-body system, which is magnified by the light-matter coupling strength. We observe the pair-correlations of the gas directly in the optical spectrum in a weakly-destructive manner [73]. As a direct application, we could perform measurement of the dynamics of the gas, which represents a notoriously difficult problem that could be tackled by quantum simulation [74]. It also provides an observable with minimal disturbance, allowing to study the dynamics of a single system, which is beneficial as it is independent of preparation noise. On a similar aspect, the dispersive coupling between a strongly interacting Fermi gas and cavity photons gives a direct access to the number of particle in the gas with a weak destructivity due to the strong dispersive coupling strength that reduces the heating from spontaneous emission [75]. These measurements are very promising and make our experiment a suitable platform to study slow dynamics such as transport in strongly correlated system, another problem where quantum simulation is pertinent due to the complexity of coming from both the dynamics and the strong correlations in the gas [74]. The strong coupling to molecular transitions represents also an interesting realization as the ability to control molecular transitions with a quantum field would be an interesting new tool for the production and study of degenerate gas of dipolar molecules [58].

The manuscript is organized as follows:

- In **Chapter** 2, I will describe the design of the vacuum system permitting to combine strong magnetic fields and a high finesse optical cavity. The design and properties of the high finesse cavity as well as a new type of bulk-machined electromagnets particularly suited for cold atoms experiment are presented in this chapter.

- In **Chapter** 3, I will discuss the experimental sequence that we use to produce large and degenerate clouds of ^{6}Li with strong atom-atom interactions. After an overview of the sequence, I will detail step by step each phase of the production sequence from laser cooling to evaporative cooling to quantum degeneracy. In this chapter, I will present in details the stabilization scheme used to ensure both a relative and absolute frequency stability between all the lasers and the science cavity. I will also discuss how we make use of the longitudinal mode of the resonator to create a lattice-free cavity trap, making it possible to perform an efficient evaporative cooling directly in the cavity-based

optical dipole trap. Finally I will introduce the probing techniques we use to characterize our system.

- In **Chapter** 4, I will describe atom-atom interactions in the context of dilute quantum gases with contact interactions. I will then discuss how the presence of a Feshbach resonance allows to tune the interaction strength by applying an external magnetic field, leading to a strongly correlated Fermi gas. In this strongly correlated regime, treating the two-body scattering problem is not enough to describe such systems. I will introduce the experimental consequences of the many-body Hamiltonian, leading to the existence of pairs and superfluidity in the ground state of a strongly interacting Fermi gas. I will finally explain how we experimentally characterize these properties.

- In **Chapter** 5, I will show the first experiments where the strong light-matter coupling is reached between the cavity photons and the strongly interacting Fermi gas. I will first describe the general features of light-matter interaction in the context of cavity QED, with the emergence of dressed-states mixing photons of the cavity and atoms of the Fermi gas, forming polaritons. I will detail how we can accurately describe the mode structure of our cavity, giving us the possibility to have reasonable predictions for the energy spectrum of the system that we probe by the mean of cavity transmission spectroscopy. I will present the transmission spectra for a spin-balanced and a spin-polarized Fermi gas, showing good agreement with the simulations. The experimental confirmation of the coherent coupling of the cavity photons with the atoms is obtained by measuring the scaling of the collective light-matter coupling strength with the number of atoms in the gas.

- In **Chapter** 6, I will discuss the strong-coupling regime that we reached on molecular transitions addressed by photoassociation. I will present a simple model explaining the emergence of photoassociation transitions in a quantum gases. After some discussions on the complexity of an accurate description of the reality of these interaction potentials, I will show that we can probe such transitions and observe them performing cavity transmission spectroscopy measurements. The strong light-matter coupling to these transitions creates new dressed-states hybridizing pairs of atoms of opposite spins and photons, the pair-polaritons. We can thus coherently address the many-body excitations of the quantum gas. In the second part of this chapter, I will show that such dressed-states are sensitive to the short-range physics of the strongly interacting Fermi gas, giving us access the universal quantity that describes this physics, Tan's contact. Finally, I will discuss a last promising experimental result showing that the pair-polaritons are suitable to perform real-time, weakly-destructive measurements of the short-range two-body correlation function.

- In **Chapter** 7, I will present the first experiments where the strongly-correlated Fermi gas is coupled dispersively to the cavity light field. In this regime, we show that weakly destructive measurements of atom number are made possible as the enhanced emission in the cavity mode compared with spontaneous emission reduces spurious heating. In the second part of this chapter, I will present experiments where the atomic density couples dynamically to the cavity field, leading to optomechanical Kerr non-linearities probed by cavity transmission spec-

troscopy. We measure this characteristic non-linearity as a function of the short-range interactions and observe a clear dependence. Ongoing work is being carried to connect this non-linearity to the short-range physics of the strongly correlated Fermi gas. Last I will present the first steps to realize a strongly interacting Fermi gas with cavity-mediated long-range interactions. We have observed self-organization of the cloud by pumping the cloud with a small angle compared with the cavity axis, characterized by the emergence of a superradiant phase. This constitutes the experimental smoking gun of the presence of cavity-mediated long-range interactions in the gas.

- In **Chapter** 8, I will conclude with a short review of the long term perspective of the experiment, both regarding quantum simulation and quantum sensing of strongly correlated systems.

Part I

COMBINING CAVITY QED AND STRONGLY INTERACTING FERMI GAS

2 EXPERIMENTAL APPARATUS

In this chapter I will describe the specificities of our experiment which brings in the same apparatus a high finesse cavity and a deeply degenerate Fermi gas with large interactions. The vacuum system is designed around a single science chamber where all the production stages and the measurements are performed. This approach allows for a fast experimental cycle of ~ 4s. I will first describe the vacuum system and then focus on the science chamber which accommodates a trichroic optical cavity as well as large magnetic fields. I will then detail the technical characteristics of the optical resonator. In a second part, I will present the ensemble of electromagnets used to create various bias magnetic fields or gradients of magnetic field specifically designed to fit around the science chamber hosting the cavity. Finally I will close this chapter with a description of the program used to computer-control program apparatus and dynamically produce the degenerate Fermi gas.

CHAPTER CONTENTS

This chapter closely follows the publications :

K. Roux,B. Cilenti, V. Helson , H. Konishi and J.-P. Brantut
Compact bulk-machined electromagnets for quantum gases experiments
Scipost Physics **6**, 048 (2019)

K. Roux, V. Helson , H. Konishi and J.-P. Brantut
Cavity-assisted preparation and detection of a unitary Fermi gas
New Journal of Physics **23**, 043029 (20121)

2.1 VACUUM SYSTEM

2.1.1 General overview

W have developed an experimental platform to couple a degenerate gas of strongly interaction fermions with photons in an optical cavity. The apparatus requires to combine multiple optical accesses to address the atoms optically, large magnetic fields to tune the short range interactions between atoms and an optical cavity with high finesse, well isolated from acoustic noise. Making these specifications compatible with a ultra-high vacuum (UHV) chamber represents an important technical challenge.

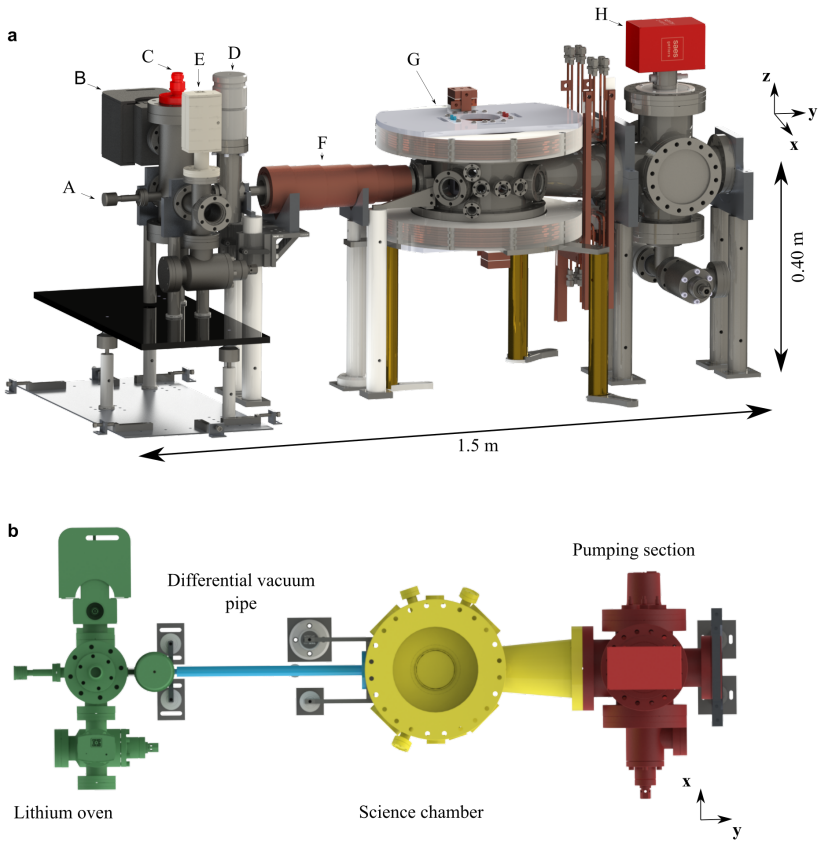

Figure 2.1: ***An apparatus for cavity QED and strongly interacting Fermi gas.*** **a** Overview of the apparatus. On the oven section where the lithium oven (A) is placed, high vacuum is maintained by an ion pump (B, *Agilent VacIon 20*) and a getter pump (C, *SAES Capacitor D400*) abd a getter pump (C). A slow beam of atoms is created by a Zeeman slower (F). The science chamber features an ensemble of electromagnets for magneto-optical trapping and for the use of Feshbach resonances (G). Ultra-high vacuum in this section is ensured by a combined getter and ion pump (H,*SAES NexTORR D1000-10*). **b** Top-view representation of the vacuum system. Colors refer to different functions of the apparatus: oven section (green), conical pipe ensuring differential pumping (blue), science chamber (yellow) and pumping section (red).

The design of the vacuum chamber was guided by the choice of realizing all the laser cooling operations as well as the cavity QED measurements in the same place, in a single main chamber called the science chamber. Per-

forming all the operations in the same vacuum chamber, without any optical or magnetic transport of the cloud allows us to speed up the experimental duty cycle of the machine, thus facilitating the day to day operation of the apparatus.

The vacuum system is depicted in figure 2.1.a. It can be separated into several parts. The section depicted in green in figure 2.1.b is the lithium oven chamber. It is connected to the science chamber (yellow) by a 40 cm differential pumping tube (light blue). The low background pressure required in the science chamber is ensured by a vacuum pump attached to the pumping section (red). The two sections are connected by a large diameter conical tube, offering the possibility for large pumping rates.

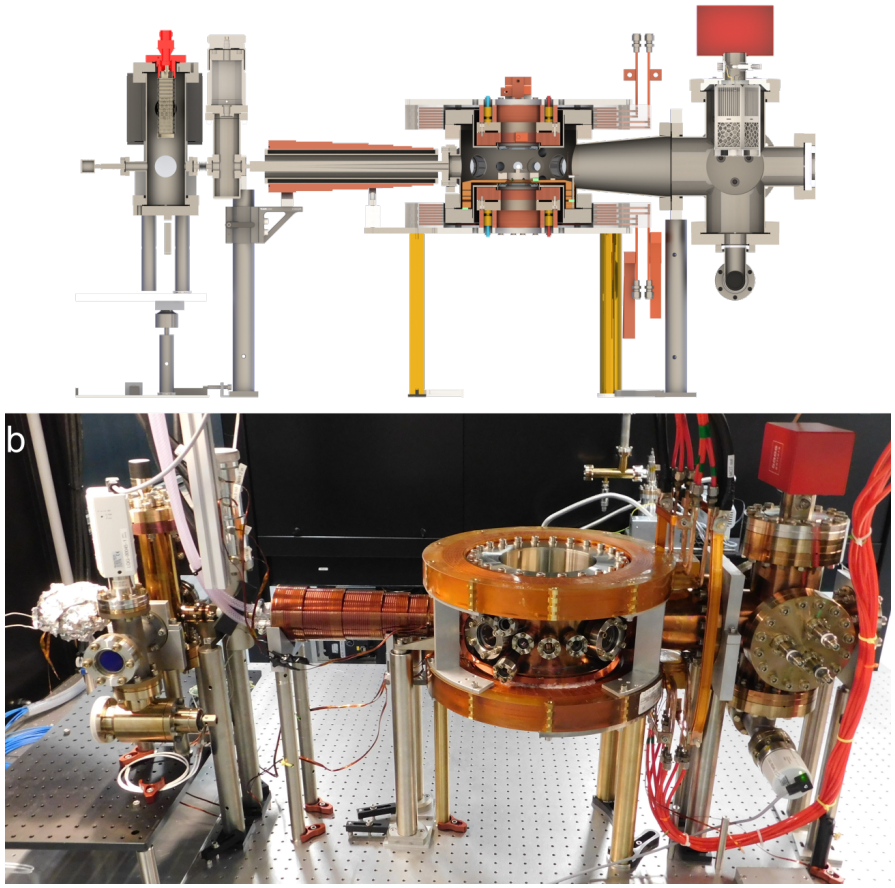

Figure 2.2: ***Overview of the vacuum system generating UHV.*** **a** Cut view of the apparatus. The oven section on the left is connected to a conical pipe which ensure a differential vacuum with the science chamber at the center. These two sections can be isolated from each other by a gate valve. The oven section is pumped with an ion pump and a getter pump. On the right the 4-way cross accomodate the large getter pump combined with a small ion pump. This section connects to the main chamber via a conical pipe of diameter 60 mm on the science chamber and 100 mm on the pumping cross. This view also shows the conical electromagnet between the oven and the science chamber as well as the ensemble of electromagnets around the science chamber. These will be presented in detail in a latter section. **b** Picture of the assembled vacuum system with all electromagnets installed.

As depicted in figure 2.2.a and .b, a tapered electromagnet is positioned around the differential pumping pipe linking the oven section with the science chamber. Moreover a complex set of electromagnets surrounds the main chamber and will be described in detail in section 2.4.

The connections between the different sections of the UHV system can have two purposes : to maximize the conductance to ensure the possibility of a high pumping rate, or to build up the largest differential pressure to isolate two sections from each other. The conical pipe linking the oven section to the science chamber is designed to isolate the two sections, while the conical pipe between the science chamber and the pumping section is dimensioned to ensure the largest conductance possible. We model each connecting element to extract their conductances and then extrapolate either the corresponding maximal pumping capability or the pressure reduction due to the connection. The conduction of a tube is given by [76] :

$$C = \alpha v A/4 \tag{2.1}$$

with α a function of the transition probability proportional to $1/L$ with L the length of the tube. $v = \sqrt{8k_B T/\pi m}$ is the average velocity of the gas species considered, m the mass, T the temperature and k_B the Boltzmann constant. A is the cross section of the tube aperture. Similarly just an orifice of section A has a conductance given by :

$$C = vA/4 \tag{2.2}$$

The $L = 360$ mm conical tube combined with the pinhole aperture of diameter $d_1 = 5$ mm at its input and $d_2 = 12$ mm allows to build up a differential pressure given by the conical pipe conductivity between the lithium oven section and the science chamber [76] :

$$C = \frac{4\pi v}{3}\left(1 + \frac{d_1^2 d_2^2}{(d_1 + d_2)L}\right) \tag{2.3}$$

giving a conductance of $C = 0.58$ L/s for H_2. On the other end, the conical connection between the science chamber has an aperture with a diameter of 104 mm on the pumping section side and of 79 mm on the science chamber one and a length of 158 mm. This gives a conductance of $\sim 1.8 \times 10^4$ L/s for hydrogen and $\sim 6.6 \times 10^3$ L/s for nitrogen. In this case the conductance of the section is not limiting compared with the nominal pumping rate of the vacuum pumps installed on the setup.

In the following I will describe in detail each of the different vacuum chamber sections.

2.1.2 Oven chamber

The oven section is the place where the solid pieces of lithium placed in a small crucible (figure 2.3.a A) are heated up to create a hot vapour of ^{6}Li. A resistive heating wire is wound on the outside of the crucible, the temperature of which can be tuned by adjusting the value of the current running through the wire. This part is carefully isolated with several layers of insulating wool, ceramics and aluminium sheets. A thermocouple is placed in a

small aperture machined on the back of the crucible to monitor the temperature of the oven in a reproducible manner. The crucible and the tank of the lithium oven section machined out of non magnetic austenitic stainless steel 316L (DIN:1.4404).

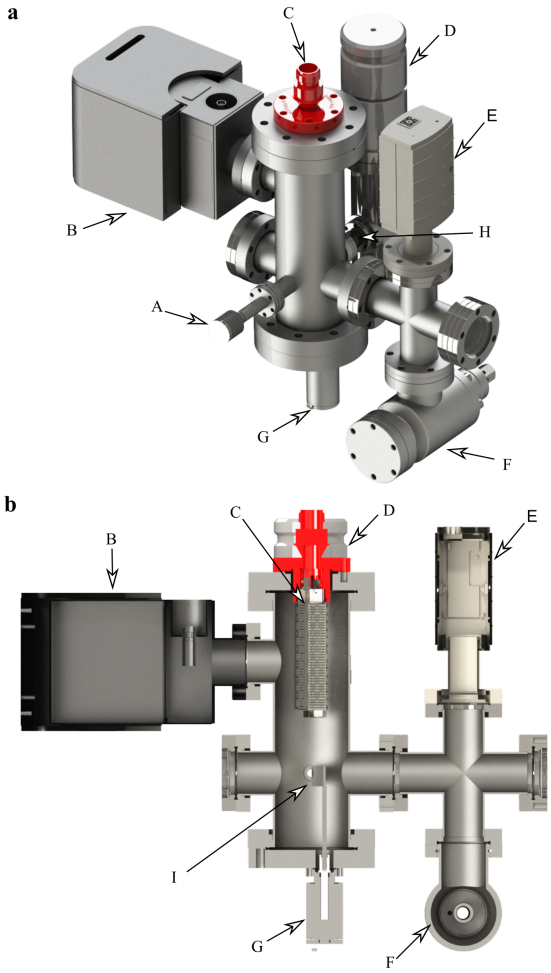

Figure 2.3: ***Lithium oven vacuum section.*** **(a,b)** A 3-D view of the oven section. A small crucible of cylindrical shape (A) is used to host the solid lithium which is then heated up to 350 °C to produce a hot vapour of ^{6}Li. Part of this vapour travels through the oven tank where the atomic flux can be blocked by a metallic flag (I) controlled by a stepper motor (G). It first crosses the gate valve (D) and then the pinhole positioned at the entrance of the conical pipe to then be slowed inside the Zeeman slower tube. The oven tank pressure is brought to 5×10^{-10} mbar using an Agilent ion pump (B) (20 L/s) and a passive getter pump (C). A pressure gauge (E) monitors the oven tank pressure and an angled valve(F) makes it possible to connect a turbopump group in order to pre-pump the chamber starting from atmospheric pressure. The oven tank and the conical pipe are connected by an all-stainless-steel bellow (H) used to align the ^{6}Li oven in direct view with the center of the science chamber, thus maximizing the atomic flux to the center of the science chamber.

During the operation of the experiment, the oven is heated up to ~ 350 °C, inducing a large outgassing rate of this section. In order to not degrade the

vacuum quality in the science chamber, this section is as isolated as possible from the main one, as shown by the calculation of the small conductance between them. We also have a large pumping capability in the oven section to limit the increase of pressure even at high oven temperatures. For this purpose, two vacuum pumps are installed. An Agilent VacIon StarCell ion pump (figure 2.3.a B) and a non-evaporable getter (NEG) pump SAES Capacitor D400 (figure 2.3 a D) allow for about 400 L/s of pumping capability for H_2, 100 L/s for N_2 (mainly pumped by the NEG pump) and about 10 L/s for heavier elements (mainly by the ion pump). The pressure of this chamber is monitored with a Pfeiffer PBR260 pirani pressure gauge (figure 2.3.a E). The typical pressure reached in operating conditions is about 5×10^{-10} mbar. The oven section can be isolated from the rest of the setup by a VAT CF16 all-metal gate valve (figure 2.3.a D).

As the flux of hot lithium is quite high, it can coat transparent glass surfaces, making them almost fully reflective. To avoid the viewport in direct view of the oven on the other side of the apparatus getting coated, a small piece of stainless steel is fixed on a post (figure 2.3.b I) itself mounted onto a stepper motor (figure 2.3b G). It also avoids having the flux of hot lithium atoms hitting the cloud in the chamber while performing experiments, which would drastically reduce the lifetime of the trapped cloud.

2.1.3 Science chamber

Generating ultra-high vacuum

The ultra-high vacuum necessary to operate quantum gases experiments is made possible in this apparatus by using a combined NEG pump with a small ion pump (SAES NexTORR D1000-10). They are positioned on the pumping section, consisting in a 4−way cross made out of non magnetic austenitic stainless steel. The residual gas in the main chamber is pumped through the conical pipe connecting the two sections. The large 79 mm diameter on the main chamber side and CF100 flange on the pumping cross side (figure 2.4 A) ensure a large conductivity as calculated in the previous section.

The pressure in this section is monitored using a cold cathode pressure gauge Pfeiffer IKR 270 (figure 2.4 C) with a minimum measurable pressure of 5×10^{-11} mbar. As this gauge is placed fairly far from the science chamber, with reductions from CF100 to CF40 flanges and two 90° elbows, it is expected to measure a pressure about 8 times larger than the actual one in the science chamber. We measure pressures of about 5×10^{-10} mbar, consistent with a background pressure in the science chamber of about 10^{-11} mbar. On the opposite side of the CF40 3-way cross where the gauge is attached, an angle all-metal VAT valve connects to the pumping group used to pump the setup while baking the ensemble. In direct line of view with the connection to the science chamber, a CF63 sapphire viewport is installed, giving a large optical access used to slow down the atomic beam (see Chapter 3). The last CF100 flange is used to connect 3 coaxial electrical feedthroughs (figure 2.4 B) that are used to electrically control piezoelectric actuators and send radio-frequency signals to an antenna in the science chamber (see section 2.3).

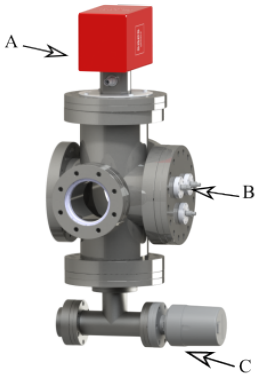

Figure 2.4: ***Pumping section.*** The pumping section is built around a custom CF100 4−way cross. One connection links the pumping section to the main science chamber. One port hosts 3 electrical feedthroughs while the other one is kept blind. At the bottom port a CF reduction from 100 to 40 holds a 3−way cross hosting the pressure gauge on one side and an angled VAT valve on the other. The turbopump group can be attached there. On the top CF100 port, a pump combining a getter and an ion pump is fixed. This pump is the only element that actively pumps the background gas in the main chamber once the turbopump is disconnected.

Combining large magnetic fields and a high finesse cavity : details of the science chamber design

The science chamber is based on a CF200 cylinder (see figure 2.5). This cylinder is made out of non magnetic austenitic stainless steel 316L. It is connected to the differential pumping tube by a CF40 flange. On the opposite side, a conical tube is soldered on the body of the CF200 cylinder with an aperture of 158 mm diameter. The end of the pipe is attached to the pumping section with a CF100 flange. The top and bottom CF200 flanges are closed with two reentrant viewports (UKAEA) (figure 2.5 B). The large 60 mm clear optical aperture of these viewports come 45 mm away from the center of the science chamber, where the atoms will be located. It offers a maximal numerical aperture of 0.63.

Tuning the interatomic interactions for ^{6}Li requires to reach magnetic fields of the order of 800 G. Moreover, trapping and cooling a thermal cloud requires large magnetic field gradients. For these reasons, several sets of electromagnets are installed around the science chamber. Two pairs of coils based on hollow-core copper wire (figure 2.5 D) realize both a magnetic field gradient at the center of the chamber and a quartic magnetic field bias as they are close to the Helmholtz configuration. In addition, a set of electromagnets is placed inside the reentrant viewport (figure 2.5 C) to create a large bias magnetic field up to 1100 G. Small compensation coils are placed on this electromagnet block to finely tune the position of the saddle point of the magnetic field.

Lastly, the science chamber hosts the heart of this experiment, the high finesse Fabry-Perot cavity (figure 2.5 A). The cavity is placed on a science platform positioned on top of several elements which isolate it from acoustic noise coming from the environment. This part will be presented in detail in section 2.3 dedicated to the optical cavity.

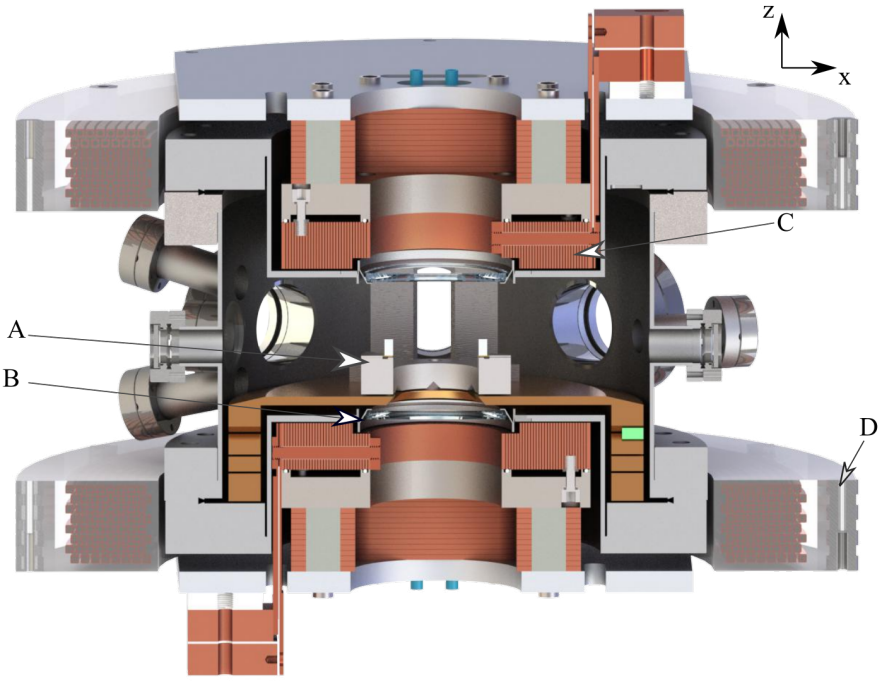

Figure 2.5: ***The science chamber.*** The science chamber is designed around a CF200 cylinder. The top and bottom accommodate reentrant viewports (B). The science cavity platform (A) sits at the center of the chamber. Electromagnets are positioned around the chamber (D) and in the reentrant viewports (C) to create large bias magnetic fields as well as magnetic field gradients.

The science chamber has additional optical accesses positioned all around the CF200 cylinder. Two CF16 viewports are positioned along the cavity axis(defined as the x-axis in figure 2.5). From this axis 4 CF40 viewports are positioned in the horizontal plane, tilted with an angle of $\pm 45°$. Four CF16 viewports make an angle of $\pm 18°$with respect to the cavity axis. All these optical access are used to laser-cool and trap the atomic cloud during the experimental sequence (described in Chapter 3). An additional set of four CF16 viewports are positioned with a $\pm 15°$angle with respect to the horizontal plane and tilted horizontally with respect to the cavity axis by $\pm 25°$. They can be used to add an optical lattice along the vertical direction for example. This geometry grants us all the necessary optical access to perform the cooling procedure, reach the quantum degenerate regime and perform the cavity quantum electrodynamics experiments in the same chamber.

2.1.4 Preparation procedure for UHV components

All the vacuum components presented in the previous sections have been carefully prepared in order to limit the possible contaminations that would have increased the outgassing rate of the apparatus and consequently lead to higher background pressure. Here I present the main steps that have been followed and successfully lead to a background pressure compatible with quantum gases experiments.

- All the stainless steel parts making up the vacuum chamber have been carefully cleaned with solvents (acetone and isopropanol) using an

ultrasonic bath. For pieces that were previously machined with oil, a precleaning with a TiCKOPUR solution was performed. Once this step is completed an extra step of cleaning with deionized water to remove all possible traces of solvents is performed.

- The stainless steel parts were baked at air, at high temperature for durations from 24 to 48 h. This procedure, is called air firing. As the production of stainless steel produces a large quantity of dihydrogen, that ends up trapped inside the material, the outgassing of stainless steel parts is mainly due to the hydrogen diffusing through the material and outgassing in the vacuum. As dihydrogen is a small molecule, the entire volume can outgass dihydrogen contrary to heavier elements that can only be outgassed from the surface. Several procedures, with different degrees of complexity, can help to reduce this outgassing rate. One solution is to coat the inner surface of the chamber with a layer of oxide (TiO_2) which would act as a barrier and consequently trap the dihydrogen inside the stainless steel. Another approach consists in using as active material to coat the inner surfaces. Then these surfaces would act as a pump, and reduce the background pressure. Non-evaporable-getter (NEG) material can be vaporized to coat such surfaces in the limit where they are relatively flat, simple and with large radii of curvature. Both techniques requires complex manufacturing processes. Moreover the NEG coating needs to be thermally activated to start acting as a pump. This activation temperature is about 100 °C. In our case, we applied the air firing technique to create a layer of oxide due to a high temperature air baking. The typical temperature is about 400 °C and needs to be kept below 450 °C in order not to modify the crystalline structure of the austenetic stainless steel which would lead to unwanted magnetization. This oxidation procedure gives the gold color of the vacuum chamber as it can be seen in figure 2.2.b.

- All parts installed inside the vacuum chamber were cleaned with solvents and then baked inside a small vacuum chamber, pumped with a scroll pump attached to a turbopump. The outgassing was monitored on a residual gas analyzer (RGA). The baking was stopped when the outgassing of heavy elements reached the background detection of the RGA. A small table 2.1 summarizes the baking temperatures of different elements used on the experiment.

Table 2.1: Typical baking temperatures for in-vacuum parts.

	Vacum baking	Air Firing
Stainless steel (316L/1.4404/1.4435)	280 °C	400 °C
Titanium	250 °C	-
Viton	200 °C	-
Cavity mirror	150 °C	-
Coaxial cables (Accuglass)	200 °C	-

- The entire apparatus, without the viewports, was baked under vacuum at 280 °C for several days.

- Once all components and viewports were installed, the entire setup was baked under vacuum to a temperature of 150 °C in order to not damage the dielectric coating of the viewports and mirrors. The NEG elements of the pump were also heated up to 250 °C during this baking to reduce their outgassing rate, while they were activated. This baking lasted as long as the background pressure of all heavy elements was above the background detection of the RGA.
- At the end of the baking procedure, the NEG pumps were activated by heating the NEG elements to 400°C for 1 h. Then, the ion pump was also activated and the turbopump disconnected by closing the angle, all-metal valve.

2.2 LITHIUM 6 ATOM

Lithium is an alkali metal with 3 electrons. Two electrons fill the 1s shell. One valence electron occupies the 2s shell. The valence electron of ^{6}Li has consequently a principal quantum number $n = 2$ in its ground state. Two isotopes exist in nature, ^{7}Li which is a boson and the one used in this project, ^{6}Li, which is a fermion.

	D1 line	D2 line
Mass m_{Li6}	$9.988341 \cdot 10^{-27}$ kg	
Wavelength λ	670.992477 nm	670.977380 nm
Frequency ν	446.789596 THz	446.799649 THz
Fine Splitting Δ_{FS}	10.052778 GHz	
Lifetime τ	446.789634 ns	
Natural linewidth Γ_0	$2\pi \cdot 5.8724$ MHz	
Recoil temperature T_r	3.53581152 µK	

Table 2.2: *Optical properties of ^{6}Li.* Reproduced from [77].

The 2S state has an orbital angular momentum $L = 0$, while the 2P state has $L = 1$. In addition, the ^{6}Li valence electron has an intrinsic spin $S = 1/2$. The nucleus made out of 3 protons and neutrons leads to a total nuclear angular momentum $I = 1$, which is constant as the quantum state of the nucleus is not influenced by manipulations of the valence electron. The internal structure is affected by different couplings emerging from :

- The spin-orbit interaction between $\vec{\mathbf{L}}$ and $\vec{\mathbf{S}}$. The interaction energy between the two dipole moments reads

$$\hat{H}_{SO} = \frac{\mu_B}{2mec^2\hbar}\left[\frac{1}{r}\frac{d\hat{U}(r)}{dr}\hat{\mathbf{L}}\hat{\mathbf{S}}\right] \tag{2.4}$$

  with e the elementary charge, m the mass of the electron, c the speed of light, $\hat{U}(r)$ the Coulomb potential produced by the nucleus and the core electrons and r the radial coordinate. $\mu_B = e\hbar/2m$ is the Bohr magneton.

  This interaction term lifts the degeneracy for electronic states of orbital angular momentum $L > 0$. In our case, the 2P state has two different states emerging from the spin-orbit coupling. In the presence of

Property	*Value*
$2S_{1/2}$ Magnetic dipole constant $a_{2S_{1/2}}$	152.136 840 7 MHz · h
$2P_{1/2}$ Magnetic dipole constant $a_{2P_{1/2}}$	17.386 MHz · h
$2P_{3/2}$ Magnetic dipole constant $a_{2P_{3/2}}$	−1.155 MHz · h
$2P_{3/2}$ Electric quadrupole constant $b_{2P_{3/2}}$	−0.10 MHz · h
Orbital g-factor g_L	$1 - m_e/m_{^6Li} = 0.999\,995\,87$
Electron g-factor g_S	2.002 319 304 362
Nuclear g-factor g_I	−0.000 445 587 1

Table 2.3: *Hyperfine constants of ^6Li.* Reproduced from [77].

the spin-orbit interaction, the good quantum number to describe the eigenstates of the system is the total angular momentum $\hat{J} = \hat{L} + \hat{S}$, as it commutes with the Hamiltonian. The possible values for J are given by $|L - S| \leqslant J \leqslant L + S$. The so called fine splitting of the 2P states leads to two states of total angular momenta $J = 1/2$ and $J = 3/2$. They are separated by 10.056 GHz at zero magnetic field. The transition from the $2S_{1/2}$ to the $2P_{1/2}$ state is called the D_1 line and the one between the $2S_{1/2}$ and the $2P_{3/2}$ state is called the D_2 line. The properties of these two lines are summarized in table 2.2.

- A second set of interactions affects the internal structure leading to the so-called hyperfine structure. It is first due to the coupling between the nuclear spin $\hat{I}$ and the magnetic dipole electric quadrupole electric fields created by the valence electron. Second, the Fermi contact interaction between the nuclear and the electronic spin also contribute to the modification of the level structure. The contact interaction vanishes for orbital angular momentum $L \neq 0$. This term is responsible for the hyperfine structure emerging from the $2S_{1/2}$ state. The magnetic dipole and electric quadrupole interaction terms are non zero when the electronic wavefunction is not spherically symmetric ($L \neq 0$). This term lift the degeneracy of the states $2P_{1/2}$ and $2P_{3/2}$. As shown in [78], in the limit of the Hartree-Fock approximation, the magnetic dipole and the contact interaction Hamiltonian can be written as,

$$\hat{H}_D = \alpha \left[\frac{\vec{\hat{I}} - \vec{\hat{S}}}{r^3} + \frac{(\vec{\hat{S}} \cdot \vec{r})\vec{r}}{r^5} \right] \cdot \vec{\hat{I}} + \xi \vec{\hat{S}} \cdot \vec{\hat{I}} \tag{2.5}$$

The hyperfine interaction Hamiltonian simplifies into

$$\hat{H}_{HF} = a(L, J) \vec{\hat{J}} \cdot \vec{\hat{I}} \tag{2.6}$$

with a the hyperfine constant reported in table 2.3 for each of the manifolds, accounting for the three different interaction mechanisms.

To describe the hyperfine structure it is convenient to define a total atomic angular momentum $\hat{\mathbf{F}} = \hat{\mathbf{J}} + \hat{\mathbf{I}}$. The quantum number F can take two values respectively 1/2 and 3/2 for the $2S_{1/2}$ and $2P_{1/2}$ states. For the state $2P_{3/2}$, $J = 3/2$ leads to three hyperfine states with $F = 1/2$, 3/2 and 5/2 respectively.

This completely describes the internal structure at zero magnetic field has shown in figure 2.6a.

We now study how the energy of these electronic states evolves in the presence of an external magnetic field applied along the vertical direction $\vec{B} = B_z \vec{e}_z$. Thus the Zeeman energy change is described by :

$$\hat{H}_z = \mu_B \left(g_L \hat{L}_z + g_S \hat{S}_z + g_I \hat{I}_z \right) B_z \tag{2.7}$$

with g_L,g_S and g_I the g-factors for the orbital, electronic and nuclear momemta respectively (given in table 2.3). There are two interesting regimes to be considered when comparing the strength of the Zeeman shift compared with the hyperfine coupling. For what we will be interested in, the spin-orbit coupling leading to the fine structure will always be larger than both the Zeeman and the hyperfine energies.

- For small Zeeman energy compared with the hyperfine coupling constant a. In this casen the total atomic angular momentum is the good quantum number to describe the level structure (as at zero magnetic field). The total atomic Hamiltonian reduces to

  $$\hat{H} = \mu_B g_F(L, J, F) \hat{F}_z B_z \tag{2.8}$$

  with g_F the total g-factor that can be calculated using the Lande expressions. It leads to a linear dependence of the energy levels with the projection of the total spin m_F along the quantization axis fixed by the direction of the magnetic field:

  $$E(L, J, F) \simeq \mu_B g_F m_F B_z. \tag{2.9}$$

  For low magnetic fields, the energy displacement is linear and given by the possible values of m_F for each hyperfine state.

- Once the Zeeman energy is comparable or larger than the hyperfine splitting, it can no longer be treated as a perturbation and F is not a good quantum number to describe the energy splitting between the hyperfine states. When $B \sim a/\mu_B$, which for ^{6}Li corresponds to about 100 G, the states are labelled independently by their total electronic angular momentum J and by the nuclear one I. The interaction Hamiltonian reads

  $$\hat{H} = \mu_B \left[g_J(L, J) \hat{J}_z + g_I(I) \hat{I}_z \right] B_z + a \vec{\hat{J}} \cdot \vec{\hat{I}} \tag{2.10}$$

  with energy levels approximated by

  $$E(L, J, I) \simeq \mu_B \left(g_J m_J + g_I m_I \right) B_z + a m_J m I \tag{2.11}$$

  The energy levels again split linearly (figure 2.6.b), dominated by the electronic angular momentum projection m_J as it is significantly larger than the nuclear one m_I. The offset is governed by the different nuclear states and the hyperfine coupling a. This regime where the contribution of the nuclear and the electronic angular momenta are decoupled

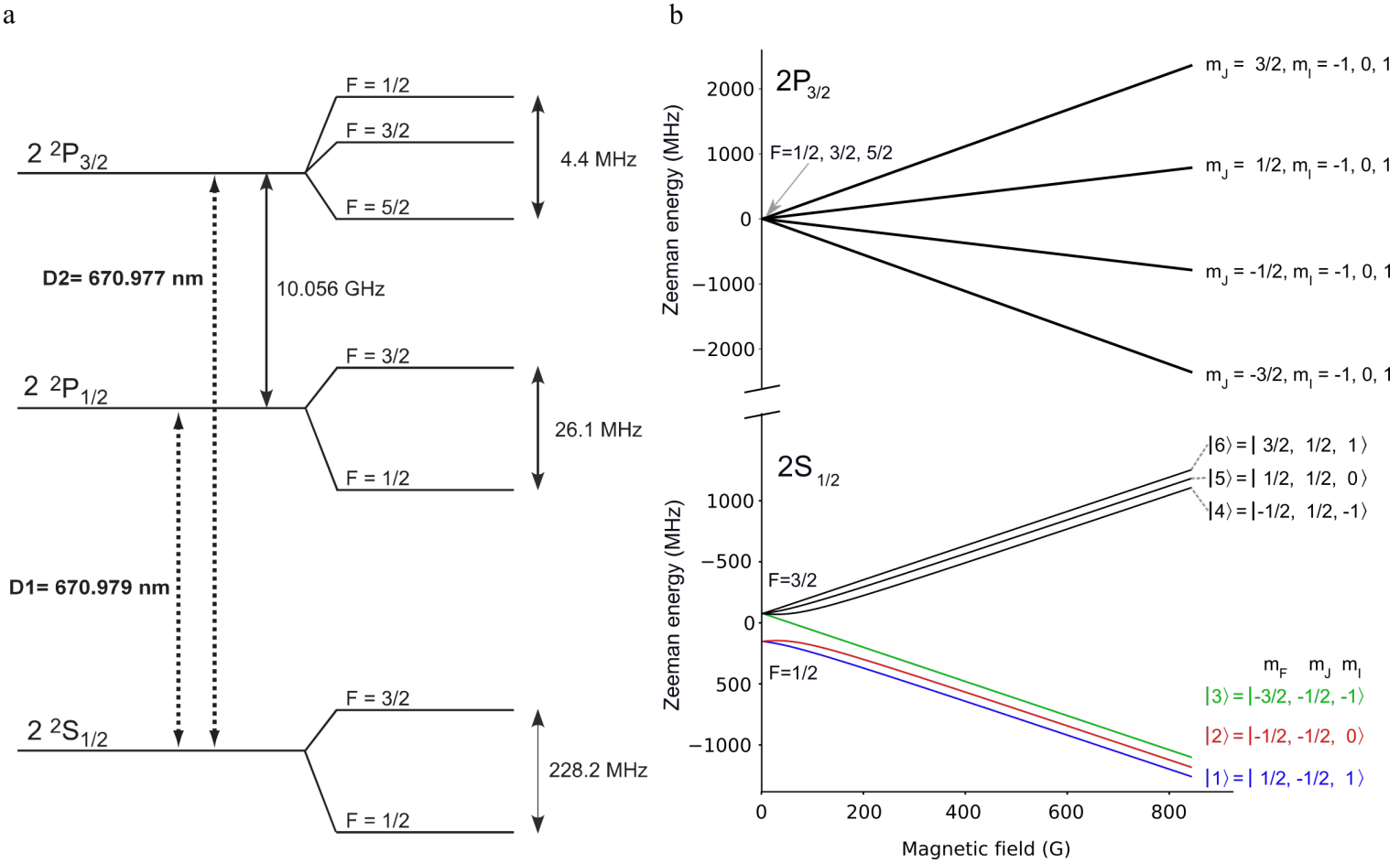

Figure 2.6: ***Energy level diagram of*** ^{6}***Li*** **a** Complete energy level strucutre at zero magnetic field, including the hyperfine structure. It shows the optical frequencies of the D−1 and D_2 lines. As the hyperfine splitting of the excited state is 4.4 MHz, compared with the natural linewidth of the excited state $\Gamma \sim 2\pi \times 6$ MHz, the hyperfine states of the $2P_{3/2}$ manifold are not resolved. **b** Variation of Hyperfine energy levels as a function of the magnetic field B. m_F, m_J, m_I denote the magnetic quantum number of the total angular momentum, of the total electronic angular momentum and of the nuclear spin, respectively.In the so-called Pashen Back regime (for $B > 100$ G), the magnetic field dependence of the levels is determined by m_J. This figure is inspire from the PhD thesis of Sebastian Krinner [79]

corresponds to the so-call Pashen-Back regime. The work presented in this thesis will be performed with magnetic fields ranging from 550 to 1200 G, thus all performed in deeply in the Pashen-Back regime. As an important property of this regime, the optical transitions from the three lowest hyperfine states to the excited state manifold in the $2P_{3/2}$ state, corresponding to states $|m_j = -3/2, m_I = -1, 0, 1\rangle$, are almost perfectly closed [77]. This means that, under these specific conditions, atoms in states $|1\rangle$,$|2\rangle$ and $|3\rangle$ can be modelled as two level systems up to a few percent correction.

We will work with atoms populating the first three Zeeman states usually denoted as $|1\rangle$, $|2\rangle$ and $|3\rangle$ (figure 2.6.b). Their energy decreasing for increasing magnetic fields, they are high-field seekers, meaning that they experience a magnetic force when sensing a magnetic field gradient. This means that the atoms in the three lowest hyperfine states sit at the maximum of the magnetic field. Controlling the population between the different hyperfine states at large magnetic fields will be a major concern of the preparation sequence (see Chapter 3). It is possible to control the relative population between these three lowest hyperfine states by shining radio-frequency (RF) fields onto the atomic cloud with an antenna. Figure (2.7) shows the frequency difference between these three states at different magnetic fields namely 568, 690 and 832 G which are the relevant ones practically used in this work.

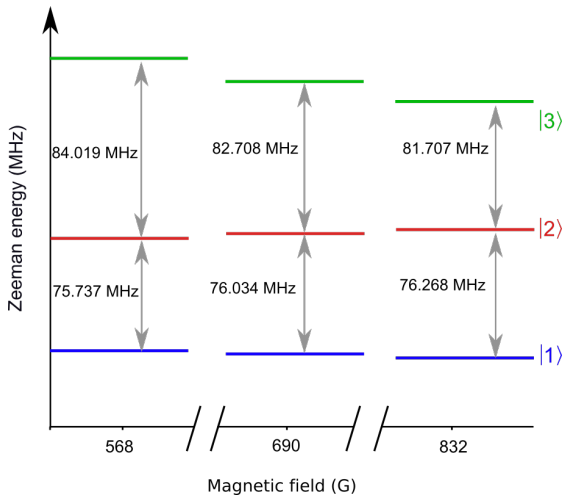

Figure 2.7: ***Zeeman splitting between the three lowest hyperfine states at high magnetic fields.*** The figure shows the frequency differences between the three lowest hyperfine states $|1\rangle$,$|2\rangle$ and $|3\rangle$ at 568, 690 and 832 G. These three situations correspond to particular interaction strengths that are of interest and are used in the next chapter.

The transitions $|1\rangle \longrightarrow |2\rangle$ and $|2\rangle \longrightarrow |3\rangle$ do not have the exact same frequencies and the transition $|2\rangle \longrightarrow |3\rangle$ shows a larger variation across the range of magnetic fields explored. The RF antenna used to drive these transitions needs to be doubly-resonant at these two different frequencies. This part of the experimental system is detailed in a section 2.4.4.

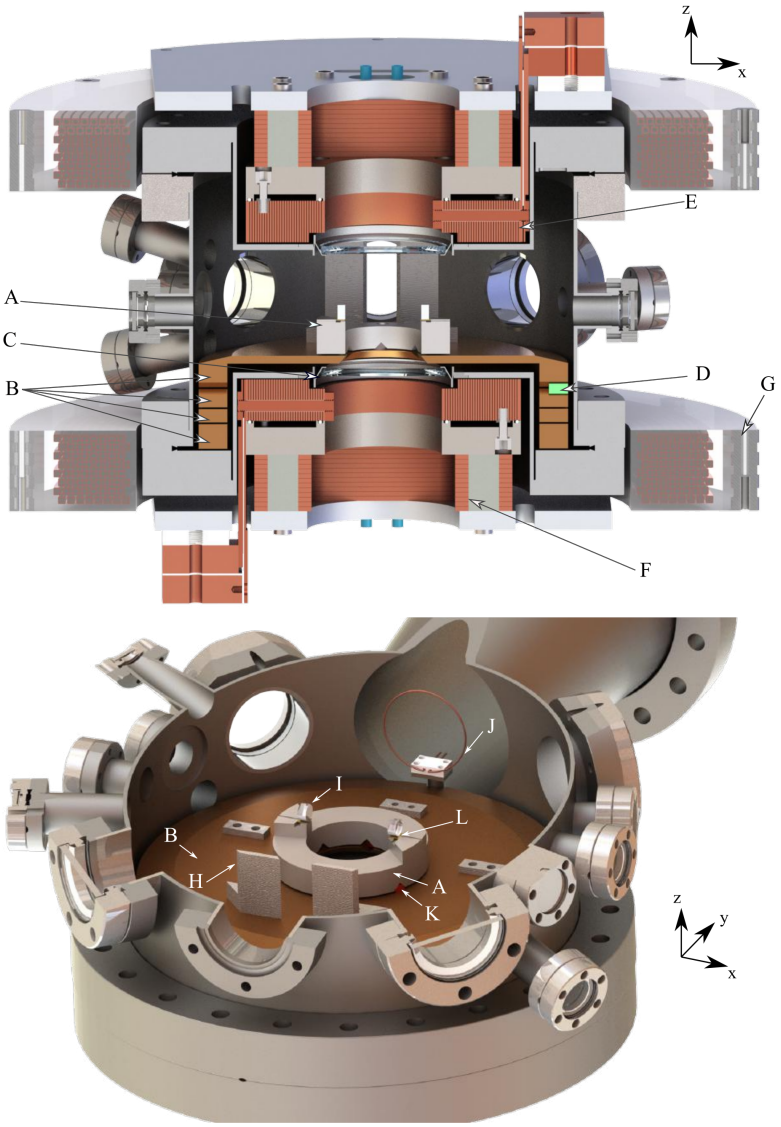

Figure 2.8: ***Detailed view of the science chamber.*** **(a)** Vertical cut view of the science chamber. The science platform (A) hosting the cavity mirrors lies on several stages of vibration isolation made of non-magnetic stainless steel (B) separated by Viton dampers (D). On the top and bottom, reentrant viewports (C) allow for a large optical access, up to a numerical aperture of 0.63. An ensemble of two pairs of coils (G) provides a magnetic field gradient for magneto-optical trapping and a homogeneous bias. In the reentrant viewports a compact ensemble of electromagnets combines compact bulk-machined coils (E), allowing to reach up to 1200 G with a finite curvature, and cloverleaf coils (F) to precisely align the magnetic field saddle point on the cavity mode position. **(b)** View of the science chamber with the cavity mirrors (I) and piezoelectric actuators (L) glued on a stiff titanium holder (A). The holder itself is isolated from the isolation stacks (B) via Viton dampers (D,K). A single loop radio-frequency antenna (J) is positioned close to the cavity. Titanium shields (H) avoid direct coating of the cavity mirror by the beam of atoms coming from the oven.

2.3 OPTICAL RESONATOR

The heart of this experiment is the high-finesse optical cavity that we use to couple the photons of a specific cavity mode, with the quantum gas of fermions. In this section, I will first detail the design that we developed to integrate the optical cavity in the science chamber together with all the electromagnets. Then, I will present the basic equations and physical quantities to describe the properties of a Fabry-Pérot cavity and specifically the properties of the cavity used in this work. I will give an overview of the assembly procedure and how the cavity has been experimentally characterized.

2.3.1 Design and assembly

The 4 cm-long Fabry-Perot cavity is positionned at the center of the science chamber as depicted in the cut views of figure 2.8.a and .b. In figure 2.8.a we see that the cavity is sitting on top of several consecutive non-magnetic stainless steel (DIN:1.4435) rings (2.8.a)B) separated by Viton dampers (2.8.aD), which are themselves resting on the flange of the bottom reentrant viewport. The last stage of these isolation stacks consists of a ring machined out of titanium (2.8.a.bA) where two piezo actuators (Noliac CSAP02-C03) are glued (2.8.bF). The mirrors (2.8.bI) are themselves glued on the piezoelectric actuators. As the entire setup is placed under vacuum it is important to limit the outgassing rate of all these elements. To remove all movable elements on the science platform that could move during baking and thus misalign the cavity, we choose to glue the cavity mirrors and piezoelectric actuators with an epoxy (Masterbond EP21TCHT-1) compatible with UHV operations.

Moreover, this glue can be cured at room temperature which is a great advantage in order to limit the different heating ramp applied to the mirror that could degrade their highly reflective dielectric coatings. Another UHV compatible glue (EPOTEK H72 epoxy) has been tested but required a curing at 100 °C. This curing lead to a degraded finesse in a reproducible manner, which led us to choose an epoxy with a room temperature curing. We attributed the degradation of the finesse to mechanical strain due either to the heating ramps during the curing or to the CTE mismatch between the glass and the epoxy. Electrical connections to the piezoelectric actuators and to the RF antenna (2.8.b)(J)) are clamped on the last isolation stack (2.8.b)(B)) at several positions to avoid direct coupling of the cable vibrations to the piezoactuators. As the titanium holder is isolated from the last isolation stack with Viton dampers (2.8.b)(K)) and that direct coupling to acoustic vibrations is impossible due to the UHV conditions in the chamber, this guarantees a good isolation overall. On the science platform, two plates of titanium are installed in order to shield the cavity mirrors against the flux of hot atoms coming from the oven section. Only the center of the atomic beam go through and intersect the center of the chamber. This shielding is necessary as lithium coating the cavity mirror surface would degrade drastically the quality of the reflectivity and increase optical losses.

All the electromagnets are carefully positioned not to contact the science chamber to avoid vibrations. The set of electromagnets surrounding the science chamber (2.8.aG)) is attached directly onto the optical table. An ensemble of electromagnets, including the one providing a large magnetic field bias (2.8.aE,F)) is positioned inside the reentrant viewport. This allows the

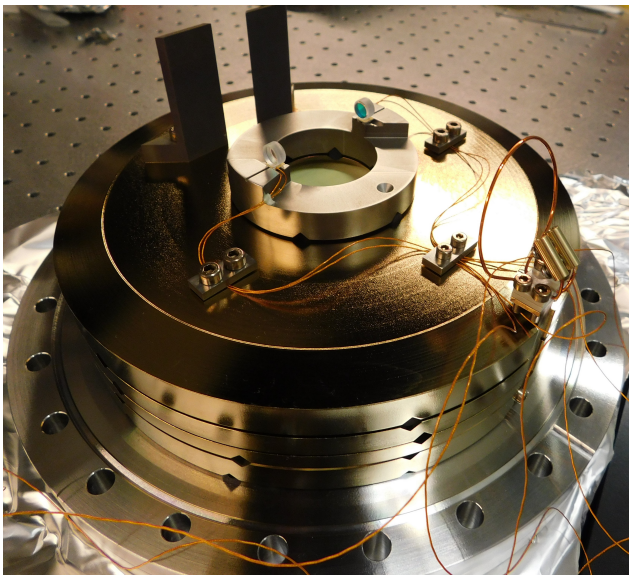

Figure 2.9: ***The cavity QED platform.*** Photograph of the science cavity ensemble prior to installation in the vacuum system.

electromagnets to come as close at 45mm from the geometric center of the chamber.

Figure 2.9 shows a picture of the entire science cavity platform prior to its installation in the science chamber. The gold color of the stainless steel rings is due to the air firing procedure explained previously. The atomic flux coming from the oven will be aligned to go through the cavity center. The size of the RF antenna allows to send a laser beam through to slow down the atomic beam exiting the oven. The RF antenna is fixed on the first isolation ring, at the very bottom, and does not contact any other rings, in order to make sure any vibration coming from the coaxial cable feeding the antenna would couple to the cavity platform.

Assembly procedure

I detail here the assembling procedure of the cavity. We made the choice of having not adjustable part inside the vacuum to minimize the risk of a misalignment of the mirror at the baking stage. We therefore pre-aligned the cavity before installing it in the science chamber and tested it by applying consecutive heating ramps to ensure that the assembly would not misalign. We carefully chose the different materials and glue in order to minimize any thermal expansion effects. To position the mirrors and glue them onto the piezoelectric actuators a simple procedure has been followed:

- Two homemade mirror mounts have been designed to hold the mirrors. These mounts leave the top half of the mirrors completely free. A small plastic screw on the side allows to keep the mirrors fixed during operation.
- These mounts are fixed onto 3−axis translation and a tip-tilt stages. This guarantees all the necessary degrees of freedom.
- A guiding laser beam (532 nm) is aligned horizontally. This will be the cavity axis reference for the rest of the procedure. The output cav-

ity mirror is placed in the beam path and therefore reflects the laser beam. Using the translation and tip-tilt platforms the mirror is positioned such that the back-reflection overlaps perfectly with the incoming beam.

- Once this alignment is correctly set, the input mirror is place in front of the output one. When the coarse alignment is completed, a weak back reflection is observed. The alignment of the input mirror is adjusted in order to align this backreflection with the incoming beam.
- Then the alignment of the resonator is optimized in order to maximize the transmission of its fundamental mode and reduce the coupling to high-order ones.
- The alignment being completed, the titanium ring where the piezoactuators have been previously glued is brought from the top and positioned upside down. As the clear surface of the mirror gives two reference points, an extra point is required to define the plane on which the cavity mirrors sit. A small tip is fixed onto the holder of the mirrors for this purpose.
- Finally a small droplet of glue is put on each mirror and the cavity holder is gently positioned to rest onto the two mirrors and the reference tip. After 24h of curing at room temperature the mirrors are very carefully removed from the temporary holding system, together with the titanium ring to which they are now glued.

This procedure is rather simple and allowed us to build the cavity used in this work. However, the critical part where the holder is positioned onto the mirrors for gluing led to a very small displacement of the mirrors. This broke the cylindrical symmetry of the resonator and led to the need to tilt the incoming beam by $\sim 5°$ to couple to the TEM_{00} mode of the resonator. This technique has since been improved by the second cavity experiment of the laboratory.

2.3.2 *Theory of Fabry-Perot resonators*

The calculations presented in this section can be found in many references, such that [80],[81]

Modes of a symmetric resonator

A Fabry-Perot optical cavity is composed of two mirrors of diameter d separated by a distance L as shown in figure 2.10. This type of resonantor is composed of concave mirrors which allows for many relative positions sustaining a stable cavity mode of the electromagnetic field inside the resonator. Here we will describe the different mode structures of such a resonator. We write the Helmholtz equation describing the electric field in the resonator :

$$\nabla^2 \vec{E}(\vec{r}) + k^2 \vec{E}(\vec{r}) = 0 \tag{2.12}$$

with $k = 2\pi/\lambda$ the wavenumber at the wavelength λ.

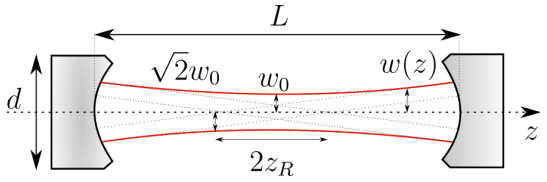

Figure 2.10: ***Fabry-Perot optical cavity.*** Two concave mirrors with a radius of curvature of R_c and diameter d are separated by a distance L. The fundamental mode of the resonator is a gaussian mode with a waist w_0, located at the cavity center and a longitudinal dependence characterized by the Rayleigh length z_r.

Starting with equation 2.12 and inserting the ansatz for the shape of the electric field as $E(r,z) = \Psi(r,z)e^{-ikz}$ we deduce one possible shape of the electric field in a cylindrical coordinate system (r,z) :

$$\Psi(r,z) = \sqrt{\frac{2}{\pi}} E_0(z) \frac{w_0}{w(z)} e^{-i\left(\Phi(z)+\frac{k}{2R(z)}r^2\right)-\frac{r^2}{w(z)^2}} \tag{2.13}$$

The mode sustained in the cavity has a Gaussian profile in the transverse plane. It is characterized by its beam radius $w(z) = w_0\sqrt{1+\frac{z}{z_R}}$.$E_0(z)$ is proportional to $\cos(kz)$, due to the standing wave nature of the intracavity field. In this expression, w_0 is the beam waist at the center of the cavity for $z = 0$ and $z_R = \pi w_0^2/\lambda$ the Rayleigh length. The curvature of the wavefront that cancels at the cavity center and is maximum around the $\pm z_R$ is captured by $R(z) = \frac{z_R^2}{z} + z$. The term $\Phi(z)$ is the so-called Gouy phase given by $\tan(\Phi(z)) = \frac{z}{z_R}$ (figure 2.10).

This solution represents the fundamental mode existing in the resonator with its characteristic Gaussian amplitude in the transverse plane. However, this is not a unique solution to equation 2.13. The boundary conditions fixing the field curvature on the mirror surfaces can allow more complex amplitudes described with the Hermite-Gauss polynomials in the Cartesian coordinate system (x,y,z) :

$$\Psi(r,z) = E_0(z)A_{n,m}(x,z,y)\frac{w_0}{w(z)}e^{-i\Phi_{n,m}(z)}e^{-i\left(\frac{k}{2R(z)}r^2\right)-\frac{r^2}{w(z)^2}} \tag{2.14}$$

$$A_{n,m}(x,z,y) = \sqrt{\frac{2}{\pi}}\left(\frac{1}{2^{n+m}n!m!}\right)^{1/2} H_n\left(\frac{\sqrt{2}x}{w(z)}\right) H_m\left(\frac{\sqrt{2}y}{w(z)}\right) \tag{2.15}$$

$$\Phi_{n,m}(z) = (n+m+1)\left(\Phi(z)-\Phi_0\right) \tag{2.16}$$

In these expression H_i are the Hermite polynomials of order i. They are defined recursively :

$$\begin{aligned} H_0(x) &= 1 \\ H_1(x) &= 2x \\ H_{n+1}(x) &= 2xH_n(x) - 2nH_{n-1}(x), \end{aligned} \tag{2.17}$$

For $(n, m) = (0, 0)$, we recover the fundamental Gaussian mode presented before. The different modes defined by the integers (n, m) forms the transverse mode structure of the Fabry-Perot cavity. We see that the Gouy phase is different depending on the order of the Hermite-Gauss mode (2.16). Consequently, each of these transverse electric modes (TEM) of the resonator have different resonance frequencies. In Chapter 3 I will explain how we make use of this transverse mode structure in the experiment.

In addition, we have to consider the boundary conditions imposed by the cavity compared to a free-space mode. It imposes that the length of the cavity represents an integer number of π phase shifts such that the electric field acquires a 2π phase shift for one roundtrip in the resonator. This translates into a relation between the length of the cavity L and the wavelength λ :

$$L = p\lambda/2 \quad p \in \mathbb{N} \tag{2.18}$$

In addition to the transverse modes, we see here a structure of consecutive longitudinal modes spaced by a frequency $\nu_{FSR} = c/2L$ which is called the free spectral range (FSR). Here c denotes the speed of light in vacuum.

For each of these longitudinal modes, defined by their wavevector k, there is a substructure composed of transverse modes that differs from the fundamental one by their transverse amplitude profile. For a longitudinal mode of order q and a transverse mode (n, m) the resonance frequency is given by :

$$\nu_{p,n,m} = \frac{c}{2\pi L}\left((p+1) + (n+m+1)\right)\arccos(g) \tag{2.19}$$

For two consecutive transverse modes $(n+m) \rightarrow (n+m+1)$ belonging to the same longitudinal mode $q = 0$, we obtain the transverse mode spacing for a symmetric cavity ($g = 1 - L/R_c$ with R_c the radius of curvature of the mirrors) to be :

$$\nu_{TEM} = \frac{c}{2\pi L}\arccos(g) \tag{2.20}$$

The cavity mirror parameter g is used to classify the Fabry-Perot cavity geometries and their intrinsic stability. If the distance between the two mirrors combined with the chosen radius of curvature are not properly adapted, the cavity does not support a stable cavity mode. The stability condition is given by [81] :

$$0 < g_1 g_2 < 1 \tag{2.21}$$

The special case where the distance is chosen to be equal to the radius of curvature ($g = 0$) is called a confocal cavity. This is the most stable configuration which can tolerate misalignment between the two mirrors forming the cavity. In this specific case, all the transverse modes are perfectly degenerate in frequency. As our cavity differs from this configuration, we observe the presence of several transverse mode families at finite frequency from the fundamental mode of the resonator.

Finesse of a Fabry-Perot cavity

After having briefly described the mode structure of a Fabry-Perot cavity I will now show some properties of the cavity field and how they relate to the properties of the mirrors. The mirrors have reflection, transmission and loss coefficients r, t and l for the field amplitude.

We write down the total cavity field amplitude for an incident power on the input mirror E_{in}. As shown in figure 2.11, the field E_{tr} transmitted by the cavity as a function of the frequency of the incoming beam $\omega = 2\pi c/\lambda$ with c the speed of light and λ the wavelength reads

$$E_{tr} = E_{in} t^2 e^{-i\frac{\omega}{c}L} \left(\sum_{n=0}^{\infty} r^{2n} e^{-i\frac{\omega}{c}L(2n)} \right) \tag{2.22}$$

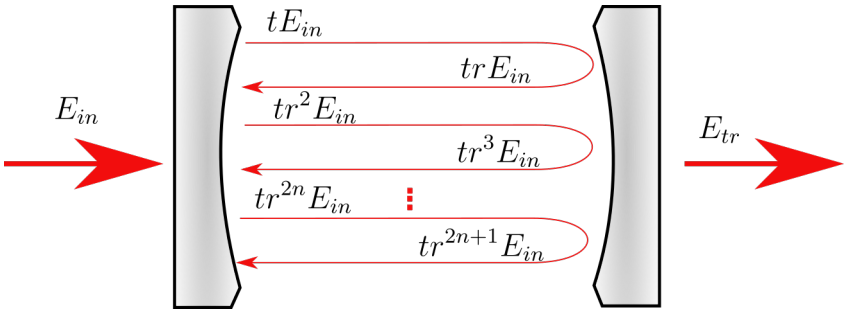

Figure 2.11: ***Intracavity light field.*** The cavity is injected with a light field of amplitude E_{in} and power $P_{in} = |E_{in}|^2$. Each mirror has a reflection coefficient r and transmission coefficient t for the field amplitude. The length of the cavity L induces a phase shift per round trip in the cavity e^{i2kL}. Part of the light leaks out through the cavity output mirror with a field amplitude E_{tr}.

By taking the modulus square of equation 2.22 we get the power P_{tr} exiting the cavity relatively to the input power,

$$P_{tr}/P_{in} = T^2 \frac{1}{1 + R^2 - 2R\cos(\nu/\nu_{FSR})} \tag{2.23}$$

with $\nu_{FSR} = c/2L$ the Free Spectral range as defined previously and $R = r^2$ and $T = t^2$ the reflection and transmission coefficients in intensity. We express the ratio between the FSR and the full width at half maximum of the cavity transmission, $\mathcal{F} = \nu_{FSR}/2\delta\nu$ that corresponds to the finesse of the cavity. This finesse can be interpreted as the number of roundtrips experienced by a photon that couples into the cavity before exiting it. Using equation 2.23 in the limit of low losses, we write down the finesse as :

$$\mathcal{F} = \frac{\pi\sqrt{R}}{(1-R)} \simeq \frac{\pi}{1-R} \tag{2.24}$$

The typical decay time of the cavity light field is governed by the losses of the cavity and consequently by the value of the finesse. The cavity linewidth $\kappa = 2\delta\nu = 1/2\pi\tau_c$ with τ_c the photon lifetime in the cavity. Measuring the exponential decay of the cavity light field gives a direct measurement of κ and thus of the finesse.

We can also link the finesse to the power-build up of the cavity. Writing down the intra-cavity amplitude of the electric field as the sum of electromagnetic waves propagating in the forward and backward direction (figure 2.11) :

$$E_c = E_{in} t \left(\sum_{n=0}^{\infty} r^{2n+1} t e^{-ikL(2n+1)} + \sum_{n=0}^{\infty} r^{2n} t e^{-ikL(2n)} \right) \tag{2.25}$$

Considering that the cavity is pumped resonantly, the complex terms vanish,

$$E_c/E_{in} = t\,(1+r) \left(\sum_{n=0}^{\infty} r^{2n} t \right) \tag{2.26}$$

By taking the modulus square of equation 2.26 we can get the cavity power build up at the center :

$$P_c/P_{in} = t^2 \frac{(1+r)^2}{(1-r^2)^2} = \frac{\mathcal{F}}{\pi r} (1+r)^2, \tag{2.27}$$

This simplifies even further in the case where both the losses and the transmission are small compared with the reflection coefficient (in the case of this cavity $T + L < 0.1\%$),

$$P_c/P_{in} \simeq \frac{4\mathcal{F}}{\pi}, \tag{2.28}$$

This feature is very interesting as it will allow for the creation of deep optical potentials using a very small amount of laser power, as it will be explain in Chapter 3.

Measurement of the cavity finesse and linewidth

As we have just shown the decay of the cavity intensity directly links to the linewidth κ of the cavity. Knowing both the linewidth and the FSR gives a direct access to the cavity finesse. To measure the decay of the cavity field we perform a ring-down measurement, as shown in figure 2.12.c. A laser beam at 671 nm is set resonant with the cavity frequency and abruptly turned off in a time short compared to the expected decay rate of the cavity. The light intensity decay is recorded by an avalanche photodiode allowing us to extract a time constant $\tau_c = 2.06$ µs leading to a linewidth of $\kappa = 77.4$ kHz. This technique is extremely convenient as the signal to noise ratio allows for very precise determination of κ. However, it requires that the cavity length and the frequency of the laser beam are stable with respect to each other. This was not available at the time when the cavity was tested and then installed inside the vacuum chamber.

Consequently we used another technique that does not rely on such a frequency stability. In this measurement, neither the laser frequency nor the cavity length are stabilized. The cavity is left free-running while the laser frequency is swept by a few GHz over 100 ms such that the laser beam frequency is scanned across the cavity resonance. As the laser frequency is swept through the cavity resonance, the transmitted light acquires

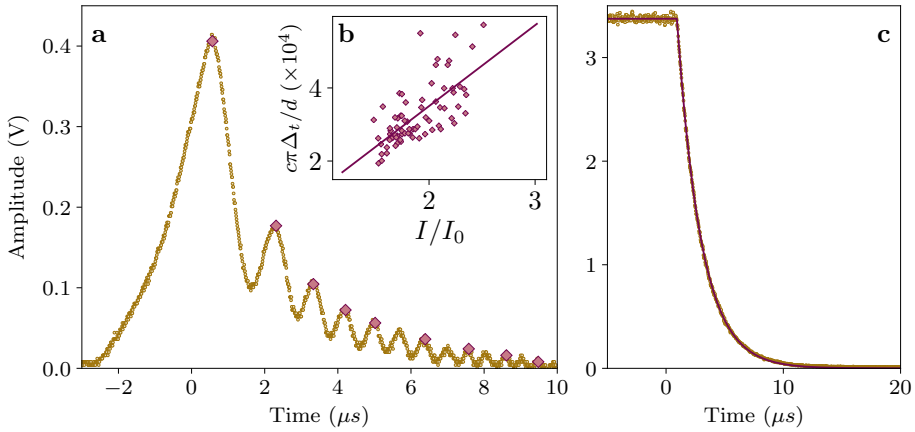

Figure 2.12: ***Characterization of the cavity finesse.*** **a** The laser beam frequency is swept through the cavity resonance inducing oscillations of the cavity transmission signal due to interferences between the transmitted and reflected light. These oscillations capture the finesse of the cavity in the ratio of the amplitude and the period. **b** Many realizations of the ringing sweeps (violet diamonds) where the ratio between the normalized speed of the sweep is plotted versus the amplitude ratio of the first two oscillations. A linear fit (violet solid line) gives the value of the finesse $F = 5 \times 10^4$. **c** The laser beam frequency is set to be resonant with the cavity resonance frequency. There the laser beam amplitude is set to zero in a time faster than the expected cavity intensity decay rate. The intensity decay (yellow circles) is recorded on an avalanche photodiode. An exponential decay fit allows to extract the value of the decay constant $\kappa = 1/(2\pi\tau_c) = 77.4$ kHz.

a time-dependent phase leading to interferences as it is shown in figure 2.12.a. Reference [82] gives the expression of the time dependent phase

$$\varphi(t) = (2n-1)\varphi_1(t) - \pi n(n-1)\frac{\Omega}{\nu_{FSR}} \tag{2.29}$$

with n the number of round-trips in the cavity, $\phi_1(t) = 2\pi d(t)/\lambda$ the phase due to the time dependent displacement of the cavity mirror $d(t)$ and $\Omega = 2v/\lambda$ the sweep rate of the cavity resonance frequency. The fact that the light field in the cavity at time t has a different frequency with respect the one entering the cavity at time $t + \delta t$ leads to interferences that modulate the Lorentzian envelope of the cavity transmission. This is possible if the frequency sweep rate is faster than the typical cavity decay rate given by κ. The frequency and the contrast of this interference relates to the value of the finesse [82] :

$$\frac{\pi c}{d}\Delta t = \frac{\mathcal{F}}{2}\left(\frac{I}{I_0} + 2 - e\right) \tag{2.30}$$

where I and I_0 are the amplitudes of the first two interference peaks (figure 2.12.a) and Δt the time difference between the same two peaks. Varying the scan speed, e.g $\frac{\pi c}{d}\Delta t$, in order to obtain ratios of $I/I_0 \simeq e$ will give a value for the finesse. As this measurement cannot be accurate without a great control on the frequency sweep rate between the cavity resonance and the laser frequency we realize many measurements and perform a linear fit of $\frac{\pi c}{d}\Delta t$ around the point where $I/I_0 \simeq e$ as shown in figure 2.12.b.

This measurement give a finesse of 5×10^4, leading to a value of the cavity linewidth $\kappa = 2\pi \times 77$ kHz, very close to the more precise one obtained with the ring-down measurement ($\kappa = 2\pi \times 73(4)$ kHz).

2.3.3 *Optical properties of the science cavity*

Here we summarize the optical properties of the science cavity used in this work. The science cavity is resonant at three different wavelengths that we use for different purposes in the experiment :

- 671 nm which is the wavelength resonant with the D-line of ^{6}Li.
- 1064 nm is far from any atomic resonances and is used used to trap the atoms.
- 532 nm is also far from any atomic resonances and is used to stabilize the length of the science cavity.

Table 2.4: Science cavity optical properties.

	671 nm	532 nm	1064 nm
Cavity length	4.131(1) cm		
Free spectral range (ν_{FSR})	3.6277(1) GHz		
Transverse Mode Spacing (ν_{TEM})	2.634(1) GHz		
Mirror diameter	7.75 mm		
HR coating transmission	T $\simeq$ 50 ppm	T $<$ 0.1 %	
Finesse	$4.7(1) \cdot 10^4$	$2.4(1) \cdot 10^3$	$3.6(1) \cdot 10^3$
Linewidth $\kappa/2\pi$	0.077(1) MHz	1.5(1) MHz	1.0(1) MHz
TEM_{00} Mode waist	45.0(3) µm	40.1(3) µm	56.6(3) µm

All the wavelengths are reflected by the dielectric coating deposited on the cavity mirror surface. This coating is chosen to have high reflectivity and low losses at 532 and 1064 nm. At 671 nm, it is specifically designed to have a very large reflectivity ($\simeq$ 50 ppm of transmission) combined with very small losses ($\simeq$ 10 ppm). These quantities govern the linewidth of the cavity κ. As the cavity has a much larger reflectivity at 671 nm compared with the two other wavelengths, the cavity will have a much smaller linewidth at this wavelength. The measurement of the cavity linewitdh and finesse for each wavelength are reported in table 2.4.

We have spectroscopically measured both the longitudinal and transverse mode spacing of the cavity. From the FSR, $\nu_{FSR} = 3.6277(1)$ GHz we obtain the length of the cavity L while the transverse mode spacing links to the radius of curvature of the mirror, thus to the cavity mode waist. All numerical values of the science cavity properties are reported in table 2.4.

Another cavity is used on this experiment in order to stabilize the frequency of the different lasers with respect to each other and to reference them onto the same frequency reference given by the transition frequency of ^{6}Li. The properties of this cavity are described in Appendix A, table A.1. More details about the design of the transfer cavity can be found in the appendix A.

2.4 ELECTROMAGNETS

2.4.1 General overview and simulation of magnetic fields

A complex ensemble of electromagnets surrounds the science chamber hosting the optical cavity to create various magnetic fields needed during the experimental sequence. In this section, I will present all the electromagnets installed on the apparatus. I will show how the entire electromagnet setup has been simulated and how this simulation has been compared with the coils used on the experiment. More specifically, I will detail the set of electromagnets that provides the large bias magnetic field with an integrated water cooling, fitting in the constrained space left inside the reentrant viewport. Lastly, I will present the RF antenna and its the impedance matching circuit which makes it possible to obtain a doubly resonant circuit suited for the RF spectroscopy of ^{6}Li at high magnetic field.

2.4.2 Summary of coil properties

We have multiple sets of electromagnets on the experiment :

- A tapered and horizontal water-cooled coil placed around the pipe connecting the oven section and the science chamber : the Zeeman slower coil (figure 2.13).
- A set comprising several pairs of water-cooled electromagnets placed around the science and inside the reentrant viewport. The blue and orange coils are the Helmholtz and MOT coils (figure 2.13). The red coils inside the reentrant viewports are the Feshbach coils (figure 2.13), that provides the large bias magnetic field.
- Several compensation coils, sustaining small currents that are used to create small magnetic fields in order to compensate for magnetic field offsets (figure 2.13).

All the coils are visible on figures 2.2.b and 2.5.a. In order to specify these coils, a numerical model of the entire apparatus has been produced based on the Radia library developed at the ESRF [83]. Figure 2.13 shows a 3D view of the electromagnets of the apparatus. Each of this coil is characterized by a given volume to which is attributed a current density. This way of defining them allows to reproduce complex shapes, such that the one of the Feshabch coils (see section 2.4.3).

I will now describe the main characteristics of each coil shown in figure 2.13.

- First one can first see that the Zeeman slower coil is composed of 7 concentric coils. The first six are connected in series and driven by a single power supply. The last coil (the closest to the science chamber) is controlled with a different power supply.

  An example of simulation is shown in figure 2.14. Here, the field of the Zeeman slower coils is simulated for 24 A flowing through the first 5 coils and 15 A in the last section (dashed yellow and violet lines). This simulated magnetic field B_y along the Zeeman slower axis y is compared to the measured one (yellow circle an violet diamonds). The grey solid line shows the simulated total field created by all the

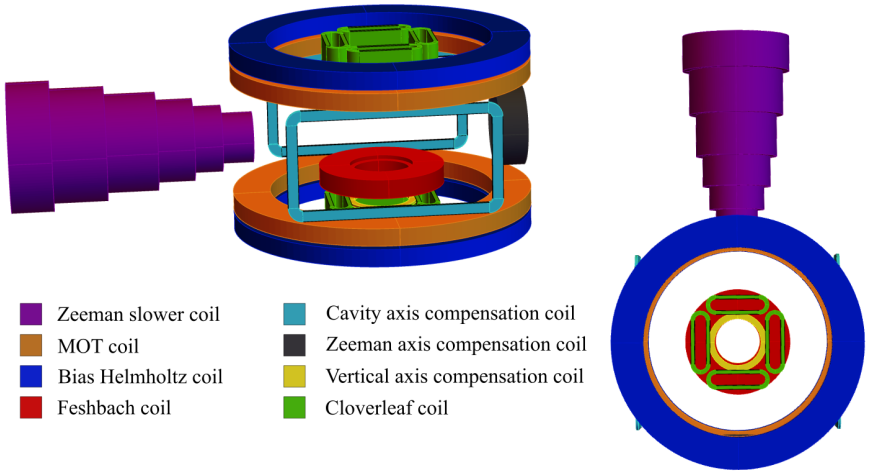

Figure 2.13: ***Radia simulation of the electromagnet setup.*** Each electromagnet is reproduced in this two 3D-view of the simulation with a side view on the left and a top-view on the right. Each electromagnet corresponds to a different color on the figure. For each electromagnet a density of current can be attributed in order to simulate the magnetic field at any point in space.

sections of the Zeeeman slower coil. We see that the Radia simulation is in very good agreement with the measurement of the magnetic field profile of the Zeeman slower coil.

- It is clearly visible in figure 2.5.a that the coils positioned around the science chamber are composed of two different sets of electromagnets. In blue, the coils create a flat bias field as the current run through both coils in the same direction and that they are positioned to follow the so-called Helmholtz condition $d = R$ with d the distance separating the two coil and R their radii. The orange pair of coils are connected in such a way that both coils have current flowing in opposite directions, thus creating a gradient of magnetic field crossing zero at the geometric center of the chamber.

- Inside this pairs of coil, we see an ensemble comprising : (i) the Feshbach coils (figure 2.13 in red) that come deep in the reentrant viewport. These coils provide a large bias field at the center of the chamber, as well as a negative field curvature of 25 G/cm^2 producing a weak trapping potential for the atoms in the horizontal plane. The design of these coils will be presented in details in section 2.4.3. (ii) A set of four coils in the cloverleaf configuration (figure 2.13 in green). Each vertical pair has the same current polarity with the symmetric pair having the opposite polarity. This configuration provides a tunable magnetic field gradient along the two directions in the horizontal plane, suited to displace the saddle point of the magnetic field created by the Feshbach coils. These coils are controlled by one power supply for each direction in the horizontal plane.

- A small pair of coils (figure 2.13 in yellow), with low inductance and identical polarity that allows to compensate for magnetic field offsets in the vertical direction.

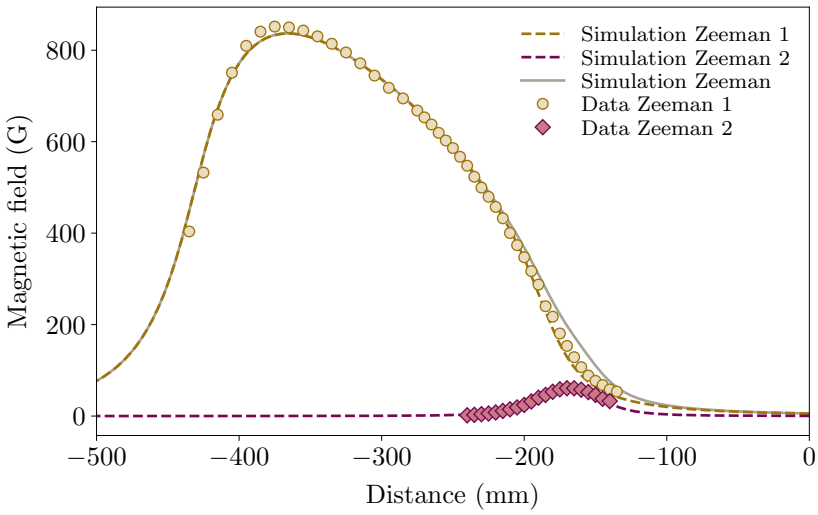

Figure 2.14: ***Zeeman slower magnetic field : simulation and measurement.*** The Zeeman slower coil is composed of 5 sections in serie (indicated in yellow) and a last section driven with an independent power supply (in violet) creating two independent magnetic field distributions. The figure shows the comparison between the magnetic field distributions measured along the axis of the Zeeman slower (yellow circles and violet diamonds) and the distribution obtained from the Radia simulation (yellow and violet dashed lines respectively). The total field is indicated by the solid grey line.

- Last, small compensation coils are placed around the vacuum chamber. A first pair of compensation coils is placed along the cavity axis (figure 2.13 in light blue). Second, a coil is wound directly around the conical pipe connecting the science chamber to the pumping section. This one has the opposite polarity compared with the last coil of the Zeeman slower. These two coils allow to finely compensate the magnetic field in the direction orthogonal to the cavity axis.

The table 2.5 summarizes the properties of the main electromagnets of the experiment presented above. It shows that four of the electromagnets require an active cooling as they dissipate more than 400 W of electrical power.

- The cooling of the Zeeman slower coil is ensured by its holder. Its support is made out of two concentric tubes creating a duct of water. This cooling works relatively well for the thin section but the first two large ones are very poorly cooled, their thickness being larger. This coil is made of 3mm insulated rectangular wire, which makes the cooling of the outer layers very limited. To cure this issue, we have wired a 6 mm diameter water pipe around the Zeeman slower, which reduces the heating of the ambient air by this hot sections, therefore increasing the stability of the experiment.
- The large MOT and Helmholtz coils are based on hollow-core copper wire (square 4 mm with 1 mm diameter hole at the center). The coolant is flowing through the hole at the center of the wire. This cooling is extremely efficient but the length of wire used to make the coils

Table 2.5: Main electromagnet properties.

	Power supply	Number of turns (per coil)	Total Resistance (in Ω)	Typical Power dissipated (kW
MOT	Delta Elektronika SM18 – 220	32	0.145	3.5
Bias Helmholtz	Delta Elektronika SM18 – 220	32	0.144	3.5
Feshbach	2 Delta Elektronika SM18 – 220	31	0.045	4.5
Zeeman 1	Delta Elektronika SM70 – AR – 24	[180, 190, 144, 78, 40]	0.745	0.4
Zeeman 2	Matsusada RK – 80L – LRmf	22	0.017	0.003
Cloverleaf	Matsusada RK10 – 40	50	0.305	0.088

induce a large pressure drop, thus requiring either a high-pressure water circuit or the parallelization of the cooling of the different sections, leading to the necessity of having height water connections for each of the coil block below and above the chamber.

- The Feshbach coil are water-cooled by bringing the coolant fluid directly in contact with the upper surface of the coil. This will be presented in section 2.4.3.
- The other electromagnets are used with low enough current that they do not require any active cooling. However, four coils among the cloverleaf coils that were used to finely positioned the saddle point of the Feshbach field across the cavity axis have shown significant heating as they were used at more than 20 A. The heating was significant enough that a manual displacement of the Feshbach coils has been necessary to reduce the position correction to lower currents, avoiding this unnecessary heating source. The electrical properties of this compensations coils are summarized in table 2.6.

2.4.3 *Compact bulk-machined electromagnets for quantum gases experiments*

This section is inspired from [84].

Table 2.6: Auxiliary electromagnet properties.

	Power supply	Number of turns	Resistance (in Ω)
Cavity axis compensation	Matsusada RK − 80L − LRmf	1×10	0.046
Zeeman slower compensation	Matsusada RK − 80L − LRmf	5×11	0.144
Vertical compensation	Matsusada RK − 80L − LRmf	1×15	0.345

Motivation

Quantum gases requires large magnetic fields for a variety of application, from laser cooling to magnetic trapping [85]. A very appealing feature of some atomic species is the existence of very strong, short-range interactions that are tunable by applying an external magnetic field [71] which are of great interest for quantum simulation of strongly correlated materials. However combining large electromagnets with the prerequisites of optical access for a quantum gas experiment is an important technical challenge that has been tackled by several groups in the past years in order to combine, in extremely compact design, efficient water cooling and large currents. For example innovative design for Zeeman slower coils [86, 87] as well as Bitter-type electromagnets [88–90] has been developed and brought to experimental setups. Moreover miniaturizing atom traps using in-vacuum electromagnets [91–93] or atom chips [94, 95] has allowed to reduce further down the need for high current and consequently the necessity of active cooling.

In contrast with this route that diminish the need of cooling but increase significantly the complexity of the vacuum system, we based our approach on improving the heat management [96], keeping the system as simple as possible compared with the usual design consisting in wound copper wire. This design is usually sufficient for low current applications. However, when large magnetic fields are needed the wires need to be adapted in order to be efficiently water-cooled. This is usually done by the use of hollow-core copper wire where the coolant fluid circulates directly inside the wire all along the coil, as for our MOT and Helmholtz coils presented in the previous part. The main drawback of this approach lays into the intrinsic conductance drop induce by a small section - long pipe design. In this case, a typical coil would represent a 100 m long pipe with a diameter of about 1 mm which leads to a very restricted flow rate in usual water circuit which are limited to pressures of about 4 bar. Consequently water-cooled electromagnets typically used in quantum gases experiment require either the use of compressors to obtain large over pressure (40 bar), or the need to parallelize the cooling inside the coil by dividing the cooling circuit into several sub-coils, all assembled in parallel on the main water circuit. Both solutions lead to an increase either in complexity, or in risk of water leaks that can be quite detrimental on sur-

rounding optical systems routinely used. Moreover this approach requires the full coil to be casted into epoxy resin in order to hold the wires in place. This increase the size of the ensemble, making it quite complicated to use in constrained space as it is often required in experimental apparatus.

As explored by the Bitter-type approach [88–90], configurations where the coolant circuit does not follow exactly the electrical current path provides very efficient cooling. However, this type of electromagnet requires each winding of the coil to hold a coolant connection making it complex to realize. Some improvements have been proposed on this technique [97] as well as for hollow-core copper based coils [98]. For the design we have developed in this work, we use a similar idea as in [96] where all the rings composing the coils are water cooled in parallel using a coolant duct than runs directly on top of the coil. This combined with a single-block, machinable at-wish design allows to reduce greatly the footprint of the electromagnet, making it a serious candidate for a use in quantum gases apparatus where available space around the vacuum chamber is extremely reduced.

Design

The design of the bulk-machined coil, called Feshbach coil on the apparatus, is based on a copper ring that is machined using an electro-erosion procedure to cut out a spiral from a massive cylinder of copper. This constitutes the body of the coil. The coolant circuit flows on the top face of the copper cylinder, making each turn of the coil in direct contact with water (figure 2.15.b). This duct is made leak-tight by pressing a PEEK[1] cap against the coil body, itself compressing EDPM[2] orings that ensure a proper contact between the two pieces. The cloverleaf coils are mounted onto this PEEK cap and the entire coil block is held by an aluminum plate itseld fixed onto the MOT coil block around the chamber (figure 2.15.a). The bottom of the Feshbach coils come at about 1 mm from the glass surface of the reentrant viewport, hence bringing the bottom of the coil at 45 mm from the atomic cloud. As showed in figure 2.15.a.b.c the electrical connection is 2 mm thick and runs against the outer diameter of the coil. The current is brought along one of the plate. The plate contacts a copper bar inserted inside the coil body (isolated from it using a ceramic cylinder around it) bringing the electrical current to the start of the spiral on the inner diameter of the copper block. There, the current follows the spiral until the end of it, on the outer diameter. On the way back the electrical current flows up, following the other copper bar. This configuration allows to cancel out the field due to the cable bringing in and out the current from the power supply. The copper rod inside the coil body does break the rotational symmetry of the coil but the tilt of the magnetic field axis is not measurable.

The raw oxygen-free copper cylinder of inner and outer radii 32 and 72 mm, respectively, is electro-eroded in order to draw a spiral with a cut out of 0.38 mm width, leaving a copper pitch of 0.92 mm. The spiral consists of 31 turns with a height of the coil body of 22 mm. The body of the coil where the spiral has been machined is then filled with glass-fiber spacers and finally with epoxy prior to the final shaping of the coil. This makes the coil body perfectly single block. The detail of machining and assembly procedure will be explained in the next paragraph.

1 Polyether ether ketone
2 Ethylene Propylene Diene Methylene, EDPM 70, Shore A, 1.5 mm cord and 6 mm

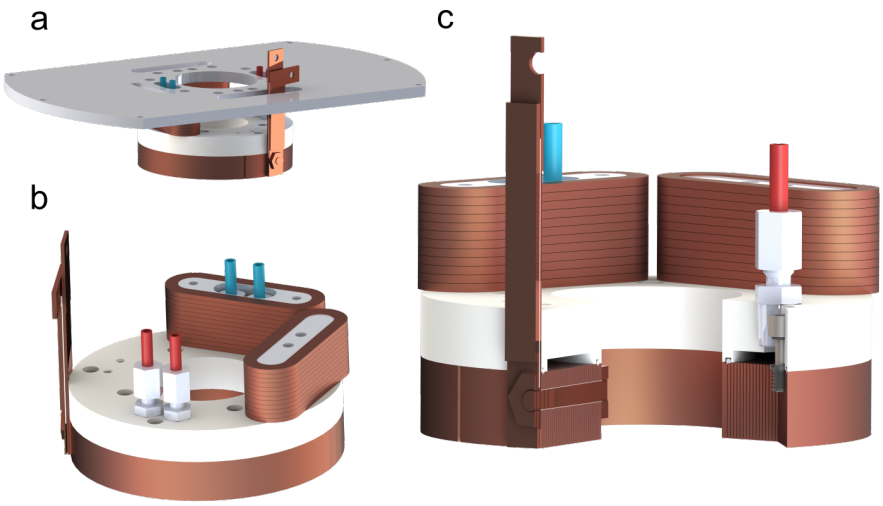

Figure 2.15: ***CAD view of the Feshbach electromagnets.*** **a** The bloc of coils containing the Feshbach coil and a set of four auxiliary electromagnets in the cloverleaf configuration are attached onto an aluminum support plate fixed directly onto the MOT coil. **b** The support plate is fixed into the PEEK cap used to create the duct where the water is circulating on top of the Feshbach coil. The water inlets and outlets are accommodated in the mount of two of the cloverleaf coils. The electrical connections of the Feshbach coil are fixed onto the aluminium plate. **c** The inner and outer turns of the Feshbach coil are connected to the electrical connection via a copper screw oriented radially throught the coil body. Standard SERTO connectors are screwed directly into the peak cap ensuring tight water connections. The duct of 4 mm height allows for a large coolant flow with a reasonable differential pressure of 4 bars. The PEEK cap is pressed against the copper body by titanium screws. PEEK M4 inserts are fixed into the coil body which avoid the titanium screw to create short circuit between consecutive turns. EDPM orings are installed in ridges at the inner and outer perimeter as well as below the titanium screws to make sure the ensemble is completely leak tight.

Our design makes it possible to bring water on the upper surface of the coil, into the duct created between the PEEK cap and the upper surface of the coil 2.15.c. The PEEK cap is pressed against the coil body by titanium screws that are tightened directly into the coil body 2.15.c. PEEK inserts are tightened in the M6 threaded holes made in the coil body. These inserts have an M4 inner thread such that the titanium screws pressing the PEEK cap are not in direct contact with the copper spiral, avoiding electrical short circuit. The head of the crew presses against the PEEK cap with a EPDM orings[3] sealing the connection.

The cloverleaf coils are fixed on top of the PEEK cap, making them symmetrically positioned around the magnetic field profile created by the Feshbach coils along the vertical axis. Long titanium screws presses the aluminum plate against the PEEK cap, compressing the cloverleaf coils in between. The entire coil block is consequently held by four titanium screws. The water inlets and outlets consists in standard SERTO connectors which are tightened directly in the PEEK cap with silicon placed in the thread to ensure proper connections. The coil body, once casted into epoxy, is machinable at will. In our case a ridge has been cut out on the bottom side on the coil, removing 5 mm in height and 10 mm from the inner radius to fit the

3 Ethylene Propylene Diene Methylene, EDPM 70, Shore A, 1.5 mm

reentrant viewport as closely as possible. A total of 8 threaded holes are drilled on the upper surface of the coil and a last stage of machining to clear out the glue on the upper surface is performed right at the end of the assembly procedure. This feature of the design facilitate to fit the electromagnet in very crowded space as usually encountered in quantum gases experiments.

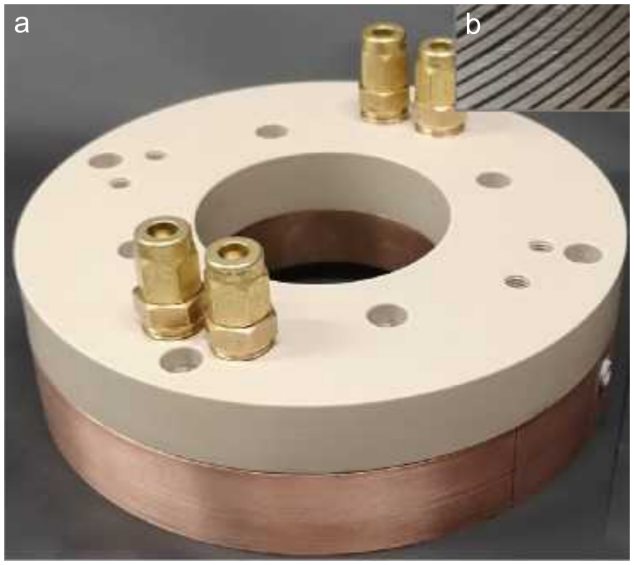

Figure 2.16: ***Assembled Feshbach coils.*** **a** Picture of the assemble Feshbach coil with the SERTO connections (yellow) mounted onto the PEEK cap (light grey) itself pressed against the coil body (copper) **b** Close view of the top surface of the coil after machining showing the copper turns (0.92 mm wide) of the coil separated by spaces of 0.38 mm filled with homemade epoxy glue.

Figure 2.16.a shows the final assembly of the Feshbach coil. The top surface of the coil (figure 2.16.b) is machined to ensure the direct contact between the copper of the spiral and the coolant fluid. This picture shows the possibility of machining the coil body after all the gluing procedure. In fact no short circuits between consecutive wire have been observed after the machining of the surface neither of the threaded holes. One could imagine texturing the upper surface in order to increase the heat exchange between the coolant fluid and the copper, thus improving the cooling capability of this design.

Assembly procedure

The assembly of this electromagnet is quite simple but nevertheless requires fine tuning of many parameters. I will go through each step and describe the critical points and the references of the material used. This technique has also been applied by the second experiment of the laboratory to reproduce similar electromagnets and following these steps led to a flawless result.

- A raw piece of oxygen-free copper is machined to bring it to a cylinder shape. To avoid the machined coil to expand like a metallic spring after machining, it is important to keep the spiral attached at its start and end. Thus, the inner diameter is cut smaller that the target one and the

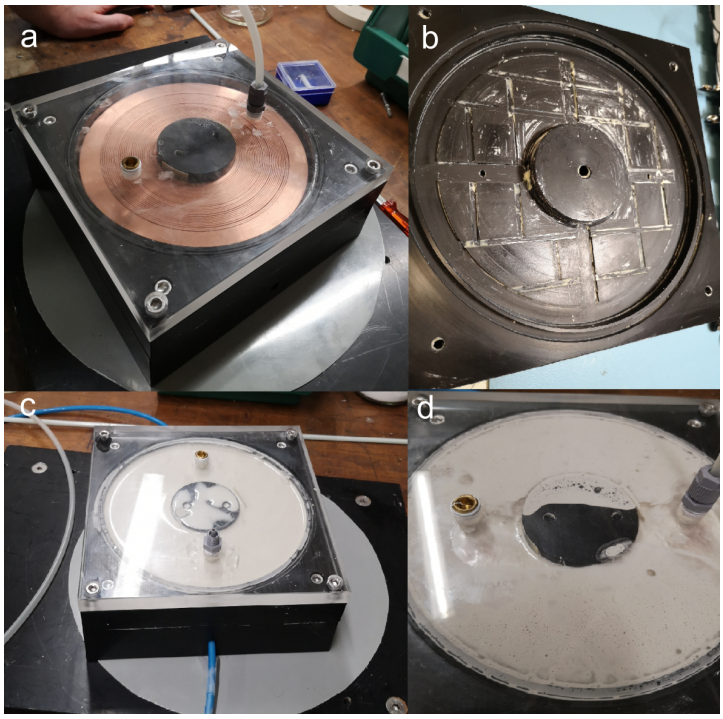

Figure 2.17: ***The gluing procedure for bulk-machined electromagnets.*** **a** The coil after wire electroerosion machining. Fiber glass spacers are inserted in between consecutive turns along the spiral. It is then placed in a plastic mold hermetically closed with a plastic cap and orings. **b** The mold is machined with ridges on the bottom face to allow the epoxy to spread on the entire bottom face of the coil. Two holes are drilled from the outside into these ridges to inject the epoxy. Wax is spread on the full inside face of the mold to avoid the glue to fix the coil in the mold after the drying stage. **c** A reservoir of homemade filled epoxy is connected to the bottom face of the mold (blue pipe). From the top, a scroll pump is connected in order to generate a primary vacuum of $\sim 10^{-2}$ mbar inside the mold. This permit the glue to migrate from the reservoir to the top side of the mold. **d** Once the glue has uniformly been injected in the structure, it is left 24 h in order to dry and solidify. Afterwards the mold (made of several plastic pieces) is dismantled and the bloc is machined to remove the excess of glue on the top and the bottom face and bring the inner and outer radius to the specified ones.

outer is kept significantly larger. A small hole is made where the spiral is supposed to start in order to insert the wire of the electro-erosion machine. Once the full cut out of the spiral is done, a small (2mm long) radial cut out is made towards the outer diameter.

- The coil is placed inside a mold 2.18.a. There fiber glass reinforced spacers are placed to guarantee a uniform spacing between each consecutive turns. Prior to placing the coil in the mold, wax is applied on the full inner surface.
- The mold is made of different assembled parts such that it can be dismantled to free the coil after the epoxy impregnation. The bottom of the mold is machined with many ridges (figure 2.18.b) that will ultimately allow the glue to spread all over the coil.
- The mold is hermetically closed. A primary vacuum pump is connected to it on the top panel (figure 2.18.c). The bottom plate of the

mold has several holes allowing to inject the glue from the bottom. The glue in the reservoir is pumped through the coil spiral by the pump until the full coil is impregnated with the epoxy.

- The epoxy used to fill the spiral gaps is a critical point. It needs to be fluid enough to completely fill the spiral. Moreover because of thermal expansion coefficient mismatch with the copper it ideally need to dry at relatively low or even room temperature. Finally post machining requires the epoxy to not crackle. For these purposes we have developed an homemade epoxy based on a commercial, low viscosity room temperature curing epoxy [4]. This epoxy is filled with 10% of 0.25 µm fiber-glass flake and 30% aluminium nitride (AlN) powder[5]. AlN improves heat dissipation through the inter-turns spacing as well as it hardens the epoxy. The flakes avoid that craks develop through the glue which would lead to water leaks through the coil.
- Once the glue has properly filled the full mold (figure 2.18.d) and dried for 24 h the mold is dismanteled to free the coil.
- Finally the coil is machined to bring the inner and outer diameter on specifications. The upper surface is machined to clear the copper and allows perfect contact with water.
- Last all holes for the electrical connection rod (5.5 mm through hole) and for the screws (M6 threaded holes) that will press the cap against the coil are made.

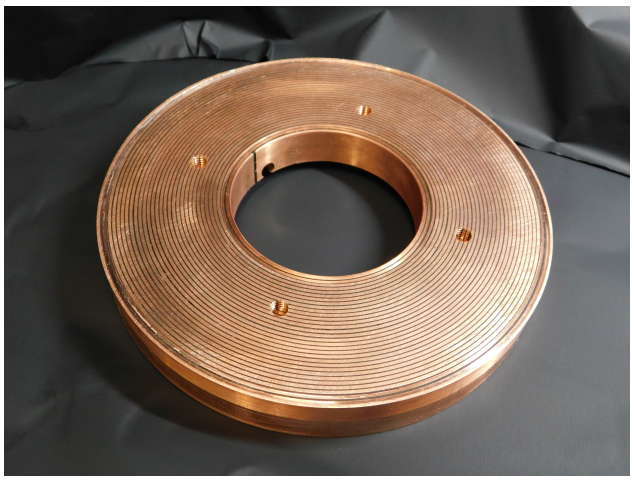

Figure 2.18: ***Bulk-machined electromagnet.*** Picture of the bulk-machined electromagnet after the last set of machining to provide a direct and clean copper interface on the top for direct water cooling. The threaded holes drilled in the coil accommodate M6 to M4 PEEK adaptors. This will be used to press the PEEK cap against the coil body, compressing the Orings placed in the ridges machined in the coil body on the inner and outer diameter.

Applying this procedure leads to an ensemble that is composed of copper up to 70% of the total volume, which is very beneficial in term of thermal conductivity. The U-shaped PEEK cap is then attached with 8 screws to the

4 Sicomin SR1710/SD7820
5 Sigma Aldritch 10 µm, > 98% purity

coil body and presses the EDPM orings on the inner and outer diameter to make the connection leak-tight. Allowing to leave a few mm of raw copper on the inner and outer diameters would permit the oring to lay only on a copper band making the connection safer. Moreover it would guarantee that the first and last turns of the spiral are in direct contact with water, which is not the case with this design as they are exactly below the oring, avoiding direct cooling by water circulating in the duct.

It is possible to carve almost any shape on the bottom side of coil body once it is impregnated with glue. Leaving a minimal space of 5 mm between the upper and lower carved surface should guarantee the absence of leak through the coil. We carved a rectangle of 5 mm within the 22mm of the coil total height with 10 mm width in order to adapt to the shape of the bottom face to the exact profile of the reentrant viewport. This procedure did not show any weakening of the coil at this location. This locally increases the resistance of the wire as their height is reduced by 25% without showing any increased heating compared with the rest of the coil body.

Magnetic fields

We used the Radia simulation package to simulate the full magnetic field distribution. This takes into account the ridge on the bottom side and the electrical connection rod going through the coil. We simulate the vertical component of the magnetic field B_z along the axis of the coil z (solid yellow line in figure 2.19.a) (which is also the vertical axis on the experiment). We also simulate the magnetic field B_z in the plane, along the x−axis, located 52 mm away from the coil center along the vertical axis (solid yellow line in figure 2.19.b). This position corresponds to the position of the atomic plane in the real apparatus.

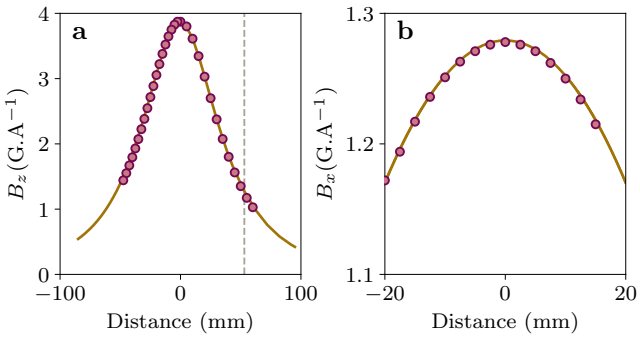

Figure 2.19: ***Magnetic field created by one Feshbach electromagnet.*** **(a)** and **(b)** display the magnetic field created by a single Feshbach coil. **(a)** shows the evolution of the magnetic field along the axis of the cylinder while **(b)** shows the field variation in a plane located 45mm away from the bottom of the coil (grey dashed line), corresponding to the expected position of the atomic cloud. The violet diamond shows the measured magnetic field which is compared with the Radia simulation (yellow solid line) accounting for the exact shape of the coil.

This simulation is compared with measurement realized with a Hall sensor [6] displaced using a translation platform. Results are shown in figure 2.19.a.b) with violet circles. We see that the simulation describes accurately

6 Lakeshore 425 / HMNA-1094-VR

the actual field distribution for one electromagnet with a maximum field in the atomic plane of 1.28 $G{\cdot}A^{-1}$. In the actual setup we have calibrated the magnetic field created by the pair of Feshbach coils to be 2.7013 $G \cdot A^{-1}$. This means that reaching the Feshbach resonance at 832 G would require typical current of the order of 308 A.

Thermal properties

We can now take a closer look to the thermal properties of coil based on a cooling from the top surface. Heat exchange can only happen in three different manners in such systems :

- Heat conduction within the bulk of the coil. This would translate into temperature differences across the coil ΔT_c.
- Heat transfer at the coil-coolant flow interface, measurable in the temperature between the coolant fluid and the coil surface temperature ΔT_w.
- Heat transfer between the coolant flow and the assembly. This leads to a temperature increase of the coolant flow between the inlet and the outlet ΔT_f.

Our design is in the *transfer-limited* regime, where no observable heating of the coolant flow is observed meaning $\Delta T_f << \delta T_c + \Delta T_w$.

To evaluate the design, we first consider the heat transfer across the coil wire along the vertical direction. For this, and assuming no heat transfer between consecutive windings, we write the temperature difference between the top side, in contact with the coolant, and the bottom one as :

$$\Delta T_c = \frac{I^2}{w^2} \frac{\rho_{Cu}}{2\lambda_{Cu}} \tag{2.31}$$

with I the electrical current flowing in the winding, ρ_{Cu} and λ_{Cu} the copper resistivity and heat conductivity respectively and w the width of one winding. In our case, the temperature increase expected for $w = 1$ mm and $I = 400$ A is about 3.4 K.

This result has a strong meaning : it is mainly useless to have a coolant-copper contact on the entire surface of a wire. Copper heat conductivity being large enough if one side is properly cooled, no temperature gradient will build up inside a single wire. Moreover the dependence on the height of the wire H drops out of the equation. This is because if H is reduced, the resistivity of the winding increases also linearly leading to an increase of the dissipated power which is compensated by a more efficient heat conduction through the winding height as it is reduced.

We have now to estimate the efficiency of the heat transfer and the surface of the winding which is in direct contact with it. Assuming a water flow in the duct of 0.23 L/s that imposes a forced convection at the interface one can write the heat flux at the interface :

$$h_w(T(H) - T_w) = Hp \tag{2.32}$$

with H the height of the wire, p the dissipated power, T_w the temperature of the coolant flow and $T(H)$ the one of the coil evaluated at the height H as

previously described. h_w is the heat transfer coefficient at the surface. With the typical water flow stated previously we obtain a Reynolds number of $\sim 6.4 \times 10^3$ yielding to conclude that we operate in the turbulent flow regime. We can consequently extrapolate the heat transfer coefficient $h_w = 5 \times 10^3$ $W \cdot m^{-2}K^{-1}$. We obtain :

$$\Delta T_w = I^2 \frac{\rho_{cu}}{H w^2 h_w} \tag{2.33}$$

leading to a ratio $\Delta T_c/\Delta T_w = 0.14$ showing that the heat exchange at the coolant-copper interface is the limiting one in this design by contrast with existing designs such as Bitter-type electromagnets or hollow-core copper wire based coils.

Similarly we can study the increase of coolant flow temperature based on the conservation of the energy leading to :

$$\Delta T_f = I^2 \frac{R}{C_w Q} \tag{2.34}$$

with R the total electrical resistance, Q the flux of coolant fluid and C_w the volumetric heat capacity of water. With our experimental parameters, it leads to a temperature increase of $\Delta T_f = 0.7\,K$ at 400 A. This shows that this design is expected to be insensitive to water flow as compared with most of the other designs. The large aspect ratio of the coil windings does not degrade the heat transfer properties as this is accompanied with a decrease of the resistivity.

We characterized their thermal properties experimentally as shown in figures 2.20 and 2.21. First we measured the temperatures at different locations on the electromagnets once they have reached a steady state for different electrical powers. The blue diamonds correspond to the temperature of the coil body on the opposite side compared with the one directly in contact with the coolant (2.20.b). The yellow circles monitor the temperature of the first inner winding, not directly in contact with the coolant because of the Oring and the violet squares show the temperature of the outlet of the coolant circuit. We observe a linear dependence of these temperatures (figure 2.20.a) for increasing electrical power with the electrical current ranging from 20 to 300 A, running continuously in the electromagnet. The water flux is set to 0.23 Ls^{-1} with a water temperature of 17.5°C at the inlet.

Remarkably, even when running 300 A continuously, the coil body temperature never exceeds 30° C and the water outlet temperature 18° C as expected from the heat transfer calculations. The linear fits of the temperature increase of the coil (dashed lines in figure 2.20.a) give a heating rate for the coil body of $9.4\,K \cdot kW^{-1}$. The only important temperature increase is measured on the first inner winding (and observed also on the last outer one). As this specific windings are not in direct contact with the coolant, their cooling relies entirely on conduction along the winding from the ones directly cooled by water. This process being very limited, the increase of temperature is significant. However, if the electromagnet is run in typical experimental conditions with 308 A and a duty cycle of 30%, the hottest point located on the inner winding reaches about 30 °C which allows to operate the machine in safe conditions, with limited heating of the surroundings. Using a variable pitch machining to widen the first inner and outer

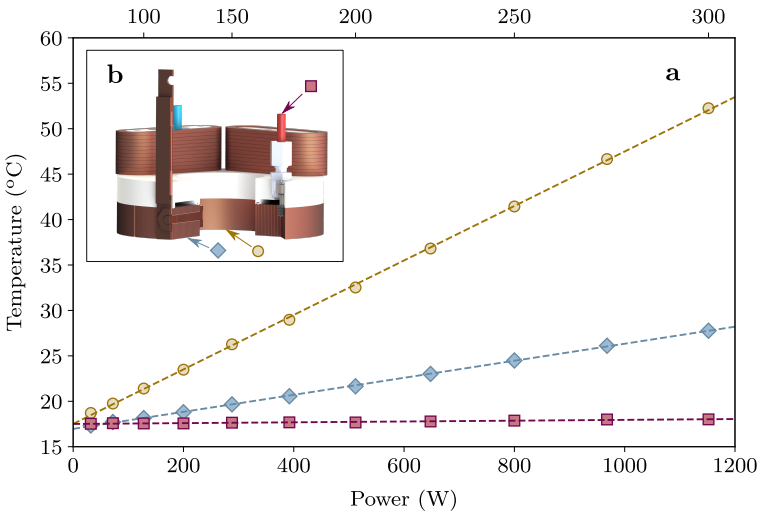

Figure 2.20: ***Evolution of the coil temperature.*** **a** and **b**Evolution of the temperature of three points of the coil, the inner electrical connection (yellow circles), the coil body (blue diamonds) and the water outlet (violet squares) as a function of the input current. Dashed lines shows a linear fit of the temperature increase for increasing electrical power.

winding in order to guarantee a direct contact with water would reduce the temperature inhomogeneities in the electromagnets, thus forced convection will be the principal cooling mechanism for all the windings.

Similarly we studied the transient dynamics of the temperature of the coil (figure 2.21.a). We measured the temperature of the coil body and the inner winding as a function of time when turning the current on at 300 A at $t = 0$. The blue dots show the evolution of the coil body temperature while the yellow ones show the inner winding temperature. The solid lines are exponential fits of the temperature evolution to extract the typical time constant of the cooling mechanism. The coil body reaches the steady state regime with a time constant of 15.26 s, which is fast as forced convection at the winding surface is really efficient. This measurement of the time constant $\tau \sim wC_{cu}/h$ allows to extrapolate the value the heat transfer coefficient to be $h \sim 5 \times 10^3\ W \cdot m^{-2}K^{-1}$ compatible with the one calculated from our expectations. In comparison, the inner winding being only cooled down by conduction, its thermalization is much slower with a time constant of 81.1 s. Both timescales are compatible with a reasonably fast thermalization allowing to operate the full machine in stable conditions after ten minutes of warm up of the electromagnets. We also measured the evolution of the coil body temperature for varying coolant flux as shown in figure 2.21.b. We observe a decrease of temperature for an increase of coolant flux. In this design the flux is limited by the pressure drop in the pipes bringing water from the wall inlet to the coil. The large duct produces in minimal pressure drop through the coil, allowing to reach flux of about $0.26\ l \cdot s^{-1}$ for a moderate overpressure of 3.5 bar.

This design of compact, bulk-machined electromagnets offers a large flexibility of shape even in constraint location in addition of a very efficient cooling mechanism. This electromagnets are routinely used for more than three years on this experiment without having shown any leak or heating

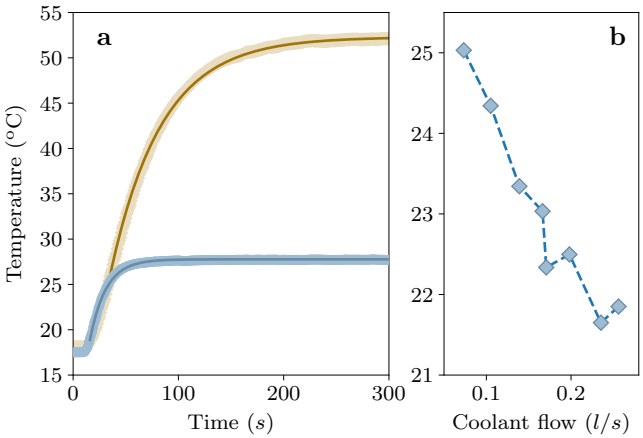

Figure 2.21: ***Dynamical evolution of the coil temperature.*** **a** Temperature evolution of the coil body (light blue) and the inner electrical connection (light yellow) over time. An exponential fit to each curve is displayed with the solid lines. The time constant for the coil body, in direct contact with water is one order of magnitude smaller than the time constant of the electrical connection, only cooled by conduction through the first turn of the coil. **b** Evolution of the coil body temperature as a function of the coolant flow. For large flows, it only shows a 2°C temperature increase compared with the temperature of the water inlet.

problem even for large currents of about 440A and entire days of operation for more than 10 consecutive hours. Their compactness has been a great advantage in order to guarantee large optical access from the top and bottom of the chamber. We could consequently accommodate the cloverleaf coils in the same reentrant viewport for fine tuning of the magnetic field saddle point position.

2.4.4 Radiofrequency doubly resonant circuit

In order to drive transitions between the three lowest hyperfine states $|1\rangle$, $|2\rangle$ and $|3\rangle$ at different magnetic fields a radio frequency (RF) antenna is installed on the science platform as depicted in figure 2.8.b. It consists in a single loop with a diameter of 4 cm made out of copper wire with a section of 20 AWG with Kapton insulation.

This antenna, connected to the outside of the chamber with a 1 m long coaxial cable, has an intrinsic inductance $L = 220$ nH and capacitance $C = 32$ pF. As this behaves as standard LC circuit it will have a resonance at a frequency $\nu = 1/2\pi\sqrt{LC}$. This resonance would be located at about 60 MHz which is too low compared with the frequency transition we want to address. Moreover, as we want to drive transitions between states $|1\rangle$ and $|3\rangle$ and states $|2\rangle$ and $|3\rangle$ the circuit should have two resonance frequencies, separated by a couple of MHz.

For this purpose a doubly-resonant LC circuit, shown in figure 2.22.a, has bees designed to impedance match the antenna and the high power amplifier in order to have the ensemble resonant at the proper frequency. It consists in two tunable LC circuits in parallel and two capacitor in series as shown in the circuit layout (2.22.b). The four capacitors are tunable, making it possible to finely adjust the position of the two resonances to the

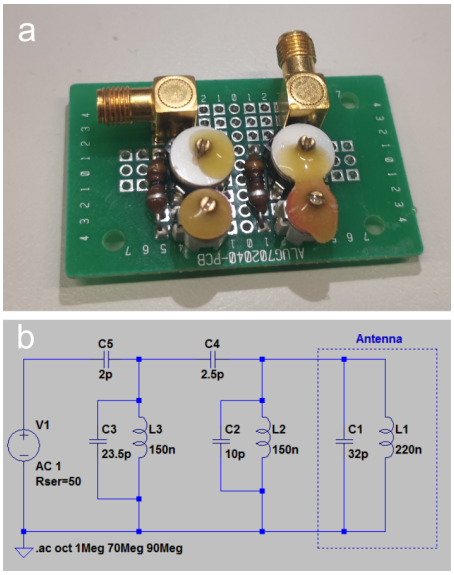

Figure 2.22: ***The dual frequency RF antenna impedance matching circuit.*** **(a)** Picture of the impedance matching circuit used to create a doubly resonant impedance matching. This will allow to drive with the same circuit transitions between the lowest hyperfine states $|1\rangle$-$|2\rangle$ and $|2\rangle$-$|3\rangle$ at different magnetic field values. **(b)** The circuit is composed of two LC circuit mounted in parallel with the antenna which is itself modelled by a LC circuits. The inductances are fixed while the capacitance are tunable in order to position precisely the resonances of the circuit at specific frequency values.

desired value. This circuit is fed with three arbitrary waveform generator *Siglent SDG* 5122 which can be connected to the circuit by using several RF switch ZYSWA − 2 − 50DR+. Then, one RF switch allows to turn on and off the RF signal that is fed into a high power 100 *W* RF amplifier ZHL − 100*W* − 251XS+. The output is connected to the impedance matching circuit which is itself directly plugged on the BNC electrical feedthrough that connects to the antenna inside the vacuum chamber. The impedance matching circuit has to handle the large power output of the amplifier making it complicated to find electronic components sustaining such high RF power.

In order to characterize and tune the resonance frequency we looked at the reflection of the circuit when sending a frequency sweep from 65 to 95 MHz. This is done using a vector network analyzer. In figure 2.23, we show the amplitude of the reflected signal measured on the network analyzer. By adapting the value of the capacitors we can easily tune the resonance to 76.1 and 84.02 MHz. This makes it possible to drive the $|1\rangle - |2\rangle$ transitions from 568 to 850 G. As the relative magnetic dipole moment of state $|2\rangle$ and $|3\rangle$ differs by a larger amount and due to the quality factor of the resonance, the $|2\rangle - |3\rangle$ transition can only be addressed at 568 G. It would be possible to decrease the quality factor of the resonance by adding resistive components, which would extend the range of magnetic field where we can address this transition. This circuit is used to drive the hyperfine transitions in order to control the relative populations in each hyperfine states and to perform RF spectroscopy of the strongly interacting Fermi gas.

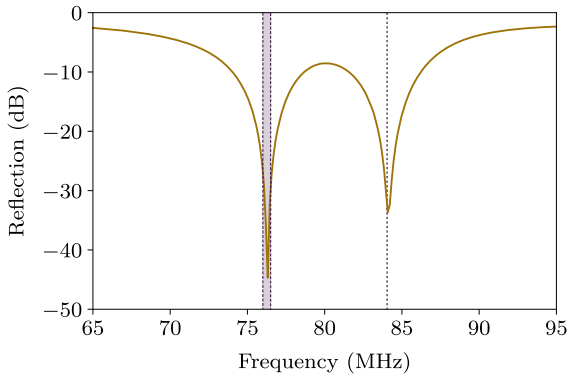

Figure 2.23: ***Characterization of the impedance matching circuit.*** Measured reflexion (S11 coefficient) from the impedance matching plugged onto the RF antenna using a network analyzer (yellow solid line). We set the capacitance values to obtain one resonance around 76 MHz and around 84 MHz. While the second one only allows to drive $|2\rangle$-$|3\rangle$ transition at 568 G, the first one is set such that it is possible to drive the $|1\rangle$-$|2\rangle$ transition from 568 to 850 G (indicated by the light violet area and the dashed violet line indicating the frequency transition at these magnetic fields).

2.5 EXPERIMENTAL COMPUTER CONTROL

2.5.1 Labscript presentation

A typical quantum gas experiment requires to control a large number of instruments in a sequential manner for a duration that lasts between a few seconds to minutes. In our specific case the duration of the experimental sequence is from 3 to 7 s where laser amplitude, frequencies and measurement devices needs to be turn on and off and controlled. For this purpose we use a Python library designed to create an interface between a user interface that consist in a Python code and a series of instruction that are transmitted to the hardware used on the experiment. The Python suite is called Labscript [99].

In our case we use several part of this suite :

- **RUNMANAGER** is the interface that allow us to enter all the numerical values of each output we want to control during the sequence. In addition the events of the sequence are written in a Python script that is taken as an input by Runmanager. Runmanager outputs an hdf5 file containing all the values of all the outputs used during the sequence. This file will be used to send the instructions to the hardware and will be used to collect the data acquired at the end of the sequence.
- **BLACS** is the device interface. It will send the instructions to the hardware in a sequential way. Different classes can be added to Blacs in order to control scientific cameras, arbitrary waveform generators or RedPitaya FPGAs. Blacs will control when each instrument is called in the sequence and when each measurement is saved in the hdf5 file.
- **LYSE** is the data analysis interface. It can run single shot or multi shot analysis scripts. It takes as an input the analysis codes and run them automatically when a new shot is received.

Combining these three tools allows to obtain a very adaptable experimental computer control system. Along the years we have added several

classes for cameras and arbitrary wavefront generator. On-the-fly data analysis including optimization processes are made particularly convenient. In the next part I will describe the detail of the computer control architecture on the apparatus.

2.5.2 General architecture

The computer control of the apparatus is based around two main computers that are used to initialized the hardware, prepare the instructions sent during an experimental sequence, gather the data from the instrument and perform the data analysis. Both computers share the same local network allowing the master computer (*PC1*) to send instructions to instruments connected to the second computer (*PC2*).

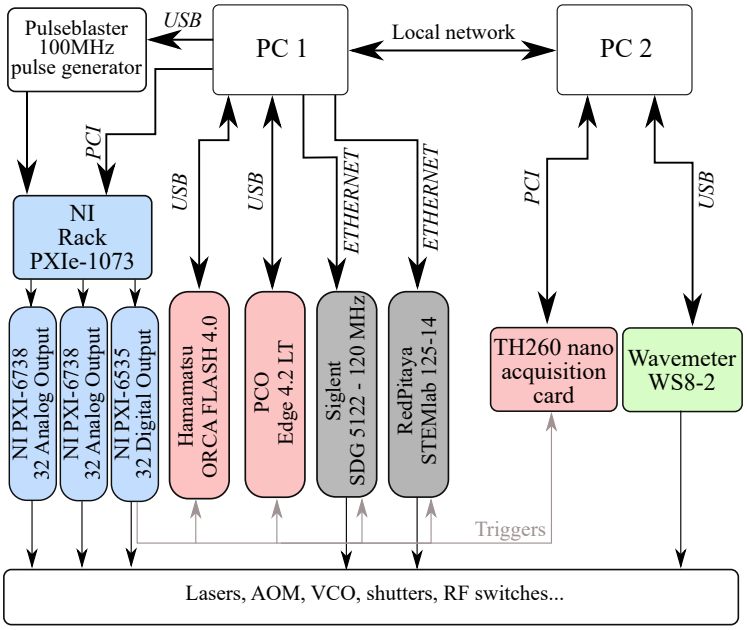

Figure 2.24: ***Computer control architecture.***

The Labscript suite is installed on PC1 as well as an arbitrary waveform generator (*Pulseblaster*) that is used as a the master clock for the experiment. A specific Labscript class allows the clock rate to be adapted during the sequence in order to optimize the actual number of instructions send to the hardware depending on the fastest process over part of the sequence. This allows to have slow clock rates during phases of the sequence that last for seconds and where instructions just need to stay constant and to only use the largest time resolution where it is actually required, optimizing the computing resources on a very elegant manner [99].

As described in figure 2.24 a *National Instrument* card is connected onto *PC1*, allowing to have both analog control outputs and digital ones. The digital outputs are used as triggers for many instruments such as arbitrary waveform generators or scientific cameras and to control TTL components as switches or shutters. The analog outputs are used to control voltage controlled oscillators (VCO) or the power or both laser beams and RF signals. All the instructions contained in the hdf5 file are parsed by BLACS and sent to the different NI cards during the experimental sequence.

On the same computer Siglent DDS and RedPitaya FPGAs are used to produce RF signal and clean variable voltage set point. They are programmed at the beginning of each sequence and triggered by a digital output signal of the NI card at the required time stamp during the sequence. The two scientific CMOS cameras are also connected to the same computer and their acquisition is triggered by the digital outputs. The images are read out at the end of the sequence and saved in the HDF file containing all the sequence.

The *High-Finesse* wavemeter *WS8-2* and the acquisition card of the photon counter are connected to the second computer (figure 2.24). The acquisition of the photon counter is also triggered by a digital output of the NI card and the data are retrieved and save and the device initialized on a similar way as for the cameras. The wavemeter communicates the value of the frequencies of the laser read on each of its eight ports a sequential manner. The software of the wavemeter contains a PID for each of the input allowing to feed back a control voltage on the lasers to regulate their frequencies if necessary. This is used at the beginning of each sequence to tune the frequency of lasers before starting the experimental sequence.

3

PREPARATION OF A STRONGLY INTERACTING FERMI GAS IN A HIGH FINESSE CAVITY

In this chapter, I will describe the technique used to produce a degenerate Fermi gas with strong atom-atom interactions, within the mode of the high finesse optical cavity. I will first present the basics of the interaction between a two-level atom and an electromagnetic field, providing the building blocks we routinely use to cool down and trap the atoms. I will then detail the experimental sequence we use to produce, with a typical duty cycle of 4 s, a large and strongly interacting cloud of about 7×10^5 atoms in a deeply degenerate regime. The intracavity dipole trap and evaporative cooling which represents a significant improvement compared with existing apparatus will be emphasized in this section. I will show how we can control the hyperfine state populations obtained after the preparation. Finally I will conclude on the different probing techniques we have at our disposal to study this strongly interacting system.

CHAPTER CONTENTS

The content of this chapter closely follows our publication:

K. Roux, V. Helson , H. Konishi and J.-P. Brantut
Cavity-assisted preparation and detection of a unitary Fermi gas
New Journal of Physics **23**, 043029 (20121)

3.1 BASICS OF LIGHT-ATOMS INTERACTION

The ability to use coherent light to cool, trap and control atoms is at the foundation of quantum gases experiment [100–104]. We routinely use the tools of laser cooling and trapping to create deeply degenerate quantum gases starting from a hot atomic vapour of ^{6}Li. In this section I will briefly introduce two effects of the light-atom interaction that allows for laser cooling, namely the radiation pressure force and the dipole force that is at the origin of optical trapping. For this, we will consider a two-level atom with an ground state denoted $|g\rangle$ and a excited state $|e\rangle$, illuminated with a plane wave of wavevector $\vec{k}$.

3.1.1 Radiation pressure force

The radiation pressure force is the force that dominates when the frequency of the laser illuminating the atom is close to the one of the atomic transition [100]. It is at the basis of Doppler cooling where the two-level atom undergoes repeated absorption-emission cycles that result in a decrease of the its velocity. The absorption in the mode of the monochromatic laser source, together with the spontaneous emission in any direction of space, will produce a momentum transfer of $-\hbar\vec{k}$ for each absorption-emission cycle.

We define the typical lifetime of the excited state Γ and the detuning between the atomic transition frequency and the one of laser $\Delta = \omega_L - \omega_a$. The light-matter Hamiltonian in the rotating wave approximation can be written as

$$\hat{H} = \frac{\hbar}{2}\begin{pmatrix} \Delta & \Omega^* \\ \Omega & -\Delta \end{pmatrix} \tag{3.1}$$

with $\Omega = dE$ the Rabi frequency of the transition from $|g\rangle$ to $|e\rangle$, proportional to the dipole matrix element of the atomic transition d and to the amplitude of the electric field. It is possible to derive the force on the atom induced by the interaction with the laser field that depends on the wavevector of the plane wave,

$$\vec{F} = \hbar\vec{k}\frac{\Gamma}{2}\frac{s}{1+s} \tag{3.2}$$

with s the saturation parameter given by $s = 2\Omega^2/\left(\Gamma^2 + 4\Delta^2\right)$. It can be rewritten as a function of the saturation intensity defined as $I/I_{sat} = 2\Omega^2/\Gamma^2$ characteristic of the atomic transition such that

$$s = \frac{I/I_{sat}}{1 + 4\Delta^2/\Gamma^2} \tag{3.3}$$

This force reaches a maximum for large s, $\vec{F} = \hbar\vec{k}\Gamma/2$. It allows to slow down the hot atomic beam and cools the atoms in the Magneto-Optical-Trap (MOT) in combination with a gradient of magnetic field that creates a trap for the atoms [100]. The cooling force can be expressed as a function of the speed of the atoms $\vec{F} = \hbar k^2 s(-2\Delta\Gamma)/\left(\Delta^2 + \Gamma^2/4\right)$ [105]. This viscous force is the one responsible for Doppler cooling that is the basic tool routinely used on cold atom experiments to produce cold clouds down to temperatures of the order of 100 µK. As seen from the dependence of the force on

the speed of the atom, the magnetic field profile of the Zeeman slower coil allows to address several velocity class due to the spatial dependence of the frequency of the atomic transition due to the spatially variable Zeeman shift. Doppler cooling leads to a minimum temperature that depends directly on the linewidth of the excited state Γ that is the so-called Doppler temperature $k_B T_{Doppler} = \hbar\Gamma/2$ which is equal to 142 µK for ^{6}Li.

In addition to the radiation pressure there is a second one proportional to the gradient of the intensity and that will dominate over the radiation pressure force when the frequency of the laser beam is far detuned with respect to the atomic transition frequency [106]. This force, called the dipole force, is detailed in the following part.

3.1.2 Dipole force

Considering a two-level atom in the oscillating electric field of the laser beam we can write the associated dipole potential energy

$$V = -\frac{1}{2}\langle \vec{p}\vec{E} \rangle \tag{3.4}$$

with, as previously, $\vec{E}$ the electric field and $\vec{p} = \alpha\vec{E}$ the dipole moment for a complex atomic polarizability α. The imaginary part of this quantity links to the absorption of the photons from the light field and relates directly to the radiation pressure force discussed previously with $\Gamma_{sc} = -\frac{1}{2\hbar\epsilon_0 c} Im(\alpha) I(\vec{r})$, ϵ_0 the vacuum permittivity and c the speed of light. The real part links to the dipole potential as described by

$$V = -\frac{1}{2\epsilon_0 c} Re(\alpha) I(\vec{r}) \tag{3.5}$$

As we study a two-level system we can approximate these relations by

$$V = \frac{3\pi c^2}{2\omega_a^3}\frac{\Gamma}{\Delta} I(\vec{r}) \tag{3.6}$$

$$\Gamma_{sc} = \frac{3\pi c^2}{2\hbar\omega_a^3}\left(\frac{\Gamma}{\Delta}\right)^2 I(\vec{r}) \tag{3.7}$$

For $\Delta > 0$, the dipole force will be repulsive while it will become attractive for $\Delta < 0$. This process will be used to trap the laser cooled cloud in a far-off-resonant laser beam, where evaporative cooling will be performed. At large detuning, scattering from the trapping laser beam will be greatly reduced as it scales with $1/\Delta^2$. It allows to trap the atoms without large heating due to spontaneous emission induced by the trap laser for large enough detuning. the combination of the radiation pressure and the dipole force permit to achieve an all-optical production of a degenerate gas of ^{6}Li [107] without the magnetic trapping. In the following part, I will give an overview of the preparation sequence we use to produce a strongly interacting and degenerate gas of ^{6}Li.

3.1.3 Overview of the experimental sequence

The preparation sequence has a total duration of 3.3 s to produce a degenerate Fermi gas. Then the probing part can vary from a few milliseconds in

the case of a time-of-flight imaging to a few seconds when we want to look at very slow variation of atom number using the transmission spectroscopy through the cavity.

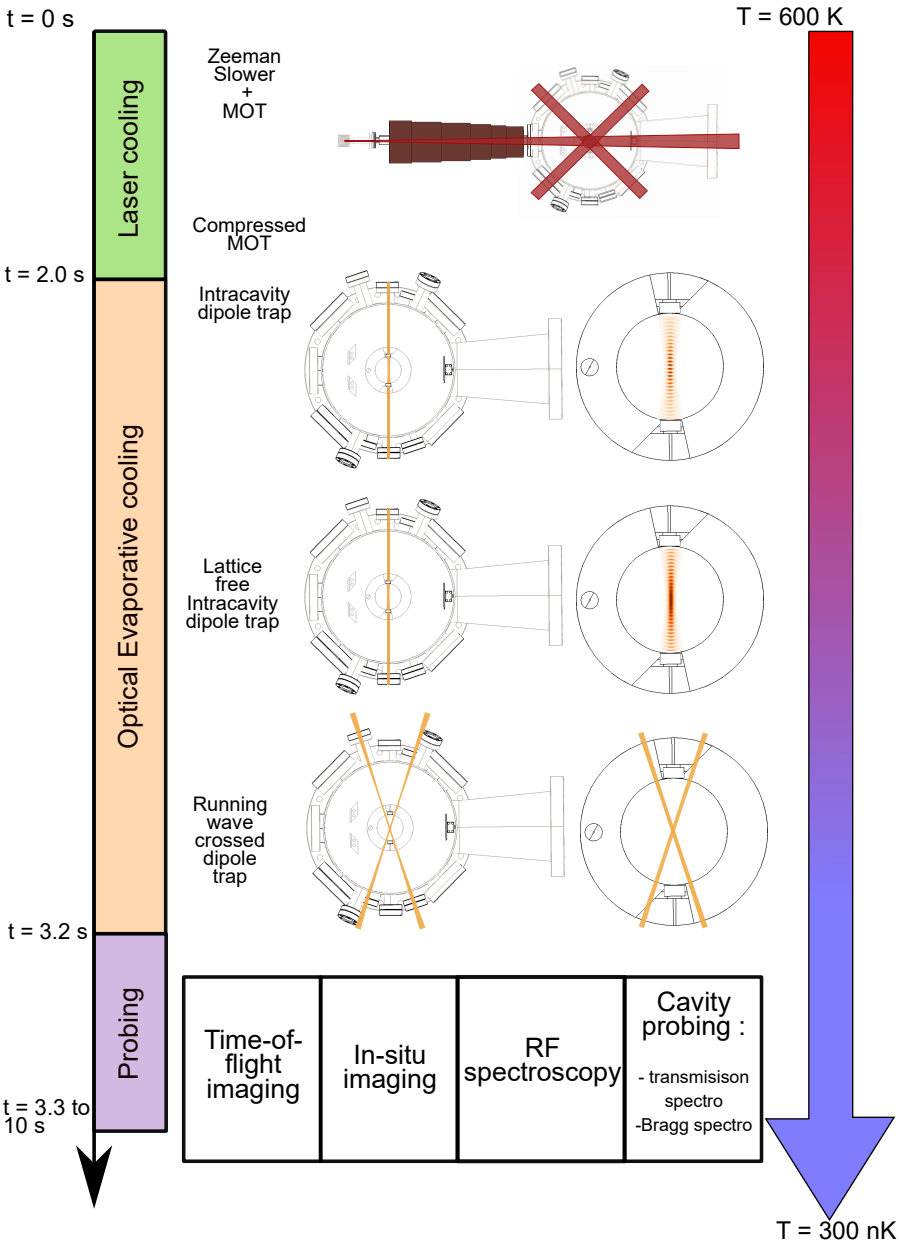

Figure 3.1: ***Overview of the experimental sequence.*** The sequence starts with a stage of slowing down the atoms to capture them in the MOT. After this laser cooling stage the cloud is trapped into an intracavity dipole trap where a first evaporative cooling is performed. There the cloud is transferred into the lattice-free cavity trap for a second evaporation ramp. Finally the cloud is transferred into a running wave crossed optical dipole trap to perform a last stage of evaporative cooling allowing to produce a deeply degenerate Fermi gas. Then the cloud is held in this trap where it can be probed with several tools.

The short duty cycle is possible first, because the entire preparation is made using optical trapping. Moreover, the laser cooling, the optical evaporation and the cavity QED measurement are all performed at the same

location, the center of the science chamber. The absence of any transport of the cloud from a MOT to a science chamber greatly reduces the experimental duty cycle. Second, the large atom-atom interactions induce a fast thermalization during the evaporative cooling sequence. This fast duty cycle represents a major advantage and is comparable with state of the art production of quantum gases [108, 109].

The experimental sequence is composed of several steps as described in figure 3.1 :

- The loading of the MOT. For a total duration of 2 s the Zeeman slower slows down the hot atomic beam exiting the Lithium oven. These atoms are captured at the crossing of three retro-reflected beams at 671 nm, resonant with the D_2-line of ^{6}Li, where the MOT cools them down to mK temperatures.
- Then the MOT cloud is compressed in order to cool it further down to the Doppler temperature and to reduce its size from about a cm to a mm.
- The cloud is loaded into the intracavity optical dipole trap made by a far-off resonant 1064 nm laser beam injected into the cavity. At the same time, the bias magnetic field is ramped up to the location of the broad Feshbach resonance of ^{6}Li [71], where atom-atom interactions are large. The trap optical power is then decreased to perform a first stage of evaporative cooling.
- Then, the cloud is loaded into a second intracavity dipole trap where the lattice structure intrinsic to the standing wave of an intracavity light field is cancelled. this is possible by taking advantage of the consecutive longitudinal mode structure of the cavity and their relative phase shift. Once the cloud is transferred into this trap a second stage of evaporative cooling is performed where the cloud can shrink at the center of the cavity mode.
- At this stage the cloud is transferred into a running wave crossed optical dipole trap made by two focused beams, crossing at the center of the cavity mode. A last stage of evaporative cooling takes place and brings the gas to quantum degeneracy.
- The cloud can be kept in this crossed dipole trap or released in one of the two arms adiabatically.

In the following sections I will describe in more details each of these different parts of the sequence with the timelines of the relevant experimental parameters, the laser system and the main results and characterizations we have performed.

3.2 LASER COOLING STAGE

3.2.1 MOT and Zeeman slower

The experimental sequence starts with a first 2 s stage of laser cooling which consists in having simultaneously the Zeeman slower and the MOT turned on. The Zeeman slower acts as a viscous force that slows down the atoms from speeds of the order of 1000 $m \cdot s^{-1}$, coming from the the Lithium oven

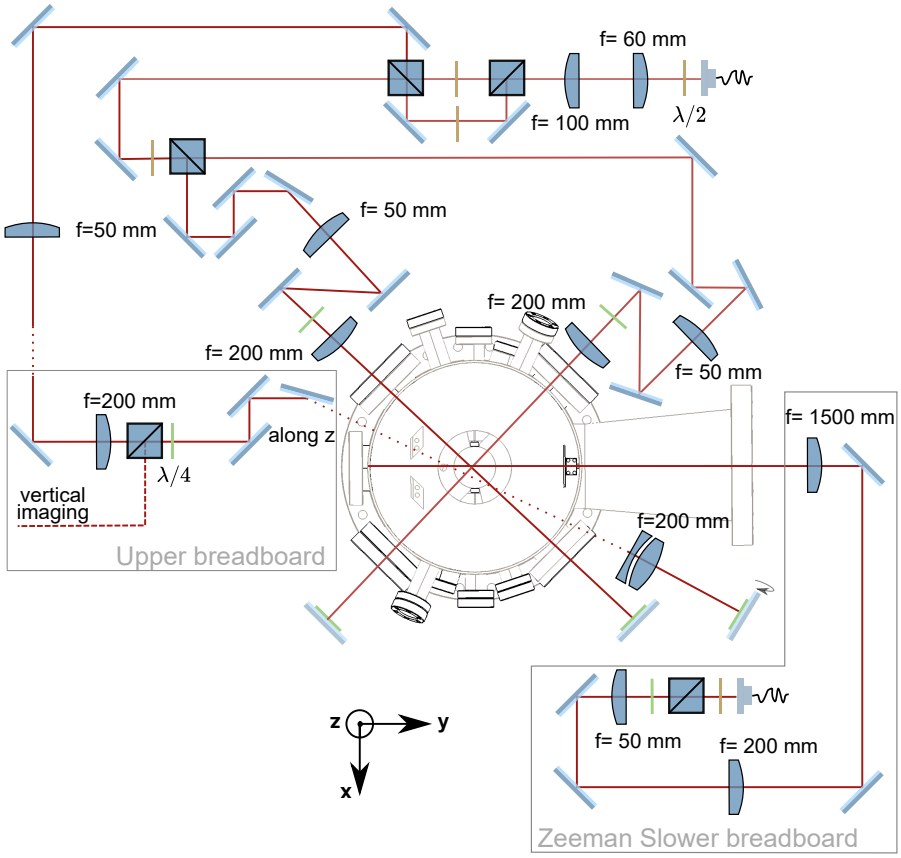

Figure 3.2: *The Magneto-Optical-Trap beamlines around the science chamber.*

heated up to 350 °C, down to the capture velocity of the MOT which is about 100 $m \cdot s^{-1}$. As the atoms are decelerated along the 40 cm-long Zeeman slower tube, it is mandatory to adapt the transition frequency in order to compensate for the velocity-dependent Doppler effect [110]. The tapered Zeeman slower coil plays this role by creating a space dependent Zeeman shift of the atomic transition frequency that matches the deceleration of the atomic beam, allowing the Zeeman slower beam to stay resonant with the $|2S_{1/2}, m_J = 1/2\rangle \longrightarrow |2P_{3/2}, m_J = 3/2\rangle$. The Zeeman slower beam has a total power of 172 mW which is focused down into the Lithium oven (figure 3.2). The beam diameter is approximately 2.5 cm at the center of the chamber which leads to a saturation parameter $s = I/I_{sat} = 14$ with $I_{sat} = 2.54\ mW \cdot cm^{-2}$ the saturation intensity of the D_2 line. Thus the Zeeman slower operates with the maximal radiation pressure thanks to the large saturation parameter permits to reach a scattering rate $\Gamma_{sc} = \Gamma/2$ limited by the natural linewidth of the transition. Moreover, the large value of s at the beginning of the Zeeman slower where the beam is focused broadens the atomic transition, reducing its sensitivity on the exact laser frequency.

The atomic beam is captured by the MOT at the center of the science chamber. The MOT is composed of 3, 2.5 cm diameter retroreflected beams that cross at the science chamber center, with a relative angle of 90° (figure 3.2). They are circularly polarized. Each beam consists in two frequencies corresponding to a cooler and a rempumper beam, driving respectively the transitions $|2S_{1/2}, F = 3/2\rangle \longrightarrow |2P_{3/2}, F = 5/2\rangle$ and $|2S_{1/2}, F = 1/2\rangle \longrightarrow$

$|2P_{3/2}, F = 3/2\rangle$. Combined with these beams, a quadrupole field is created by the MOT coil, which together with the radiation pressure force of the MOT beams, result in a effective trapping around the zero crossing of the quadrupole field [111]. The repumper light ensures that atom pumped into the $|2S_{1/2}, F = 1/2\rangle$ state are optically pumped back in the $|2S_{1/2}, F = 3/2\rangle$ in order to cycle the cooling transition. The cooler and repumper beams have a total power of 67.5 and 33 mW for the vertical beam and 33.75 and 16.5 mW for each horizontal beams. This leads to a total saturation parameter $s = 10.8$ for the cooler and 5.3 for the repumper allowing to operate in the high saturation regime.

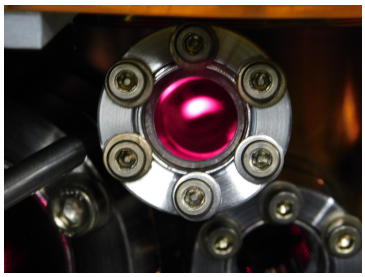

Figure 3.3: *Picture of the fluorescence of the MOT cloud in the science chamber.*

3.2.2 Laser system

The MOT and Zeeman slower beams are derived from two independents 671 nm *Toptica TApro* tapered amplifiers [112] as shown in figure 3.4. A first TApro generates a total output power of approximatively 500 mW. A small part is sent to a double double-pass Acousto-Optic modulator (AOM) and then to a spectroscopy cell filled with a ^{6}Li gas at 250 °C. This is used to generate a saturation absorption spectroscopy signal [113]. It provides an error signal to stabilize the frequency of this laser on the crossover signal at 114 MHz in between the $|2S_{1/2}, F = 1/2\rangle$ and the $|2S_{1/2}, F = 3/2\rangle$ states. The two AOMs shift the spectroscopy beam by respectively 114 and -114 MHz. By introducing a frequency difference δ of opposite sign on both AOM, we can dynamically tune the frequency of the TA from being exactly resonant with the crossover signal to a detuning of 2δ. The light of the spectroscopy cell is sent to the wavemeter *High Finesse WS8-2* to be used as a frequency reference for the rest of the experiment. The wavemeter is able to generate an error signal and stabilize laser frequencies with respect to this reference at a few hundred kHz level.

From the main beam line, we create two beams with a relative power balance of 2 : 1, corresponding to the cooler and repumper beams. Each beam is then frequency shifted by 114 and -114 MHz using AOMs (*ATM-115, Intraaction*). Both beams are recombined with crossed polarization and sent to the experiment using single-mode, polarization maintaining optical fibers. Each beam power can be individually controlled using AOMs and with an optical shutter (*SRS470, Stanford Research Systems*).

A second TApro is frequency stabilized with respect to the MOT TA using one of the wavemeter PID channels. After a stage of beam reshaping it is frequency shifted by an AOM allowing to control the beam intensity and

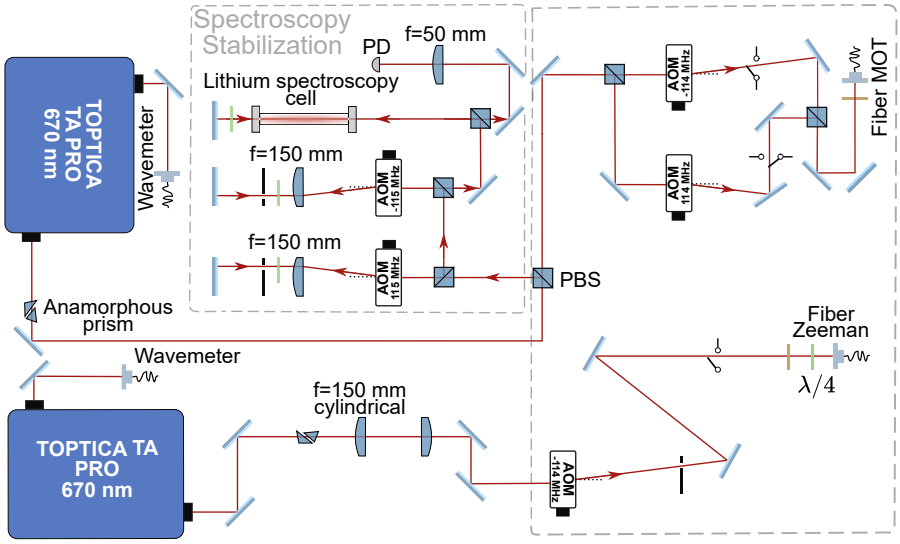

Figure 3.4: *The Magneto-Optical-trap and Zeeman slower laser setup.*

then sent to the experiment where it will be used as the Zeeman slower beam.

3.2.3 *Experimental sequence*

The laser cooling sequence proceeds as follows :

- For a total duration of 2 s the cooler, repumper and Zeeman slower beams are set to their maximum power (see figure 3.5). The cooler and repumper beams are frequency detuned by approximatively -10Γ and the Zeeman slower by -24Γ from the atomic resonances, $\Gamma/2\pi = 5.87$ MHz being the natural linewidth of the excited state.
- Once the MOT loading is completed the Zeeman slower is turned off and the compensation coils along the cavity and Zeeman slower axis are turned on to position the zero of magnetic field on the geometric center of the cavity mode. The detuning of the MOT beam is then ramped down linearly over 48 ms from -10Γ to -0.9Γ (see figure 3.5). The power of the cooler is reduced to 16 mW while the repumper is reduced to 0.5 mW. As the repumper is almost turned off during this compression stage, the atoms are optically pumped into the dark state $|2S_{1/2}, F = 1/2\rangle$ at the end of the MOT compression (CMOT) while final detunings and power are held for 4 ms. This compression phase is necessary to maximize the loading into the optical dipole trap. The typical size of the MOT cloud is of the order of a cm with temperature around a few mK, while the usual size of an optical dipole trap is of the order of 100 µm and its depth about a mK. The CMOT creates a dense cloud of about a millimetre close to the Doppler temperature $T_D \approx 140$ µK.

After such a CMOT stage and a loading of 2 s we obtain a cloud of about 4×10^7 atoms (figure 3.6) optically pumped into the $|2S_{1/2}, F = 1/2\rangle$ state before ramping up the magnetic field close to the Feschbach resonance. The CMOT atom number saturates after 5 s of loading (figure 3.6).

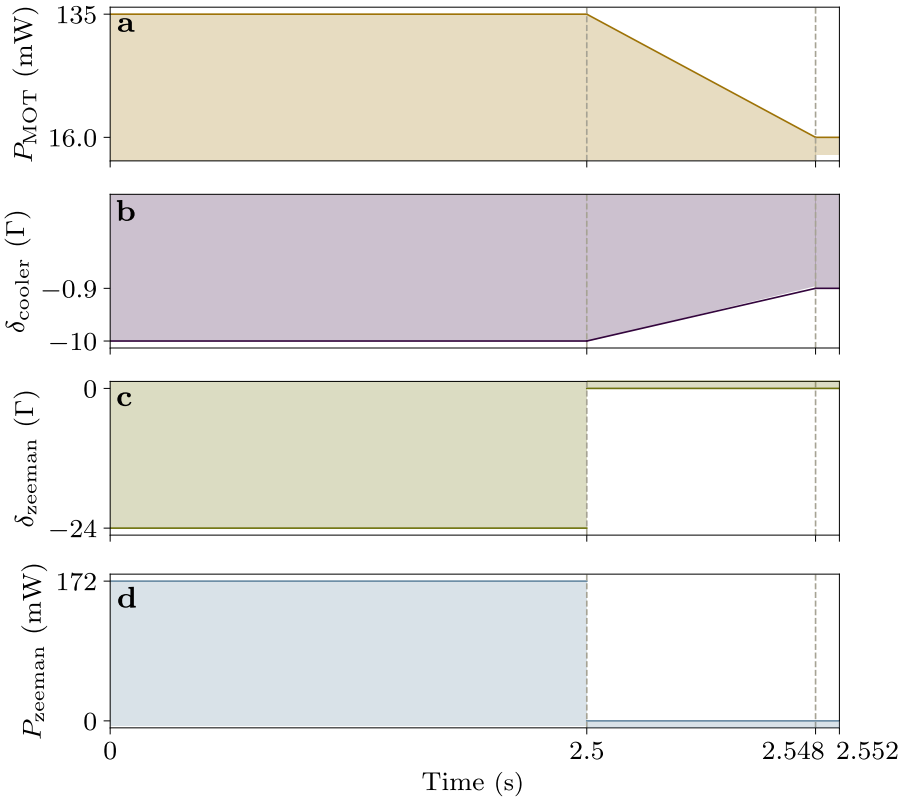

Figure 3.5: ***The laser cooling sequence.*** **a-d** Time evolution of the cooler power, the MOT detuning, the Zeeman slower detuning and power respectively during the laser cooling phase of the sequence. We can differentiate two main phases : first a long loading phase for 2.5 s followed by a short MOT compression reducing the size and temperature of the cloud and optically pumping the atoms into a dark state.

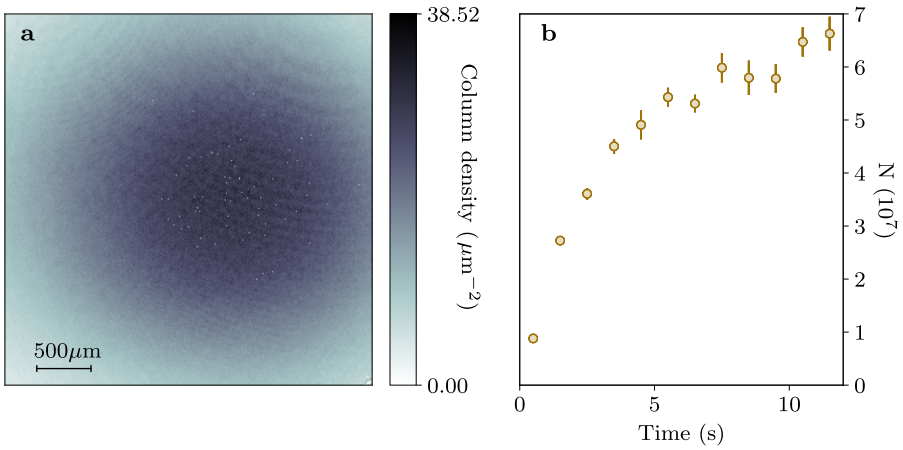

Figure 3.6: ***Loading of the CMOT.*** **a** Absorption image of the CMOT cloud after a time-of-flight of 0.350 ms. **b** Evolution of the atom number in the CMOT as a fucntion of the duration of the loading phase.

As pointed out previously, the resulting ^{6}Li cloud after laser cooling is large and hot compared with other species like Potassium or Rubidium. It is due to its light mass and its unresolved hyperfine structure in the excited state preventing Sisyphus cooling to cool down the gas to sub-Doppler tem-

perature as it was observed in the first MOT in the 1980's [101, 114]. Thus transferring the laser-cooled cloud into a conservative trap requires for ^{6}Li both large beam waists to overlap with the laser cooled cloud and a deep trap of the order of a mK. Such optical traps involves state of the art laser technologies as it typically requires about 200 *W* of laser power far-detuned from the atomic resonance, with a beam waist of about 60 µm to fill these requirements.

However, two approaches have been explored to circumvent this problem. First, improved laser cooling have been developed, relaying either on narrow-transitions cooling, thus reducing the Doppler temperature [115], or on gray-molasses demonstrated both for Potassium or Lithium atoms [116–118]. These two techniques are able to bring down the temperature of laser-cooled cloud of ^{6}Li at about 50 µK which is 4 times smaller than the one obtained after a MOT compression sequence on the D_2 line. The other approach consists in creating deep and large optical dipole traps taking advantage of the power build-up obtained by using a Fabry-Pérot cavity [119, 120]. In this experiment, we take advantage of the presence of the cavity to leverage it at the preparation stage and use it as a deep optical dipole trap. Compared to previous work using Fabry-Pérot cavities to create optical dipole traps, we propose to apply a lattice-cancellation technique [121] to get rid off the intracavity lattice structure intrinsic to a standing wave existing in-between two mirrors. This way, we will show that we can go one step further, using the cavity not only to create a deep trap, but also to perform an efficient evaporative cooling sequence in this trap and reach a regime close to quantum degeneracy. This aspect will be treated in detail in the following section.

3.3 CAVITY LENGTH STABILIZATION

In this section, I will present the main use of the optical cavity : trapping and probing the cloud. For this we need to stabilize the cavity length to control its resonance frequency during the experiment. I will present in detail the three wavelengths we use and how we leverage the transverse mode structure of the cavity to optimize each application. Moreover the cavity resonance needs to be stable compared with the frequency of the laser that will probe the cavity as well as with the frequency of the atomic transition of ^{6}Li. For these we stabilize all the laser frequencies with respect to each other compared with the cavity resonance frequency. In addition all these frequencies are referenced, using the wavemeter, onto an atomic reference based on the frequency of the ^{6}Li D_2 line. I will detail the experimental techniques we apply to obtain this relative and absolute frequency stability.

3.3.1 Trichroic Fabry-Pérot cavity : probing, trapping and stabilizing

As presented in the chapter 2, the cavity placed at the center of the vacuum chamber is resonant at three different wavelengths used for different applications :

- At 532 nm. This wavelength is used to continously measure the cavity length with very low power and far-off resonant from the atomic transition. This mitigates the effects of the dipole potential created by the intracavity lattice that would affect the behaviour of the atoms.

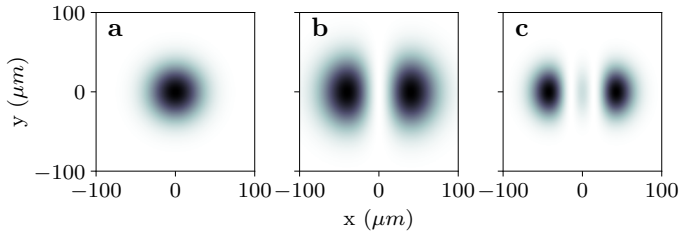

Figure 3.7: ***Using TEM modes of the Fabry Pérot cavity at different wavelengths.*** In our experiment we take advantage of the existence of higher order TEM modes existing in the cavity. **a** The probe laser beam at 671 nm, close to atomic frequency is mode-matched with the fundamental TEM_{00} mode. **b** The intracavity optical dipole trap light is mode-matched with the TEM_{10} to increase the trap volume and maximize the loading of atoms from the laser-cooled cloud. **c** The light used to generate the PDH signal at 532 nm is coupled to the TEM_{20}in order to minimize the residual antitrapping potential seen by the atoms, positioned at the center of the TEM_{00} mode.

- At 1064 nm. We use light at this wavelength which is far-off resonant on the red side of the atomic transition in order to create an attractive potential, thus trapping the atoms. We will use two different beams from this laser line to create two intracavity traps, a standing wave and a lattice free dipole traps.
- At 671 nm. We use this wavelength to probe the coupled atoms-photons system inside the Fabry-Perot cavity. This beam frequency needs to be close to the atomic resonance either on the D_2 or D_1 lines of ^{6}Li. The light used to probe the light-matter coupled system is derived from a *Toptica DLpro* diode laser with a long lasing cavity, offering the possibility to narrow down the laser linewidth.

As shown in figure 3.7 we take advantage of the transverse mode structure of the resonator presented in Chapter 2. The close-to-resonance light at 671 nm is mode-matched in order to couple to the fundamental, Gaussian TEM_{00} mode with a mode waist of 45.0(1)µm. The 1064 nm light used to create an attractive potential in order to trap the atoms is mode-matched to a higher order TEM_{10} mode. This allows to artificially increase the volume on which the light intensity is spread. This consequently increases the capture efficiency of the trap. Moreover, the expected cavity power build of the cavity at 1064 nm is $P_c/P_{in} = 4580$ at 1064nm based on the calculation presented in Chapter 2, allowing to create deep dipole traps with low optical power. The light at 532 nm is coupled to an even high order TEM_{20} mode in order to minimize the overlap between this light and the atomic cloud positioned at the center of the TEM_{00} cavity mode. As it appears clearly in figure 3.7.c, the intensity is spread in lobes away from the cavity center, leaving very little light actually seen by the atoms.

3.3.2 General architecture

The architecture of frequency stabilization in the experiment works the following way (see figure 3.8))

- The *NKT Photonics Adjustik* laser provides a beam at 1064 nm with a laser linewidth of about 10 kHz. This light is frequency doubled, hence providing a beam at 532 nm. By construction the 532 and 1064 nm frequencies are stabilized with respect to each other.
- The laser beam at 532 nm is sent to the science cavity. There the Pound-Drever-Hall (PDH) [122] technique is used to stabilize the length of the science cavity onto the frequency of the 532 nm beam line. Consequently the science cavity resonance frequency is locked onto the frequency of the 1064 nm laser.

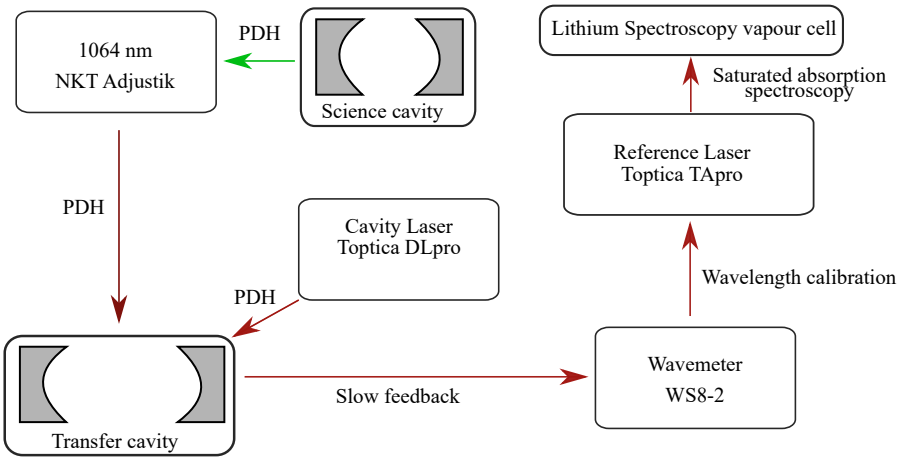

Figure 3.8: ***Architecture of the frequency stabilization of the laser frequencies and cavity length.***

- Some light of the 1064 nm laser is sent to the transfer cavity. There the length of the transfer cavity is locked onto 1064 nm laser. More precisely, we imprint a frequency modulation onto this 1064 nm laser creating frequency sidebands at a variable frequency from the carrier ν_F. The transfer cavity length is locked onto these sidebands using the standard PDH technique. By varying the phase modulation frequency, we can dynamically change the frequency of the 1064 nm laser, and consequently of the science cavity, compared with the frequency resonance of the transfer cavity.
- A *Toptica DLpro* laser at 671 nm laser is employed to probe the cavity and its frequency is stabilized onto the transfer cavity. A fast feedback allow us to narrow down its linewidth to a fraction of the cavity linewidth. The frequency of the probe laser is read out using the *High Finesse WS8-2* wavemeter, itself referenced onto the atomic saturation spectroscopy locked onto the D_2 line of ^{6}Li.
- We can adjust the frequency of the probe laser by using the wavemeter build-in PID that can feedback onto the piezo of the 1064 nm laser to adjust the length of the transfer cavity in order to obtain the desired frequency for the probe laser. The frequency of the proble laser is measured by the wavemeter. The feedback signal is fed to the piezoactuator of the 1064 nm laser. Changing the setpoint frequency of the probe laser modifies the frequency of the 1064 nm laser and the science and

transfer cavity length. This tuning knob make it possible to chose arbitrarily the absolute frequency between the science cavity and the probe laser with respect to the atomic reference frequency.

This architecture gives us a relative frequency stability between all the lasers and the science cavity thanks to the transfer cavity. The detuning between the atomic transition and the frequency of the probe laser Δ_a (and the science cavity resonance) is set by the wavemeter setpoint. The detuning between the probe laser frequency and the science cavity resonance Δ_c is controlled by the modulation frequency of the 1064 nm laser beam sideband ν_F. We thus have full control on all the frequency detunings to perform cavity QED experiments.

3.3.3 1064nm *laser systems*

The 1064 nm beam line is made by a narrow linewidth laser *NKT Photonics Adjustik* which is sent into a Yb-doped fiber amplifier (*Azurlight ALS-IR*) that amplifies the seed laser up to 8.1 *W* (figure 3.9).

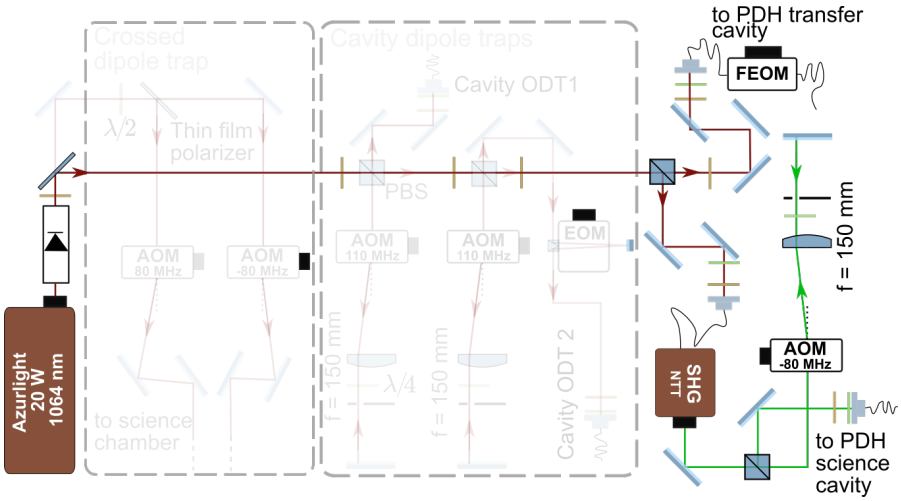

Figure 3.9: 1064 nm ***laser system for the science cavity and the transfer cavity PDH.***

Concerning the lock chain of the experiment, two secondary beam lines are picked up from the main one :

- A first part of the light is sent to a fiber-pigtailed frequency doubler (*NTT electronics WH-0532*) that creates the beam line at 532 nm (figure 3.9). There the remaining 1064 nm is filtered out by an interference filter. One could expect that, if the beam at 532nm is resonant with the science cavity (as the science cavity is stabilized on it), a beam from the 1064 nm laser would be automatically resonant, as it has exactly twice the wavelength of the PDH beam. However, because of the difference of penetration depth in the coating stacks, the optical paths differ between the two wavelengths which makes it necessary to introduce a frequency shift in order to have both beams resonant with the cavity simultaneously. For this purpose, a double-pass AOM is placed in order to introduce a controlled frequency shift between the 1064 nm and the frequency converted 532 nm (figure 3.9). Finally

this laser beam is sent to an optical fiber to the science chamber in order to stabilize the science cavity length.

- A second part of the main beam line is sent to a broadband fibered-Electro-optics modulator *Photline NIR-MPX-LN-05* (fEOM) where two different modulation frequencies are applied (figure 3.9). The first frequency ν_F is generated by a signal generator (*Siglent SSG3021X*) which can be varied from 9 kHz to 2 GHz. The second is a fixed frequency at 30 MHz that will allow to realize a PDH lock on the transfer cavity.

3.3.4 *Science cavity stabilization laser systems*

The 532 nm beam sent from the laser table is used to generate a PDH signal in order to stabilize the length of the cavity on the 1064 nm laser. A free space phase modulator (*Qubig EO-T30M3-VIS*) generates sidebands at a frequency detuning of 30 MHz from the carrier (figure 3.10). Both the transmission through the cavity and the reflection are monitored. The reflected signal is demodulated at 30 MHz in order to obtain an error signal that we make use of to stabilize the cavity length.

The 532 nm light coupled into the cavity induces a repulsive dipole force as it is blue-detuned with respect to the atomic transition. This effect modifies the density profile due to this repulsive lattice potential. To mitigate this effect, we couple the 532 nm beam to the TEM_{20} mode of the cavity. This reduces significantly the peak dipole potential seen by the atoms as the optical power penetrating in the cavity is spread over a larger area (approximatively a factor 2 larger). In addition, we imprint a deep phase modulation where a majority of the power is contained in the sidebands that are fully reflected when cavity is locked. This minimizes further the peak dipole potential seen by the atoms that is kept below 46 nK, small compared with the actual temperature of the degenerate Fermi gas we will work with.

3.3.5 *Transfer cavity laser systems*

The transfer cavity is a 15 cm-long Fabry-Perot cavity which properties are detailed in Appendix A. We will describe the laser system that is designed to give a relative frequency stability between the 1064 nm beam line and the cavity probe laser at 671 nm.

First, the transfer cavity is locked onto the frequency of the 1064 nm laser. For this the broadband fibered EOM imprints two phase modulations leading to a first sideband at a variable frequency ν_F from the carrier 3.11. The second frequency is kept fixed at 30 MHz in order to create three error signals, one for the carrier and two for each sideband at a variable frequency from the carrier. The transfer cavity is locked onto the frequency of one of the sideband, making the resonance frequency of the transfer cavity tunable with respect to the frequency of the 1064 nm laser and the science cavity resonance. The overall frequency resonance of the transfer cavity can also be adjusted by changing the frequency of the 1064 nm laser. For stability all EOMs are temperature regulated to minimize the variation of polarization in the crystal [123]. Moreover we lock the cavity on the third harmonic of the phase modulated signal to reduce the influence of residual amplitude modulation [124].

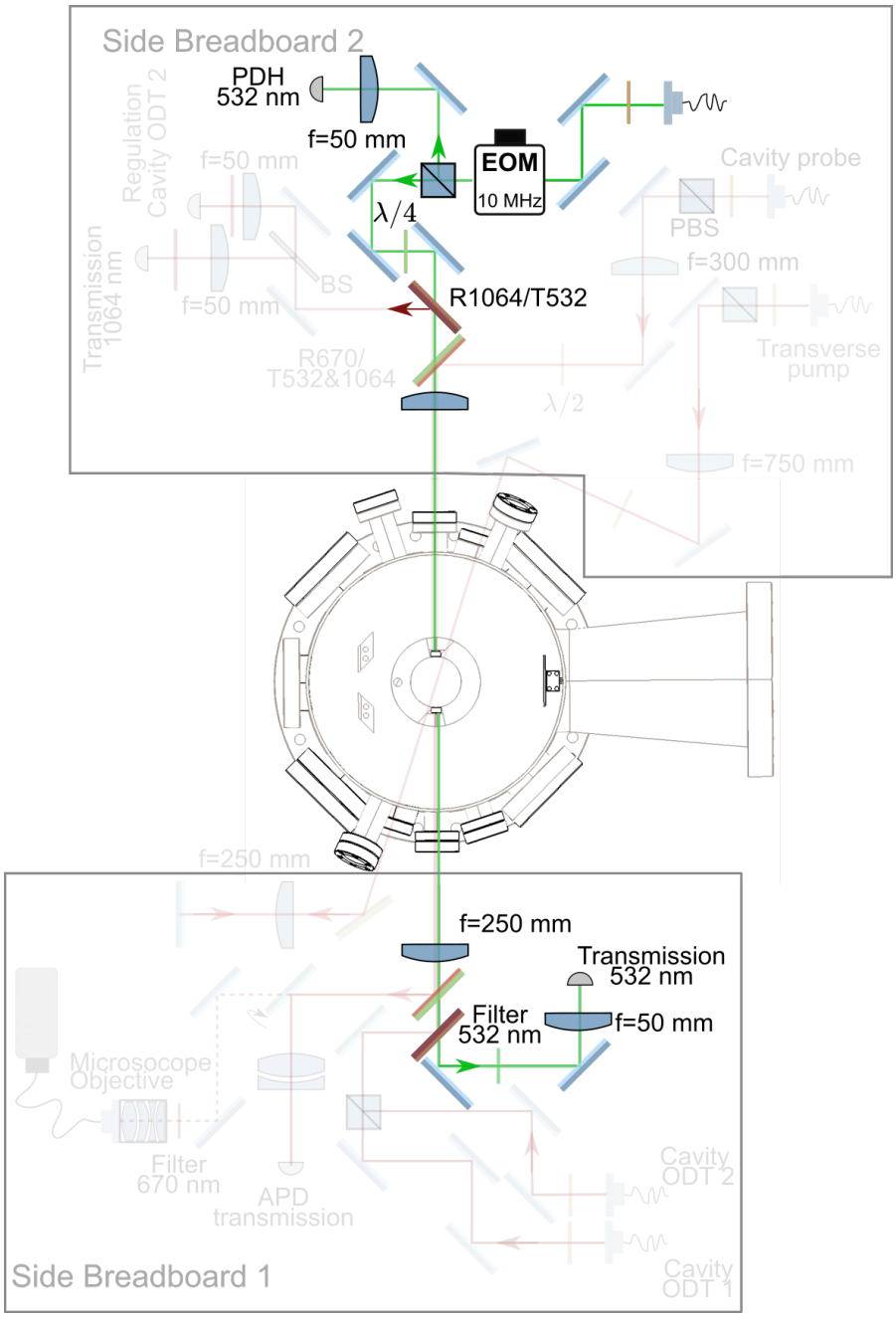

Figure 3.10: *Cavity length stabilization optical setup.*

The cavity probe laser (*Toptica DLpro*) is routed to the same transfer cavity via an optical fiber, thus performing a cleaning of the spatial mode of the diode laser. A small amount of power is picked up before in order to measure the wavelength of the laser on the wavemeter. A single-pass AOM is employed to power regulate the beam line of the cavity probe laser. A free-space EOM (*Qubig EO-F30L3-NIR*) generates sidebands 30 MHz from the carrier frequency to perform a PDH stabilization. This PDH stabilization has two major interests :

- The frequency of the probe laser, the 1064 nm laser and the science cavity frequency resonance are all frequency-referenced to each other.

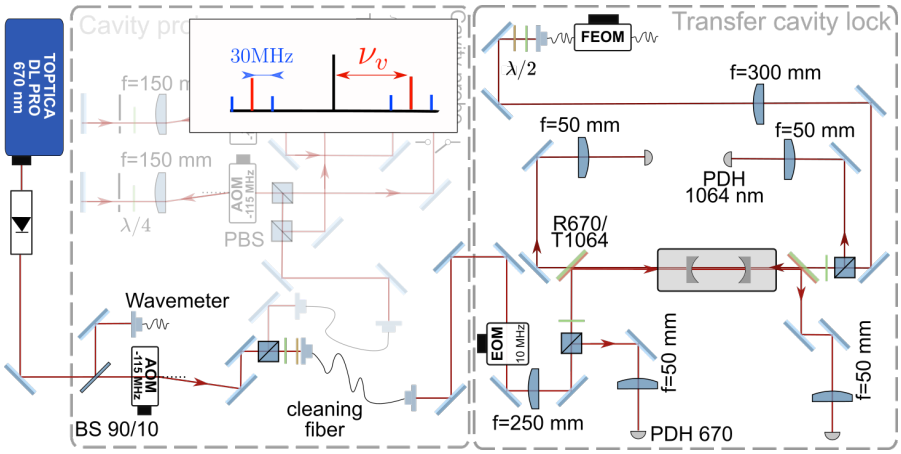

Figure 3.11: ***The transfer cavity setup for relative frequency stability between the different lasers of the experiment.*** The inset shows the phase modulation at variable frequency ν_F and the fixed modulation at 30 MHz. The transfer cavity is locked on the error signal generated by the variable frequency sideband.

The frequency resonance of the science cavity can be shifted with respect to the probe laser frequency by changing the frequency ν_v generating the variable sidebands in the fibered EOM.

- The transfer cavity linewidth being 31 kHz, which is much narrower than the linewidth of the laser, a fast-feedback on the current of the laser diode using a fast PID (*Toptica FALC*) makes it possible to lock the laser on the transfer cavity and consequently to narrow down its emission linewidth to a fraction of the transfer cavity linewidth. We estimate the laser linewidth to be in the range of 10 kHz by measuring the RMS fluctuation of the error signal in closed-loop compared with the peak-peak value of the error signal in an open-loop configuration.

With the different setups presented so far, we can fix and tune the relative frequency between the cavity resonance frequency and the probe laser. It is also necessary to reference this frequencies with respect to the atomic transition frequency of ^{6}Li also in order to provide an absolute frequency stability. To do so, we take advantage of the built-in PID module of the wavemeter that is referenced onto the saturated absorption spectroscopy giving a resolution of about 100 kHz to the wavemeter reading close to 671 nm. The wavemeter PID takes as an input the frequency of the probe laser and feedback onto the piezoactuator of the 1064 nm laser. As a consequence, it shifts the resonance of the transfer and science cavities to make them resonant with the frequency of the probe laser that is desired. In such a way, we can choose arbitrarily the detuning between the atomic transition and the cavity resonance frequency.

3.3.6 *Probing the light-matter coupled system with the cavity*

In order to probe the coupled atom-photon system we send near resonant light through the cavity. We will be able to map out the energy spectrum of this hybrid system by monitoring the transmission of the science cavity (see Chapter 5) as a function of the different frequency detunings between

the probe light, the cavity resonance frequency and the atomic transition frequency.

The cavity probe laser

Here we come back to the transfer cavity optical setup depicted in figure 3.12.

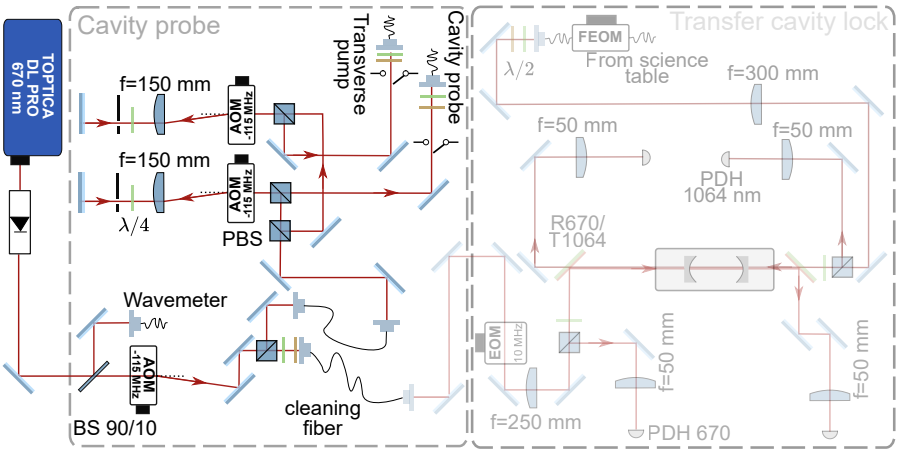

Figure 3.12: *Probe laser optical system.*

The main beam line is split into two beams as depicted in figure 3.12

- One beam line is used to probe the cavity transmission. The laser beam is sent to a double-pass AOM in order to control its frequency and its intensity dynamically during the experimental sequence. It is then fiber coupled to the breadboard aside the vacuum chamber. An optical density is placed before the fiber coupler to reduce the power by 4 orders of magnitude. We typically send a few nW to the cavity. This beam constitutes the on-axis pump that is mode-matched with the fundamental TEM_{00} of the Fabry-Pérot resonator.
- The second beam line is used to pump transversally the atoms. The frequency and amplitude control is ensured by an identical double-pass AOM compared with the on-axis probe. This beam line provides a total output power of 3 mW at the optical fiber input.

We want to realize frequency scans of the on-axis probe beam through the cavity resonance in order to probe the transmission of the cavity. As we will see later in this manuscript, fast frequency sweeps allow to 'flash' the on-axis pump potential to measure the energy spectrum of the system or the atom number for example. As this sweep rate will be faster that the dynamical response of the atoms, we can consider them as fixed during this measurement. Much slower sweeps will show dynamical response of the atomic density to the cavity field that will imprint part of the strongly interacting Fermi gas properties into the optical signal that we will measure. For fast sweeps we want to scan the laser frequency over 20 MHz. In this case, the on-axis probe only is used and its AOM is driven by a voltage-controlled-oscillator (VCO) that allows for frequency sweeps of several MHz. For pump-probe experiments where we send simultaneously the on-axis pump and the transverse one we want to scan a narrow frequency

window and control the relative frequency detuning of the two-pumps at the Hz level. In order to realize these two configurations, the AOMs are fed with the same RF frequency coming from a Siglent DDS ensuring the phase stability between the two RF signals. A voltage-controlled attenuator allows to dynamically tune the RF power sent to the transverse pump AOM. Using the frequency-modulation of the DDS allows to fix a specific detuning between the frequency of the on-axis probe and the transverse pump. This will be used to perform cavity-assisted Bragg spectroscopy [45].

Cavity transmission spectroscopy and cavity-assisted Bragg spectroscopy setup

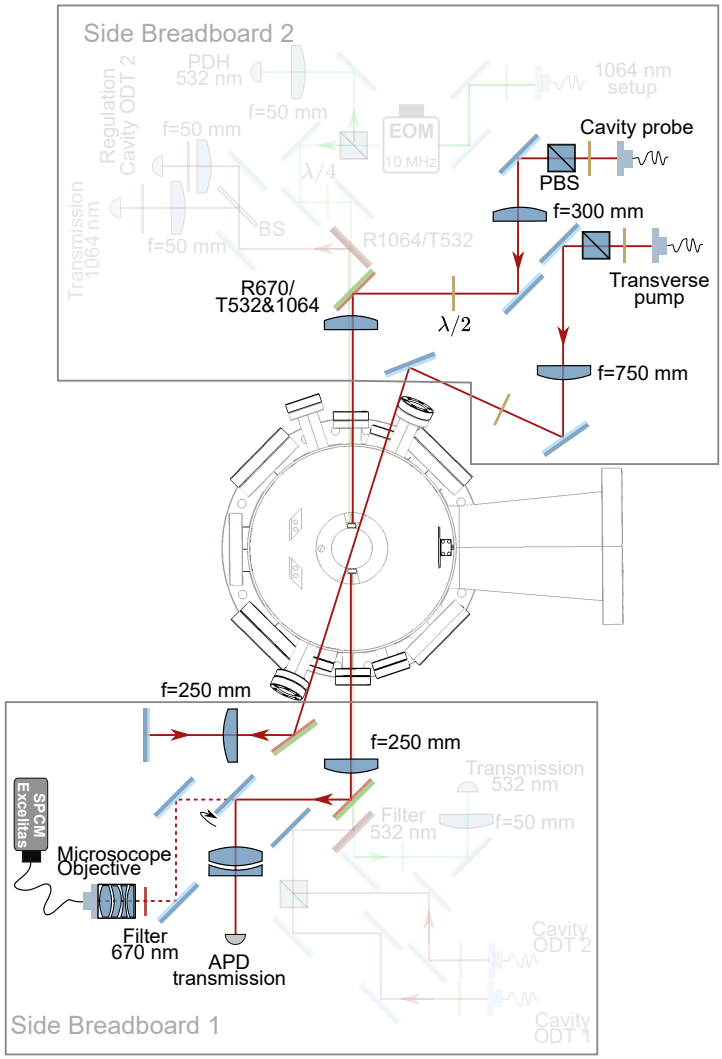

Figure 3.13: ***On-axis cavity probe and transverse pump optical setup around the vacuum chamber.***

The on-axis probe, as well as the transverse pump, are sent to the breadboard aside the vacuum chamber. There the on-axis polarization is cleaned up with a polarizing beam splitter. A half-wave-plate combined with a quarter-wave-plate allows to tune the polarization of the probe light. If the polarization is aligned with the vertical quantization axis, only the π—atomic transition can be driven, while if the probe is polarized horizontally, the

probe beam will couple to the $\sigma^{\pm}-$ atomic transitions of the D_1 and D_2 atomic lines. A dichroic mirror makes it possible to overlap the PDH light, the cavity dipole trap and the on-axis near resonant probe. The transmitted light is collected on the other side of the chamber where we can chose on which detector we collect the transmitted photons. For alignment purposes an avalanche photodiode detects large photon count rates. When we perform experiments with little amount of light injected into the cavity, the transmission is sent to a multimode optical fiber that is connected to a single photon counter module (SPCM) (*Excelitas ARQH-14-FC*). A flip mirror allows to chose between the two detectors.

The transverse pump beam is also controlled in polarization. It is sent on the same axis as one of the arm of the crossed optical dipole trap, meaning an angle of 18° with respect to the cavity axis. It is focused onto the atomic cloud with a $f = 750$ mm lens, corresponding to a beam waist of 200 µm in the atomic plane. After one pass through the science chamber, the beam is focused onto a mirror an back-reflected in order to create a 1D optical lattice at 671 nm. The characterization of this optical lattice will be detailed in a later chapter.

3.4 ALL OPTICAL EVAPORATIVE COOLING TO QUANTUM DEGENERACY

In this section I will present in detail how we make use of the Fabry-Pérot cavity in order to produce a deep and relatively large trap to maximize the transfer efficiency from the CMOT cloud obtained after the laser-cooling stage of the sequence. Moreover I will explain how we can cancel the lattice structure of the standing wave [121], thus enabling an efficient evaporative cooling inside the intracavity trap. This was so far not accessible with existing cavity based traps, as the lattice structure makes the collisions between atoms that allows for thermalization inefficient as they only occur between atoms belonging to the same site of the 1D lattice of the cavity trap.

3.4.1 *Intracavity dipole trap and evaporative cooling : a lattice-free intracavity trap*

We take advantage of the Fabry-Pérot cavity to create a deep trap with a moderate laser power benefiting from the cavity power build-up defined in the previous chapter as $4\mathcal{F}/\pi$ with $\mathcal{F}$ the finesse of the resonator. I will first present the laser setup that produces the two laser beams used to create the standing wave and the lattice free trap. I will then detail the experimental sequence and finally focus on the advantage of cancelling the lattice structure of the trap to increase the phase-space density after the evaporative cooling in the resonator.

Laser system

We want to have two laser beams injected in the cavity in order to create two different optical dipole traps: first, a high-power dipole trap, with a standing-wave structure that has been shown to increase the capture from the CMOT cloud. In addition, a second trap with lower optical power is used durin gintracavity evaportaion on which we implement the lattice-cancellation technique to evaporate efficiently the atomic cloud. For this, two beam lines are derived from the main output of the Yb-doped fiber amplifier. The

first beam line corresponds to the first cavity trap (Cavity ODT1 in figure 3.14). Its frequency and intensity are controlled with a double-pass AOM (*AA optoelectronics MT110-A1*). It is then fiber coupled to the science chamber breadboard.

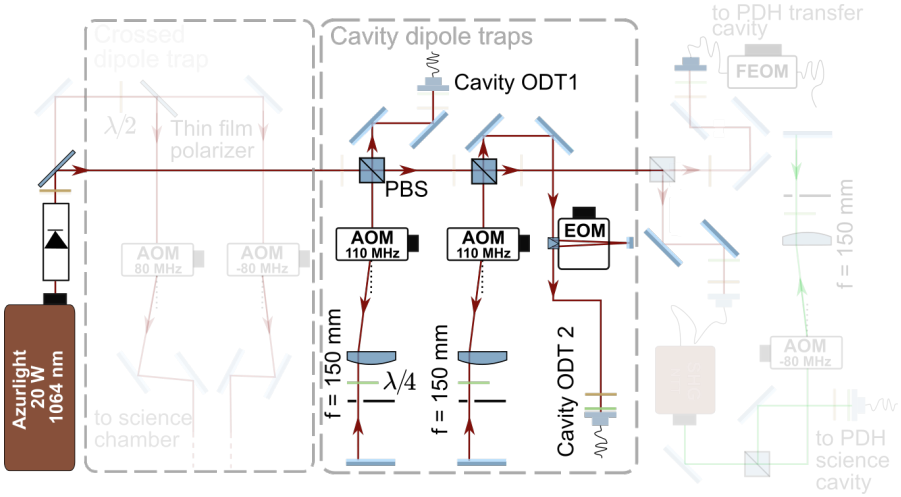

Figure 3.14: ***Laser system for the cavity optical dipole traps.*** Two beam lines are independently controlled in frequency and power in order to realize a standing wave trap for the CMOT loading, and a lattice-free trap to perform an efficient evaporative cooling directly in the cavity trap.

The second beam line that is used to create the lattice-free trap (cavity ODT 2 in figure 3.14) is also controlled in amplitude and frequency with a double-pass AOM (*AA optoelectronics MT110-A1*). In addition, a free-space double-pass EOM (*Qubig Pm9-NIR-F3.6*) modulating the phase of the trap beam at about 3.6 GHz is installed prior to be fiber coupled to the science chamber.

The optical setup around the science chamber is depicted in figure 3.15. The two cavity dipole traps are overlapped with crossed polarisations using a polarized beam splitter. Then a lens focuses them down at the center of the chamber, achieving the necessary mode matching with the cavity mode. The transmission of both beams are measured after the cavity on two different photodiodes. The standing wave cavity trap is regulated in power by measuring a leak through a mirror before the cavity. The lattice-free trap is power regulated by measuring the transmitted power through the cavity. The experimental sequence will allow to go from one regulation loop to the other on a smooth manner, keeping the intracavity power constant when transferring the cloud from one trap to the next [125].

The cavity trap beams are mode-matched with a transverse TEM_{01} mode of the resonator. Thus, it is required to adapt the frequency difference between the frequency of the 532 nm lock light and the one of the dipole trap in order to match the transverse mode spacing and the difference of refractive index in the substrate of the mirror. The double-pass AOMs on both paths play this role, adjusting the frequency difference and making the cavity trap beams resonant with the locked science cavity.

I will now explain the details of the experimental sequence corresponding to the loading and the evaporative cooling in the intracavity trap.

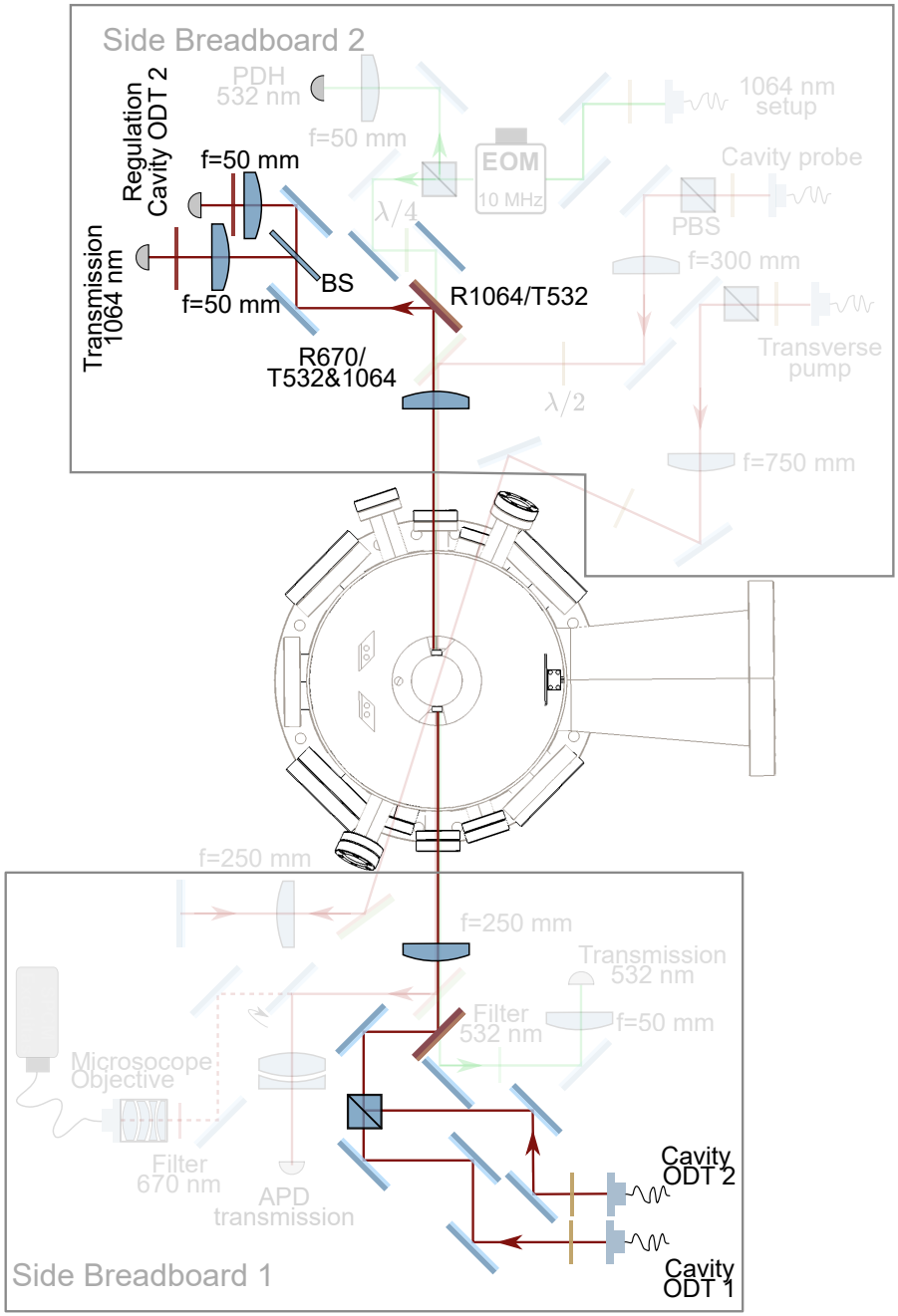

Figure 3.15: *The cavity dipole trap optical system around the science chamber.*

Experimental sequence

After the CMOT and a phase of optical pumping in the $|2S_{1/2}, F = 1/2\rangle$ state, the atoms are transferred in the first cavity optical trap which consists in a standing wave, with the transverse intensity profile of the TEM_{01} mode. We inject a total of 244 mW in the first cavity trap beam that corresponds to a peak power at the center of the cavity of 671 W with a beam waist of 56.6 μm. The peak trap depth is then about 8 mK compared with a temperature for the laser cooled cloud of about twice the Doppler temperature $T \sim 300$ μK. We load about 1.5×10^7 atoms from the CMOT, comparable with experi-

ments using improved laser cooling techniques [116]. The cavity trap is kept at full power for a duration of 100 ms, while the magnetic field is ramped up to 832 G corresponding to the Feshbach resonance for the $|1\rangle - |2\rangle$ spin mixture (figure 3.16.c). When ramping up the magnetic field we create an incoherent mixture of atoms in the two lowest hyperfine states (see Chapter 2). At the Feshbach resonance the scattering length a diverges leading to strong atom-atom interactions [71]. This will be explained in detail in Chapter 4, however at the preparation stage it is of great help as it allows the cloud to thermalize extremely quickly when the trap depth is reduced during the evaporative cooling process. This makes ^{6}Li a very convenient atom to cool down to quantum degeneracy with an all-optical production sequence [97, 107, 126].

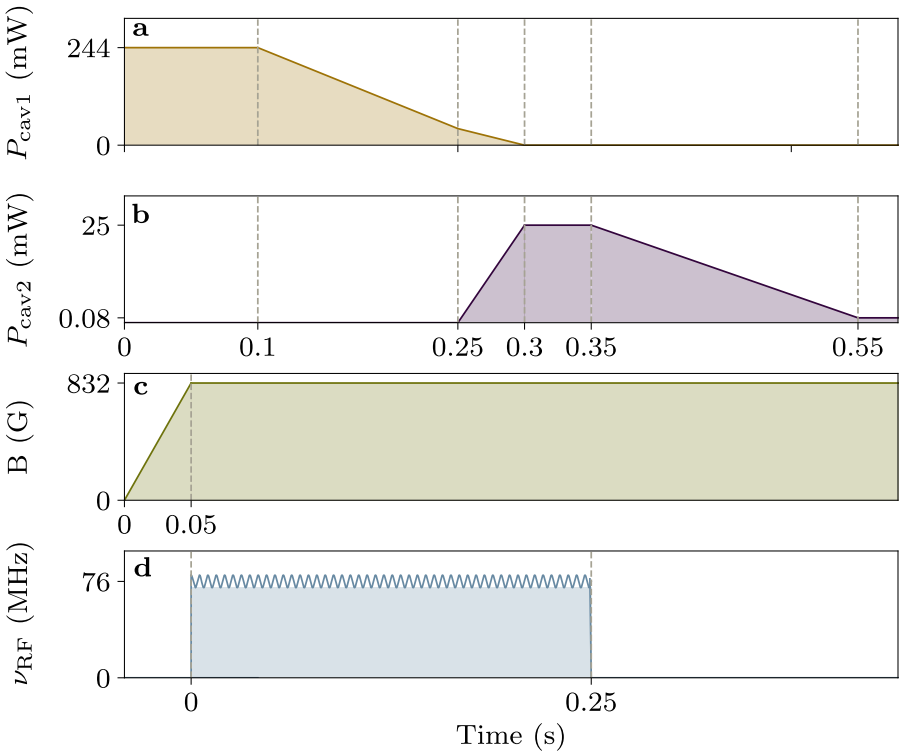

Figure 3.16: ***Optical evaporative cooling sequence in the optical resonator.*** **a-b** shows the evolution of the optical power of the standing wave P_{cav1} and lattice-free P_{cav2} cavity traps respectively. **c** shows the ramp of magnetic field prior to the optical evaporation in order to reach 832 G, the location of the broad Feshbach resonance magnetic field. Panel **d** displays the RF frequency sweeps realized during the first evaporation ramp in the standing wave trap. These multiple Landau-Zener frequency sweeps produce the balanced incoherent mixture in the two lowest hyperfine states.

When the magnetic field reaches 832 G, the trap is held at full power for 50 ms. Afterwards, the power of the first cavity beam is linearly decreased down to 25 mW over 150 ms (see figure 3.16.a). This corresponds to a peak power at the center of 68 W. During this ramp the photodiode monitoring the cavity transmission saturates and consequently the second cavity dipole trap is turned off. While the power of the first cavity trap is decreased, the photodiode monitoring the cavity output power desaturates and starts to increase the power of the second trap to compensate for the decrease of the first one. Operating the first trap in the saturation regime of the photodiode

allows us to smoothly transfer the cloud for the first to second trap as we have a controlled crosstalk between the two regulation loops. After the first linear ramp the standing wave cavity dipole trap is smoothly turned off over 50 ms giving enough time for the regulation of the lattice free cavity dipole trap to compensate for. At this point the cloud is fully transferred in the lattice-free dipole trap and a second linear ramp brings to intracavity power at the center of the trap down to 70 mW (figure 3.16.b). The lattice-free trap has the same transverse intensity profile as the standing wave trap, both addressing the same TEM_{01} cavity mode.

The population in the two lowest hyperfine states obtained after the laser-cooling stage is not reproducible and dependent on the exact conditions of the optical pumping at the end of the CMOT. As we want to obtain a balanced population between these two states, we apply an RF frequency sweep around a frequency $\omega_{12} = 76.034$ MHz of the transition from state $|1\rangle$ to state $|2\rangle$. We modulate this frequency with a modulation depth of 300 kHz around ω_{12} at a rate of 10 kHz (see figure 3.16.d). These multiple Landau-Zener RF frequency sweeps are applied for a total duration of 250 ms and create a balanced incoherent mixture of atoms in the two lowest hyperfine states.

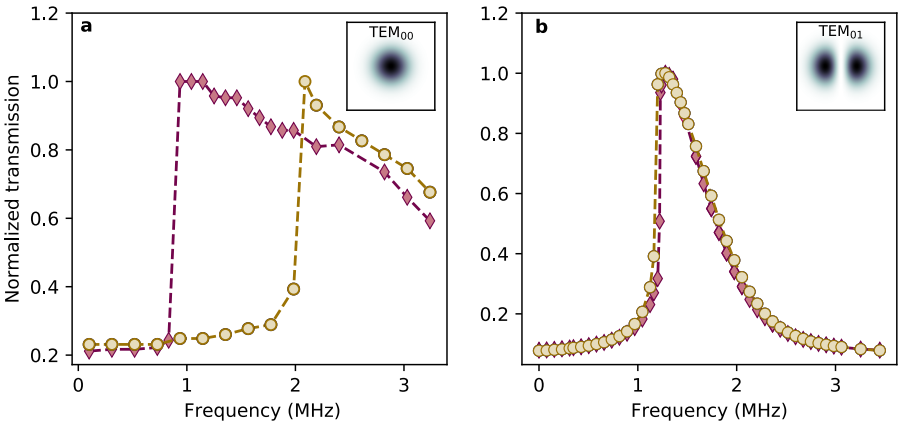

Figure 3.17: ***Thermal effect in the mirror substrate for different cavity transverse mode.*** The figure shows the evolution of the transmitted power through the cavity while scanning the frequency of the laser around the cavity resonance in the case of a TEM_{00} mode (**a**) and a TEM_{01} mode (**b**). The yellow circles shows frequency scan for increasing frequencies while the violet diamonds correspond to decreasing frequencies. The larger mode surface on the mirror in the case of the TEM_{01} mode greatly reduces both the bistable and hysteretic profile observed with the fundamental mode of the cavity. Using a higher order transverse mode gives the possibility to regulate the intracavity power by monitoring the cavity output power which is practically impossible in the case of the TEM_{00} cavity mode due to the optical bistability.

As previously described the cavity trap beams are mode-matched with the transverse TEM_{01} mode of the cavity with two lobes oriented in the plane of the cavity [120]. Even though this will produce two different clouds in each lobe of the cavity trap it does provide two very beneficial features.

- Indeed, for a given laser power coupled into the cavity, spreading the power over a TEM_{01} mode reduces the peak intensity on the surface of the mirrors. We observed a strong bistable and hysteretic behaviour when coupling the same optical power into the fundamen-

tal TEM_{00} mode of the cavity as a function of the frequency of the trapping beam compared with the cavity resonance (figure 3.16.a). We attribute this effect to heating at the mirror surface due to the large intracavity power. Practically, this behaviour made it extremely complicated to regulate the intracavity power by measuring the cavity output power as a small power fluctuation would make the laser power jump from one branch to the other of the bistable profile. This induces large preparation noise as an unregulated intracavity laser power leads to strong heating and losses while performing the evaporative cooling procedure in the resonator. Comparing with the same power incident on the cavity but coupled to the TEM_{01} mode the hysteretic behaviour is completely suppressed and the bistability is greatly diminished when scanning the laser frequency of the incoming beam (figure 3.16.b). This is first due to a combination of the reduced intensity on the mirror that mitigates the heating, and consequently minimize the bistability. Second, it appears that the coupling efficiency to the TEM_{01} mode is reduced to 50% compared with the 80% of coupling efficiency on the TEM_{00} mode. In fact comparing both situation at equivalent intracavity power still shows a clear reduction of the thermal effects on the mirror leading to this bistable behaviour.

- The second main advantage is an increase of the trap volume. As the TEM_{01} has a mode volume twice larger than the fundamental mode, it increases the trap volume by a factor two and consequently maximizes the overlap with the laser cooled cloud. As the trap depth at the center of the cavity is about 8 mK we can easily tolerate the reduction of the coupling efficiency, the trap depth not being the limiting factor when loading the cavity dipole trap[1]. Obtaining a two-cloud structure is not problematic in our case as the standing lattice is cancelled out at the trap center (see next section), allowing the atoms trapped in the two lobes to be captured efficiently by the standing wave trap. Hence, it will be possible to transfer the two clouds in a running wave dipole trap without any losses as they can move along the longitudinal direction of the cavity beam.

Now that the intracavity evaporative cooling sequence has been detailed I will describe the method that has been used to cancel the intrinsic lattice structure of the second cavity dipole trap and how this allows for an efficient intracavity evaporative cooling compared with a regular standing wave cavity trap.

Lattice-free cavity optical dipole trap

Even though cavities have been considered to be used to create large and deep optical potential for several decades [119] and employed in many laboratories, the role of these traps have been limited to capturing the atoms from the MOT before transferring them into a running-wave optical dipole trap to perform the evaporative cooling. This is due to intrinsic lattice structure of the standing wave of the intracavity field. In this configuration, and as optical powers are usually pretty large, each site of the 1D lattice of the cavity standing wave is filled with atoms from the MOT cloud. Each of these lattice sites is isolated from the other due to the large depth of the lattice.

1 In the future one could think of reducing the cavity mode volume to increase the light-matter coupling strength while using even larger order TEM modes to keep a large trap volume.

Consequently even if the atomic density is rather large for each lattice site, the evaporative cooling proceeds in each site independently, thus limiting the efficiency of the cooling process. Moreover, transferring these atoms into a running-wave optical trap is complicated, only the atoms in the lattice sites overlapping with the running-wave trap will be efficiently transferred while the other will not be able to move along the lattice direction due to the large lattice depth.

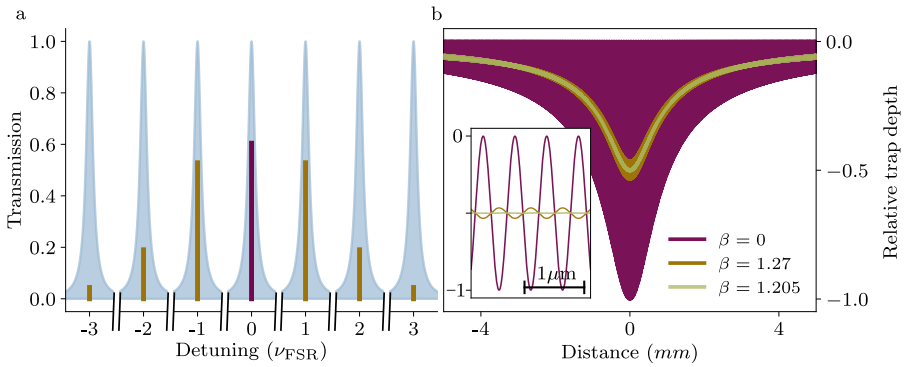

Figure 3.18: ***Suppression of the lattice-structure of the cavity dipole trap : principle.*** **a** Sidebands are created at multiples of the FSR of the cavity. About 50% of the total power is contained in the sidebands for a modulation depth $\beta = 1.27$ rad. **b** The dipole potential created by the cavity standing wave exhibits a large lattice structure (violet curve) while the dipole potential in the presence of the phase modulation shows a flat behaviour around the center of the cavity (light green and dark yellow curves). At the optimum modulation depth $\beta = 1.27$ rad, the potential is perfectly flat at the center (inset). The optimum modulation use on the experiment that maximizes the phase space density shows a very weak lattice at the center.

To circumvent this problem we make use of the longitudinal mode structure of a Fabry-Pérot cavity. We exploit the phase relation between adjacent longitudinal modes by coupling simultaneously several longitudinal modes with a controlled relative intensity (figure 3.18.a). As a reminder from the previous chapter, two consecutive longitudinal modes correspond to the same intra-cavity field with a phase difference of $\pi/2$, meaning that the cosine-square intensity profile of consecutive longitudinal modes are spatially shifted with respect to each other by $\pm\lambda/2$. In the case of our science cavity the longitudinal modes are separated in frequency by $\nu_{FSR} = 3.6277$ GHz. Thus, the resulting optical potential will simply be the sum of the potentials created by each longitudinal mode. Interferences between the field created by each longitudinal mode will oscillate at a frequency $\nu_{FSR} = 3.6277$ GHz, which make it possible to neglect them as it is too fast for the atoms to respond. Each longitudinal mode intensity will sum up and due to their relative spatial shift of $\pm\lambda/2$, the potential at the cavity mode center will be free of any lattice.

This technique is used to obtain an homogeneous coupling between Rb atoms and the cavity field as demonstrated in [121]. The cavity standing-wave intensity profile along the cavity direction is $I(y) \propto \cos^2(k_0 y)$ with k_0 the wavevector of the cavity light field. This usually reduces by a factor 1/2 the coupling between the cavity light field and the atomic cloud, as half of the atoms are located at the field nodes. This method provides a way to obtain a homogeneous coupling of all the atoms of the cloud with the cavity field.

We use the same technique to provide a lattice-free intracavity optical dipole trap.

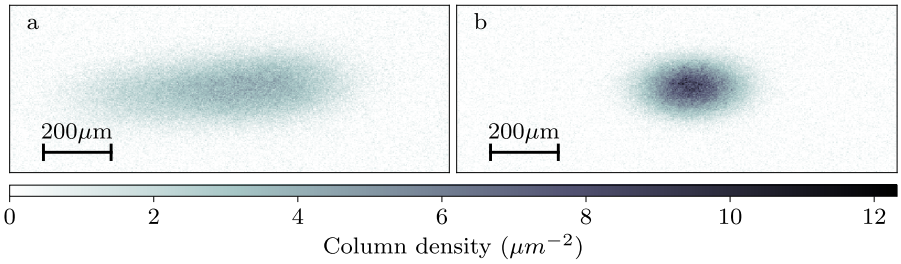

Figure 3.19: ***Suppression of the lattice-structure of the cavity dipole trap : result.*** **a-b** show absorption images along the horizontal plane, of the cloud after a time-of-flight of 2 ms without and with the lattice suppression respectively. These images are taken once the evaporative cooling in the cavity trap is performed. We observe an increase of the peak column density by a factor 2 as well as a reduction of the cloud size along the cavity direction by a factor 3 when the phase modulation is applied during the evaporation compared with the evaporation in the standing wave cavity trap.

Experimentally we use a double-pass free space EOM (figure 3.14) to create a phase modulation onto the second cavity trap beam at $\nu_{FSR} = 3.6277$ GHz. The large modulation depth (30 dbm) creates sidebands at multiples of ν_{FSR} (figure 3.18.a). Approximatively half of the total power is contained in the sidebands. The optical dipole potential can be written as :

$$I_{tot}(y) \propto V_0 \sum_{n=0}^{\infty} J_n(\beta)\cos^2\left((k_0 + \delta k_n)y + n\pi/2\right) \tag{3.8}$$

with β the modulation depth, J_n the Bessel functions of order n and $\delta k_n = n\nu_{FSR}/c$ with c the speed of light. A sideband of order n is phase shifted with respect to the reference longitudinal mode by $n\pi/2$. In figure 3.18.b we represent the optical dipole potential created by a single longitudinal mode (violet) and with the phase modulation for the modulation depth that suppresses completely the lattice structure at the mode center (light green) and the optimum modulation used on the experiment (dark yellow). The inset of figure 3.18.b shows the optical potential around the cavity center, where we can clearly see the suppression of the lattice structure. As a direct consequence of the sum of the sidebands intensities, the peak dipole potential is reduced by a factor 2 but the suppression of the lattice structure effectively increases the accessible volume of the trap by the same factor.

Once the atoms are transferred into the lattice-free cavity dipole trap, all the atoms of the cloud can collide with each other as the can move along the cavity direction. This makes the evaporative cooling process much more efficient. In figure 3.19 we show absorption images after a 2 ms time-of-flight in the absence of phase modulation (figure 3.19 .a) and with the modulation turned on for the evaporative cooling in the second cavity trap (figure 3.19 .b). Everything else kept identical, the phase-space density increases by about a factor 6 when the evaporative cooling is performed in the lattice-free cavity dipole trap. The absence of lattice structure makes it possible to transfer almost 100% of the atoms from the cavity dipole trap to the running-wave one. We can typically transfer about 1.5×10^6 atoms from the

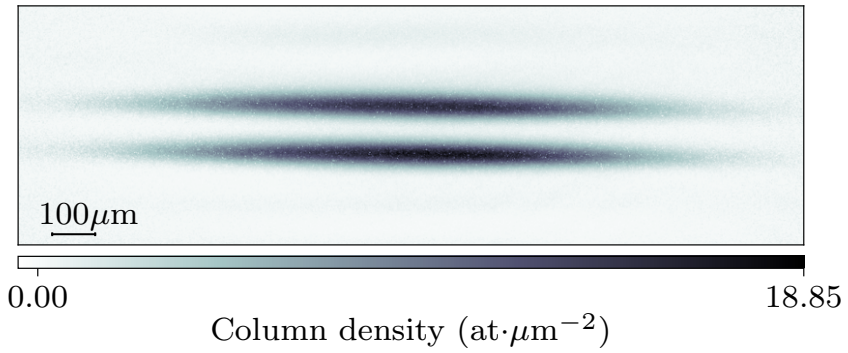

Figure 3.20: ***Absorption image of the atomic cloud in the lattice-free cavity optical dipole trap.*** The absorption image is taken almost in-situ with a very short time-of-flight (0.3 ms) in order to mitigate saturation effects. Both lobes of the TEM_{01} mode are populated. We will intersect this two lobes with a running-wave crossed optical dipole trap to transfer them for the final evaporative cooling stage to quantum degeneracy.

cavity dipole trap into the free-running trap used to perform the cavity QED experiment.

In figure 3.20, we show an in-situ absorption image of atoms in the lattice-free cavity trap taken from the vertical direction. We can clearly observe the double cloud structure due to the transverse intensity profile of the TEM_{01} cavity mode. As we want to couple these atoms to resonant light inside the cavity we have to transfer them to another dipole trap, the overlap between the TEM_{01} mode of the cavity trap and the TEM_{00} mode of the cavity at 671 nm being small. We have strong qualitative indications that we can produce clouds close to, or even below, the Fermi temperature by using our evaporative cooling sequence in the cavity trap for a total duration of 550 ms. This represents a important technical progress in speeding up the production of quantum gases with large atom number[2].

3.4.2 *Evaporative cooling to quantum degeneracy in a running wave crossed-dipole trap*

After the evaporative cooling sequence, first in the standing-wave cavity trap, then in the lattice-free cavity dipole trap, we transfer the cloud in a running-wave crossed optical dipole trap. This will maximize the overlap between the atomic density and the TEM_{00} mode of the Fabry-Pérot cavity at 671 nm for the cavity QED experiment. Moreover, as the two arms of the crossed optical dipole trap are controlled independently we will be able to choose whether the cloud is held in the crossed dipole or adiabatically released in one of the two arms.

2 A reasonable perspective would be to transfer the cloud back into a TEM_{00} cavity mode at the end of the evaporation and perform the full sequence in the cavity optical dipole trap. This would make the evaporation much more robust, the cavity trap and the probing mode at 671 nm being automatically aligned. More perspectives will be discussed in the last chapter of this manuscript.

Laser system

From the main beam line exiting the Yb-doped fiber amplifier a high power half-wave plate and a thin film polarizer are used to pick up a total amount of power of 3.5 W. A second thin-film polarizer splits it equally into two beams that are sent to two high power AOMs (*AA optoelectronics MCQ80-A2-1064-Z32-C35Sa*). The two beams are frequency shifted by ± 80 MHz respectively, in order to avoid interferences between the two arms when then cross at the cloud location (figure 3.22). It is also ensured by having the two arms of the crossed dipole trap polarized orthogonally.

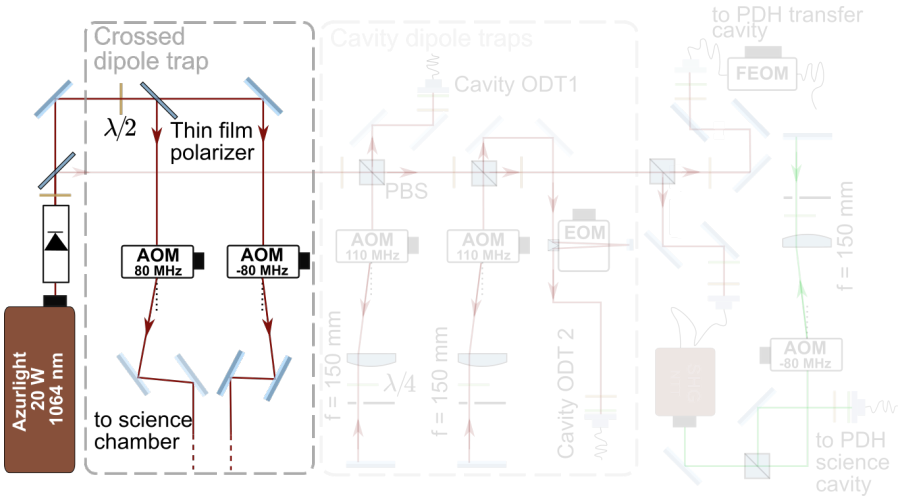

Figure 3.21: ***Crossed optical dipole trap laser setup.***

These two arms are then sent on the breadboards aside the vacuum chamber. Each of these beams have a maximum power of 1 W. The power of each arm is independently monitored on a photodiode picking up a weak leak through a mirror (figure 3.22). This signal is sent to two fast PI modules (*Newfocus LB-1005S*) that acts on the two AOMS amplitude control input to regulate the intensity of the two crossed dipole trap arms independently.

As the distance from the 1064 nm to each side of the chamber is different by about 1.5 m and that the beam exiting the fiber amplifier has a slight divergence, we need to reshape each of the beam differently to ensure that they will have the same beam waist once focused onto the atoms. The two arms of the crossed dipole trap have a 33 μm waist onto the atomic cloud. Consequently one arm is reshaped with a telescope with magnification $\times 3$ while the other arm is magnified by a factor 2.33 (figure 3.22). Both beams are focused onto the center of the science cavity with lenses of focus $f = 250$ mm with an angle of $\pm 18°$ with respect to the cavity axis.

Time line

During the evaporative cooling sequence we use the AOM on each of the crossed dipole trap arm to control the power dynamically. After the evaporative cooling in the cavity trap, the cloud is transferred into the crossed optical dipole trap at full power (1 W in each arm) for a duration of 50 ms while the lattice-free cavity dipole trap is ramped to zero. Then, a first ramp of

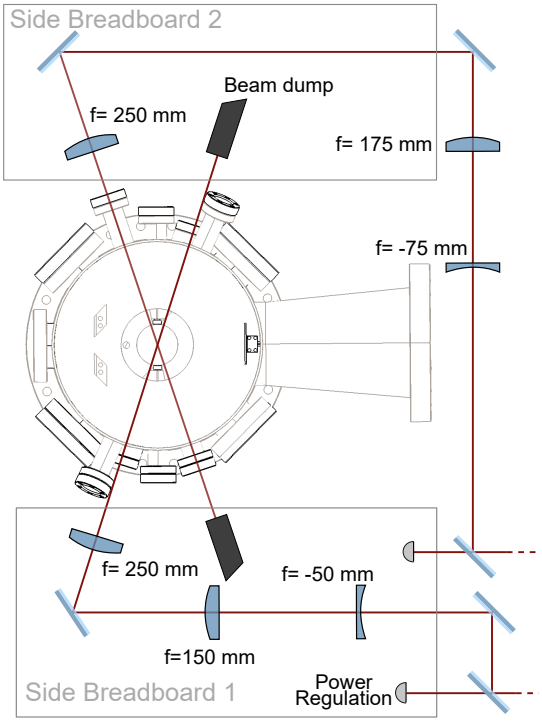

Figure 3.22: *Crossed optical dipole trap laser setup around the science chamber.*

optical power is realized using a power-law function $U(t) = A\,(t - t_0)^p + B$ with $p = 2(\eta - 3)/(\eta - 6)$, η being the ratio between the trap depth and the thermal energy and A, B some numerical constants [108]. This power law evaporation ramp lasts for 100 ms and brings the optical power in each arm to 150 mW. A last linear ramp lasting 300 ms completes the evaporative cooling sequence (figure 3.23 .a).

A zoom on the last part of the sequence is shown in figure 3.23 .b. Once the optical power of the two arm reaches 25 mW at the end of the last evaporation ramp, the trap depth is held at this value for 50 ms. Afterwards the trap is recompressed by ramping up the power in each arm to 53 mW over 50 ms to maximize the overlap between the atomic density and the cavity mode. During this recompression we can adapt the magnetic field value to the one desired for the experiment as it is shown in figure 3.23 .c.d. The magnetic field setpoint is held for 50 ms (or more depending on the exact measurement performed). Then it is smoothly ramped back to 832 G for taking an absorption image of the atomic density.

This sequence typically prepares a spin-balanced cloud in the two lowest hyperfine states, with a population in each spin state of about 4×10^5. We can adapt the duration of the MOT loading phase to obtain between 0.5×10^5 and 5.5×10^5 atoms per spin state. As a characterization, we can measure the lifetime of the gas as a function of magnetic field (and so as a function of the interaction strength as it will be detailed in the next chapter). As shown in figure 3.24, we obtain lifetimes of 2.4 and 2.6 s for the gas held at 832 and 950 G. The lifetime are obtained by fitting the variation of atom number as a function of the holding time with a double-exponential decay. In this two cases, we attribute the limited lifetime to intensity noise of the trapping laser that induce heating.

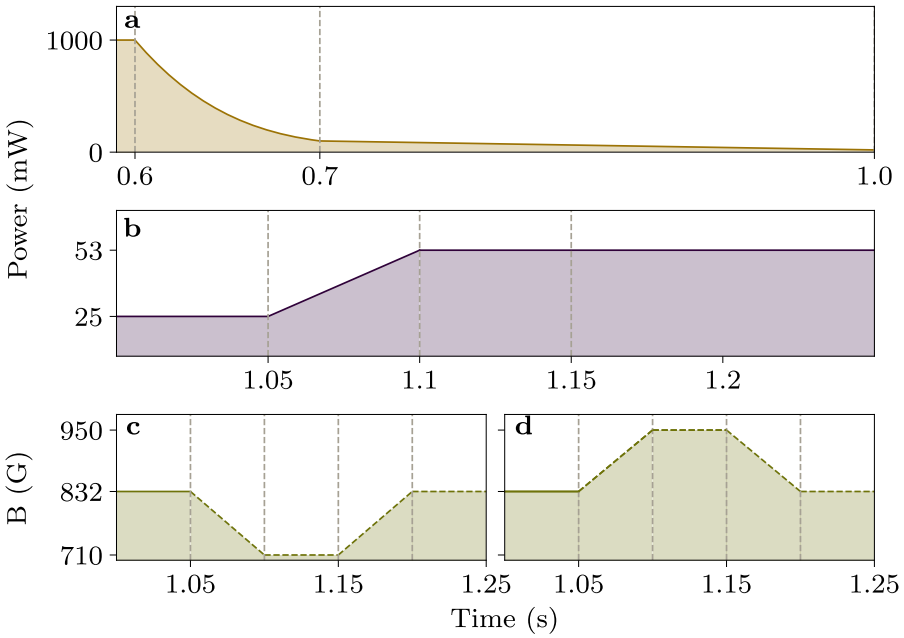

Figure 3.23: ***Timeline of the evaporative cooling sequence in the crossed optical dipole trap.*** **a** Shows the evolution of the crossed dipole trap power during the optical evaporation while **b** shows the end of the evaporation and the recompresion phase of the crossed dipole trap. The atoms will be held in the recompressed trap for the cavity QED experiment presented in this thesis.**c-d** display two possible evolutions of the magnetic field while the trap is recompressed. The cloud can then be probed at any magnetic field across the Feshbach resonance before being ramped back to unitarity for absorption imaging.

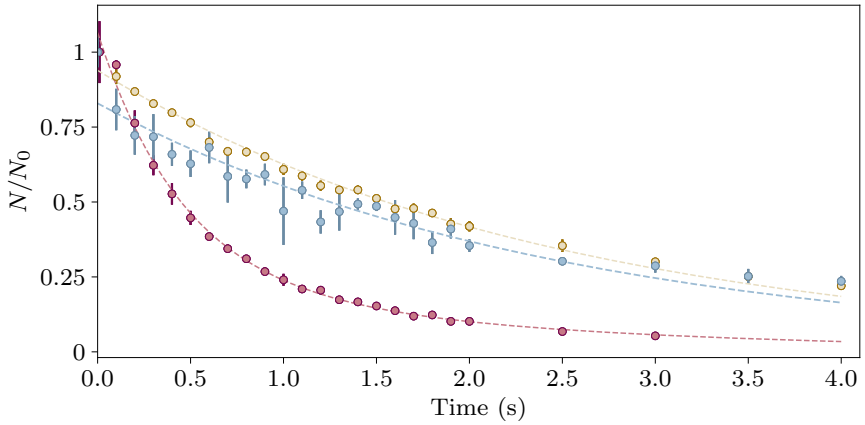

Figure 3.24: ***Lifetime of the ^{6}Li cloud across the Feshbach resonance.*** Evolution of the atom number, normalized by its inital value at $t = 0$, as a function of the holding time in the crossed dipole trap at 710 (violet circles), 832 (yellow circles) and 950 G (blue circles). The solid lines corresponds to double-exponential fit to the data. The lifetime extracted corresponds to the time constant of the first exponential decay.

At lower magnetic field, we observe a much shorter lifetime as shown by the blue circles in figure 3.24. The first decay constant obtained from the fit gives a lifetime of 0.84 s at 710 G, almost 3 times smaller than for the

two larger magnetic field value. This is expected as inelastic processes such as three-body collisions rates are known to increase when going to lower magnetic field compared with the Feshbach resonance as the atoms form bosonic molecules [127][71].

Controlling the relative spin populations

It is possible to introduce a controlled population imbalance between the two lowest hyperfine states. By comparison with the broad Feshbach resonance at 832 G due to $\mathcal{S}$-wave scattering, the $\mathcal{P}$-wave resonance [128, 129] at 214.8 G is extremely narrow because of the phase shift due to $\mathcal{P}$-wave collisions vanish at zero energy. We take advantage of this scattering resonance to induce atom losses in $|2\rangle$ prior to the evaporative cooling. As we will show in the next chapter two identical fermions cannot scatter with a $\mathcal{S}$-wave symmetry, however this process can happen when the collisions are of $\mathcal{P}$-wave type. In the experimental sequence, while ramping up the magnetic field to 832 G, the ramp is stopped at 214.8 G and the magnetic field is held at this value for a variable duration. The holding duration controls the population in state $|2\rangle$. The rest of the sequence proceeds as previously explained.

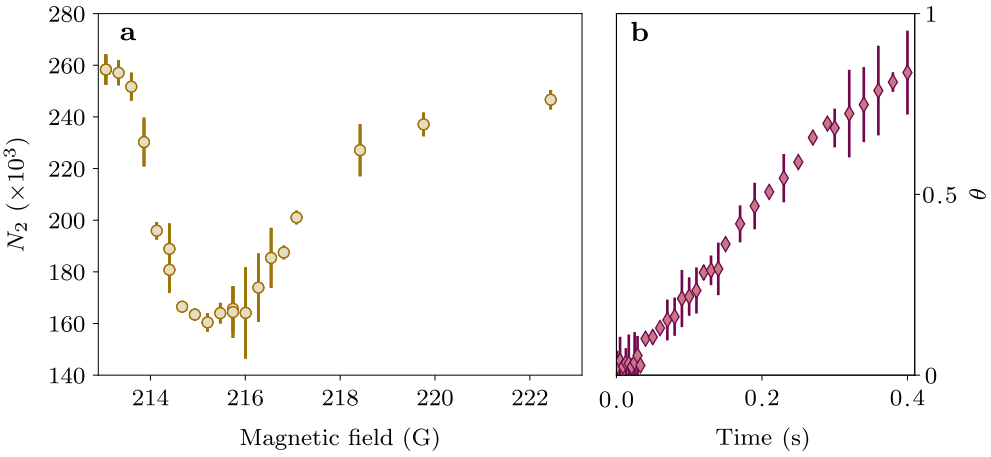

Figure 3.25: ***Controlling the spin population imbalance between states*** $|1\rangle$ ***and*** $|2\rangle$**. a** Evolution of the population in state $|2\rangle$ as a function of the magnetic field value for a holding time of 100 ms. **b** Shows the evolution of the spin imbalance $\theta = \left(N_{|1\rangle} - N_{|2\rangle}\right) / \left(N_{|1\rangle} + N_{|2\rangle}\right)$ as a function of the holding time at the $\mathcal{P}$-wave Feshbach resonance for atoms in state $|2\rangle$ (B = 214.8 G).

We show in figure 3.25a the evolution of atomic losses in state $|2\rangle$ when varying the magnetic field across the $\mathcal{P}$-wave Feshbach resonance located at 214.8 G after the entire evaporative cooling. We clearly observe a broadening compared with the state-of-the-art spectroscopic measurement [129], which is partially due to the noise of the current power supply that produces the Feshbach magnetic field. In addition, the spectroscopic data presented in figure 3.25a are taken at rather large temperature ($\sim 5 - 10$ μK) compared with previous work, resulting in a broadened resonance due to the width of the Maxwell-Boltzmann distribution at this temperature. In figure 3.25b we show the evolution of the spin imbalance parameter θ,

$$\theta = \left(N_{|1\rangle} - N_{|2\rangle}\right) / \left(N_{|1\rangle} + N_{|2\rangle}\right) \tag{3.9}$$

with $N_{|1\rangle}$ and $N_{|2\rangle}$ the atom number in the two lowest hyperfine states after the full evaporative cooling procedure. We observe that we start from $\theta = 0$ meaning that the gas is perfectly balanced. While increasing the holding time at the $\mathcal{P}$-wave Feshbach resonance ($B = 214.8$ G), the imbalance increases linearly to reach a fully spin polarized gas with atoms populating only the lowest hyperfine state for a holding duration of 0.4 s. For large spin imbalance, $\theta \simeq 1$, the population in the state $|2\rangle$ is observed to be quite unstable making it complicated to prepare stable small population($N_{|2\rangle} < 10^3$) in state 2.

Controlling the trap geometry

Having two independent arms for the crossed dipole trap allows us to choose in which trap configuration we want to probe the cloud :

- In the crossed dipole trap we will perform the cavity QED and the RF spectroscopy measurement.
- We can release adiabatically the cloud at the end of the evaporative cooling procedure in one single arm of the crossed optical dipole trap. As the optical density is quite large in the crossed dipole trap, releasing the atoms in a single beam running-wave dipole trap reduces the peak optical density, making possible to realize an almost in-situ absorption image. This will be heavily used to measure the cloud temperature and is detailed in Chapter 4.

To characterize the different traps, we have measured their trapping frequencies. For that we employ two different techniques :

- Starting from the trap we want to characterize at a given power, we ramp up the power of the dipole trap over 5 ms and then quench it back rapidly to the initial value. This triggers dipole oscillation of the cloud in the harmonic trap allowing to measure the oscillation frequency of the cloud after some time-of-flight by measuring the position of the cloud. To choose the direction in which we want the cloud to oscillate we introduce a small magnetic field gradient in this direction which act as a force on the atoms. In order to keep the cloud in the lowest region of the trap, where the harmonic trap approximation stays valid, we need to take a special care of triggering a small motion of the center of mass motion of the cloud.
- For the second measurement technique we modulate the amplitude of the trap by modulating the amplitude of the AOMs. We measure atomic losses and heating after a modulation at a given frequency for 100 ms. By reconstructing the spectrum with all frequencies we observe resonances where the modulation frequency hits the breathing mode frequency of the gas that is equal to twice the one of the dipole oscillation mode for a non-interacting Fermi gas.

In figure 3.26 we show the results of the trapping frequency measurement. For all these measurement we produce a non-interacting Fermi gas as the strong interactions affect the motion of the atoms and for example shifts the breathing mode frequency of the gas [130]. For that, we use the previously describe procedure, holding the cloud for 0.4 s at the $\mathcal{P}$-wave Feshbach resonance to create a fully-polarized, non-interacting Fermi gas. The figure 3.26a.b shows the oscillation of the cloud after a quench of the trap power

in each single arms of the crossed dipole trap. The oscillations are fitted to obtain the trap frequencies of each arm at an optical power of 75 mW. We obtain trap frequencies of 387 and 412 Hz respectively in the vertical direction. We obtained similar measurement along the other transverse direction. Along the beam direction the trapping is mainly provided by the magnetic field curvature of 25 $G \cdot cm^{-2}$ at 832 G. The dipole oscillations in this direction gives a trapping frequency of 28 Hz, consistent with the simulated magnetic field curvature created by the Feshbach coils at 832 G.

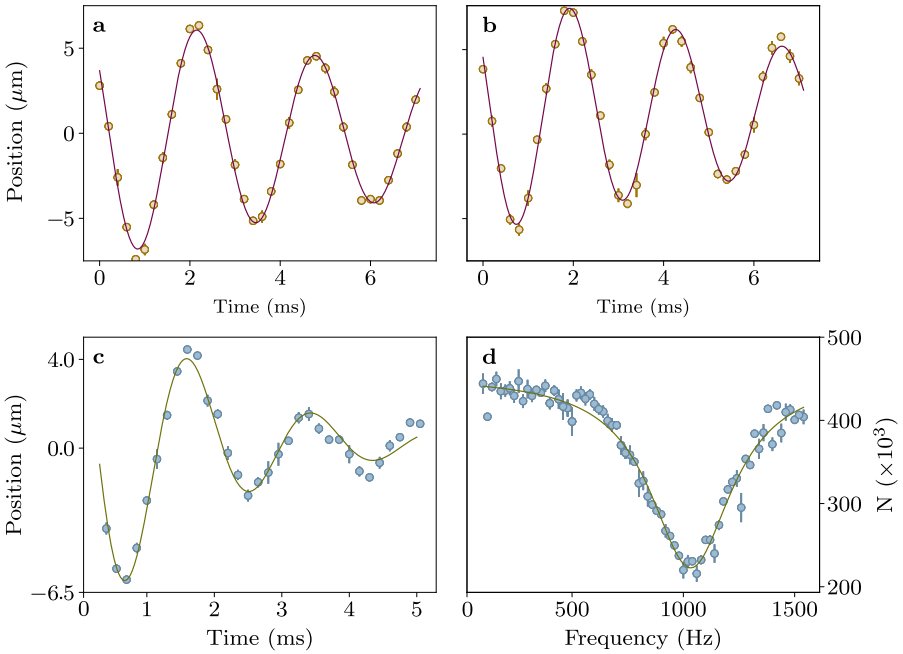

Figure 3.26: ***Trap frequency measurements for the different trap configurations.*** **a-b** Measurement of the dipole oscillations of the cloud along the vertical direction, in each arm of the crossed optical dipole trap separately after a rapid quench of the trap power. The yellow circles show the measured position of the cloud after a 1 ms time-of-flight. The violet solid line is a fit to the data, allowing to extract the trapping frequency in each of the arms.**c** Shows the same measurement in the crossed dipole trap, the green solid line being the fit to the data.**d** Shows a loss spectrum as a function of the frequency of the dipole trap intensity modulation. We observe a large increase of atomic losses around 1078 Hz obtained by fitting a Lorentzian lineshape to the data. A weaker signal at 512 Hz shows the breathing mode frequency along the cavity direction. All these measurement are performed with a spin-polarized, non-interacting Fermi gas.

We can realize the same type of measurement with the atoms held in the crossed optical dipole trap as shown in figure 3.26c where we measure a trapping frequency of 545 Hz along the vertical direction. A similar measurement along the transverse direction in the plane of the cavity gives a trapping frequency of 588 Hz. We can confirm these trap frequency values by measuring the frequency of the breathing mode of the non-interacting Fermi gas. We observe an increase of atomic losses around a frequency of 1078 Hz which gives a consistent value compared with the observation of the dipole oscillations. We can use this technique to measure the trapping frequency along the cavity direction even though the signal is much weaker compared with the one due to the transverse direction 3.26d. We find an increase of atomic losses and heating at 512 Hz corresponding to a trapping

frequency of 256 Hz along the cavity direction which is close to the expected value from simulations. To summarize the measured trapping frequencies in the crossed optical dipole trap at 53 mW in each arm are :

$$(\omega_x;\omega_y;\omega_z)/2\pi = (256(10);548(5);545(5)) \tag{3.10}$$

3.4.3 *Experimental sequence to create a $|1\rangle - |3\rangle$ mixture*

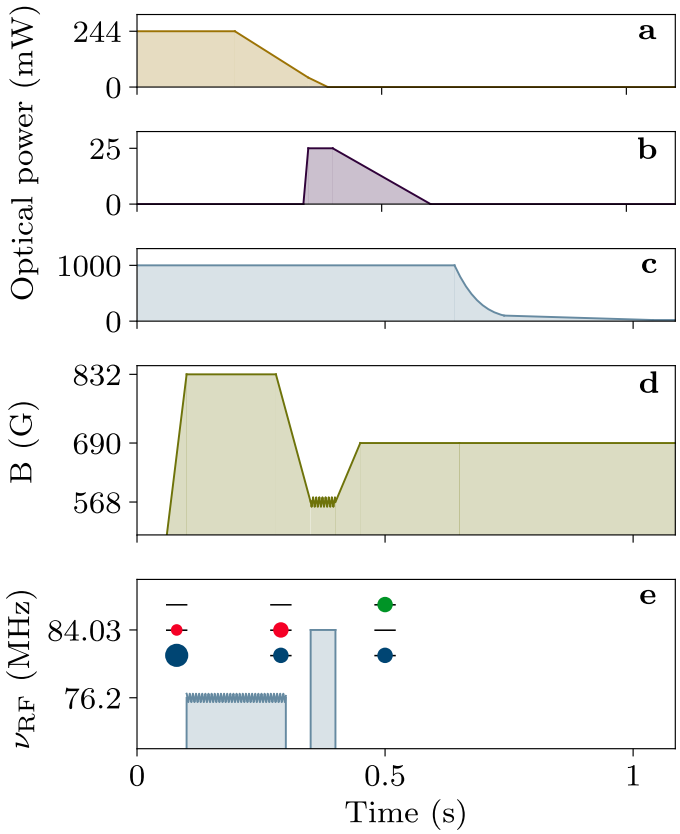

Figure 3.27: ***Production of a $|1\rangle - |3\rangle$ mixture : the experimental sequence.*** **a-c** shows the time evolution of the power of the standing-wave and lattice cavity trap and of the crossed optical dipole trap respectively. **c** represents the evolution of the magnetic field during the sequence while **d** shows the different RF frequencies applied to the cloud during the sequence. The small drawing on the last panel shows the evolution of the spin populations on a pictorial manner. Starting from a random $|1\rangle - |2\rangle$ mixture, a Landau-Zener RF frequency sweep at 832 G creates a balanced spin mixture. Then, an adiabatic passage realized around 568 G with a 20 ms Rf pulse at 84.03 MHz transfer the atoms from the state $|2\rangle$ to the state $|3\rangle$ creating a balanced mixture. The rest of the optical evaporative cooling proceeds as previously described but at a magnetic field of 690 G.

Building on the experimental sequence explained previously, we can adapt it to create a spin mixture of atoms in the hyperfine states $|1\rangle$ and $|3\rangle$. This hyperfine mixture also has a broad Feshbach resonance at 690 G which is however about a factor 3 narrower. This has an advantage as for a given magnetic field range it make it possible to explore regions with lower interaction strength both for lower and larger magnetic field.

In figure 3.27a.b.c I show the traces of the two cavity dipole traps and of the crossed dipole trap respectively during the evaporative cooling sequence. The optical evaporative cooling sequence is strictly identical to the protocol used to produce a $|1\rangle - |2\rangle$ mixture.

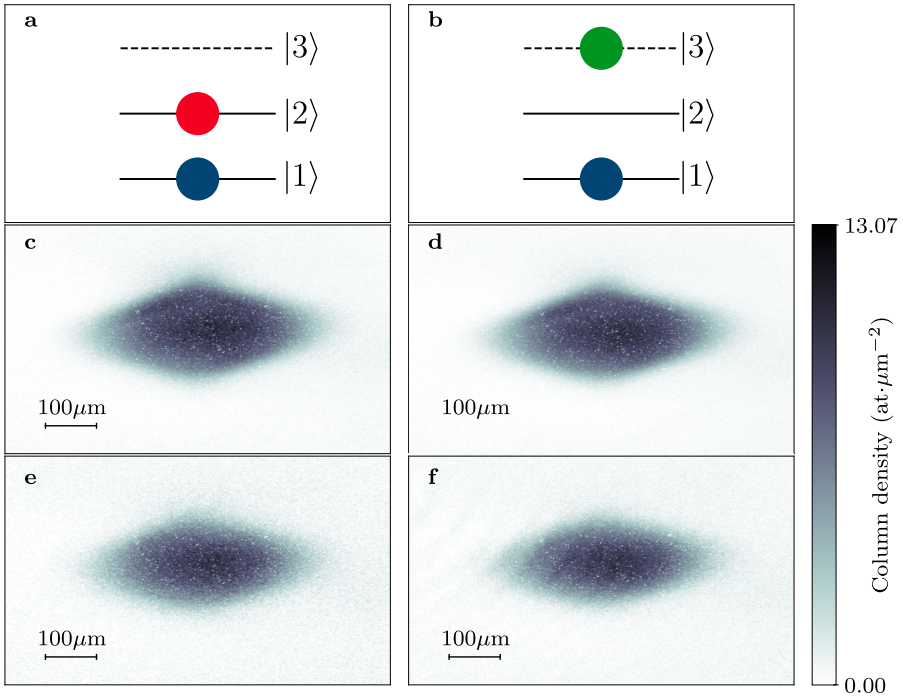

Figure 3.28: ***Comparison of the experimental production of a strongly interacting Fermi gas in states*** $|1\rangle - |2\rangle$ ***and*** $|1\rangle - |3\rangle$**. a-b** Schematic representation of the balanced $|1\rangle - |2\rangle$ and $|1\rangle - |3\rangle$ respectively. **c-e** shows absorption images taken after 3.5 ms TOF duration of atoms in states $|1\rangle$ and $|2\rangle$. **d-f** are similar for atoms in states $|1\rangle$ and $|3\rangle$

Th main difference lies on the ramps of magnetic field and on the RF pulses sequence (figure 3.27d.e). The magnetic field is ramped to 832 G before starting the first evaporative cooling ramp in the standing wave cavity dipole trap. There, for a duration of 200 ms, the same Landau-Zener RF frequency sweeps are applied to create an incoherent, balanced mixture of atoms in the two lowest hyperfine states. Afterwards the magnetic field is reduced down to 568 G, where the scattering length between the states $|1\rangle$-$|2\rangle$ and $|2\rangle - |3\rangle$ is close to zero meaning that the gas is nearly non-interacting. A 25 ms pulse of RF power is applied at the transition frequency between the states $|2\rangle$ and $|3\rangle$ at 84.03 MHz. At the same time the magnetic field is slowly ramped up from 567 to 569 G in order to realize an adiabatic passage through the resonance at 568 G. This technique allows to transfer 100% of the atoms from $|2\rangle$ to $|3\rangle$ on a robust manner. An alternative would be to apply a π-pulse at the exact transition frequency, but this would be extremely sensitive to any drift or noise on the magnetic field. Once this adiabatic passage sequence is achieved, the magnetic field is ramped back up to the Feshbach resonance for the $|1\rangle - |3\rangle$ mixture at 690 G and the evaporative cooling in the lattice-free cavity dipole trap starts.

In the figure 3.28, I summarize the points presented in this chapter.

- On one hand, we can prepare a mixture of atoms in the two lowest hyperfine states with full control on the spin imbalance. As shown

schematically in figure 3.28a., we can typically realize balanced $|1\rangle - |2\rangle$ with atom number $N = 4.0(1) \times 10^5$ per spin state. Absorption images taken after a time-of-flight of 3.5 ms are shown in figure 3.28 c.e for the two spin states $|1\rangle$ and $|2\rangle$, repectively.

- On the other hand, we can prepare a mixture of atoms in the hyperfine states $|1\rangle$ and $|3\rangle$ with full control on the spin imbalance. As shown schematically in figure 3.28b., we can typically realize balanced $|1\rangle - |3\rangle$ with atom number $N = 2.0(1) \times 10^5$ per spin state. Absorption images taken after a time-of-flight of 3.5 ms are shown in figure 3.28 d.f for the two spin states $|1\rangle$ and $|3\rangle$ repectively.

3.4.4 *Absorption imaging*

First we can take absorption images of the atomic density. For this, we send a resonant light pulse on the closed-transition in the Pashen-Back regime $|2S_{1/2}, m_J = 1/2, m_I = -1, 0, 1\rangle \longrightarrow |2S_{3/2}, m_J = -3/2, , m_I = -1, 0, 1\rangle$ to probe the atoms in the hyperfine states $|1\rangle$, $|2\rangle$ and $|3\rangle$. The resonant light beam that passes through the atomic cloud is absorbed, leading to a reduction on the optical power of the transmitted light following the Beer-Lambert law

$$\frac{\partial I(x,y,z)}{\partial u} = -\sigma(I) n(x,y,z) I(x,y,z) \tag{3.11}$$

where u is the direction of propagation of the imaging beam, $I(x,y,z)$ is its intensity profile, $n(x,y,z)$ the atomic density and $\sigma(I)$ the resonant absorption cross-section of the atoms that can be expressed, using the same formalism we have presented to derive the radiation pressure force for a two-level atom :

$$\sigma(I) = \frac{\sigma_0}{1 + I/I_{sat}} \tag{3.12}$$

with $\sigma_0 = 3\lambda^2/2\pi$ the bare scattering cross section. The intensity term at the denominator represents a reduction of the scattering cross section when the imaging beam saturates the atomic transition as a maximum population inversion of $1/2$ is allowed for a two-level system. In our case, $s = I/I_{sat} \sim 0.03$ makes us operating in the low saturation regime. In such a way, a precise characterization of the saturation effects due to large intensity is not necessary. During the experimental sequence we take three snapshots :

- One image is taken with the imaging pulse and the atoms.
- A second snapshot is taken with only the imaging pulse but without the cloud.
- A last image is taken to calibrate the background of the camera.

The first image shows the shadow of the cloud due to the photons absorbed which allows to measure the column density $n_{col}(x,y)$ integrated along the direction of propagation of the beam taken along the vertical direction z here:

$$n_{col}(x,y) = \int n(x,y,z)dz = -\frac{1}{\sigma}\log\left(\frac{I(x,y)}{I_0}\right) \tag{3.13}$$

with $I(x,y)$ the beam intensity measured on the camera in the presence of the atoms and I_0 the intensity of the imaging without any absorption. Practically, in order to reduce the influence from the dark count of the camera, we subtract the last image to the ones with and without atoms leading to the expression for the column density :

$$n_{col}(x,y) = \int n(x,y,z)dz = -\frac{1}{\sigma}\log\left(\frac{I(x,y) - I_{dark}}{I_0 - I_{dark}}\right) \tag{3.14}$$

As ^{6}Li is an very light atom, each scattered photon from the imaging beam will induce a velocity kick to the atom $\hbar k/m$. This produces a Doppler shift that will make an atom off-resonant after about 20 scattered photons at resonance. This specific property of Lithium makes it absolutely necessary to ensure that during an imaging pulse, less than 10 photons are scattered per atom on average. For this, we keep the imaging pulse short from 5 to 10 µs at very low intensity.

In this experiment, we have two absorption imaging, one along the vertical axis and one in the cavity plane along the direction of one of the crossed optical dipole trap arms. I will now present the detail of the optical setup used to control these two imaging beams.

Laser setup

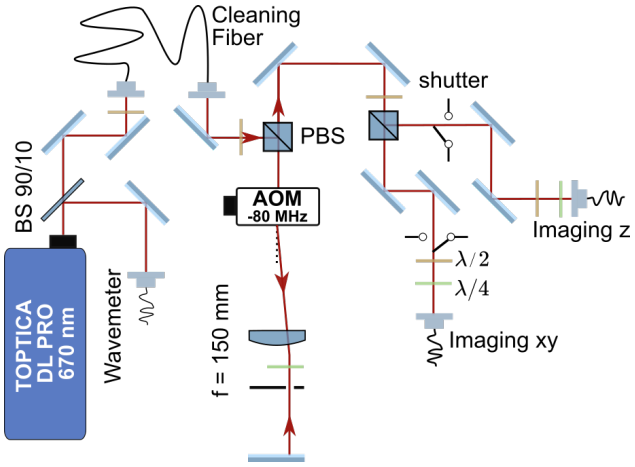

Figure 3.29: *Optical system for the absorption imaging.*

The imaging laser is a diode laser *Toptica DLpro* at 671 nm. The frequency of the laser is monitored by the wavemeter *High Finesse WS8-2*. The built-in PID of the wavemeter feeds back onto the piezoelectric actuator of the diode grating in order to stabilize its frequency at the setpoint value chosen on the wavemeter software. As shown in figure 3.29 the main output of the diode laser is fiber-coupled in order to clean the laser spatial mode which would cause some stray light onto the atoms.

The laser beam is sent to a double-pass AOM in order to fine-control its frequency and its amplitude. The beam is then split into two different beams that are fiber-coupled to the experiment. One beam is sent on top of the chamber in order to provide the vertical imaging beam while the other

is sent to an optical breadboard on the side of the chamber to obtain an absorption image in the horizontal plane.

Imaging optical setup around the science chamber

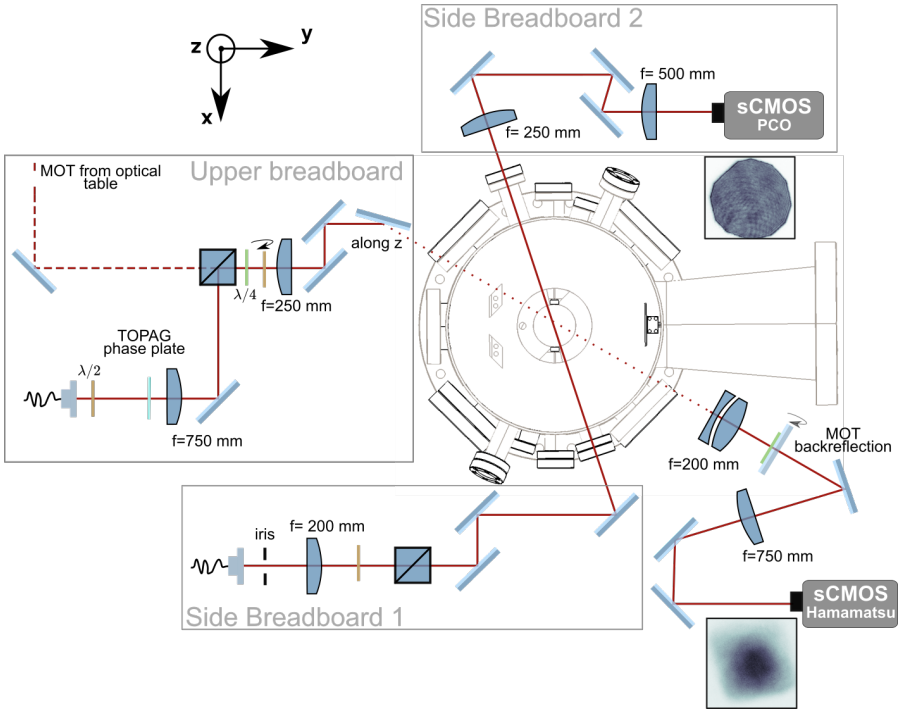

Figure 3.30: *Two-axis absorption imaging.*

In figure 3.30 we present how the two imaging beams are shaped near the vacuum chamber. First, on the upper breadboard, the laser beam is sent collimated onto a phase plate *Topag GTH-4-2.2* that transforms a Gaussian beam into a square-top-hat beam in the plane of the atoms (see the picture on the top right of figure 3.30). The beam is then focused onto the atomic density with a 750 mm focal length lens. The light is collected by a $f = 200$ mm doublet and then focused with a $f = 750$ mm lens onto a scientific CMOS camera (*Hamamatsu ORCA Flash v4*) with a surface of 2048×2048 pixels with a physical pixel size of 6.5 µm. The vertical beam propagates along the same axis as the vertical MOT beam. The collection optics of the imaging are placed after a flip-mirror that is flipped after the laser-cooling phase of each sequence. As a consequence this imaging axis is only available to image the clouds after the evaporative cooling in the cavity dipole trap. The calibrated magnification, using Raman-Nath diffraction of the atoms by a 1D periodic optical potential [131], of the vertical imaging is 4.03. Along the vertical axis the light is circularly polarized.

The horizontal beam is sent to the side breadboard where an iris is placed between the optical fiber tip and the collimating lens (figure 3.30). That way, only the very top part of the gaussian beam is selected allowing to obtain a relatively flat illumination (see top right picture in figure 3.30). The beam is sent collimated onto the atomic cloud and then collected and focused on the CMOS camera by two lenses with $f = 250$ and $f = 500$ mm respectively. The scientific CMOS camera is a *PCO Edge LT 4.2*. The measured magnification of

the horizontal imaging is 2.2. This imaging direction is co-propagating with one arm of the crossed optical dipole trap, with an angle of 18° with respect to the axis of the science cavity. As this axis is perpendicular to the vertical quantization axis set by the large magnetic field bias, the scattering cross section is reduced by a factor 2 as the beam is linearly polarized horizontally in order to couple to the σ atomic transition.

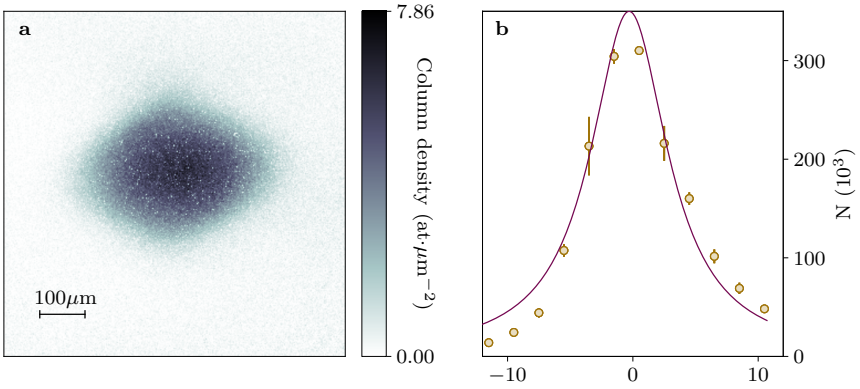

Figure 3.31: ***Vertical absorption imaging.*** **a** shows the column density obtained after a 7 µs pulse of resonant light at 832 G, looking at atoms in state $|1\rangle$ after 3 ms of time-of-flight. **b** Evolution of the atom number obtained from the absorption imaging as a function of the imaging laser frequency (yellow circles). 0 represents the frequency of the atomic resonance. The data are fitted with a Lorentzian function giving a width of 5.8 MHz consistent with the natural linewidth of the transition Γ.

In figure 3.31 .a, we show a typical absorption image taken at 832 G along the vertical axis of the atoms populating the lowest hyperfine state $|1\rangle$. As displayed in figure 3.31 .b we can look at the total atom number as a function of the imaging laser frequency with respect to the atomic frequency transition set at 0 here. The deviation to the fitted Lorentzian profile (violet solid line) is due to atoms being accelerated by the scattering of photons from the imaging beam. This leads to a underestimation of the actual atom number. We will compare this measurement with the one obtained from the cavity dispersive shift that will give us the exact correction factor for the reduced scattering cross section due to the Doppler shift.

We have now described the entire production sequence, where starting with a thermal vapour of ^{6}Li, we can create within 4 s a deeply degenerate Fermi gas at the location of the broad Feshbach resonance of ^{6}Li leading to large atom-atom interaction. We have also reviewed the optical tools that we can use to study the system by imaging the density profile of the cloud or measuring the cavity transmission probed with near resonant light. These optical techniques can be combined with RF spectroscopy in order to study the strongly interacting Fermi gas that we can now couple with photons in the science cavity.

4

CHARACTERIZATION OF A STRONGLY INTERACTING FERMI GAS

In this chapter, I will describe ultracold collisions that play a central role in quantum gases. Low energy collisions between ground states atoms interacting via a Van der Waals attractive potential lead to a variety of phenomena that are routinely used to produce strongly interacting gases and study the effect of these interactions. I will first present how this Van der Waals potential emerges from the simplest model for a pair of two-level atoms in their ground state. I will show that short-range interactions can be parametrized with a single physical parameter, the scattering length. In this regime we will show that the true interaction potential can be simplified in order to study the ultracold collisions between fermions. We will then explore the specific case of the low energy collision of discernible fermions in the s-wave regime and show that interactions can be tuned by a bias magnetic field, the so-called Feshbach resonance. In this model we will take into account the presence of many fermions to show the energy spectrum of the system and how this interactions leads to pairing in the ground state, creating a strongly correlated gas of fermions. We will then connect the thermodynamics properties of this strongly interacting Fermi gas with the one of the non interacting Fermi gas in an harmonic trap. Finally we will show that we can observe experimentally the presence of pairs, observe hints of superfluidity from the analysis of the density profiles and extrapolate the temperature of the degenerate Fermi gas even in the presence of strong atom-atom interactions.

CHAPTER CONTENTS

4.1 INTERACTION BETWEEN TWO GROUND STATE ^{6}LI ATOMS

Atoms in a quantum gases experience an interaction potential when they approach each other. The typical de Broglie wavelength of the atoms is typically more than 3 orders of magnitude larger than the typical size of an

dimere forming due to the presence of the interaction potential. This leads to several effects that will allow to simplify the mathematical treatment of the interaction term in the Hamiltonian. In the recent years several interactions have been observed in quantum gases with different systems such as the electric dipole-dipole interaction between Rydberg atoms [132, 133] or polar molecules [134–136] or a magnetic dipole-dipole interaction [137, 138] for species with large magnetic dipole moment (Dysprosium or Erbium for example). In this work we will concentrate on two neutral ground state atoms of ^{6}Li in the two lowest hyperfine states. We start first by calculating the interaction potential for the simplest model of an atom.

4.1.1 Van der Waals potential between two ground state atoms

We consider two atoms, A and B in their respective ground state, $|2s\rangle$, at a distance r along a unit vector $\vec{u}$. Here, we will consider the limit where the distance r stays larger than the respective size of the electronic cloud of each atoms. Once this criterion is fulfilled, we can study the dipole-dipole interaction between the electronic clouds with a negative charge and the nuclei with a positive one [139]. Both atoms are globally neutral. The dipole potential depending on the dipole operators for each atom reads

$$V_{Dip} = \frac{1}{4\pi\epsilon_0 r^3}\left[\hat{\vec{D}_A}\cdot\hat{\vec{D}_B} - 3\left(\vec{u}\cdot\hat{\vec{D}_A}\right)\left(\vec{u}\cdot\hat{\vec{D}_B}\right)\right] \tag{4.1}$$

At the first order of the perturbation theory, this interaction potential is zero for a ground state atom in a $|2s\rangle$ state. Going to the second order we will see that the energy of the ground state is lowered by the interaction potential, leading to an effective attraction between the atoms. By going to the second order in perturbation we actually study the effect of an oscillating dipole, lets say the atom A, polarizing the atom B an vice versa. The fact that the time-average of the dipole moment $D(t)$ is zero but its variance is not explains why this effect appears only to the second order in perturbation. The excited state of the atoms of angular momentum $J = 1$ can take three values once projected along the quantization axis, $m_J = -1, 0, 1$. The energy between the ground and the excited state is denoted $E = \hbar\omega_e$, with ω_e the frequency of the atomic transition. Instead of writing the Hamiltonian on this basis we can use the spatial basis $(\hat{x}, \hat{y}, \hat{z})$. Taking the quantization axis z oriented along the inter-particle axis $\vec{u}$ and taking the second order contribution to the potential :

$$\Delta E^{(2)} = -\sum_{\alpha=x,y,z}\frac{|\langle e_\alpha, e_\alpha|\,\hat{U_{Dip}}\,|g,g\rangle|^2}{2\hbar\omega} \tag{4.2}$$

with $\hat{U}_{Dip} = \frac{e^2}{r^3}\left[\hat{x_A}\hat{x_B} + \hat{y_A}\hat{y_B} - 2\hat{z_A}\hat{z_B}\right]$ the dipole operator decomposed on the basis of the position operators of the two atoms. We can write the action of the position operators $\langle g|\,q\hat{x}\,|e_x\rangle = \langle g|\,q\hat{y}\,|e_y\rangle = \langle g|\,q\hat{z}\,|e_z\rangle = d$ with d the reduced dipole of the atomic transition. Expanding the equation 4.1 leads to an expression for the energy shift of the ground state due to the perturbation coming from the dipole interaction :

$$\Delta E^2 = -\frac{1}{2\hbar\omega}\left(\frac{1}{4\pi\epsilon_0 r^3}\right)^2(3d^2) = -\frac{27}{16}\frac{\Gamma}{\omega}\frac{\hbar\Gamma}{(kr)^6} \tag{4.3}$$

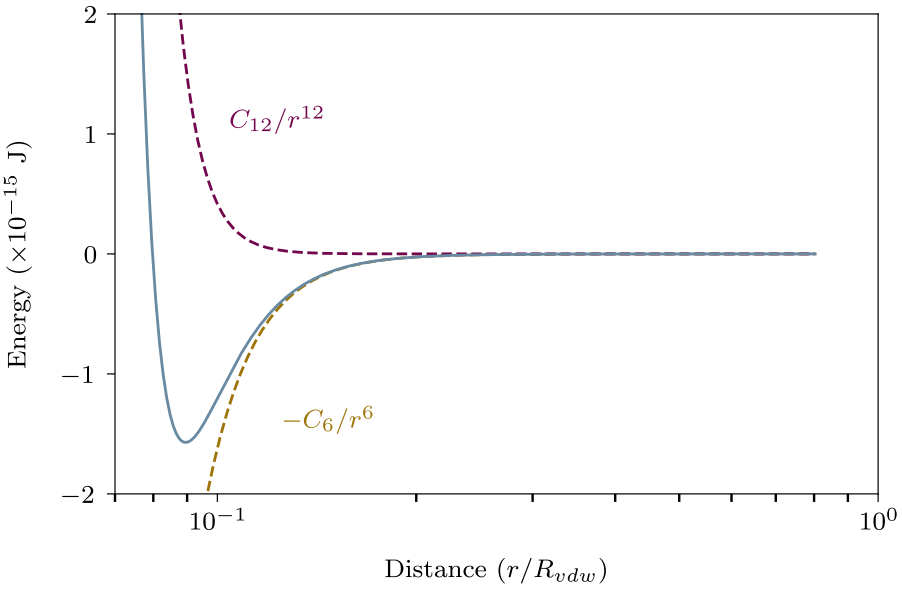

Figure 4.1: ***The Van der Waals potential for two interacting atoms.*** The figure shows the spatial scaling of the $-C_6/r^6$ (yellow dashed line) for $C_6 = 1380$ u.a for ^{6}Li. In order to model the repulsion of the electronic clouds at short distances, a repulsive potential C_{12}/r^{12} can be added, forming the so-called Lennard-Jones potential (blue solid line). We see that this potential as a local minimum at $r_0 = 0.1R_{VdW}$ which is much smaller than the range of the Van der Waals potential given by R_{VdW}.

with $k = 2\pi/\lambda$ the wave-number of the atomic transition and the linewidth of the excited state $\Gamma = (\omega^3 d^2)/(3\pi\epsilon_0\hbar c^3)$. This expression shows that the energy shift of the ground state due to the dipole-dipole interaction is negative and scales as $1/r^6$ as the Van der Waals potential. Moreover with this simple model, we can find a very good approximation for the C_6 coefficient of the Van der Waals potential which agrees at better than 5% with the measured one. The perturbative treatment stays valid while Γ/ω stays small which is the case for pretty much any atomic transitions as it is usually about 10^{-9} for standard optical transitions.

In figure 4.1, we show the Van der Waals potential $V(r) = -C_6/r^6$ with $C_6 = 1380$ u.a for ^{6}Li. In this representation the Van der Waals radius $R_{VdW} = \frac{1}{2}\left(\frac{mC_6}{\hbar^2}\right)^{1/4}$ is taken as the characteristic length-scale that gives the typical range of the potential. At short distances, the Van der Waals potential is mitigated by a hard core repulsion due to the overlap between the electronic clouds of the two atoms that is modelled here with a power law $V(r) = -C_{12}/r^{12}$. This combination of an attractive Van der Waals potential with such a repulsion at short distance is called a Lennard-Jones potential. In the next section, where we will study the scattering of two atoms, we will see that the notion of potential range becomes important as it provides a characteristic length-scale associated to the interaction potential. The de Broglie wavelength will be used to characterize the large distances while short distance will be taken to be smaller that the range of the potential, here defined as R_{VdW}.

4.1.2 Resonant scattering between two atoms at low energy

Now that we have emphasized how two ground state atoms feel an attractive potential due to the dipole-dipole interaction in their ground states, we study the scattering problem for two atoms. We want to calculate the scattering amplitude associated to the interaction potential. We treat the problem in the reference frame of the center of mass of the two atoms, where a fictitious particle of reduced mass $m_{^6Li}/2$ is scattered by the interaction potential $V(r)$:

$$\hbar^2(\nabla^2 + k^2)\Psi(r) = V(r)\Psi(r) \tag{4.4}$$

with k represents the wavenumber associated to the fictitious particle.

The solutions of this equation fulfil the Lippman-Schwinger equation :

$$\Psi_k(r) = e^{i\mathbf{kr}} + \int \mathcal{G}_0^{(+)}(r - r')V(r')\Psi_k(r')d^3r' \tag{4.5}$$

with $\mathcal{G}_0^{(+)}$ the Green's function corresponding to a spherical wave scattered out by the interaction potential. If we consider a portion of space for r large compared with the extent of the potential, the Green's function can be developed as

$$\frac{e^{ik|\mathbf{r}-\mathbf{r'}|}}{|\mathbf{r}-\mathbf{r'}|} \underset{r\to\infty}{\sim} \frac{e^{ikr}}{r} e^{-ik\mathbf{u}_f\cdot\mathbf{r'}} \tag{4.6}$$

with $\mathbf{u}_f$ the unit vector defining the direction where we look at the scattered wave.

In the regime of large distances the Lippman-Schwinger becomes:

$$\Psi_k(r) = e^{i\mathbf{kr}} + f(k, u_i, u_f)\frac{e^{i\mathbf{kr}}}{r} \tag{4.7}$$

with $\mathbf{u}_i$ the unit vector giving the direction of the incident wave onto the scattering potential. For a potential invariant by rotation the scattering amplitude simplifies in $f(k, u_i, u_f) = f(k, \theta)$ with θ the angle between the incident plane wave and the point r where we looked at the scattered wave. Even if this equation is still implicit, as the Lippmann-Schwinger is, it gives a nice physical picture of the two atoms scattering problem in the reference frame of the center of mass : the incoming atom is represented by the plane wave that is scattered by the interaction potential. The total scattered field is a spherical wave with a scattering amplitude $f(k, \theta)$. This scattering amplitude will capture the details of the scattering event of the atom by the interaction potential. This scattering amplitude has to fulfil a mathematical criterion called the Optical theorem:

$$Im[f(k, \theta = 0)] = \frac{k}{4\pi}\sigma_{tot} \tag{4.8}$$

with σ_{tot} the total scattering cross-section. It means that all the amplitude from the incoming wave that are not transmitted (hence $\theta = 0$) result from the interference between the incident wave and the scattered spherical wave

in the forward direction dephased by the interaction potential. We already see that this dephasing will be the determinant physical parameter to characterize atomic collisions.

This theorem, in the case of a Hamiltonian invariant by rotation, leads to a strong constraint on the shape of the scattering amplitude describes by

$$\sigma_{tot} = 4\pi|f(k)|^2 \tag{4.9}$$

$$\frac{1}{f(k)} = g(k) - ik \tag{4.10}$$

with $g(k)$ a real function of k. We notice here an upper limit for both the scattering amplitude and the scattering cross section $\sigma < 4\pi/k^2$, which is called the unitary limit. The scattering amplitude is unitary limited, meaning that it is governed by the de Broglie wavevector of the atom, independently of the interaction potential properties.

We write down the Hamiltonian for the two-body problem, considering a potential $V(r)$ invariant by rotation. This leads to a decomposition of the scattering wave function into a radial part $\chi(r)$ and a part depending on the angles $Y_{(l,m)}(\theta,\phi)$, the spherical harmonics functions. Considering the expression of the Laplacian in spherical coordinates and the fact that the radial part of the wavefunction can be written as $\chi(r) = \frac{u(r)}{r}$ we obtain the following Schrödinger equation:

$$-\frac{\hbar^2}{2m}u''(r) + \left[V(r) + \frac{\hbar^2 l(l+1)}{2mr^2}\right] u(r) = Eu(r) \tag{4.11}$$

In this equation we can identify the interaction potential between two ground atoms $V(r)$. In addition, the term proportional to $1/r^2$ corresponds to a centrifugal barrier that is only present for $l \neq 0$. This term creates a repulsive barrier at relatively large distance, leading to a repulsion between the atoms. With the symetrization and anti-symetrization constraints of the wavefunctions for bosons and fermions, only even values of l are allowed for bosons and odd values for fermions. Thus, S-wave scattering is cancelled out between identical fermions.

As typical quantum gases experiment work with atoms at very low temperature ($T < 1$ µK), we can make several strong assumptions that simplifies the Schrödinger equation :

- As the energy of the atoms is small, we can restrict the collisions to $S-$wave scattering, meaning that $l = 0$. For higher order collisions, the centrifugal barrier dominates and forbids the atoms to come close enough to feel the attractive Van der Waals potential.
- The typical kinetic energy of the atom $E = \hbar^2k^2/2m$ is small meaning that $1/k$, the de Broglie wavelength, will be large compared with the range of the potential (typically 1 µm).
- The extent of the atomic wavefunction being much larger that the typical extent of the Van de Waals potential, the scattering process will not depend on the details of the interaction potential as it will be "smoothened" by the extent of the atomic wavefunction.

In the model described previously, the scattering amplitude is written as a sum of Legendre polynomials,

$$f(k,\theta) = \sum_l (2l+1)P_l(\cos(\theta))(\frac{1}{2ik}(e^{2i\delta_l}-1) = \sum_l (2l+1)P_l(\cos(\theta))f_l(k) \tag{4.12}$$

with $f_l(k)$ giving the partial scattering amplitude in each of the scattering channel l with its expression fulfilling the optical theorem $1/f_l(k) = k/\tan(\delta_l(k)) - ik$, δ_l being the dephasing due to the collision. For low incident momenta compared with the depth of the scattering potential, meaning that the typical extent of the scattering potential is small compared with the de Broglie wavevector of the atoms, we can replace $V(r) = -C_6/r^6$ by a simpler potential that reproduces the scattering behaviour observed for the Van der Waals potential. For this purpose, we can express the scattering amplitude in the S-wave scattering amplitude in the general case as a function of the phase imprinted by the scattering potential onto the incident wave, as introduced in equation 4.12. The general form of the scattering into the partial waves simplifies for small momenta and isotropic scattering into:

$$\frac{1}{f(k)} \underset{k\to 0}{=} -\frac{1}{a} - ik + \frac{1}{2}r_e k^2 \tag{4.13}$$

with $a = \lim_{k\to 0} \frac{\tan(\delta_0(k))}{k}$ which has the dimension of a length and characterize the dephasing of the incident wave by the scattering potential at small momenta. This quantity, called the scattering length, is the only necessary parameter to describe scattering at low momenta. The second order term in k corresponds to the so-called effective potential range r_e [70, 71, 140]. For the description of short-range interaction in ^{6}Li this term can be safely neglected most of the time. The model for the interaction potential has to reproduce the actual scattering length of the true interaction potential. This means that one can find a much simpler mathematical form of the interaction potential that leads to the same dephasing of the incident wave, simplifying the mathematical treatment of contact interaction[141]. We notice that the scattering amplitude still fulfils the optical theorem and leads to a unitary limit for the scattering cross section for discernible particles :

$$\sigma_{max} = \frac{4\pi}{k^2} \tag{4.14}$$

which is then independent on the scattering potential but only limited by the de Broglie wavelength of the atoms. To get a bit more of physical meaning about the scattering length we can treat the case of a square potential in the radial direction as presented in figure 4.2. The range of the potential is clearly set by its width b where it takes a non-zero value $-V_0$ which is negative. Formally, the equation 4.11 takes the following form for the region of space between $r = 0$ and $r = b$ considering low energy collision leading to only scattering in the S-wave :

$$-\frac{\hbar^2}{2m}u''(r) - V_0 u(r) = Eu(r) \tag{4.15}$$

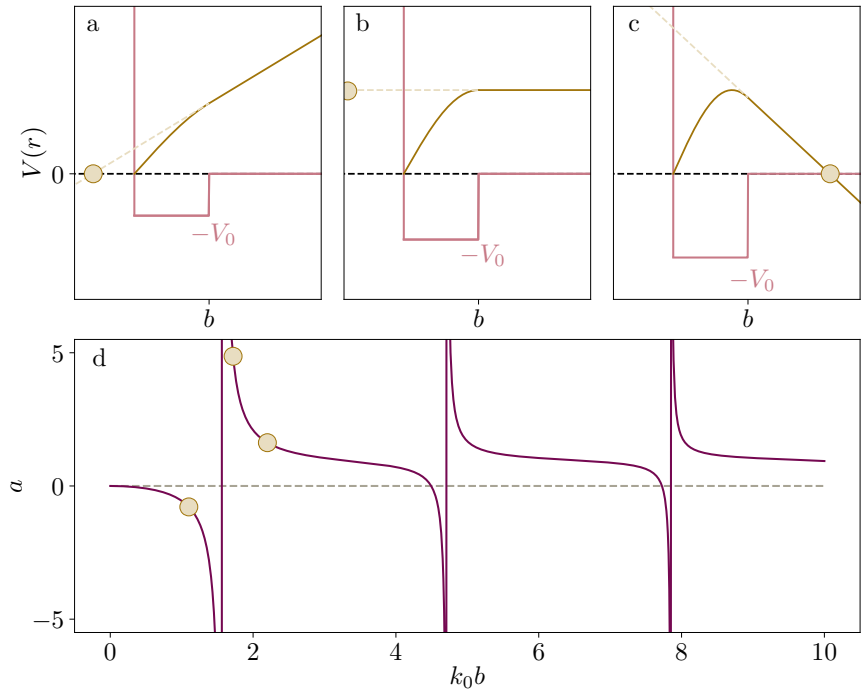

Figure 4.2: ***Parametrizing interactions : qualitative understanding of the scattering length.*** **a-c** Show the radial wavefunctions of the zero energy collision states, as the asymptotic case of a low energy diffusion state. We see that the sinusoidal wavefunction in the potential connects to a linear part for $r > b$. Taking the point where the wavefunction for $r > b$ cancels out can show three different behaviours as a function of the trap depth. We see that there can be both a positive and negative solution (panels **a** and **c**). The distance where the wavefunction cancels corresponds to the scattering length of the well potential. In between these two regimes there is a specific well depth that creates a diverging scattering length, corresponding to the unitary limit of the two body collision problem. **d** Shows the full solution of the contact condition giving a as a function of the square well depth. The yellow circles corresponds to the scattering lengths described in panel **a**, **b** and **c**

In order to look at the asymptotic shape of the radial wave function, we take the limit $k = 0$ for the incident wave. Consequently the solutions of the differential equations for the two regions of space are :

$$r < b \quad u(r) = A \sin(k_0 r) \tag{4.16}$$

$$r > b \quad u(r) = \alpha r + \beta \tag{4.17}$$

with $V_0 = \hbar^2 k_0^2 / m_{^6\mathrm{Li}}$ associated to the depth of the square potential. The continuity of the wavefunction and its derivative in $r = b$ allows to express the scattering length :

$$a = b - \tan(k_0 b)/k_0 \tag{4.18}$$

which gives the shape of the asymptotic wavefunction for $r > b$ to be $u(r) \propto r - a$. a corresponds to the common node of the asymptotic radial

wavefunction. In figure 4.2.a.b.c we show the radial wavefunction solutions of the Schrödinger equation for different potential depth V_0. At short distances the wavefunctions oscillate as a sine and is then linear in the region where the interaction potential is zero. In the case of figure 4.2.a the linear part of the radial wavefunction for $r > b$ never intersects 0 for positive distances. However it virtually cancels for a negative distance, corresponding to a negative scattering length. In the case of figure 4.2.c the scattering length is positive as the wavefunction cancels out for a positive distance. When $V_0 = \frac{\hbar^2\pi^2}{m_{^6Li}4b^2}$ the slope of the wavefunction at large distances cancels out leading to diverging scattering length (figure 4.2.b).

The variation of the scattering length with the depth of the scattering potential is summarized in figure 4.2.d, showing multiple scattering resonances where $a \to \infty$ for particular values of the potential depth (figure 4.2.b). At the resonances, the scattering cross section reaches the unitary limit which only depends on the de Broglie wavevector as previously described. These divergences correspond to the apparition of a new bound state in the potential while increasing the potential depth. We can then understand the physics behind the resonant scattering : there is a bound state of the scattering potential very close to the continuum which can couple almost resonantly to the low energy free particle states of the continuum. When the depth increases even more, the binding energy of this new bound state increases, making the energy mismatch with the entrance state larger and thus reducing the value of the scattering length.

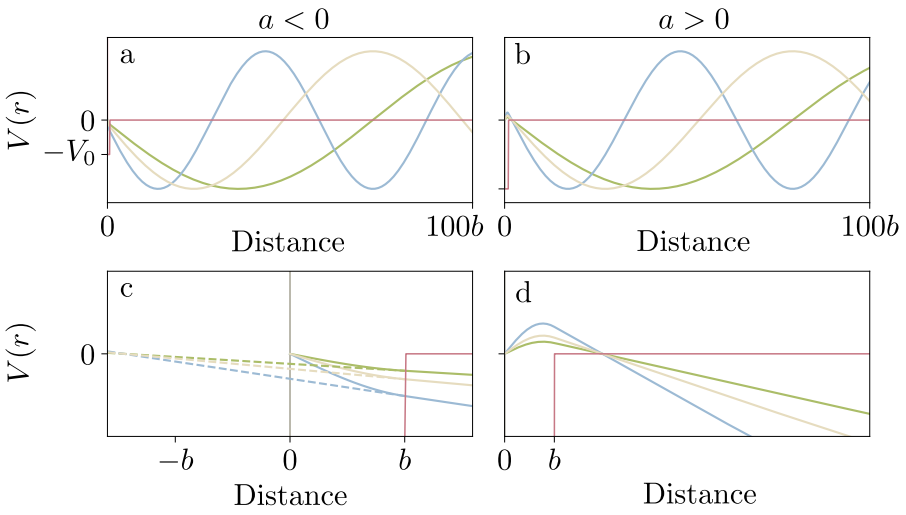

Figure 4.3: ***Low energy diffusion states for the square-well potential.*** **a-b** Show the solutions of the Shrödinger equation for low energy scattering states $(k/k_0) = (0.02, 0.03, 0.05)$ (blue, yellow and green solid lines, respectively). At large distances, $r > 1/k$ the wavefunction is a fine of wavector k. At short distances in the potential it has the same mathematical form with a wavevector $k'^2 = k^2 + k_0^2$. **c-d** show a zoom for regions where $r < 1/k$. We see that in the positive scattering length case, all the radial wavefunctions have a common node at $r = a$. We will see that this qualitative feature will turn into a way to remove any scattering potential from the problem to replace it with a proper boundary condition called the Bethe-Peierls condition.

In the same spirit we can look at low energy incident states with $k = (0.02, 0.03, 0.05) \times k_0$. In that case a quick look at the Schrödinger equation

shows that at large distances, where the scattering potential has no influence, the radial wavefunction is a sine wave. The wavefunctions in the potential range ($r < b$) oscillate at a frequency depending both on the incident wavevector and on the depth of the potential with a relative phase $\delta_0(k)$ compared with the incident wave. In the limit of $k \to 0$, we find back the very same expression for the scattering length as the one calculated above in the case of $k = 0$. In the low energy limit, the shape of the wavefunction at large distances will behave as $u(r) \propto \sin(k(r-a))$, very similar to the previous calculation (actually a Taylor expansion in k would give the same result). The wavefunctions are displayed in figure 4.3.a for negative scattering length, and in figure 4.3.b for positive ones. We first see that, at the scale of the incident wavevector k, the detail of the potential is irrelevant to look at the radial wavefunction at large ditances. By zooming in close to the potential range $r = b$ (figure 4.3.c.d), we see that in the case of a positive scattering length all the wavefunction share a node at a distance corresponding to the scatterring length. For negative scattering length the node is displaced for negative distances and thus is only virtual. This common node makes it then possible to reproduce the same set of wavefunctions by imposing boundary conditions to the free-particle radial wavefunction. This corresponds to the Bethe-Peierls boundary conditions that imposes the shape of the total wavefunction to be,

$$\Psi_k(r) \underset{r\to 0}{=} A\left(\frac{1}{r} - \frac{1}{a}\right) \tag{4.19}$$

We have reviewed the scattering processes behind the short-range interactions in quantum gases. So far we can explain how discernible particles can resonantly interact while new bound state with very small binding energies appear in the scattering potential. We will now see that another toy potential can reproduce the scattering length as previously calculated for the first order in perturbation k.

Pseudo-potential

In order to reproduce properly the scattering length in the ultracold collision regime we could even hope for a simpler zero-range potential of mathematical form $V(r) = g\delta(r)$ with $\delta(r)$ the Dirac function. We can test this potential with a Born approximation in power of the scattering potential $\Psi_k = \Psi_k^{(0)} + \Psi_k^{(1)} + \Psi_k^{(2)}$.... Up to the first order there is no mathematical problem appearing. However, to the second order, the Dirac function has to be applied to the free particle Green's function $\mathcal{G}$, $\propto e^{ikr}/r$ that diverges in $r = 0$. For this purpose, we have to modify the interaction potential in order to regularize it around $r = 0$, thus removing the divergence in the Born approximation to the second order. The so-called pseudo-potential can be defined by its action onto the wavefunction $\Psi(r)$,

$$V_{pp}\left[\Psi(r)\right] = g\delta(r)\frac{\partial}{\partial r}\left[r\Psi(r)\right] \tag{4.20}$$

which once applied to the Green's function, does not lead to any divergence anymore as $V_{pp}\left[e^{ikr}/r\right] = igk\delta(r)$. This potential, in 3D only, has one bound state if the coupling strength g is positive. By looking at the free

particle states of the continuum, we can derive the scattering amplitude for this potential finding

$$\frac{1}{f(k)} = -\frac{1}{a} - ik \tag{4.21}$$

with $a = (g m_{^6Li})/(4\pi\hbar^2)$ which is the scattering length associated to the pseudo-potential. The scattering amplitude of the pseudo-potential is independent of the angle θ without any approximation, thus particularly suitable to describe the low energy isotropic collisions. By construction, the δ-potential only allows for s-wave scattering. The shape of the scattering amplitude fulfil the Optical theorem ensuring the unitarity and has zero effective range. In this framework we can again calculate the wavefunction of the scattering states with the Bether-Peierls boundary conditions.

We have so far considered a single scattering channel. In practice even if early work have explored this phenomenon [142], the scattering process we want to describe for ^{6}Li at large magnetic field requires to consider a two-channel model.

4.1.3 Feshbach resonance

The Feshbach resonance corresponds to non-interacting atoms in a low kinetic energy state, coupling to a bound state of the scattering potential. The position of the bound state of the closed channel with respect to the free particle open channel can be tuned by applying an external magnetic field bias. Thus, as these two channels couple via hyperfine interaction, when the two states have almost the same energy the coupling is resonant and leads to a diverging scattering length, corresponding to the unitary limit for the collisions.

Two-channel model

This process takes place between ^{6}Li atoms that populate different hyperfine states. The valence electrons of the pair can be either in a triplet or singlet state that defines two different interaction potentials shown in figure 4.4 [71]. Atoms separated by large distances see the interaction potential of the triplet state (in yellow in figure 4.4) as we work at high magnetic field. The entrance channel of the collision is a low energy free-particle state of the triplet interaction potential. It couples, due to the hyperfine interaction, to a bound state of the interaction potential of the singlet state (in purple in figure 4.4). Both potentials, as they emerge from triplet and singlet states, have different magnetic moment μ. It allows to tune the energy offset between the asymptotic free particle state in the open channel and the position of the bound state in the closed channel with a bias magnetic field. It is noticeable that the bound state in the closed channel would not be energetically accessible in the absence of hyperfine coupling as it appears in figure 4.4. Atoms in the continuum of the open channel will couple to the bound state of the closed channel thus experiencing an actual scattering process before exiting the collision back, into the continuum of the open channel. The coupling strength varies with the energy difference between the bound state in the closed channel and the energy of the free particle state in the open channel denoted ΔE in figure 4.4. This process is called a Feshbach resonance [143] that was predicted first in the field of nuclear collisions.

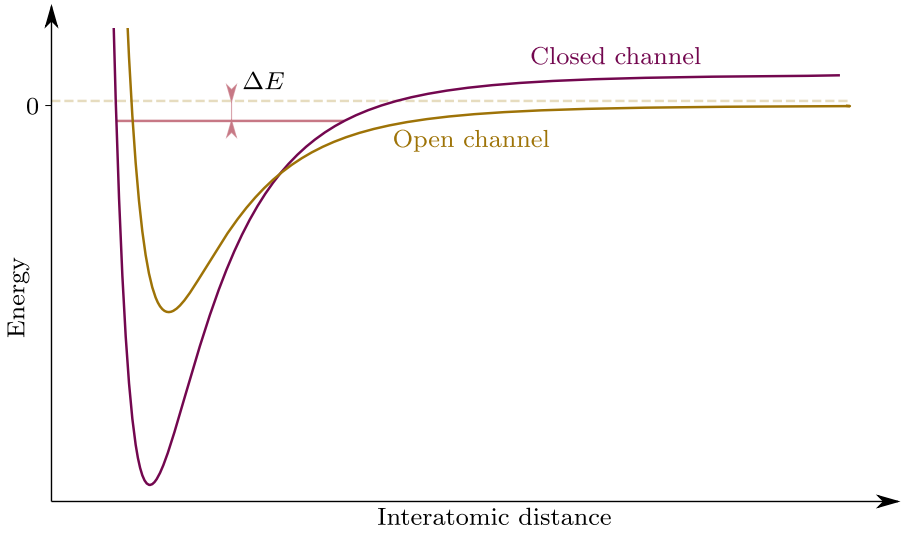

Figure 4.4: ***Two-channel model : description of the Feshbach resonance.*** The violet solid line represents the Van der Waals potential of the triplet state, while the yellow solid line describe the singlet state one. The entrance channel of the collision is a low energy free particle state of the triplet state, called the open channel. In the presence of hyperfine coupling, the open channel couples to a bound state in the closed channel where atoms will experience an interaction. The bound state state in the closed channel is described by its energy difference with the free particle state of the triplet potential ΔE.

A full treatment of the two channel scattering model [144] shows the following structure of the scattering length, as a function of the bias magnetic field

$$a(B) = a_{bg}\left(1 - \frac{\Delta B}{B - B_0}\right) \tag{4.22}$$

with B_0 the position of the Feshbach resonance, ΔB the width of the resonance and a_{bg} the background scattering length. The ^{6}Li Feshbach resonance at 832 G is considered as unusually broad compared with other alkali atoms [71]. It also has a much larger background scattering length $a_{bg} \sim -1600a_0$, that is due to the actual depth of the open channel potential, being close to support an extra bound state, virtually located a few hundred of kHz above the continuum. For these reasons the Feshbach resonances of ^{6}Li have several advantages :

- For broad resonance the effective range term of the scattering amplitude $\frac{1}{2}r_{eff}k^2$ can be safely neglected. This leaves the scattering problem described by a universal parameter depending on the scattering length and the Fermi wavevector $1/k_F$, the only relevant length scales in the problem.
- The broad resonance makes the strongly interacting gas long lived, the molecular state where inelastic collisions appear being very weakly populated. Thus it is very well described with a single channel model. Moreover the width of the resonance is directly linked to which of the two channels is the dominant one. In the case of ^{6}Li, the open channel dominates quite largely as the population in the close channel stays

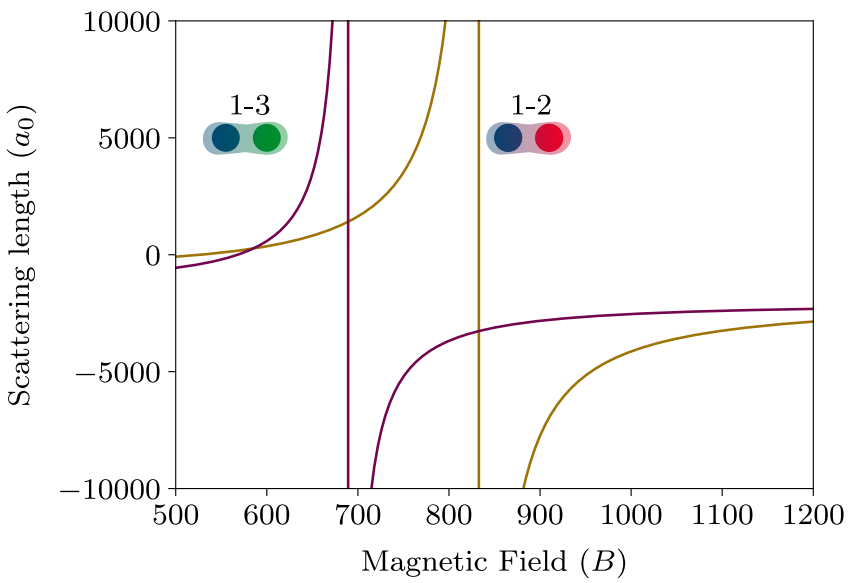

Figure 4.5: ***Feshbach resonance for the*** $|1\rangle - |2\rangle$ ***and the*** $|1\rangle - |3\rangle$**.** Feshbach resonances for the $1-2$ and the $1-3$ mixtures of ^{6}Li atoms. Data taken from [145]. The $1-2$ is located at 832 G while the $1-3$ resonance is at 690 G. It is clearly visible that the resonance for the $1-3$ mixture is significantly more narrow than for the $1-2$ mixture.

rather small (about 10^7 at unitarity) for the broad Feshbach resonance at 832 G [72].

- The width of the resonance being very large, the magnetic field accuracy required to tune the interaction strength is not very high.

In figure 4.5 we show the evolution of the scattering length for the spin mixtures $1-2$ and $1-3$ [145]. The table below summarizes the properties of these two Feshbach resonances :

Table 4.1: ^{6}Li Feshbach resonances.

	1-2	1-3
ΔB (G)	262	167
B_0 (G)	832.2	689.7
a_{bg} (a_0)	−1582	−1770

As depicted in figure 4.5, the two Feshbach resonances for the $1-2$ and $1-3$ mixture have a zero crossing at 527 and 566 G. This is the region where we prepare the $1-3$ mixture as RF transitions can be driven without being influenced by strong interactions between the different hyperfine states.

By scanning the magnetic field from 500 to 1000 G the scattering length can be adjusted from positive to negative values, crossing the unitary regime where the scattering length diverges. Remarkably, if one would like to go to large magnetic fields in order to reduce the scattering length to recover a non interacting Fermi gas, the large background scattering length will never

allow to enter a regime where interaction effects can be discarded. As the gas is strongly interacting over this full range of magnetic field, with large positive and negative scattering length, the Feshbach resonance of ^{6}Li is a very well suited system to study strongly interacting fermions. In the next section we will show with a simple model one of the most striking consequence of this large short range interactions : the presence of pairing.

4.2 FROM TWO-BODY TO MANY-BODY PHYSICS

We have looked in detail at the two-body problem in the presence of short--range interactions. In order to study quantum gases it is necessary to go beyond a model accounting only for two atoms colliding together and add the effect due to all the other atoms of the gas. In a first place we will study a model [146] where the two colliding fermions are confined in a box potential, in order to mimic the effect of the Pauli principle. This model gives already a good description of the energy spectrum of the many-body system as we will see now.

4.2.1 One fermion in a box : a minimalistic model of the BEC-BCS crossover

We consider a simple model of the strongly interacting Fermi gas in order to calculate the energy spectrum of the interacting Fermi gas accross the Feshbach resonance, which realizes the so called BEC-BCS crossover [70, 71]. We follow the reasoning presented by Pricoupenko and Castin in [146]. This model simplifies a system with N fermions, equally populating two spin states and interacting via a Van der Waals potential (figure 4.6.a). This situation is simplified by considering a box with radius R that mimic the Pauli principle with the $N-2$ atoms left. The scattering problem for the two fermions in the box is treated in the center of mass reference frame of the pair, leaving a single particle in the box, with a mass equal to half of the one of a Lithium atom that interacts with a contact scattering potential in $r = 0$.

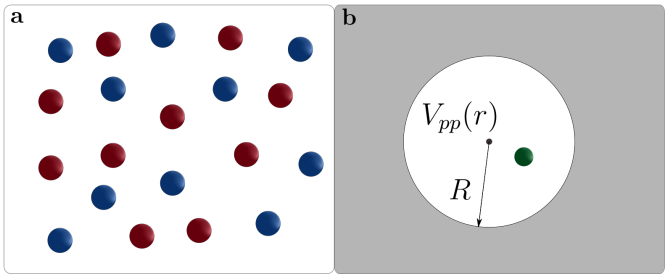

Figure 4.6: ***Minimalistic model of the BEC-BCS crossover : one fermion in a box.*** **a** Shows the system of interest : N fermions, equally populating two spin states and interacting via a Van der Waals potential. **b** Corresponds to the simplified model where a fictitious particle, of reduced mass $m = m_{^6\mathrm{Li}}/2$, confined in a box of radius R, fixed by the Fermi energy of the $N-2$ fermions. The particle scatters onto a contact potential at $r = 0$, simulating the scattering between two fermions with opposite spin.

The energy of a non-interacting free Fermi gas, composed of N atoms is given by,

$$E = \frac{3}{5} N \epsilon_F = 1/2 N \epsilon \tag{4.23}$$

with ϵ_F the Fermi energy and ϵ the energy of the fictitious particle in the box. The ground state of the non interacting fermion in a box of radius R is given by $\epsilon_0 = \frac{\hbar^2 \pi^2}{m R^2}$ allowing to link the radius of the box with the Fermi energy of the non-interacting gas,

$$k_F R = \left(\frac{5}{3}\right)^{1/2} \pi \tag{4.24}$$

We replace the effect of the interactions by the Bethe-Peierls boundary conditions

$$\frac{\partial_r u(r)}{u(r)} = -\frac{1}{a} \tag{4.25}$$

$u(r)$ is the radial wavefuntion as described in the previous section, solution of the following Schrödinger equation :

$$-\frac{\hbar^2}{m} \Delta u(r) = \epsilon u(r) \tag{4.26}$$

This equation can be solved for positive and negative energy of the fictitious particle leading to two set of solutions with the contact condition imposed by the Bethe-Peierls boundary conditions :

$$u(r) = A \sin(k(r - R)) \quad \text{and} \quad \tan(kR) = ka \quad \text{for} \quad \epsilon > 0 \tag{4.27}$$

and

$$u(r) = A \sinh(\kappa(r - R)) \quad \text{and} \quad \tanh(\kappa R) = \kappa a \quad \text{for} \quad \epsilon < 0 \tag{4.28}$$

The resulting energy spectrum is shown in figure 4.7. Let us take a look at the ground energy branch in some limiting cases. The energy branches as well as the radial wavefunction for limit cases over the BEC-BCS crossover are shown in the figure 4.7.

- We first look at the solution for $a \to \infty$. The first solution to the contact condition for positive energies gives $\tan(kR) \to \infty$, meaning $kR = \pi/2$. This point in figure 4.7 corresponds to $-1/k_F a \to 0$ with an energy $\epsilon = \frac{\hbar^2 \pi^2}{4 m R^2} = \frac{\epsilon_0}{4}$. Thus the energy is decreased compared with the free fermion gas showing the existence attractive interactions at unitarity where the scattering length diverges. The radial wavefunction reads $u(r) = A \cos(kr)$. In the unitary limit the scattering length drops out of the problem leaving us with the de Broglie wavelength as the characteristic length-scale.

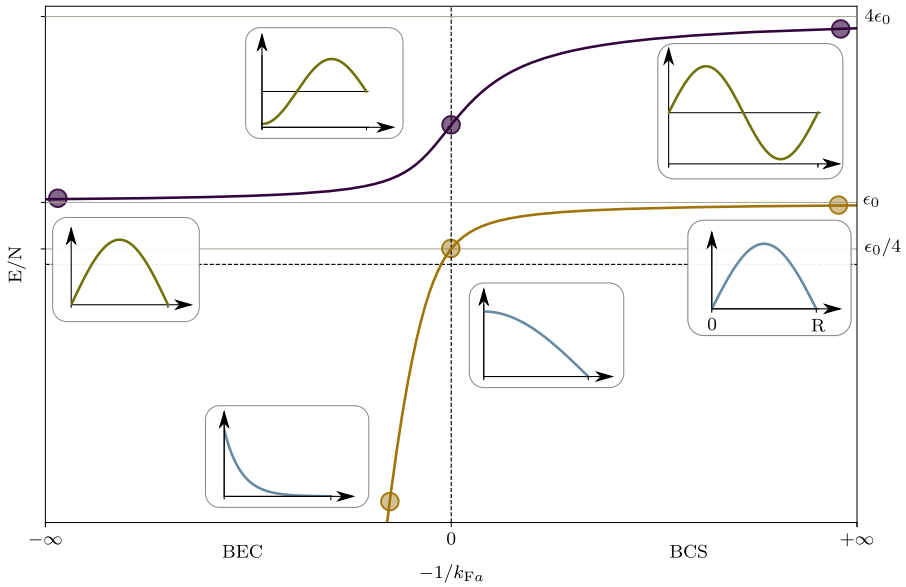

Figure 4.7: ***Ground and first excited branch of a minimalistic model describing the BEC-BCS crossover.*** We show the evolution of the first two energy branches as a function of the interaction parameter $-1/k_F a$. The ground branch asymptotically connects to the energy of the non interacting Fermi gas for $a \to -\infty$. It continuously decreases until the energy becomes negative for negative values of $-1/k_F a$. In the limit of $a \to \infty$, the energy of the ground branch scales as $1/a^2$, corresponding to the binding energy of the molecules on the BEC side of the resonance, as shown by the exponentially decaying wavefunction on the BEC side. The shape of the two-body radial wavefunction is plotted on the BEC side, at unitarity and on the BCS side to show its qualitative evolution. In the ground branch the interaction between particles is attractive as the energy is smaller than the non interacting Fermi gas one at any interaction strength. The first excited branch exhibits a larger energy, corresponding to repulsive interactions. In the excited branch the wavefunction dephases continuously when going from the BCS to the BEC side of the resonance.

- In the limit where $a \to 0^+$, the lowest energy solution corresponds to the negative energy contact condition $\tanh(kR) = ka = 1$. The energy reads $\epsilon = -\hbar^2/ma^2$. We see the existence of pairs in a bound state with a binding energy going to $-\infty$ for decreasing and positive scattering length e.g. $-1/k_F a \to -\infty$. This corresponds to the BEC part of the crossover where atoms form bound molecules with an asymptotic radial wavefunction $u(r) = Ae^{-r/a}$ which localizes the pair at the center of the box. In this case the size of the box R drops out of the problem as the bound molecules are bosons.

- Looking at the asymptotic case $a \to 0^-$, the first solution corresponds to $\tan(kR) = 0$ and $kR = \pi = ka$. Hence, the energy of the particle in the limit where $-1/k_F a \to +\infty$ tends to the non interacting Fermi gas $\epsilon = \epsilon_0$ and a radial wavefunction $u(r) = A\sin(kr)$.

The energy of the ground branch is always decreased by the contact interaction, highlighting the attractive nature of the interaction. The first excited branch, that one can reconstruct following the same reasoning as above, tends to the free Fermi gas energy on the far BEC case and increases to four times the free Fermi gas ground state energy on the far BCS side. There, the

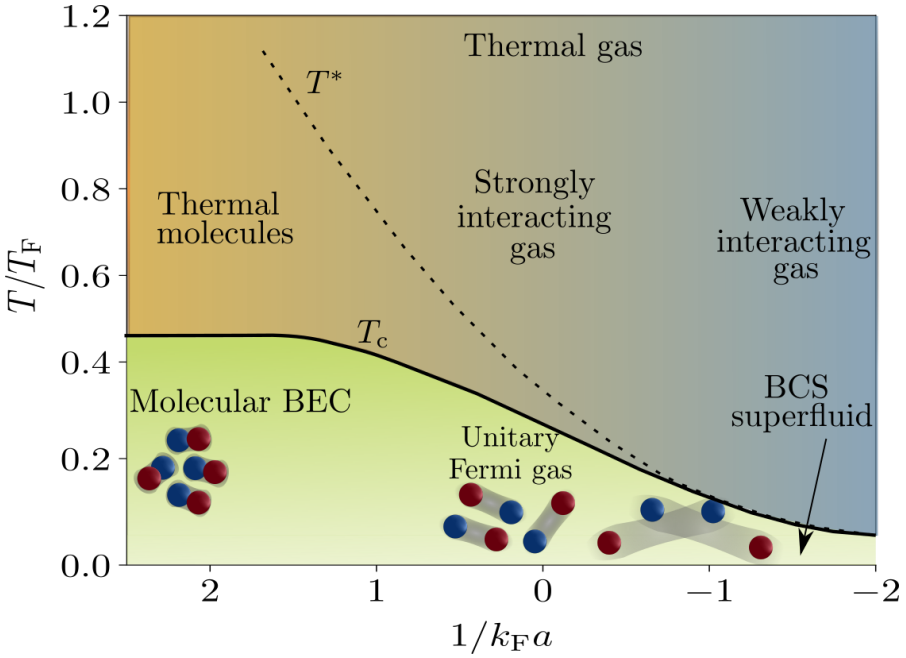

Figure 4.8: ***Phase diagram across the BEC BCS crossover [150].*** The figure shows the phase diagram of a strongly interacting Fermi gas over the BEC-BCS crossover as a function of temperature and interactions. On the BEC side, for positive values of $-1/k_F a$, dimers of ^{6}Li forms bosonic molecules. At $T > T_c$ the system is a gas of thermal molecules while below the critical temperature a superfluid BEC phase appears with $T_C = 0.52 T_F$. The size of the dimers decreases for increasing values of $-1/k_F a$. On the BCS side, for negative values of $-1/k_F a$, the gas is a weakly interacting thermal gas at above T_F. In this regime both the pairing and critical temperature decreases exponentially with $-1/k_F a$, making the superfluid phase composed of Cooper pairs to appear at very low temperature. The unitary regime at $-1/k_F a = 0$ is universal as it does not depend on the value of the scattering length any more. The diverging scattering length leads to large atom-atom correlations between atoms. The size of the pairs at unitarity are of the order of the interparticle distance given by $1/k_F$. At $T < T_c$ with $T_c = 0.22 T_F$, we obtain a strongly correlated fermionic superfluid. At $T = 0$ the system is superfluid at any interaction strength for the entire crossover.

interactions are repulsive [147–149] as one can see on the radial wavefunctions that has a node between $r = 0$ and $r = R$.

4.2.2 *The BEC-BCS crossover: towards many-body physics*

This simple model has the great merit of allowing us to reconstruct the energy spectrum and the shape of the pair wavefunctions across the BEC-BCS crossover. A more complicated treatment based on the BCS theory would provide even more insight about the behaviour of the pairs across the BEC-BCS crossover [69, 144, 150]. We show the phase diagram of the BEC BCS crossover (figure 4.8) as a function of temperature and interactions, in order to describe qualitatively the nature of the system that we study in this manuscript.

- **BEC side : strongly interacting Bose gas of Feshbach molecules**

  For large and positive scattering length, the atoms tends to populate bound states corresponding to ^{6}Li dimers. When the scattering length

decreases, the typical size of these pairs decreases, their size being given by the scattering length. These pairs behave like bosons and can form a Bose-Eistein condensate. The dimer-dimer scattering length is given by the atomic one with $a_m = 0.6a$ [151], which make this Bose-Einstein condensate also strongly interacting. Going far enough to the BEC side, thus reducing the scattering length, the critical condensation temperature for a weakly interacting BEC reads :

$$T_{BEC} = \frac{\hbar\overline{\omega}}{k_B}\left(\frac{N}{\zeta(3)}\right)^{1/3} \tag{4.29}$$

with N the number of dimers, $\overline{\omega}$ the geometric average of the trap frequencies and ζ the Riemann zeta function. The presence of a condensate fraction can be probed by measuring the bimodal density distribution after time-of-flight. It can be noted that on the far BEC regime, the size of the dimers becomes comparable with the wavelength of resonant light. The molecules are then transparent to the resonant imaging pulses. As T gets lower that the $T_{BEC} = T_c$ the gas becomes superfluid 4.8. As pictures in the phase diagram, the apparition pairs, e.g the formation of molecules, appears at much higher temperature than T_c, where the gas is composed of thermal molecules. The BEC dispersion relation is composed of a linear branch at low wavevector corresponding to collective phononic excitations that turns into a free particle dispersion relation at large wavevector [152]. As $\mu > \Delta$ the excitation spectrum is gapeless. This system have been studied extensively and superfluidity has been demonstrated via the observation of vortices [153].

- **The unitary Fermi gas :**

  The unitary limits corresponds to $1/k_F a \to 0$. The scattering length drops out of the equations describing the system and the interaction strength is limited by the imaginary part of the scattering amplitude (figure 4.8). In this regime the typical size of the pairs is of the order of $1/k_F$, meaning of the order of the interparticle spacing. The physics of this system is controlled by a universal function of T/T_F, the Bertsch parameter $\xi = 0.370(5)$ [145] for an homogeneous system at zero temperature. To connect the physical quantities defined for an homogeneous system, it is possible to consider a trapped gas locally homogeneous, thus integrating the homogeneous quantities over the trap region, applying the local density approximation (LDA). We can then define several quantities of interest in the following way for a gas trapped in an harmonic potential :

  The chemical potential:

  $$\mu = \sqrt{\xi}E_F = 0.60E_f \tag{4.30}$$

  The critical temperature[154]:

  $$T_c = 0.217T_f \tag{4.31}$$

  The gap [155]:

  $$\Delta = 0.59E_F \tag{4.32}$$

In this regime, the critical temperature is large compared with the largest high T_c superconductor which make this system be superfluid are rather high temperatures. The intermediate phase predicted where pairs are formed in the absence of superfluidity (figure 4.8 between T_c and T^*) is still not completely understood [69].

- **BCS side : weakly bound Cooper pairs**

  In the BCS limit the scattering length a is large and negative. There, pairs are also present at low enough temperature and get more and more delocalized in space when going deeper in the BCS regime [144]. The dispersion relation of this BCS gas shows a gap at k_F which is the order parameter of the superfluid. When the scattering length reduces on the far BCS regime, the gap closes and no pairs are present in the gas any more. In this regime the pair size is larger than $1/k_F$ and corresponds to the Cooper pairs of the standard BCS theory.

  The gap depends exponentially on the scattering length with $\Delta \propto E_F e^{-\pi/2k_F a}$, leading to an exponentially low critical temperature $T_c \propto (1/k_B) e^{-\pi/2k_F a}$ (figure 4.8).

We have now reviewed some of the main properties of the strongly interacting Fermi gas through the BEC-BCS crossover. We will see how we can experimentally connects the analysis of the density profiles with the properties of the strongly interacting Fermi gas such as its temperature and observe superfluidity.

4.3 ANALYSIS OF DENSITY PROFILES OF A STRONGLY INTERACTING FERMI GAS

To characterize the strongly interacting Fermi gas produced on the experiment we want to measure its temperature, observe the appearance of superfluidity at low enough temperature and the presence of pairs due to the strong interactions. While the temperature measurement of a trapped, non-interacting Fermi gas, is relatively trivial such measurements are challenging for a strongly interacting gas. I will discuss the properties of density profiles of a trapped non-interacting Fermi gas and how it relates its temperature.

4.3.1 The density profile of a non-interacting Fermi gas

We want to understand the connection between the density profiles of the trapped gas and its temperature in the absence of interaction. We will see that fitting the density profile gives access to the fugacity q which connects to the temperature of the cloud. We consider the non-interacting Fermi gas in an harmonic trap characterized by its trapping frequencies $(\omega_x, \omega_y, \omega_z)$, with the geometric average $\overline{\omega} = (\omega_x \omega_y \omega_z)^{1/3}$. This defines the Fermi energy in an harmonic trap $E_f = \hbar\overline{\omega}(3N)^{1/3}$ with N the total atom number, defines with respect to the peak density at the trap center. The trapping potential reads :

$$V(\mathbf{r}) = \frac{1}{2}\left(\omega_x^2 x^2 + \omega_y^2 y^2 + \omega_z^2 z^2\right) \tag{4.33}$$

In the Thomas Fermi approximation, where the thermal energy is taken to be larger that the level spacing in the potential, the phase space occupation is given by

$$f(\mathbf{r},\mathbf{k}) = \frac{1}{e^{(\frac{\hbar^2 k^2}{2m}+V(r)-\mu)/k_B T}+1} \tag{4.34}$$

Thus, the 3D density distribution is expressed as [70] :

$$n_{3D}(\vec{r}) = \frac{n_{3D}(0)}{\lambda_{dB}} Li_{3/2}\left(\exp\left[q-\left(\frac{x^2}{R_x^2}+\frac{y^2}{R_y^2}+\frac{z^2}{R_z^2}\right)f(e^q)\right]\right) \tag{4.35}$$

with $\lambda_{dB} = \sqrt{\frac{2\pi\hbar^2}{m k_B T}}$ the de Broglie wavelength, $Li_n(x)$ the n^{th} Polylogarithm, $f(x) = \frac{1+x}{x}\log(1+x)$ and $q = \mu k_B T$ the fugacity and $R_{x,y,z}$ the Thomas Fermi radii for each trapping direction . At zero temperature, the size of the cloud is given by the Thomas-Fermi radius $R_{x,y,z}(0) = \sqrt{2E_F/m\omega_{x,y,z}^2}$.

At finite temperature,for $T < T_F$, because of the trapping potential, $T/T_F < 0.1$ only relates to the central density. There, the density profile is very close to the zero temperature one. However looking at the density away from the center, the local Fermi energy decreases such that the cloud density is described by the thermal density profile presented above. At low temperature the information we want to extract is actually contained in the wings of the cloud, described by the thermal density profile in equation (4.35). As a direct consequence only a small portion of the cloud, the wings of the distribution, is sensitive to temperature changes at low temperature, complicating the fit procedure.

Practically, we measure the doubly integrated density profile, integrated along the two large trap frequency axis, in the radial direction of the trap. This 1D density profile is fitted with the following expression [70] :

$$n_{1D}(x) = n_{1D}(0)\frac{Li_{5/2}\left[q-\frac{x^2}{R_x^2}f(e^q)\right]}{Li_{5/2}(e^q)} \tag{4.36}$$

The fit parameters are the Thomas-Fermi radius along the longitudinal trap direction R_x, the fugacity q and the peak density $n_{1D}(0)$. At least, in the low temperature regime and assuming that the peak density is already saturated, both the Thomas Fermi radius and the fugacity are coupled as the both depend on the temperature.

The temperature of a strongly interacting Fermi gas from density profiles

The equations presented in the previous section relies on the analytical knowledge on the equation of state $n(q) = \frac{1}{\lambda_{dB}} f_n(q)$. This equation of state has no analytical expression as this would require to account for the effect of strong atom-atom interaction at finite temperature. Similarly the expansion of the gas [156] is strongly influenced by interaction effect making any interpretation about temperature difficult after a time-of-flight.

The equation of state as been measured by several groups [157, 158] allowing to extract a temperature from density profiles. However, this measurements stays quite challenging for technical reasons. Reconstructing the

full density profile by in-situ imaging requires most of the time a shallow trap or low atom number to be free of saturation effects of the absorption imaging. In our case, taking an in-situ image of the atoms in the crossed optical dipole trap is practically impossible as the cloud is too dense, reaching typical optical density of the order of 2 at the trap center. Even in the single beam dipole trap, the large atom number deforms the density profile that saturates close to the trap center. Some experimental procedures have been developed to reconstruct the full density profile by combining an in--situ image and one taken after time of flight, thus allowing to obtain the peak density in the trap after measuring its hydrodynamic expansion [159]. Another solution consists in using a saturating imaging pulse, giving direct access to the density at the trap center, but reducing the absorption signal in the low density regions.

In our case we choose to use a different technique that provides at the same time a thermometry and a qualitative behaviour showing the superfluid nature of the gas.

4.4 EXPERIMENTAL CHARACTERIZATION OF A STRONGLY INTERACTING FERMI GAS

4.4.1 Experimental method

To perform the thermometry of the gas, we release adiabatically the cloud from the crossed optical dipole trap into a single arm of the trap. For these, we turn off the power of one of the arm smoothly over 300 ms while we increase slightly by 20% the power in the second arm. To first check the adiabaticity of the transfer, we measure the position and width of the cloud after the transfer for different expansion times, thus confirming that no collective oscillation modes are excited during the transfer. Second, we realize this operation, capture the cloud back in the crossed optical dipole trap and release it again in the single arm trap. We thus check that no atom are lost along the different transfers and we can, with the technique explain in the following section, estimate the heating due to the procedure which stays small. This confirms that in a good approximation, the change of trap geometry can be performed almost adiabatically.

The second important change is that for this measurement we introduce a population imbalance between the two spin states (corresponding to the two lowest hyperfine states $|1\rangle$ and $|2\rangle$). We can take an absorption images of the two clouds (corresponding to the two spin states) after a short time of flight of typically 0.8 ms (figure 4.9.a), decreasing the peak atomic density without showing a significant expansion of the cloud along the longitudinal direction of the trap (as the trap period in this direction is 3.5 ms). In the condition presented in figure 4.9, the spin majority contains $N_{|1\rangle} = 1.9(1) \times 10^5$ atoms while the spin minority atom number is $N_{|2\rangle} = 0.70(5) \times 10^5$, corresponding to an imbalance $\theta = 0.45$. At low enough temperature, the cloud separates in two phases for $T < T_c$ [160, 161]. The core of the cloud is composed of fully paired fermions in a superfluid phase. The surrounding shell is composed of a normal spin imbalance gas. Far away from the center of the trap, the cloud is fully spin-polarized, with atoms only in the spin majority states. As we discussed in the section about collisions in quantum gases, the only relevant scattering channel corresponds to s-wave scattering which is forbidden for identical fermions. Thus this part of the gas is a

purely non-interacting Fermi gas and a temperature can be extracted from a fit of the wing density.

4.4.2 *Superfluidity*

We can also observe a direct manifestation of superfluidity using a spin-imbalance Fermi gas [161–164]. The introduction of a spin imbalance, leading to different chemical potential for the two populations, will create a competition between pairing due to the large interactions and a spin-polarization of the cloud. We prepare a cloud with a population imbalance between the two lowest hyperfine states $|1\rangle$ and $|2\rangle$ We associate two atomic densities $n_1(x,y,z)$ and $n_2(x,y,z)$ to the two population in states $|1\rangle$ and $|2\rangle$ and an spin imbalance θ.

In the limit where the correlation length of the system is small compared with the typical density spatial variation and that the trap depth is large enough such that the cloud stays confined in the region where the trapping potential can be approximated by an harmonic potential :

- We write the potential as $V(x,y,z) = \frac{1}{2}m\left(\omega_x^2x^2 + \omega_y^2y^2 + \omega_z^2z^2\right)$. As we use a single beam optical dipole trap along the x-axis, we have $\omega_y = \omega_z = \omega_r$ the radial trap frequency.
- We describe the system in the local density approximitation (LDA) limit where we can define thermodynamic quantities locally considering that each of these local regions behave as an homogeneous system.
- As the typical lengths are large, we can reasonably rule out any effect of the finite resolution of the absorption imaging.

We can obtain images of the densities of each spin component integrated along the z-axis directly from the absorption images as shown in figure 4.9.a.b corresponding to :

$$\tilde{n}_{1,2}(x,y) = \int dz\, n_{1,2}(x,y,z) \tag{4.37}$$

Figure 4.9.c displays the integrated column density $\hat{n}_{1,2} = \int dzdy\, n_{1,2}(x,y,z)$. The cloud density is then integrated along the second radial direction of the trap $\omega_y = \omega_y = 2\pi \times 412$ Hz. The remaining spatial variation corresponds to the longitudinal direction of the trap with a trap frequency $\omega_z = 2\pi \times 28$ Hz given by the curvature of the bias magnetic field. To decrease the large optical density at the center of the trap (optical density of about 1.8) that saturates the absorption imaging, we image the cloud after a time-of-flight short compared with the oscillation period of the cloud in the longitudinal direction. In figure 4.9.c we show the doubly integrated density difference of the two spin state densities, exhibiting a flat top profile at the center of the trap. Morevover we observe a region at rather large distance from the trap center where the atomic density is only composed of the spin majority components acting as an ideal Fermi gas.

We extract interesting informations from these density profiles. First, as described in [162] where this technique has been used to derive the equation of state of the strongly interacting Fermi gas, the doubly integrated profiles

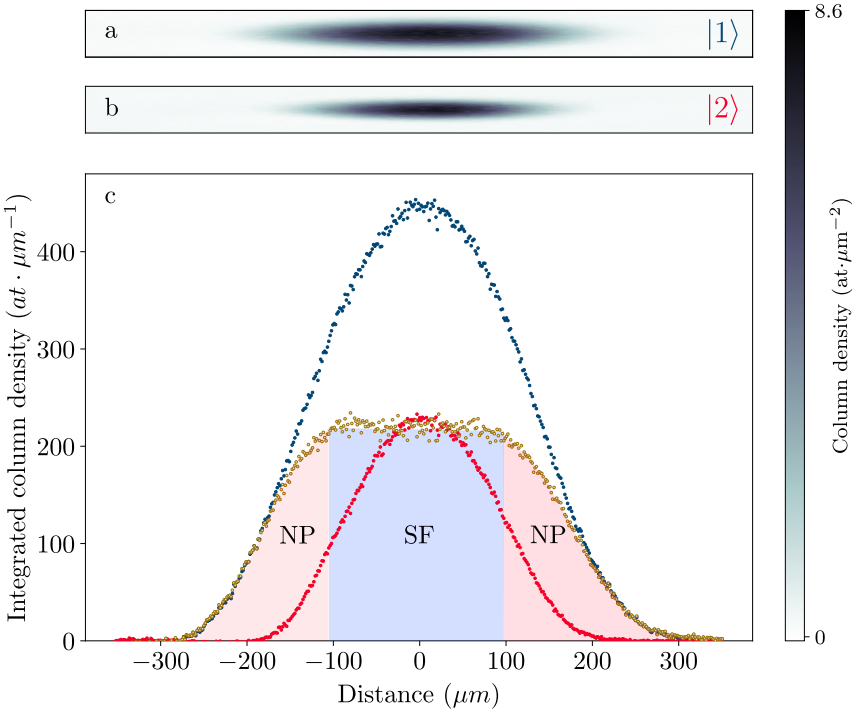

Figure 4.9: ***Superfluid and phase separation in a unitary Fermi gas.*** **a-b** Show the colmun density of the spin majority and minority component after a short 0.7 ms long time of flight. the spin majority ($|1\rangle$) comprises $1.9(1) \times 10^5$ atoms, and the spin minority ($|2\rangle$) $0.70(5) \times 10^5$ atoms. Panel **c** shows the doubly integrated density profile of the spin majority (red dots) and the spin minority (blue dots). The difference of the two integrated column densities (yellow dots) show a flat top profile, characterizing a fully paired and superfluid core, surrounded by a spin imbalance shell.

directly links to the local pressure in the gas. The Gibbs-Duhem relation gives:

$$dP = -SdT + n_1 d\mu_1 + n_2 d\mu_2 \tag{4.38}$$

with $\mu i = \mu(0)_i - V(\vec{r})$ the chemical potential of each spin component, T the temperature, S the entropy of the system and P the pressure. The expression simplifies into

$$dP = -m\omega_r^2 y(n_1 + n_2)dy \tag{4.39}$$

Integrating along y and z gives the pressure profile along the longitudinal x-axis :

$$P(\mu_1, \mu_2, x) = \frac{m\omega_r^2}{2\pi} \int_0^\infty (n1 + n2) 2\pi r dr \tag{4.40}$$

$$= \frac{m\omega_r^2}{2\pi} \int_0^\infty (n1 + n2) dy dz \tag{4.41}$$

$$= \frac{m\omega_r^2}{2\pi} (\overline{n}_1 + \overline{n}_2) \tag{4.42}$$

Similarly the difference of the doubly integrated column densities gives an indication on the presence of a fully paired superfluid phase[163],

$$\frac{d\overline{n}_d(x)}{dx} = -2\pi\frac{\omega_x^2}{\omega_r^2}x\,(\overline{n}_1(x) - \overline{n}_2(x)) \tag{4.43}$$

The central region of the figure 4.9.c up to a distance of 102 µm from the trap center shows $\frac{d\overline{n}_d(x)}{dx} = 0$ meaning that $\overline{n}_1(x) - \overline{n}_2 = 0$ despite the difference between the chemical potential of each spin component. The concentration $\frac{d\overline{n}_1}{d\overline{n}_2}$ shows sudden increase at the position of the phase transition where the gas is superfluid as characterized by previous works [160, 164].

As T_c has been accurately measured by several groups [157, 158], we know that for a trapped gas the critical temperature, defined with respect to the Fermi energy for a trapped gas is $T_c = 0.217\,T_F$. In addition of providing a qualitative observation of the presence of a superfluid core, this measurement gives an upper bound on the temperature of the cloud as for the data presented here the large superfluid core ensures that $T < T_c$.

4.4.3 *Thermometry*

The imbalance Fermi gas, deep in the superfluid phase, offers another great advantage to quantitatively estimate the temperature. The phase separation creates an outer shell where the gas is almost purely spin polarized, thus behaving as an ideal Fermi gas. As presented in the previous section although the EoS of a strongly interacting Fermi gas is not known analytically and require large efforts to be measured, the problem for the ideal Fermi gas in an harmonic trap is well under control. As a thermometry, we measure the temperature of the wings of the spin majority population (where $\overline{n}_2 = 0$). As the cloud is at thermal equilibrium the temperature of both spin components are identical. The trap frequencies being known with a good accuracy, a fit of the wings of the density integrated along x gives us T/T_F and consequently the temperature of the gas.

Figure 4.10 shows the doubly integrated column densities of both the spin majority and minority components, averaged over 10 different clouds taken in the same experimental conditions. We fit the wings of the spin majority where the density of the minority is zero with the function :

$$n_{1D}(x) = n_{1D}(0)\frac{\mathrm{Li}_{5/2}\left[q - \frac{x^2}{R_x^2}f(e^q)\right]}{\mathrm{Li}_{5/2}(e^q)} \tag{4.44}$$

with the free parameters being the fugacity q, the peak atomic density n1D(0) and the Thomas Fermi radius R_x. As the peak density of a non-interacting gas should be smaller than the one for an interacting gas due to the attractive nature of the short-range interactions, the peak density is forced to be smaller than the one of the measured spin majority distribution [165]. The data used for the fit are shown with a shaded area in figure 4.10. The density profile reconstructed from the fitting procedure is shown with the dark yellow solid line. Its corresponds to a fugacity $q = 10.9(5)$, a Thomas Fermi radius $R_x = 282$ µm and a population of $1.2(1) \times 10^5$. The fugacity links directly to the relative temperature with :

$$\frac{T}{T_F} = [-6\mathrm{Li}_3(-e^q)]^{-1/3} \tag{4.45}$$

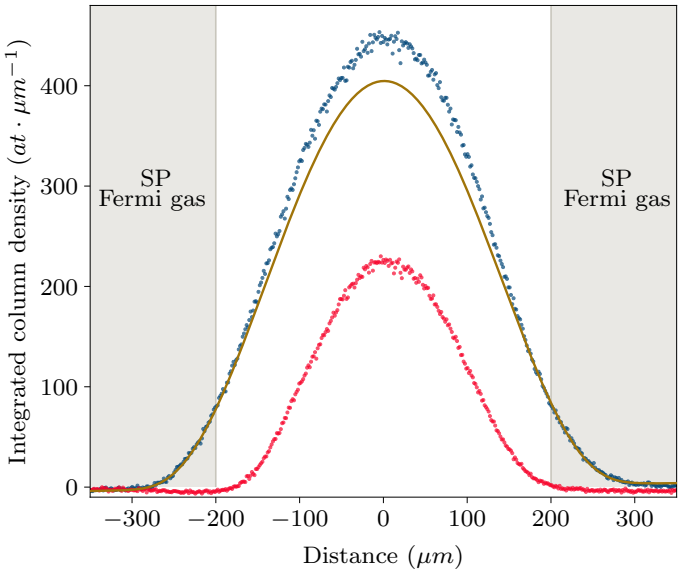

Figure 4.10: ***Temperature measurement with an imbalance unitary Fermi gas.*** The blue and red points correspond to the doubly integrated density profiles for the spin majority and minority, respectively. The atomic densities are obtained by absorption imaging after a short time of flight duration of 0.7 ms. The shaded grey area corresponds to the outer shell of the cloud where the density of atoms in the minority components vanishes, allowing us to fit these wings as a non-interacting Fermi gas (yellow solid line). We obtain a temperature, for the spin majority of $T/T_F = 0.075(5)$.

leading a numerical value of $T/T_F = 0.09(1)$ for the non-interacting distribution. Knowing $T_F = 730$ nK for the fictitious non-interacting cloud we can determine $T = 65$ nK for the temperature of the cloud at equilibrium, leading to an actual $T/T_F = 0.075(5)$ for the spin majority components. This result is consistent with the observation of a large superfluid fraction at the center of the cloud as the temperature is much smaller that the critical temperature of the superfluid transition.

We have calibrated the heat deposited on the cloud due to the change of trap geometry to be about $0.01\,T/T_F$ for optimal ramp parameters, which is within the accuracy of the measurement. The systematic influence of the trap depth in which the cloud is held, the duration of the time-of-flight and the spin-imbalance are shown in figure 4.11.a.b.d. The evolution of the temperature as a function of the final trap depth after the optical evaporative cooling is shown in figure 4.11.c.

- Figure 4.11.a shows the influence of the short TOF expansion, decreasing the peak optical density. We see that at short TOF duration, the measured temperature is slightly higher but more importantly, the error bars on the temperature estimate are larger. This most likely comes from the deformation of the cloud for short TOF duration where the OD is too large and produces some diffraction effect of the imaging beam onto the dark atomic density. We see that from 0.6 to 1 ms the temperature estimate is stable and that in this regime the TOF duration does not introduce any systematics.

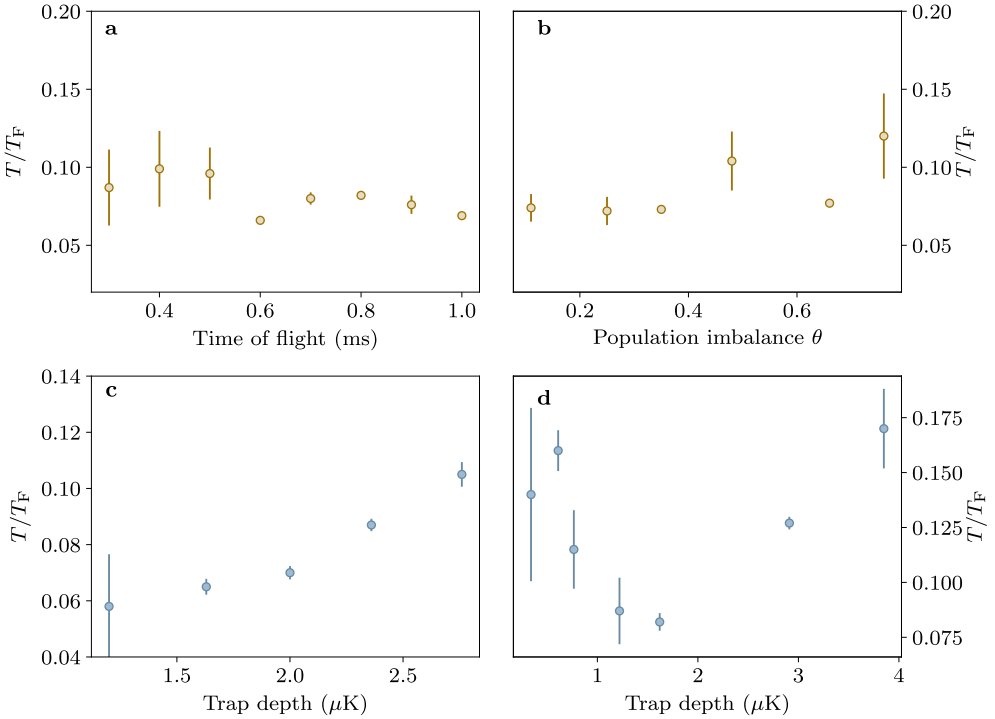

Figure 4.11: ***Estimation of the cloud temperature: preparation and systematics effects.*** **a** shows the estimate of the temperature as a function of the small duration of the time of flight we use to reduce the peak optical density of the cloud. We observe a small effect toward a reduction of T/T_F by 0.02 for longer TOF. For short TOF, the error bars increase due to the deformation of the density profile because of diffraction of the imaging light onto the cloud, distorting its shape. **b** shows the influence of the spin population imbalance θ. We see a small tendency for large imbalance as the evaporative cooling proceeds on a much less efficient way for low population in the minority spin component. The estimate of T/T_F is constant up to $\theta = 0.4$. **c-d** shows the temperature variation as a function of the trap depth after the recompression of the crossed dipole trap and of the final trap depth at the end of the evaporative cooling, respectively.

- In figure 4.11.b we show the variation of the temperature as a function of the spin imbalance $\theta = (N_1 - N_2)/(N_1 + N_2)$. We typically perform the measurement with a spin imbalance $\theta = 0.42$. We see no effect of the imbalance except for large values where it appears that the optical evaporation efficiency is decreased if there are not enough atoms left in state $|2\rangle$. Moreover, for small imbalance, the region used to fit the non-interacting profile decreases making the measurement sensitive to noise, thus requiring more averages of the absorption images. We also deduce from the evolution of T/T_F for small imbalance that the temperature does not show any important decrease when approaching the spin-balanced gas, meaning that a reasonable spin-imbalance will give a good estimate of the temperature of the spin-balanced gas with reasonable trust.

- In figure 4.11.c we show the evolution of the temperature as a function of the trap depth after recompression. We see in figure 4.11.c that the increase of optical power induce a small but measurable heating of the cloud.

In addition of these systematic effects we can use our temperature measurement technique to optimize the final trap depth of the optical evaporative cooling (figure 4.11.d) which shows a clear optimum corresponding to the lowest reachable temperature for our system. For trap depth lower than 1 µK, T/T_F increases meaning that atom losses does not translate into a lower temperature. For values larger that 2 µK, we observe that evaporative cooling still works efficiently as the temperature is reduced. We typically reduce the trap depth to 1.4 µK before recompressing it to ~ 2 µK. This way we can produce on a reproducible manner Fermi gases down to $0.075\,T/T_F$.

We have shown that we can extract both a qualitative proof of the superfluidity of the cloud by measuring the difference of the doubly integrated column density, showing a fully paired superfluid core, and that with the same data we can extract a value of the temperature consistent with a gas at temperatures smaller than T_c. We will now quickly discuss another technique showing the presence of pairs in the degenerate regime that we can use for example to gain qualitative insight on the degeneracy of the gas after the evaporative cooling in the optical resonator.

4.4.4 Observing pairing with RF-spectroscopy

Performing a spectroscopic measurement by driving transitions between the lowest hyperfine states has proven to be a powerful too to study the formation of pairs in a strongly interacting Fermi gas when reaching quantum degeneracy [166–170]. A lot of the quantities described in the previous section when reviewing the BEC-BCS crossover can be extracted from RF spectra. Among others the pairing gap and the binding energy can be obtained from the response of an homogeneous gas to resonant RF driving. We want to use the RF spectra to characterize the gas after the evaporation inside the cavity dipole trap to estimate its temperature and the possibility to use it to produce degenerate gases in the future.

However, as shown in [167], great care needs to be taken when dealing with a $|1\rangle - |2\rangle$ mixture as the final state $|3\rangle$ has a large scattering length with both initial states leading to systematic effects on the spectra. However at the qualitative level, we can use RF spectra as an indication of entering the degenerate regime while evaporating the interacting gas in the optical resonator.

As it has been seen in the previous section there is a temperature T^* that has been predicted theoretically where atoms start to form pairs, before the gas becomes actually superfluid. As shown in figure 4.8, while $T^* \sim T_c$ on the BCS side of the crossover, the two temperatures differ more and more when going to the BEC side, where Feshbach molecules can form even at large temperature compared with T_c.

As shown in figure 4.12, the presence of pairs translates into the presence of two peaks on the RF spectrum while scanning the frequency of the RF pulse. The narrow peak at lower frequency corresponds to the bare atomic transition frequency, corresponding to unpaired atoms. The width of this peak is ultimately Fourier limited and in our case dominated by the noise on the current power supply used to create the magnetic field bias. The peak on the right, at larger frequency, corresponds to paired atoms, and consequently driving them to another internal state requires additional energy.

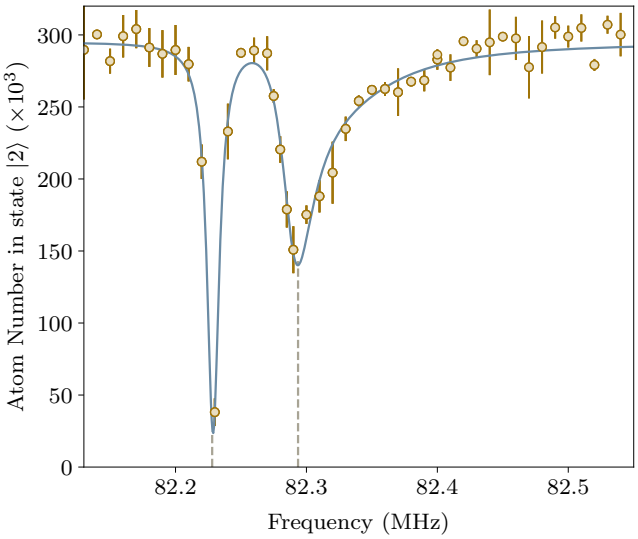

Figure 4.12: ***Observation of pairing in the strongly interacting regime after evaporation in the lattice-free cavity optical dipole trap.*** We show the variation of atom number (yellow circles) in state $|2\rangle$ after sending an RF pulse of 1 ms at variable frequency for an interacting Fermi gas held in the lattice-free cavity trap at 770 G. We observe a narrow peak at 82.22 MHz, corresponding to the unpaired atoms. The peak on the right, with its characteristic asymmetric shape corresponds to the paired fraction of the atoms in the gas. The spectrum is fitted with a Lorentzian profile for the bare atomic transition peak and with a Voigt profile for the paired atoms peak (solid blue line). We can deduce that approximately half of the atoms are paired, meaning that $T < T^*$.

In this experiment presented in figure 4.12, we only use the intracavity optical dipole trap for the evaporative cooling sequence. We have changed the duration of the second ramp to 400 ms in the lattice-free trap. After the evaporative cooling is performed at 832 G, the magnetic field is set to 770 G, where we obtain a ultracold mixture of atoms in state $|1\rangle$ and $|2\rangle$. We observe a broader peak, shifted to higher frequencies by 80 kHz, with an asymmetric profile towards larger frequencies, characteristic of pairs in a strongly interacting Fermi gas [167]. We cannot make any quantitative measurement of the gap nor of the temperature. Performing the RF spectroscopy sequence on the $|1\rangle - |3\rangle$ mixture at 660 G would greatly reduce final state interaction effect as $(a_{12}, a_{13}, a_{23}) = (949, 5445, 663)a_0$, thus the possibility to make quantitative measurements from the RF spectra.

We can still compare the fraction of atom paired in the gas after the evaporative cooling sequence in the cavity with the pairing temperature T^* at $1/k_F a \sim 0.5$. A 770 G, $T^* \simeq 0.55 T_F$ and we can estimate a paired fraction of about 0.5. These estimates makes it very reasonable to believe that the gas obtained after evaporation in the lattice-free cavity optical dipole trap is reaching temperatures about $T/T_F \sim 0.4$, thus already in the degenerate regime. This insight of quantum degeneracy gives reasonable hopes that an all-optical intracavity evaporative cooling can be used to produce deeply degenerate clouds.

We will now move on to the second part of my thesis where we will look at the interaction between this strongly correlated gas of fermions and

photons. This will bring us to show that it is possible to couple photons to the very essence of a strongly correlated superfluid : the fermion pairs, bringing cavity QED into a new regime going beyond the coupling to single atomic transitions.

Part II

CAVITY QED WITH STRONGLY CORRELATED FERMIONS

5

STRONGLY CORRELATED FERMIONS STRONGLY COUPLED TO LIGHT

In this chapter, I present the first experiment reaching the strong light-matter coupling regime for a degenerate, strongly interacting gas of fermions. I will first introduce the basics of cavity QED and the theoretical tools to describe our system. Reaching the strong coupling regime between atoms and photons leads to the appearance of dressed states hybridizing photons with atoms, called polaritons. We reveal the existence of this dressed states in our system by mapping out the energy spectrum using transmission spectroscopy on the system. This experimental technique makes it possible to locate the position of the polaritons as well as their photonic character, imprinted onto the intensity of the light transmitted through the cavity mirrors. We will show that our system requires to account for more than a single cavity mode in order to understand the transmission spectrum obtained from the experiment. We will finally show that the coherent coupling between many atoms and light leads to a particular scaling of the collective coupling strength with the number of emitters coherently coupled to the light field. We observe this coherent scaling on the experiment and make a quantitative comparison between a single cavity mode case, the theoretical model accounting for a multimode cavity and the experiment. This gives us a quantitative comparison from which we can infer a specific contribution from the high-order modes of the cavity that couple to the atoms.

CHAPTER CONTENTS

The results presented in this chapter closely follows the publication[1] :

K. Roux, H. Konishi, V. Helson ans J.-P. Brantut
Strongly correlated fermions strongly coupled to light
Nature Communications **11**, 2974 (2020)

1 Parts of this chapter are directly taken from this publication

5.1 CONTEXT AND MOTIVATION

Strong and coherent light-matter interaction is at the core of emerging quantum technologies, enabling the observation and control of matter at the level of single quanta [171]. In many-body systems, it is reached quantitatively when the collective cooperativity $C_N = 4Ng_0^2/\kappa\Gamma$ exceeds unity, e.g. when the fraction of photons coherently scattered into one particular mode of the electromagnetic field, singled-out by a high-finesse resonator, dominates over incoherent loss processes [172]. Here g_0 is the coupling strength between a single photon and a single matter excitation, N is the number of identical emitters, and κ and Γ are the incoherent decay rates of photonic and matter-line excitations, respectively. Strong-coupling to light would be highly beneficial for the quantum simulation of interacting fermions where first-principle theoretical calculations are inherently difficult [74]. Indeed, recent theoretical work in both cold atoms and solid state systems suggests that strong coupling would make the realization and control of new quantum states of matter [173–181] possible, as well as high-precision, quantum-limited measurements [182].

The strong coupling regime has been achieved with optical photons in various systems with weakly interacting emitters, from semiconductors and 2D material microcavities [183, 184], to atoms and trapped ions [36, 42, 185], including recently thermal fermionic atoms [39]. Combining evaporative cooling with high finesse cavities [43, 44, 186, 187] enabled the production of weakly interacting Bose-Einstein condensates strongly coupled with photons. Recently, bosonic Mott insulators have been dispersively coupled to light [33, 34], representing the only example combining strongly correlated quantum matter and strong light-matter interactions to date.

5.2 LIGHT-MATTER INTERACTION IN CAVITY QED : THE BASICS

In this section we will define the two quantities that quantify the coupling between an atom, located at the center of the cavity mode, and the cavity light field. First g_0, the light-matter coupling strength, gives the exchange rate between atomic and photonic excitations. Second, C_0 the cooperativity, quantifies the ratio between the scattering from the atom into the cavity mode compared with the scattering in free-space, given by the natural linewidth of the excited state Γ.

5.2.1 The light-matter coupling strength g_0

We consider linearly polarized light (in the cavity plane) driving the atomic transition $|2S_{1/2}, m_j = -1/2\rangle \longrightarrow |2S_{1/2}, m_j = -3/2\rangle$. We start with the definition of the cavity field amplitude :

$$\hat{\vec{E}} = i\mathcal{E}_0(\hat{a} - \hat{a}^\dagger)\vec{e}_x \tag{5.1}$$

where $\vec{e}_x$ is a polarization vector. The field amplitude $\mathcal{E}_0$ represents the vacuum fluctuations:

$$\mathcal{E}_0 = \sqrt{\frac{2\hbar\omega_c}{\pi\epsilon_0 w_0^2 L}}$$

where the cavity frequency is ω_c, the cavity waist is w_0 and the cavity length is L [171].

The dipole moment of the atom is decomposed onto the basis of circularly polarized vectors $\vec{\hat{\mu}} = \hat{\mu}_+ \vec{e}_+ + \hat{\mu}_0 \vec{e}_z + \hat{\mu}_- \vec{e}_-$ and $\vec{e}_\pm = \frac{1}{\sqrt{2}}(\vec{e}_x \pm i\vec{e}_y)$. We introduce the eigenstates of the atoms in the presence of the strong magnetic field $|i\rangle$, $i = 1, ..., 6$ for the ground states, and $|e\rangle$ for the excited state. A calculation of the matrix elements reveals that up to a 3% effect, only one excited state is coupled for each of the ground states $|1\rangle, |2\rangle$ and a given polarization. Moreover, the transition driven by the σ^- component of the probe light is almost optically closed at large magnetic field, thus making it possible to neglect any optical pumping effects. Consequently, we restrict the atomic states to the first two states $|1\rangle, |2\rangle$ which are actually populated in the experiment. Moreover we disregard the coupling to other excited states and restrict the analysis to $|1\rangle, |2\rangle, |e_1\rangle, |e_2\rangle$ and write the dipole operator as,

$$\hat{\mu}_- = \langle e_1| \hat{\mu}_- |1\rangle |e_1\rangle \langle 1| + \langle e_2| \hat{\mu}_- |2\rangle |e_2\rangle \langle 2| \tag{5.2}$$

As the linear polarization in the horizontal plane corresponds to a superposition of σ^+ and σ^- polarization along the vertical quantization axis, we have to also consider the matrix element coupling to the atomic transition $|2S_{1/2}, m_j = -1/2\rangle \longrightarrow |2S_{1/2}, m_j = 1/2\rangle$,

$$\hat{\mu}_+ = \langle e_1'| \hat{\mu}_+ |1\rangle |e_1'\rangle \langle 1| + \langle e_2'| \hat{\mu}_+ |2\rangle |e_2'\rangle \langle 2| \tag{5.3}$$

We compute the value of the matrix elements to be $\hat{\mu}_+ = -0.58\mu_0$ and $\hat{\mu}_- = -0.998\mu_0$ at 832 G, with $\mu_0 = 1.9885 \times 10^{-29}$ Cm. Consequently, we can consider that the σ^- component drives a perfectly closed transition, allowing us to treat the atoms as simple two-level systems. Considering the transition $|2S_{1/2}, m_j = -1/2\rangle \longrightarrow |2S_{1/2}, m_j = 1/2\rangle$, in addition of a reduced coupling strength, we would need to account for the other transitions due to optical pumping as it cannot be considered optically closed.

The light-matter interaction Hamiltonian, considering the two different polarization components reads

$$\begin{aligned}\hat{H} &= -\vec{\hat{\mu}} \otimes \vec{\hat{E}} \\ &= \frac{i\mathcal{E}_0}{\sqrt{2}} \left[\left(\langle e_1| \hat{\mu}_- |1\rangle |e_1\rangle \langle 1| + \langle e_2| \hat{\mu}_- |2\rangle |e_2\rangle \langle 2| + \langle e_1'| \hat{\mu}_+ |1\rangle |e_1'\rangle \langle 1| + \langle e_2'| \hat{\mu}_+ |2\rangle |e_2'\rangle \langle 2| \right) \right] \otimes (\hat{a} - \hat{a}^\dagger)\end{aligned} \tag{5.4}$$

As the two atomic transitions driven by the σ^+ and σ^- polarization components are separated by > 2.5 GHz at 832 G, and considering that we drive the σ^- almost resonantly, we can discard the other polarization component that will only induce a small light shift of the ground state leading to

$$\hat{H} = -\frac{i\mathcal{E}_0\mu_0}{\sqrt{2}} \left(\hat{a} |e_1\rangle \langle 1| - \hat{a}^\dagger |1\rangle \langle e_1| \right) = \frac{\Omega_0}{2} \left(\hat{a} |e_1\rangle \langle 1| + \hat{a}^\dagger |1\rangle \langle e_1| \right) \tag{5.5}$$

with $\Omega_0 = 2g_0$ the single-particle Rabi splitting that connect to g_0 the single-atom coupling strength. For our experiment, at 832 G and with light polarized linearly in the horizontal plane, we obtain:

$$\Omega_0 = \frac{2i}{\sqrt{2}} \mu_0 \mathcal{E}_0 = \frac{2i}{\sqrt{2}} h \cdot 478.8\,\text{kHz} \sim h \cdot 677.1\,\text{kHz} \sim h \cdot 2 \cdot 338.55\,\text{kHz} \tag{5.6}$$

We obtain $g_0 = 338.55$ kHz for the coupling strength when driving the σ^- atomic transition with light linearly polarized in the horizontal plane, reduced by a factor $\sqrt{2}$ compared with a probe light purely σ^--polarized with respect to the quantization axis. Following the same reasoning, we calculate the g_0 for all the atomic transitions of the D_2 and D_1 lines of ^{6}Li, considering that we can pump the σ transition with light linearly polarized in the plane perpendicular to the quantization axis, and the π-transitions with light linearly polarized along the quantization axis. The numerical values are reported in table 5.1 :

Table 5.1: Light-matter coupling strengths of ^{6}Li transitions with the two linear polarizations : H along the cavity plane and V along the vertical quantization axis.

	Atomic transition	$g_0/2\pi$ (kHz)		μ ($\times\mu_0$)
		H	V	
D_2	$\|2S_{1/2}, m_j = -1/2\rangle \longrightarrow \|2P_{3/2}, m_j = -3/2\rangle$	338	0	−0.9987
	$\|2S_{1/2}, m_j = -1/2\rangle \longrightarrow \|2P_{3/2}, m_j = -1/2\rangle$	0	391	−0.8156
	$\|2S_{1/2}, m_j = -1/2\rangle \longrightarrow \|2P_{3/2}, m_j = 1/2\rangle$	194	0	−0.5767
D_1	$\|2S_{1/2}, m_j = -1/2\rangle \longrightarrow \|2P_{1/2}, m_j = 1/2\rangle$	276	0	0.8155
	$\|2S_{1/2}, m_j = -1/2\rangle \longrightarrow \|2P_{1/2}, m_j = -1/2\rangle$	0	277	0.5761

These couplings correspond to a single atom sitting at a maximum of the cavity field. In the case of a gas comprising N atoms and $R_{TF} > \lambda_c$, only half of the atoms couple to the cavity field due to the standing wave nature of the cavity field. This factor will be taken into account when considering the coupling of many-atoms to light.

5.2.2 *Geometrical parameter quantifying the light-matter interaction : the cooperativity*

Another parameter of interest characterizing the coupling between one atom and the cavity mode is the single atom cooperativity C_0. This quantity is expressed as a function of the dissipation rates of the atom Γ and of the cavity field κ, and of the coupling strength g_0 [172]:

$$C_0 = \frac{4g_0^2}{\kappa\Gamma} \tag{5.7}$$

A classical model describing the interaction of one atom as a electric dipole with a classical light field in the cavity leads to an expression of the cooperativity depending only on the geometry of the resonator,

$$C_0 = \frac{24\mathcal{F}}{\pi k^2 w_0^2} \tag{5.8}$$

with k the wavevector of the cavity light field, w_0 the waist of the cavity mode and $\mathcal{F}$ the finesse. The cooperativity relates directly to the enhancement of the scattering of light into the cavity mode compared with the scattering in free-space [172]. This is also known as the Purcell factor. The two expressions for the cooperativity shown above lead to a maximum single atom cooperativity $C_0 = 2.02$ for our experiment. The cooperativity can be

used as a figure of merit to define the strong coupling regime : when the scattering into the cavity mode dominates over spontaneous emission, the strong coupling is reached. This is characterized by $C_0 > 1$, thus our experiment operates in the limit of strong coupling regime for a single atom. For many atoms, the collective cooperativity scales with the total number of atoms N as [172]

$$C_N = NC_0 = N\frac{4g_0^2}{\kappa\Gamma} \tag{5.9}$$

With typical atom number on the order of 10^5, the coherent scattering of the cloud into the cavity dominates largely over the spontaneous emission for our experiment ,thus operating in the strong collective coupling regime. In the next section we will see that the coupling strength leads to the creation of dressed states mixing the cavity field with the atoms. The strong coupling regime will be characterized by the emergence of a large avoided-crossing between the dressed states with a splitting given by the light-matter coupling strength.

5.2.3 *Single emitter : Jaynes-Cummings model*

I want first to show that hybridizing atoms and photons is possible by placing one atom at the center of a Fabry-Pérot cavity. The eigenstates of such a system are composed of an atomic and a photonic part, thus producing a dressed state called a polariton. Analysing the energy spectrum and the eigenstate, I want to explain how transmission spectroscopy is a very convenient tool to locate the position of the dressed state in the energy spectrum. Second, adding a small perturbation such as a weak driving field that couples to the photonic part of the polariton, we will be able to map out the photonic character of the dressed states at any detuning throught the value of the transmission through the cavity.

To illustrate this, we start by describing the experimental case where a single atom sits at an antinode of the field, at the center of the cavity mode. The atom is modelled by a two-level system with a ground state $|g\rangle$ and an excited state $|e\rangle$, with a energy difference $\hbar\omega_e$. The operators describing the internal dynamics are given by the Pauli matrices :

$$\hat{\sigma}_z = \frac{1}{2}\left(|e\rangle\langle e| - |g\rangle\langle g|\right) \tag{5.10}$$

$$\hat{\sigma}_+ = |e\rangle\langle g| \tag{5.11}$$

$$\hat{\sigma}_- = |g\rangle\langle e| \tag{5.12}$$

The Hamiltonian describing the internal dynamics of the atom is written as

$$\hat{H}_a = \frac{1}{2}\hbar\omega_e\hat{\sigma}_z \tag{5.13}$$

The Hamiltonian describing the cavity light field reads

$$\hat{H}_c = \hbar\omega_c\hat{a}^\dagger\hat{a} \tag{5.14}$$

with ω_c the frequency of the cavity light field and $(\hat{a}, \hat{a}^\dagger)$ the jumps operators for the cavity photons. From now on we will set $\hbar = 1$ for simplicity..

We define the Hamiltonian describing the interaction between the cavity field and the two-level atom. The interaction strength depends on the dipole moment $\hat{\mu}$ of the two-level system :

$$\hat{H}_{int} = -\hat{\mu}\mathcal{E} \tag{5.15}$$

with $\hat{\mu} = \mu(\hat{\sigma}_+ + \hat{\sigma}_-)$ and $\mathcal{E} = i\mathcal{E}_0\left(\hat{a} + \hat{a}^\dagger\right)$. In this expression μ is the dipole matrix element of the transition.

As we have defined in the previous section the light-matter coupling strength $g_0 \propto \mathcal{E}_0\mu$ leading to the interaction Hamiltonian:

$$\hat{H}_{int} = g_0(\hat{\sigma}_+ + \hat{\sigma}_-)\left(\hat{a} + \hat{a}^\dagger\right) \tag{5.16}$$

In the rotating wave approximation limit where we neglect the off-resonant term of equation 5.16 oscillating at $\omega_c + \omega_e$, we obtain the Jaynes-Cummings Hamiltonian :

$$\hat{H} = \frac{1}{2}\omega_e\hat{\sigma}_z + \omega_c\hat{a}^\dagger\hat{a} + g_0\left(\hat{\sigma}_+\hat{a} + \hat{\sigma}_-\hat{a}^\dagger\right) \tag{5.17}$$

This Hamiltonian is the building block of all the development I will present in the following sections. It describes the interaction of a two-level system with the quantum light field of the cavity. Denoting the number of intra-cavity photons as n, the eigenstates of this Hamiltonian consist in states $|e, n\rangle$ and $|g, n+1\rangle$ all degenerates in the absence of coupling. These states are dressed due to the coupling to the cavity, the interaction Hamiltonian thus lifting this degeneracy with eigenenergies of the form

$$E_\pm = \omega_c\left(n + \frac{1}{2}\right) \pm \Omega_n/2 \tag{5.18}$$

with $\Omega_n = \sqrt{4(n+1)g_0^2 + \Delta}$ where $\Delta = \omega_c - \omega_a$.

We see that the two energies are split by a quantity $\sqrt{2(n+1)}g_0$ at resonance, creating an avoided-crossing between the two energy branches, as depicted in figure 5.1. Here we can make one important first comment, the normal mode splitting is a non linear function of the intracavity photons, leading to the possibility to use this single photon non-linearity to realize quantum gates for example [37, 188]. In this condition the driving field not included in this model plays a central role. In the work we present here, we will restrict to a regime where we can neglect the driving field, thus described by a linear response theory in the case where $n < 1$.

Second, the eigenstates of the coupled system are written under the form $|f\rangle = \cos(\theta)|g, 1\rangle + \sin(\theta)|e, 0\rangle$, the first term corresponding the to the photonic part of the state while the second term relates to its atomic part. Adding a weak drive field $\hat{\delta} = \sqrt{\kappa}\xi\left(\hat{a}e^{i\omega t} + \hat{a}^\dagger e^{-i\omega t}\right)$ we gives the expression of the coupling to the perturbation with

$$\Gamma \sim |\langle f|\hat{\delta}|g\rangle|^2\,\delta(\omega - \omega_e) \tag{5.19}$$

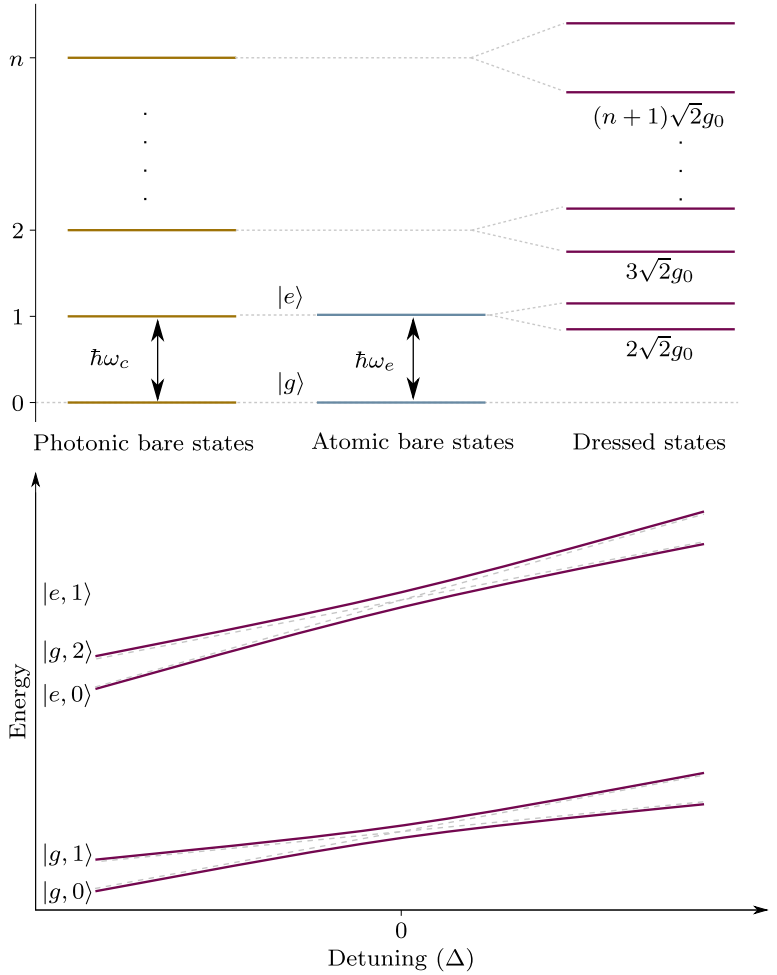

Figure 5.1: ***Energy spectrum of a single atom coupled to a single mode of the cavity : Jaynes-Cummings Hamiltonian.*** The figure shows the bare states of the cavity field on the left and the bare atomic states in the middle. Due to the coupling between the cavity field and the atom, the eigenstates of the system couple the atomic and the photonic component with $|g,1\rangle$ and $|e,0\rangle$, for the first excited state comprising one optical excitation. These two states, of same energy in the absence of coupling, are dressed leading to a splitting at resonance which increases with the number of excitation placed in the system. Observing this avoided-crossing is the experimental signal of the strong light-matter coupling regime.

where $|\langle f|\hat{\delta}|g\rangle|^2 \propto \cos(\theta)^2$ the photonic weight of the polariton. Applying this small approximate reasoning, we see that looking at the transmission through the cavity when injecting a weak on-axis pump field, the transmission directly relate to the photonic weight of the polariton. $\theta \approx \arctan(\frac{2g_0}{\Delta})$ represents the mixing angle in the limit of $n < 1$, showing that for large value of Δ the polaritons are mainly photonic as $\cos(\theta) \approx 1$ and $\sin(\theta) \approx 0$.

We see here that in addition of giving the location of the dressed state, transmission spectroscopy gives a direct link to the photonic weight of the dressed state that directly imprints onto the value of the transmission through the cavity. The appearance of an avoided-crossing in the spectrum is the experimental smoking gun that characterizes the strong light-matter coupling regime we want to observe.

5.2.4 *Many independent emitters : Tavis-Cummings model*

We have described the structure of dressed states when coupling one atom to the cavity field and how this can be unveiled using transmission spectroscopy. It is interesting to consider the case where many atoms are coupled to the same cavity mode with identical coupling strength. We will see that this leads to a very specific scaling of the collective light-matter coupling strength when many atoms couple coherently to cavity photons.

We write the Hamiltonian in the case of $N_\uparrow, N_\downarrow$ atoms, populating two internal states characterized by their transition frequency $\omega_\uparrow, \omega_\downarrow$, positioned at the center of the cavity mode defined by:

$$\hat{H} = \hat{H}_0 + \hat{H}_{int} \tag{5.20}$$

with $\hat{H}_0$ the Hamiltonian describing the cavity field and the internal dynamics of the atoms

$$\hat{H}_0 = \frac{\omega_\uparrow}{2}\sum_i \hat{\sigma}_{z\uparrow}^{(i)} + \frac{\omega_\downarrow}{2}\sum_i \hat{\sigma}_{z\downarrow}^{(i)} + \omega_c \hat{a}^\dagger \hat{a} \tag{5.21}$$

ω_c is the frequency of the cavity light field as presented previously.

$\hat{H_{int}}$ describes the interaction between the atoms and the cavity field :

$$\hat{H}_{int} = \frac{\Omega_{0\uparrow}}{2}\sum_i \left(\hat{\sigma}_{+\uparrow}^{(i)}\hat{a} + hc\right) + \frac{\Omega_{0\downarrow}}{2}\sum_i \left(\hat{\sigma}_{+\downarrow}^{(i)}\hat{a} + hc\right) \tag{5.22}$$

with $\Omega_\uparrow$ and $\Omega_\downarrow$ the Rabi frequencies for the two spin states. As all the atoms of each spin state couple coherently to the light field we define collective spin operators $(\hat{J}_+, \hat{J}_-, \hat{J}_z)$ defined with respect to the single atom Pauli matrices by :

$$\hat{J}_{z,\uparrow\downarrow} = \frac{1}{2}\sum_i \hat{\sigma}_{z,\uparrow\downarrow}^{(i)} \tag{5.23}$$

$$[\hat{J}_{x,\uparrow\downarrow}, \hat{J}_{y,\uparrow\downarrow}] = i\hat{J}_{z,\uparrow\downarrow} \tag{5.24}$$

$$\hat{J}_{\pm,\uparrow\downarrow} = \hat{J}_{x,\uparrow\downarrow} \pm i\hat{J}_{y,\uparrow\downarrow} = \sum_i \hat{\sigma}_{+,\uparrow\downarrow}^{(i)} \tag{5.25}$$

The Hamiltonian reads

$$\hat{H} = \omega_\uparrow \hat{J}_{z,\uparrow} + \omega_\downarrow \hat{J}_{z,\downarrow} + \omega_c \hat{a}^\dagger \hat{a} + \frac{\Omega_{0\uparrow}}{2}\left(\hat{J}_{+,\uparrow}\hat{a} + hc\right) + \frac{\Omega_{0\downarrow}}{2}\left(\hat{J}_{+,\downarrow}\hat{a} + hc\right) \tag{5.26}$$

describing the coupling of $N_\uparrow + N_\downarrow$ atoms coherently coupling to a single mode of the cavity. This Hamiltonian is the so-called Tavis-Cummings Hamiltonian, extending the Jaynes-Cummings Hamiltonian to the case of many atoms.

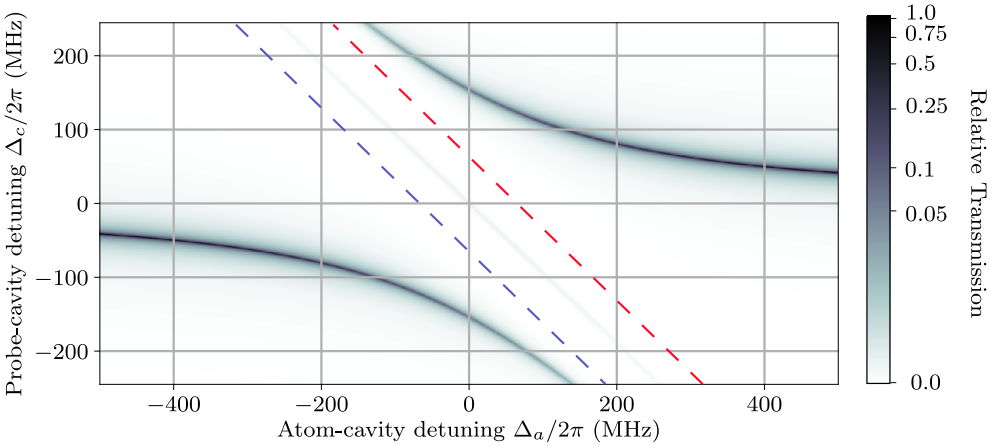

Figure 5.2: ***Transmission spectrum of a two-component gas coupled to a single mode of the cavity.*** The figure shows the transmission spectrum of a two-component gas coupled to a single mode of a cavity. The bare atomic states are indicated by the blue and red dashed lines. Δ_c indicates the detuning between the cavity resonance frequency and the probe beam frequency. Δ_a indicates the detuning between the cavity resonance and the atomic reference, taken exactly in-between the two atomic states. The spectrum shows the relative transmission with respect to the maximum transmission, far from the atomic states, in logarithmic scale. We observe three clear transmission branches, corresponding to the three dressed state of the coupled system. The presence of the two atomic mode leads to a weak polariton in-between the two atomic states. The weak transmission is due to the large collective Rabi frequency for this system compared with the hyperfine frequency splitting, making this polariton of atomic nature for any values of Δ_a.

We perform the Holstein-Primakoff transformation of the collective spin operators, defining two operators, $\hat{b}, \hat{b}^\dagger$ fulfilling the bosonic commutation relation and defined as

$$\hat{J}_{+,\uparrow\downarrow} = \sqrt{2j}\hat{b}^\dagger_{\uparrow\downarrow}\sqrt{1-\frac{\hat{b}^\dagger_{\uparrow\downarrow}\hat{b}_{\uparrow\downarrow}}{2j}} \tag{5.27}$$

$$\hat{J}_{-,\uparrow\downarrow} = \sqrt{2j}\hat{b}_{\uparrow\downarrow}\sqrt{1-\frac{\hat{b}^\dagger_{\uparrow\downarrow}\hat{b}_{\uparrow\downarrow}}{2j}} \tag{5.28}$$

$$\hat{J}_{z,\uparrow\downarrow} = \hat{b}^\dagger_{\uparrow\downarrow}\hat{b}_{\uparrow\downarrow} - j \tag{5.29}$$

with j the quantum number associated to $\hat{J}^2_{\uparrow,\downarrow}$ leading to $j = N_{\uparrow\downarrow}/2/$.

In the linear response regime, where few excitations are present in the system, the collective spin operators simplify into :

$$\hat{J}_{+,\uparrow\downarrow} = \sqrt{N_{\uparrow,\downarrow}}\hat{b}^\dagger \tag{5.30}$$

$$\hat{J}_{+,\uparrow\downarrow} = \sqrt{N_{\uparrow,\downarrow}}\hat{b} \tag{5.31}$$

yielding the Tavis-Cummings Hamiltonian within the linear response approximation :

$$\hat{H} = \omega_{\uparrow}\hat{b}_{\uparrow}^{\dagger}\hat{b}_{\uparrow} + \omega_{\downarrow}\hat{b}_{\downarrow}^{\dagger}\hat{b}_{\downarrow} + \omega_c\hat{a}^{\dagger}\hat{a} + \frac{\Omega_{0\uparrow}}{2}\sqrt{N_{\uparrow}}\left(\hat{b}_{\uparrow}^{\dagger}\hat{a} + hc\right) + \frac{\Omega_{0\downarrow}}{2}\sqrt{N_{\downarrow}}\left(\hat{b}_{\downarrow}^{\dagger}\hat{a} + hc\right) \quad (5.32)$$

The collective Rabi frequency for a single spin state populated simplifies into $\Omega_{\uparrow,\downarrow} = 2g_N = 2\sqrt{N_{\uparrow,\downarrow}}g_0$ with $N_{\uparrow,\downarrow}$ the number of atoms in each spin state. We solve the steady state Heisenberg equation for the cavity field, thus simulating the transmission spectrum of this system that reveals the presence of dressed states as presented in figure 5.2 :

We observe that we have three dressed states, mixing the two atomic mode and the photonic mode of the cavity. As we have introduced one more internal state compared with the Jaynes-Cummings Hamiltonian, we have an extra dressed state. Similarly to the single atom case, we observe a large avoided crossing due to the dressing of the atomic state by the cavity photons. We see that the supplementary dressed state appears in the middle of the large avoided crossing. This dressed state has a much lower transmission compared with the two others. In the regime where we operate the experiment, the collective Rabi frequency is much larger than the frequency difference between the two spin states populated. Hence, this polariton is mainly of atomic nature at any values of Δ_a. We also observe that the two main transmission branches interpolate smoothly between large transmission far away from atomic resonance, where absorption from the atoms is mostly reduced, to very weak transmission when they approach the atomic bare state. This variation show the evolution of the photonic weight of the dressed state as presented in the previous section.

5.3 INTERACTIONS BETWEEN MANY ATOMS AND MANY CAVITY MODES

So far we have discussed the cases of a single atom and many atoms coupled to a single cavity mode. As we discussed in Chapter 2, a Fabry-Pérot cavity has both a transverse and longitudinal mode structure. In the case of our cavity, several high-order transverse modes of different longitudinal modes are relatively close to the frequency of the fundamental mode we address with our weak probe beam. Thus we need to account for more than a single mode of the electromagnetic field of the resonator to reproduce the measurement of the experiment as the atoms will be able to scatter from the fundamental mode to higher orders ones due to the large collective Rabi frequency and the finite size of the cloud.

I will first show the structure of the high-order transverse modes in the absence of the atoms. I will then present the theoretical framework allowing to account for many atoms populating two internal state coupled to many cavity modes with different spatial profiles.

5.3.1 Multimode structure of the cavity

As discussed it in the Chapter chapter 2, the Hermite-Gauss functions are solutions of the Helmholtz equation that describes the intra-cavity field. All these different modes are described by the number of nodes they posses

along the two directions of space (y, z) orthogonal to the cavity direction, denoted (n, m). The mode functions are:

$$u_{(n,m)}(r, z) = A_{n,m}(y, z)\cos(kx)e^{-\frac{r^2}{w_0^2}} \tag{5.33}$$

with $r^2 = y^2 + z^2$, and x the spatial coordinate along the cavity axis. k corresponds to the wavevector of the standing wave and characterizes the longitudinal mode of the wave. This expression is significantly simpler compared with the one presented in chapter 2 as we neglect the phase shift effect between different transverse modes and remove the x-dependence except for the lattice structure. This approximation is legitimate as the cloud will explore a small region around the cavity mode center, still extending over several lattice sites but where the mode will be of constant transverse radius. The transverse amplitude profile $A_{n,m}(y, z)$ simplifies into

$$A_{n,m,}(y, z) = \sqrt{\frac{1}{V}}\left(\frac{1}{2^{n+m}n!m!)}\right)^{1/2} H_n\left(\frac{\sqrt{2}y}{w_0}\right) H_m\left(\frac{\sqrt{2}z}{w_0}\right) \tag{5.34}$$

with $V = \pi L w_0^2/4$ the ground mode volume defined with L the length of the resonator, w_0 the waist of the TEM_{00} mode. For what follows, we replace the indices $(k, n, m) \rightarrow \nu$ defining one mode characterized by its longitudinal and transverse mode indices. The normalized functions $f_\nu = \sqrt{V}u_{(n,m)}(r, z)$ are constructed such that the ground mode reaches an amplitude of one at the cavity center $f_0(0) = 1$. These functions are used to describe the transverse mode we will treat in the light-matter interaction problem.

In order to know which mode function we have to use to calculate the coupling between the atomic density and the cavity field, we want to characterize the transverse modes located near by the fundamental one. To characterize them, we sweep the probe laser frequency through the cavity resonance, going down to -100 MHz from the cavity fundamental mode. Scanning the probe laser frequency around the fundamental TEM_{00} mode located at $\Delta_c/2pi = 0$ where Δ_c defines the frequency detuning between the ground mode and the probe laser frequency. We observe a Gaussian mode exiting the cavity (figure 5.3) with a spectral width observed onto a photodiode monitoring the cavity transmission compatible with the cavity linewidth $\kappa/2\pi = 77.4$ kHz combined with technical noise of the order of 20 kHz. This mode is the dominant one as we inject a Gaussian beam, mode-matched with the ground mode of the cavity. However, due to the symmetry breaking of the cavity because of the imperfect alignment of the cavity mirror and to the non-perfect Gaussian mode of the injected laser, a small fraction of power couples to higher modes as presented in figure 5.3. The first mode family encountered is located at $\delta_c/2\pi = -25$ MHz. This family is of order eleven, meaning that $n + m = 11$. In principle all these modes should be degenerate. We observe several transmission peaks within 1.5 MHz as indicated in figure 5.3. This frequency shift is due to astigmatism of the mirrors, the high-order modes exploring a much larger aperture than the TEM_{00}.

Similarly to this feature appearing at $\delta_c/2\pi = -25$ MHz, we can identify other high order transverse mode families at $\delta_c/2\pi = -50$, -75 and -100 MHz corresponding to the families of order 22, 33 and 44 respectively. All these high order modes are very weakly coupled to the probe beam, about

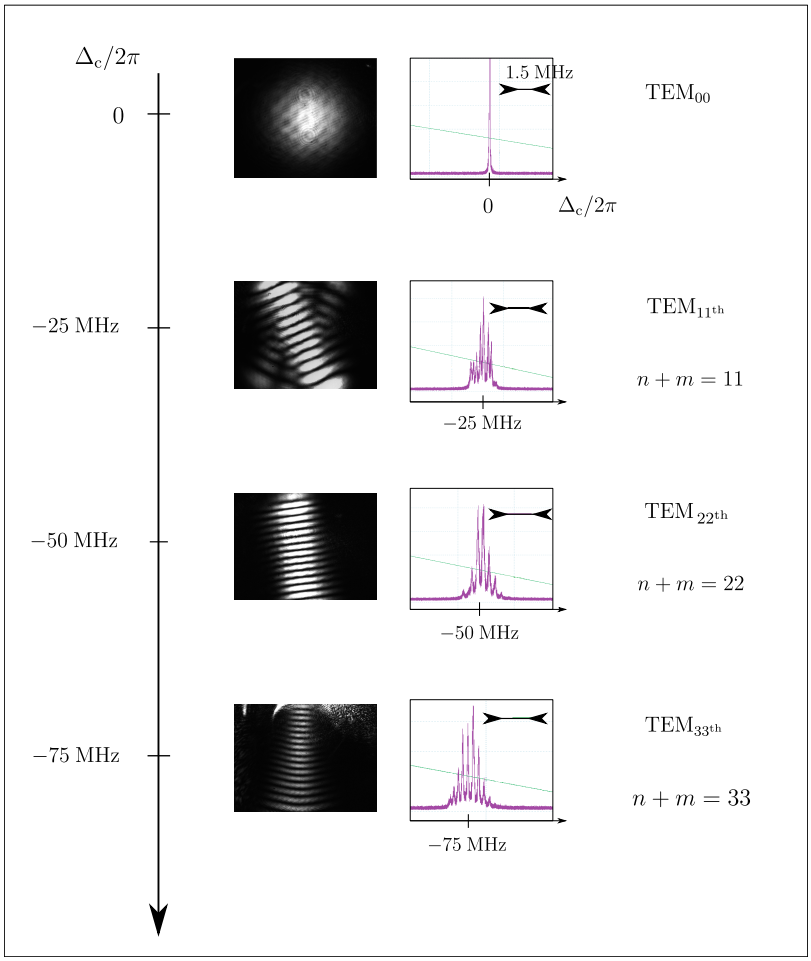

Figure 5.3: ***Multitmode structure of the Fabry-Perot cavity : pictorial view.*** The figure shows the structure of the high-order modes of the cavity that are at relatively small detuning compared with the fundamental mode, located at $\Delta_c = 0$ MHz. This high order modes correspond to the TEM families of order 11, 22 , 33 and 44 located at −25, −50, −75 and −100 MHz from the fundamental mode respectively. These modes belong to different longitudinal mode from the fundamental mode considered here. We show for each of this mode families the spatial profile of light transmitted from the cavity when the probe frequency is set resonant with the high order modes. Transmission traces when sweeping the probe laser frequency shows an internal structure within each mode family, showing that the modes are not degenerate.

10^{-3} of relative coupling efficiency, however they could not be neglected if the collective coupling strength is larger or similar to the high order mode spacings with respect to the ground mode.

In figure 5.4.a, we show the different modes observed within the family of order $n + m = 11$. We observe all the modes from a vertical mode with 11 nodes to a one with no vertical nodes and 11 nodes along the horizontal direction. We clearly see that these two extreme modes will be sensitive to an effective focal change along the two transverse axis, thus being the two edge cases regarding the frequency shift induced by the astigmatism of the cavity mirrors. In order to estimate the effect of astigmatism and thus the exact location of each of the modes inside the same family, we slightly tune the

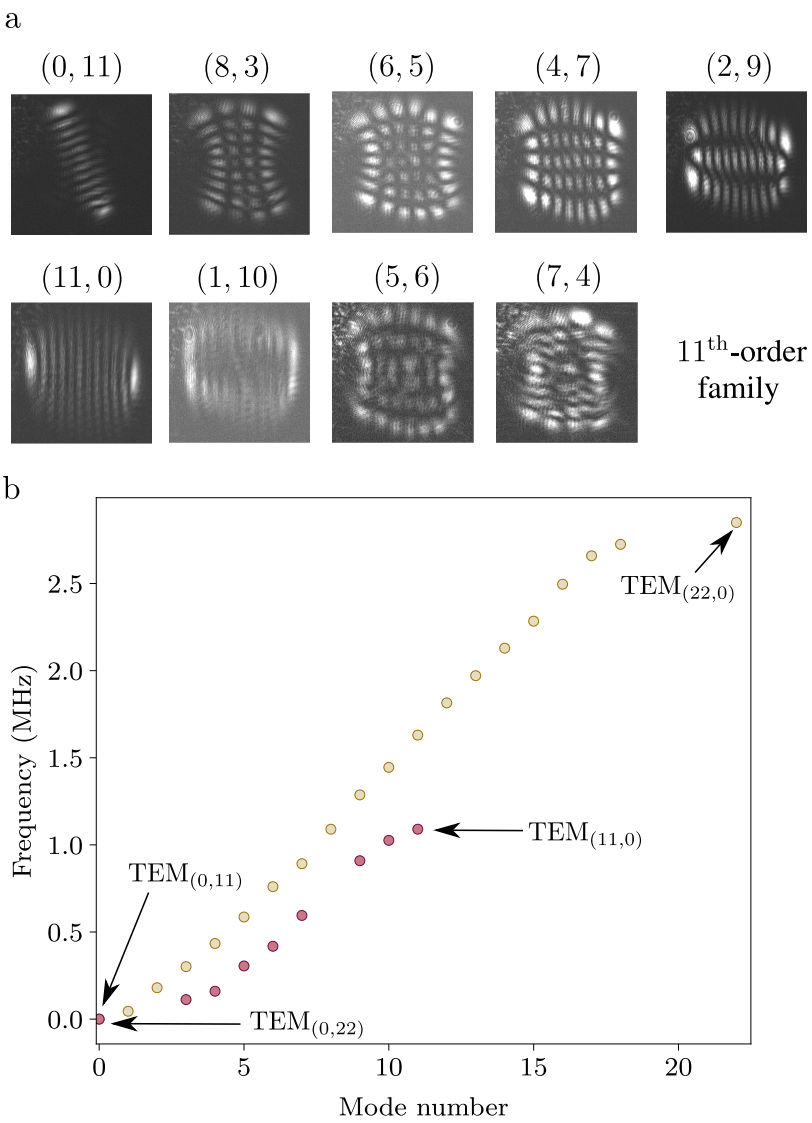

Figure 5.4: ***Astigmatism for high-order transverse modes.*** **a** Shows the different spatial profiles observed when setting the probe laser frequency resonant with a single mode of the mode family of order 11. We observe almost all the modes from the $\mathrm{TEM}_{(0,11)}$ with nodes along the vertical direction only, to the $\mathrm{TEM}_{(11,0)}$ oriented horizontally. **b** Displays the frequency difference between each mode within the families of order $n + m = 11$ and $n + m = 22$. The spacing between the modes is more important by a factor 2 for the family of order 22. This is due to the larger aperture explored by this mode family compared with the family of order 11.

beam alignment to couple more into each of the modes of a same family and record its frequency compared with the ground mode. Hence we measure the evolution of the mode frequency as a function of n, the number of nodes along the vertical direction for both families of order 11 and 22 (figure 5.4). We see that the astigmatism is more significant for the family 22 compared with the family 11, showing that the frequency shift is actually a function of the optical aperture, thus a consequence of astigmatism. Moreover, we see that the maximum frequency shift for the family 11 is about 1 MHz and about 2.7 MHz for the family of order 22, smaller than Γ the width of the dressed states close to resonance. This means that for all practical

purposes we can treat them as degenerate modes for the calculation of the dressed states close to atomic resonance, as far as Γ stays the linewidth of reference and that the collective Rabi frequency is larger than the effect of astigmatism. For larger detunings with respect to the atomic resonance, leading to a dressed state of linewidth κ, the frequency difference between each of these mode should be accounted for.

Knowing the transverse mode structure of the cavity, with the mode order and their location with respect to the ground mode, we will only consider the ones detuned by frequencies of the order of the collective coupling strength, meaning the mode families of order 11,22,33 and 44, in addition to the TEM_{00} mode. This constitutes an ensemble of 115 modes that couple to the atomic density. In order to obtain the energy spectrum we will calculate all the couplings between these cavity modes with the atoms.

5.3.2 *Ab-initio model for two atomic modes and a multimode cavity*

The Hamiltonian for one atomic state and many cavity mode

We have explored the Jaynes-Cummings Hamiltonian and its extension to the case of many identical atoms. We now combine it with the presence of the higher-order transverse modes presented in detail in the previous paragraph. For this, let us first write the Hamiltonian which now contains a sum over the atoms i and the cavity modes ν, disregarding the motional degree of freedom of the atoms,

$$\hat{H} = \sum_{\nu} \omega_c \hat{a}_\nu^\dagger \hat{a}_\nu + \omega_e \sum_i \frac{1+\hat{\sigma}_z^{(i)}}{2} - i\frac{\Omega_0}{2} \sum_{\nu,i} \left(\hat{a}_\nu f_\nu(r_i) \hat{\sigma}_+^{(i)} - hc \right) + i\sqrt{\kappa} \sum_\nu \mathcal{F}_\nu \left(\hat{a}_\nu e^{-i\omega_d t} - \hat{a}_\nu^\dagger e^{i\omega_d t} \right) \quad (5.35)$$

The first term corresponds to the cavity field Hamiltonian for each cavity mode at frequencies ω_ν, the second to the atomic part, with the frequency of the excited state ω_e. The third term represents the interaction between the atoms and all the cavity modes defined by their spatial mode functions $f_\nu(r_i) = \sqrt{V} u_\nu(r)$. The Rabi frequency is $\Omega_0 = 2\sqrt{\frac{\omega_c}{2\epsilon_0 V}} d_0 = 2g_0$, with ω_c the optical frequency resonant in the cavity, taken to be identical for all the transverse modes, ϵ_0 the vacuum permittivity and $V = \pi L w^2/4$ the volume of the fundamental cavity mode. The last term of the Hamiltonian is the coupling of the driving field to all the cavity modes. Due to the mode-matching of the driving field with the fundamental mode of the cavity, $\mathcal{F}_0 >> \mathcal{F}_{\nu>0}$.

In the RWA approximation, setting $\delta_\nu = \omega_\nu - \omega_d$ and $\Delta = \omega_e - \omega_d$ we rewrite the Hamiltonian as:

$$\hat{H} = \sum_{\nu} \delta_\nu \hat{a}_\nu^\dagger \hat{a}_\nu + \Delta \sum_i \frac{1+\hat{\sigma}_z^{(i)}}{2} - i\frac{\Omega_0}{2} \sum_{\nu,i} \left(\hat{a}_\nu u_\nu(r_i) \hat{\sigma}_+^{(i)} - hc \right) + i\sqrt{\kappa} \sum_\nu \mathcal{F}_\nu \left(\hat{a}_\nu - \hat{a}_\nu^\dagger \right) \quad (5.36)$$

The equation of motion for the cavity field

This Hamiltonian provides the general starting point to treat the interaction between the unitary Fermi gas and the cavity light field. For now we restrict ourselves to the case of a single atomic component in order to investigate the coupling between the atomic density and the cavity modes.

Making the approximation that we neglect the atom-field correlations as well as the quantum fluctuations of the cavity field, we replace the field operators for the atoms and the photons by coherent amplitudes :

$$\hat{a}_\nu, \sigma_k^{(i)} \longrightarrow \alpha_\nu, \left\langle \hat{\sigma}_k^{(i)} \right\rangle \tag{5.37}$$

As we measure the cavity transmission on the experiment, we want to calculate the steady state solution for the coherent amplitude of the field. For an operator $\hat{G}$ with expectation value $\langle \hat{G} \rangle = \mathrm{Tr}\{\rho \hat{G}\}$, ρ begin the density matrix, we write the time-evolution described by the Linblad equation [189]

$$\frac{\partial \left\langle \hat{G} \right\rangle}{\partial t} = i \left\langle \left[\hat{H}, \hat{G}\right] \right\rangle + \sum_n \frac{\gamma_n}{2} \left(\left\langle \hat{A}_n^\dagger \left[\hat{G}, \hat{A}_n\right] \right\rangle + \left\langle \left[\hat{A}_n^\dagger, \hat{G}\right] \hat{A}_n \right\rangle \right) \tag{5.38}$$

with $\hat{H}$ the Hamiltonian of the system. The second term of the right hand side of the equation is a sum over the dissipation channels :

- The spontaneous emission leading to $\hat{A} = \hat{\sigma}_-^{(i)}$ and $\gamma_n = \Gamma$ the linewidth of the atomic excited state.
- The losses through the cavity mirror, with $\hat{A} = \hat{a}_\nu$ and $\gamma_n = \kappa$ the linewidth of bare cavity.

Replacing $\hat{G}$ by $\hat{a}_\nu, \hat{\sigma}_-^{(i)}, \hat{\sigma}_+^{(i)}, \hat{\sigma}_z^{(i)}$ we obtain a set of four differential equations for the cavity and the atomic modes :

$$\begin{cases} \frac{d\alpha_\nu}{dt} & = i \left\langle \left[\hat{H}, \hat{a}_\nu\right] \right\rangle - \frac{\kappa}{2} \alpha_\nu \\ \frac{d\left\langle \hat{\sigma}_z^{(i)} \right\rangle}{dt} & = i \left\langle \left[\hat{H}, \hat{\sigma}_z^{(i)}\right] \right\rangle - \Gamma(1 + \hat{\sigma}_z^{(i)}) \\ \frac{d\left\langle \hat{\sigma}_-^{(i)} \right\rangle}{dt} & = i \left\langle \left[\hat{H}, \hat{\sigma}_-^{(i)}\right] \right\rangle - \frac{\Gamma}{2} \left\langle \hat{\sigma}_-^{(i)} \right\rangle \\ \frac{d\left\langle \hat{\sigma}_+^{(i)} \right\rangle}{dt} & = i \left\langle \left[\hat{H}, \hat{\sigma}_+^{(i)}\right] \right\rangle - \frac{\Gamma}{2} \left\langle \hat{\sigma}_+^{(i)} \right\rangle \end{cases}$$

From the optical Bloch equations obtained above, we deduce the equation of motion for the cavity field :

$$\dot{\alpha}_\nu = (-i\delta_\nu - \frac{\kappa}{2})\alpha_\nu - \frac{\Omega_0}{2} \sum_i u_\nu(r_i) \langle \hat{\sigma}_-^{(i)} \rangle - \sqrt{\kappa} \mathcal{F}_\nu \tag{5.39}$$

where we have injected the steady state solution for $\langle \hat{\sigma}_-^{(i)} \rangle$ to obtain the explicit equation for the steady state of the cavity field. We consequently solve the Bloch equation, for the steady state of the atomic operators, leading to :

$$\begin{cases} \left\langle \hat{\sigma}_z^{(i)} \right\rangle & = -\frac{\frac{\Gamma^2}{4} + \Delta^2}{\frac{\Gamma^2}{4} + \Delta^2 + 2|d_0 \mathcal{E}_i|^2} \simeq -\left(1 - \frac{2|d_0 \mathcal{E}_i|^2}{\frac{\Gamma^2}{4} + \Delta^2}\right) \\ \left\langle \hat{\sigma}_-^{(i)} \right\rangle & = -\frac{d_0 \mathcal{E}_i \left\langle \hat{\sigma}_z^{(i)} \right\rangle}{\frac{\Gamma}{2} + i\Delta} \simeq \frac{d_0 \mathcal{E}_i}{\frac{\Gamma}{2} + i\Delta} \end{cases} \tag{5.40}$$

where

$$\mathcal{E}_i = \sum_\upsilon \sqrt{\frac{\hbar\omega}{2\epsilon_0}} u_\upsilon(r_i)\alpha_\upsilon$$

denotes the classical driving field.

Replacing the solutions of equation 5.40 into equation 5.39, we obtain the steady state solution for the equation of motion of the cavity field in the presence of many atoms and many cavity modes :

$$0 = (-i\delta_\nu - \frac{\kappa}{2})\alpha_\nu - \frac{\frac{\Omega_0^2}{4}}{\frac{\Gamma}{2} + i\Delta} \sum_{i,\upsilon} f_\nu(r_i) f_\upsilon(r_i)\alpha_\upsilon - \sqrt{\kappa}\mathcal{F}_\nu \quad (5.41)$$

In the equation above we replace the sum over each atom of index i with an integral over the density of the cloud $n(r) = \sum_i \delta(r - r_i)$ such that

$$\alpha_\nu = -\frac{1}{i\delta_\nu + \frac{\kappa}{2}} \frac{\frac{\Omega_0^2}{4}}{\frac{\Gamma}{2} + i\Delta} \sum_\upsilon G_{\upsilon\nu}\alpha_\upsilon - \frac{\sqrt{\kappa}\mathcal{F}_\nu}{i\delta_\nu + \frac{\kappa}{2}} \quad (5.42)$$

where we define the coupling matrix $G_{\upsilon\nu} = \int_V d^3r f_\nu(r) f_\upsilon(r) n(r)$ that describes the coupling between a pumped cavity mode of index υ and any other cavity mode of index ν, mediated by the scattering of the atoms from the two modes. We see that even if a mode υ is not pumped, atoms are able to scatter in it as far as the overlap between the atomic cloud and these modes is non-zero [190, 191].

Calculation of the coupling matrix

In order to explicitly calculate the coupling matrix $G_{\upsilon\nu}$, we calculate the overlap integral between a cavity mode of index $\nu \to (n, m, k)$ and another one of index $\upsilon \to (n', m', k')$. k, k' characterize the longitudinal mode of the cavity while n, n', m, m' define the transverse modes. The atomic density is defined by a function of the spatial coordinates $n(x, y, z)$. Using the definition of the Hermite-Gauss modes near the cavity center, we write the coupling matrix as:

$$G_{\upsilon\nu} = \frac{1}{\sqrt{2^{n+m+n'+m'} n!m!n'!m'!}} \int_V dxdydz n(x,y,z) \cos(kz)\cos(k'z) \\ e^{-\frac{2x^2}{w_0^2} - \frac{2y^2}{w_0^2}} H_n(\frac{x\sqrt{2}}{w_0}) H_m(\frac{y\sqrt{2}}{w_0}) H_{n'}(\frac{x\sqrt{2}}{w_0}) H_{m'}(\frac{y\sqrt{2}}{w_0}) \quad (5.43)$$

with H_i the Hermite polynomials of order i.

This simplifies into :

$$G_{\upsilon\nu} = \frac{1}{\sqrt{2^{n+m+n'+m'} n!m!n'!m'!}} \frac{\delta'_{kk'}}{2} \int_V dxdydz n(x,y,z) e^{-\frac{2x^2}{w_0^2} - \frac{2y^2}{w_0^2}} \\ H_n(\frac{x\sqrt{2}}{w_0}) H_m(\frac{y\sqrt{2}}{w_0}) H_{n'}(\frac{x\sqrt{2}}{w_0}) H_{m'}(\frac{y\sqrt{2}}{w_0}) \quad (5.44)$$

taking a cloud smaller than the Rayleigh length of the cavity mode along the cavity direction and with a density profile smoother than the lattice spacing $\lambda/2$ of the cavity field. $\delta'_{kk'}$ is zero if $k \neq k' \bmod [2]$.

Considering that the cloud will be trapped in an harmonic trap created by an optical dipole potential, the density of a unitary Fermi gas as a function of its chemical potential at the center of the trap μ is $n_\sigma(\mu) = \frac{1}{6\pi^2}\left(\frac{2m\mu}{\xi\hbar^2}\right)^{3/2}$, where $\xi = 0.370(5)$ is the Bertsch parameter [145]. Thus the expression of the atomic density as a function of position reads $n(\vec{r}) = n(\mu - V(\vec{r})) = n(\mu)\left(1 - \frac{V(\vec{r})}{\mu}\right)^{3/2}\Theta(1 - \frac{V(\vec{r})}{\mu})$, with Θ the Heaviside function. We introduce the Thomas-Fermi radius for each axis of the trap as the characteristic length scale for the atomic density R_i as described in Chapter 4 :

Replacing the density by this expression in equation 5.44 with the change of variable $\tilde{x} = x/R_x$ $\tilde{y} = y/R$ and $\tilde{z} = z/R$ to rescale all distances with respect to the Thomas-Fermi radius of the cloud,

$$\int d^3r n(r) f_{n,m,k}(r) f_{n',m',k'}(r) = \frac{\delta'_{k,k'}}{2} n(\mu) R^2 R_x \times \mathcal{F}_{n,n',m,m'}\left(\frac{R}{w_0}\right) \tag{5.45}$$

R_x and R are the Thomas Fermi radii in the longitudinal and transverse directions and with the dimensionless function $\mathcal{F}_{n,n',m,m'}(\frac{R}{w_0})$ defined by

$$\begin{aligned}\mathcal{F}_{n,n',m,m'}(\frac{R}{w}) &= \frac{1}{\sqrt{2^{n+m+n'+m'} n!m!n'!m'!}} \\ &\int_{-1}^{1} d\tilde{y} \int_{-1}^{1} d\tilde{z} \int_{-1}^{1} d\tilde{x} \left(1 - \tilde{y}^2 - \tilde{z}^2 - \tilde{x}^2\right)^{3/2} \Upsilon\left(1 - \tilde{y}^2 - \tilde{z}^2 - \tilde{x}^2\right) \\ &e^{-\frac{R}{w_0}^2 (2\tilde{y}^2 + 2\tilde{z}^2)} H_n(\tilde{y}\frac{R}{w_0}\sqrt{2}) H_{n'}(\tilde{y}\frac{R}{w_0}\sqrt{2}) H_m(\tilde{z}\frac{R}{w_0}\sqrt{2}) H_{m'}(\tilde{z}\frac{R}{w_0}\sqrt{2})\end{aligned} \tag{5.46}$$

We introduce the explicit expression for the local density for a Fermi gas $N = n(\mu)R^2 R_z \mathcal{F}_{0,0,0,0}(0)$, with N the total atom number and obtain the elements of the coupling matrix :

$$\begin{aligned}G_{n,m,n',m',k,k'} = \mathcal{A}_{n,m,n',m'} &\int d^3r n(r) f_{n,m,k}(r) f_{n',m',k'}(r) \\ &= N \frac{\delta'_{k,k'}}{2} \frac{\mathcal{F}_{n,n',m,m'}\left(\frac{R}{w_0}\right)}{\mathcal{F}_{0,0,0,0}(0)}\end{aligned} \tag{5.47}$$

with $\mathcal{A}_{n,m,n',m'} = \frac{1}{\sqrt{2^{n+m+n'+m'} n!m!n'!m'!}}$.

Figure 5.5 shows the coupling matrix for 10^5 atoms populating a single ground state with a Thomas-Fermi radius $R/w = 0.25$ µm. We clearly see that the maximal coupling is reached between the TEM_{00} mode and itself as expected. We also observe that the coupling between the odd and even mode families is strictly zero while the coupling between each $TEM_{0,n}$ and itself and the families with the same parity is ranging from a few percent to about 30%. It confirms that these couplings have to be included to the model to reproduce the experiment.

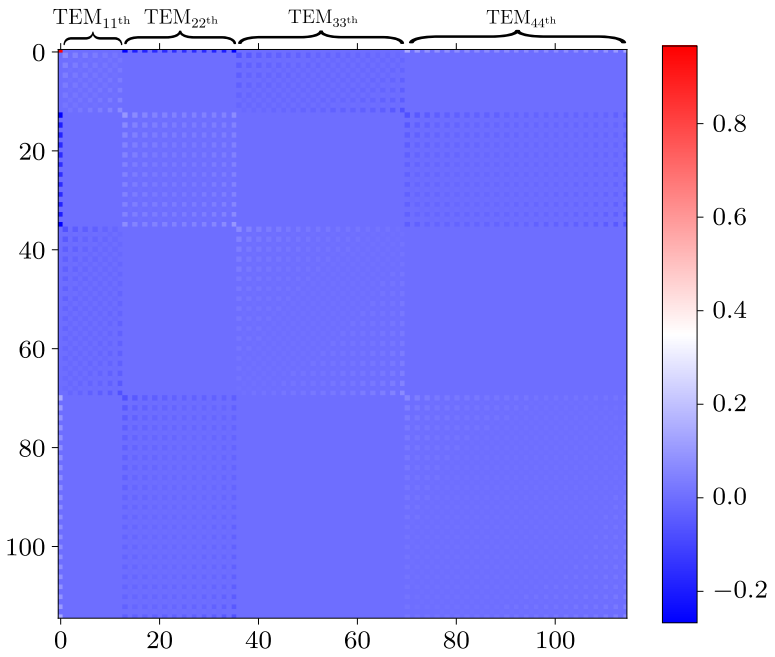

Figure 5.5: ***Coupling matrix between the fundamental*** TEM_{00} ***fundamental modes and the higher order mode families.*** The figure shows the coupling matrix for a gas comprising $N = 10^5$ atoms, positioned at the center of the cavity mode. The matrix element $(0,0)$ corresponds to the coupling of the fundamental mode to itself and is the dominant matrix element. The couplings between odd and even families is strictly zero. The coupling between the TEM_{00} and the even families is about 20% compared with the coupling of the fundamental mode. Scattering between the high-order mode families is also not negligible from the relative values of the coupling matrix elements.

In figure 5.6 we display the evolution of the coupling between the TEM_{00} mode and the $TEM_{0,n}$ with n corresponding to the mode families 11, 22, 33 and 44 when varying R compared with the cavity mode waist w. For our experimental parameters, $R_{TF}/w \simeq 0.25$. We first see that the coupling is maximum for a point-like cloud at the cavity center, with all atoms coupled maximally to the TEM_{00} mode. We also observe that in this configuration, the odd families (11 and 33) that have a node of the field at the cavity center do not couple to the TEM_{00}. The even modes still have a non-zero overlap with the ground mode function leading to a non zero coupling. This coupling is far from being negligible, as it reaches about 40% of the coupling to the TEM_{00} for the family of order 44 in the case of a point like cloud. In practice, for finite size clouds (see figure 5.6), the coupling between the fundamental mode and the high-order mode families decreases quite rapidly, vanishing at $R_{TF/w} \simeq 0.5$. In the regime of our experiment $R_{TF/w} \simeq 0.25$ (see figure 5.6)the inter-mode couplings are of the order of 10% for the high-order modes while the TEM_{00} is almost equal to 1. For large clouds we recover the orthogonality of the mode functions $f_\nu(r)$ that makes the coupling between the different modes vanishing.

We will now apply this concept to the two cases that we realize on the experiment: the spin-balanced unitary Fermi gas and an almost fully polarized, non-interacting Fermi gas. For these we will account for the fact that atoms populate the two lowest hyperfine states separated by $2\Delta_{HF} = 76.4$ MHz, the hyperfine splitting.

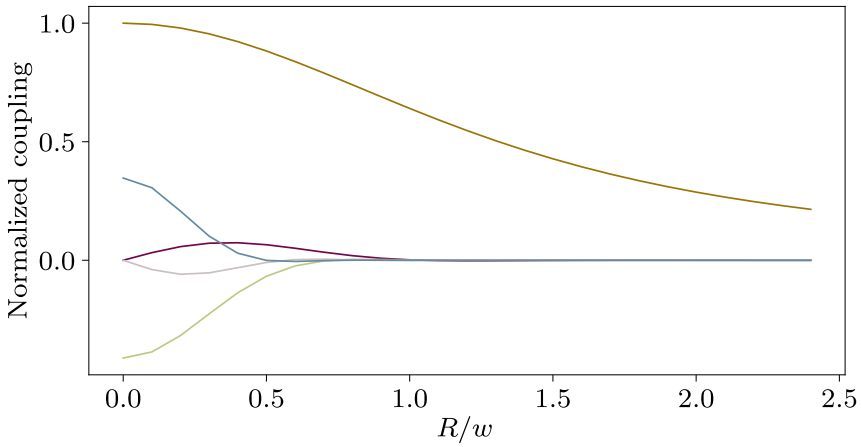

Figure 5.6: ***Scattering from the fundamental mode to thee high-order transverse mode : finite size effects.*** The figure shows the values of the couplings between the fundamental TEM_{00} mode and the modes of order $TEM_{(0,11)}$ (grey line), $TEM_{(0,22)}$ (green line), $TEM_{(0,33)}$ (violet line) and $TEM_{(0,44)}$ (blue line) as a function of Thomas-Fermi radius the cloud compared with the cavity mode waist of the ground mode. To compare the the relative strength of this coupling we display the coupling between the TEM_{00} and itself (yellow line) and normalize the other coupling with respect to this one for a point-like cloud. For a point like cloud the odd families are not coupled while the even ones are maximally coupled. For large clouds compared with the cavity mode waist all couplings vanishes due to the orthogonality of the mode functions. For intermediate regimes, like the one we will operate in the experiment $R/w = 0.25$, all high order mode families are coupled to the ground mode with coupling from 10 to 30% of the coupling to the ground mode itself. A significant part of the cavity photons will be scattered from the ground mode to the high-order mode families in this regime.

5.4 EXPERIMENTAL REALIZATION

5.4.1 Transmission spectroscopy

We now discuss how we experimentally measure the transmission spectrum of the unitary Fermi gas coupled to the cavity modes. We prepare a cloud with atoms populating the two lowest hyperfine states $|1\rangle$ and $|2\rangle$ that will provide the two spin components of the Fermi gas $|\uparrow\rangle$ and $|\downarrow\rangle$ (figure 5.7.b). The preparation follows the experimental procedure presented in Chapter 3. We can either prepare a spin-balanced gas at unitarity or an almost fully spin-polarized gas, which are the two cases we will present in this chapter. The spin-polarized gas provides a simpler model with a single atomic mode populated and no atom-atom interactions. This allow us to compare the transmission spectrum with the ab-initio model. We will be able then to compare the spin-polarized Fermi gas with the spin-balanced unitary Fermi gas and see if any differences emerge due to the presence of interactions. The cloud is held in the crossed optical dipole trap (figure 5.7.a) with trap frequencies $(\omega_x, \omega_y, \omega_z)/2\pi = (300(30), 924(40), 902(11))$. The Fermi gas is positioned at the crossing of the two arms of the dipole trap, corresponding approximately to the center of the cavity mode 5.7.a.

To map out the energy spectrum, we inject a weak probe in the cavity, mode-matched with the TEM_{00} mode of the cavity, with a weak coupling to the high order mode families. The probe beam is polarized in the

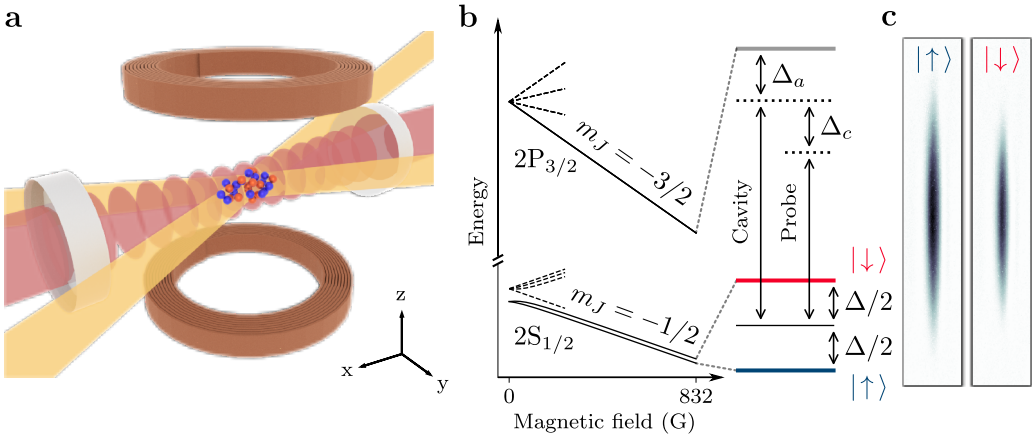

Figure 5.7: ***Combining a unitary superfluid with a high finesse cavity.*** **a** A two-component Fermi gas is trapped in a crossed-dipole trap aligned onto the mode of a high-finesse optical cavity. A bias magnetic field oriented along the z–axis controls the interactions between the atoms. **b** Relevant energy levels of ^{6}Li at 832 G including the frequencies of the probe laser and cavity resonance. In the experiment the detunings Δ_a and Δ_c are varied independently. **c** Integrated density profiles, $\overline{n}_\uparrow$ and $\overline{n}_\downarrow$, along the longitudinal direction after transfer in an elongated trap, for $9.3(5) \times 10^4$ and $6.0(3) \times 10^4$ atoms in state $|\uparrow\rangle$ (red) and $|\downarrow\rangle$ (blue) respectively.

horizontal plane compared with the strong magnetic field bias that is oriented vertically 5.7.a. Thus, the light polarization with respect to the quantization axis corresponds to a superposition of σ^+ and σ^- polarizations. For the range of frequencies explored in these measurements, we can discard the σ^+ component, that is far detuned with respect to the relevant atomic transition. Hence, we consider the probe light only addressing the $|2S_{1/2}, m_j = -1/2\rangle \longrightarrow |2S_{1/2}, m_j = -3/2\rangle$ the closed transition with a coupling strength g_0 reduced by a factor $\sqrt{2}$ due to the vertical quantization axis with respect to the cavity direction. We thus consider each atom as simple two-level system. We will reference the cavity resonance frequency with respect to the center frequency in-between the two lowest hyperfine states separated by Δ. The power of the on-axis probing beam is kept small in order to never reach the saturation threshold of the transition corresponding to $\Gamma^2/8g^2 = 38$ intracavity photons. Working with large atom number makes it extremely hard to enter a regime where we could saturate the transition, each optical excitation put in the system being shared with all atoms.

To reconstruct a full transmission spectrum, we vary the detuning between the probe laser frequency and the cavity resonance of the fundamental mode $\Delta_c = \omega_p - \omega_c$, and the detuning between the cavity resonance and the atomic transition frequency $\Delta_a = \omega_c - \omega_a$ (figure 5.7.b). For each realization of the experiment, we fix Δ_a and sweep the value of $\Delta_c/2\pi$ by 100 MHz over 1 ms. We repeat this measurement for different values of $\Delta_a/2\pi$, spanning a range of $\pm$500 MHz around the frequency reference $\Delta_a = 0$. We average each measurement three times per values of Δ_a with a resolution of 5 MHz. For each measurement, the cavity transmission is detected onto a single photon counter, with an efficiency of 0.44(5). We then pile up these cavity transmission traces to obtain the entire map of the cavity transmission, revealing the location of the dressed states.

5.4.2 *The spin-imbalanced unitary Fermi gas*

Calculation of the coupling matrix

In the case of an almost polarized Fermi gas, we cannot simplify the coupling matrix to a weighted average of the single component coupling matrix as for the spin balanced case. Thus we have to calculate the two coupling matrices for each spin of the two spin components, leading to the following expression for the Heisenberg equation of the cavity field

$$\begin{aligned} 0 = (\delta_\nu - i\frac{\kappa}{2})\alpha_\nu \\ - \frac{N_\uparrow \Omega_0^2}{4} \sum_\mu \left(\frac{1}{N_\uparrow} \int_V d^3r n_\uparrow(r) f_\nu(r) f_\mu(r) \frac{1}{\Delta_\uparrow - i\frac{\Gamma}{2}} \right) \alpha_\mu \\ - \frac{N_\downarrow \Omega_0^2}{4} \sum_\mu \left(\frac{\theta}{N_\downarrow} \int_V d^3r n_\downarrow(r) f_\nu(r) f_\mu(r) \frac{1}{\Delta_\downarrow - i\frac{\Gamma}{2}} \right) \alpha_\mu - i\sqrt{\kappa}\mathcal{F}_\nu \end{aligned} \tag{5.48}$$

with the spin population imbalance $\theta = N_\downarrow / N_\uparrow$. $\Delta_{\uparrow,\downarrow}$ denotes the detuning with respect to each ground state.

Once each coupling matrix is calculated for each of the spin state we solve the Heisenberg equation for various values of Δ_a and Δ_c, giving us the full transmission spectrum for $N_\uparrow = 9.1(7) \times 10^4$ and $N_\downarrow = 2(1) \times 10^3$ displayed in figure 5.8

We see that only the majority atomic states contributes. A very small anti-crossing remains at the location of the bare spin minority state. The dressed states show a large avoided crossing around the bare atomic state. The weak dressed state located in between the two atomic states in the two-component gas case has completely disappeared.

Dressed state spectrum

We first prepare an almost fully polarized Fermi gas with $N_\uparrow = 9.1(7) \times 10^4$ and $N_\downarrow = 2(1) \times 10^3$ (figure 5.9.a). As there is no s-wave scattering between identical fermions, this case realizes the simplest model with $N_\uparrow$ independent two-level systems that couple to the cavity modes. Figure 5.9.c shows the full transmission spectrum spanning 1.1 GHz around the atomic resonance. For each value of Δ_a we obtain a trace of the photon counter as depicted in figure 5.9.b at $\Delta_a = 0$ MHz as a function of Δ_c. For $\Delta_c > 0$ we observe one main transmission peak, while for negative values of Δ_c we observe multiple peaks due to the presence of the high-order modes. By compiling 111 of these photon counter traces for different values of Δ_a, we construct the full transmission spectrum as displayed in figure 5.9.c that can be compared with the spectrum obtained from the ab-initio calculation presented in the previous section. We observe a prominent anti-crossing around the bare atomic state $|\uparrow\rangle$ while the presence of a very small minority component leads to a small absorption at the location of the bare atomic state at $\Delta_a/2\pi = -38.4$ MHz. A peak in the transmission spectrum at $\Delta_c = 0$ is observed due to a small fraction of the light polarized linearly along the quantification axis because of the imperfect alignment of the probe beam

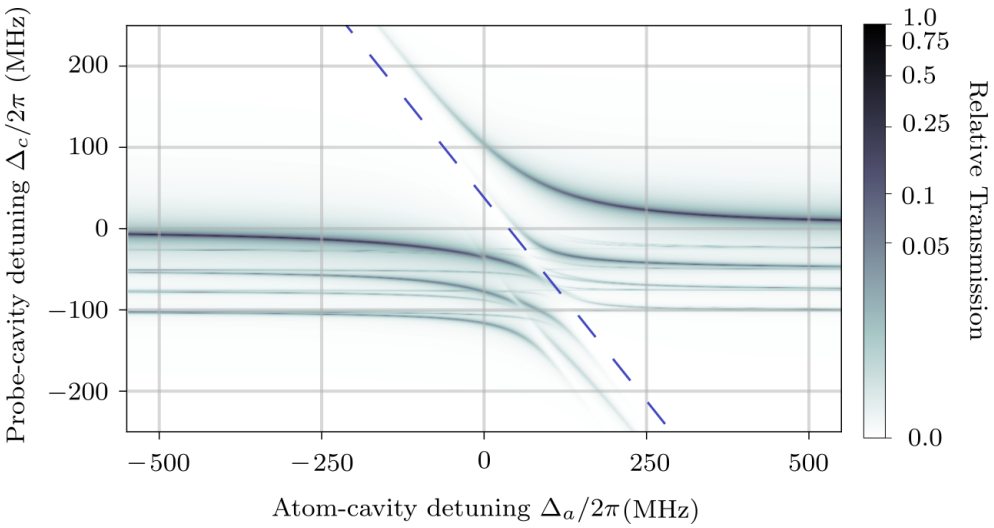

Figure 5.8: ***Simulation of the transmission spectrum for a spin-imbalanced Fermi gas.*** The figure shows the simulation of the transmission spectrum for a spin polarized Fermi gas comprising $N_\uparrow = 1 \times 10^5$ atoms in the majority spin component and $N_\downarrow = 3 \times 10^3$ in the minority spin component. The intensity of the cavity transmission is normalized by its maximum value and displayed in logarithmic scale. The blue dashed line indicates the position of the bare spin majority state. We observe two families of dressed states, above and below the bare atomic state.

polarization. This π-polarized light only couples to the the atomic transition $|2S_{1/2}, m_j = -1/2\rangle \longrightarrow |2S_{1/2}, m_j = -1/2\rangle$, located 1.56 GHz on the red-side of the σ^- transition. Thus this light is very weekly coupled to the atoms and appear close to $\Delta_c = 0$ for any value of Δ_a explored on this spectrum.

While we observe one main dressed state for positive valies of Δ_a and Δ_c, the spectrum displays a richer structure for negative values of δ_c as we observe the coupling to the high-order mode families due to the finite size of the cloud. We observe quite clearly the dressed state corresponding to the $\mathrm{TEM}_{(11)}$ mode family located around $\Delta_c/2\pi = -25$ MHz consistent with the ab-initio calculation. The coupling to the higher order mode families is less and less important for decreasing values of Δ_c. Regarding the variation of the intensity of the transmitted light, we can observe large intensities for large values of Δ_a when the dressed state is mainly of photonic nature. When the dressed states approach the atomic bare state the transmitted intensity decreases, as the dressed state becomes mostly of atomic nature.

5.4.3 *The spin-balanced unitary Fermi gas*

Calculation of the coupling matrix

We consider a spin-balanced unitary Fermi gas with 10^5 populating each spin state. The coupling matrix $K_{\mu\nu}$ can be written exactly as presented in 5.47 :

$$K_{\mu\nu} = \frac{-i}{N\delta} F(\delta) \int_V d^3r n(r) f_\nu(r) f_\mu(r) \tag{5.49}$$

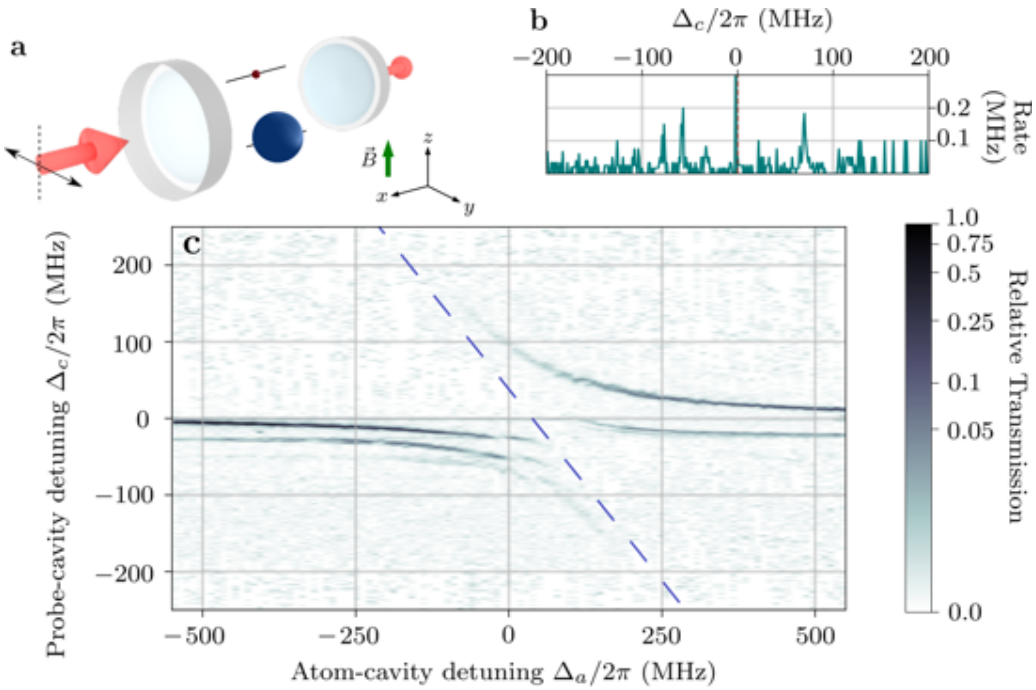

Figure 5.9: ***Transmission spectrum of a spin-polarized Fermi gas.*** **a-b** Schematic view of the experiment, the three relevant energy levels and cavity transmission signal, averaged over three realizations, as a function of $\Delta_c/2\pi$, for $\Delta_a/2\pi = 38.2\,\mathrm{MHz}$ for a spin-polarized Fermi gas with $N_\uparrow = 9.1(7)\times10^4$ and $N_\downarrow = 2(1)\times10^3$. **c** Coupled-system transmission spectrum as a function of $\Delta_c/2\pi$ and $\Delta_a/2\pi$ for the spin-polarized. The transmissions normalized by the maximum observed are displayed in logarithmic scale. The bare atomic transitions for $|\uparrow\rangle$ and $|\downarrow\rangle$ are shown with red and blue dashed lines, respectively.

with the function $F(\delta)$:

$$F(\delta) = \frac{\Delta}{\delta + \Delta - i\frac{\Gamma}{2}} + \frac{\Delta}{\delta - \Delta - i\frac{\Gamma}{2}} \tag{5.50}$$

In these expressions, δ corresponds to the detuning from the center of the two hyperfine states separated by Δ. The coupling matrix is finally a weighted average of the two coupling matrix of the atoms populating each ground state, with a weight corresponding to the relative frequency detuning.

Knowing the coupling matrix, the steady-state equation of motion reads,

$$\left(\delta_\nu - i\frac{\kappa}{2}\right)\alpha_\nu - i\frac{N\Omega_0^2}{4}\sum_\mu K_{\mu\nu}\alpha_\mu = i\sqrt{\kappa}\mathcal{F}_\nu \tag{5.51}$$

These equations are solved as a function of the cavity-probe detuning Δ_c and of the cavity-atom detuning $\Delta_a$to calculate the total DC field $\sum_\nu |\alpha_\nu|^2$. The point where $\Delta_a = 0$ corresponds to having the cavity resonance exactly placed in-between the two spin states. In figure 5.10 we show the spectrum obtained from the resolution of equation 5.51.

Dressed-state spectrum

We simulate the transmission spectrum for the spin-balanced unitary Fermi gas with $\Delta_{a/2\pi}$ spanning 550 MHz around the center of the two atomic ground states. Each ground state is equally populated with $N_\uparrow = N_\downarrow = 1 \times 10^5$. The result is shown in figure 5.10.

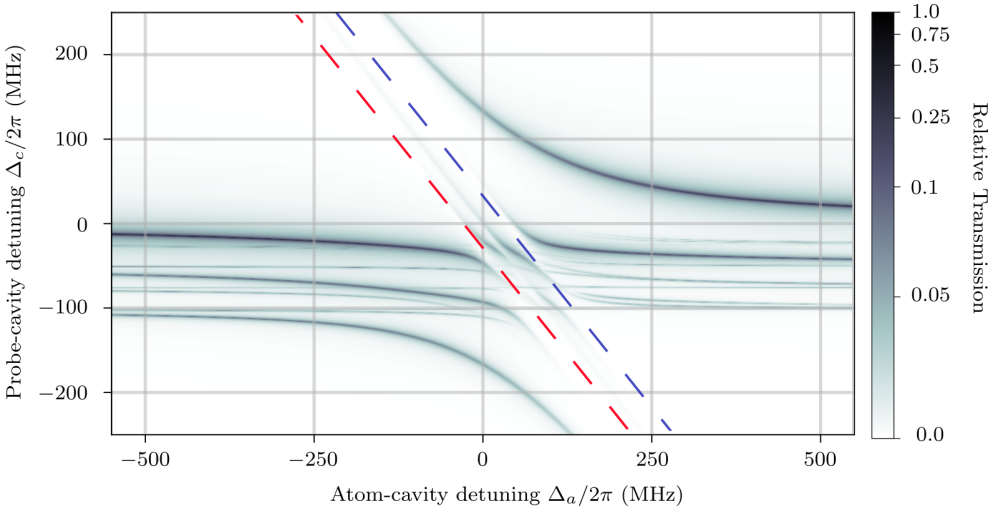

Figure 5.10: ***Simulation of the transmission spectrum for a spin-balanced unitary Fermi gas.*** The figure shows the simulation of the transmission spectrum for a spin-balanced unitary Fermi gas comprising $N_\uparrow = N_\downarrow = 1 \times 10^5$ atoms. The intensity of the cavity transmission is normalized by its maximum value and displayed in logarithmic scale. The blue and red dashed line indicate the position of the bare spin majority state. We observe two families of dressed states, above and below the bare atomic state, as well as a weak transmission signal in between the two bare atomic states.

The blue and red dashed lines in figure 5.10 represents the bare atomic states $|\uparrow\rangle$ and $|\downarrow\rangle$ respectively. The bare cavity mode corresponds to $\delta_c = 0$. We observe a similar behaviours compared with the single cavity mode spectrum with a large avoided-crossing when the dressed states approaches the bare atomic ones. When the value of Δ_a is large (positive or negative), the dressed states tends to correspond to the bare cavity modes. As we consider two atomic mode there is a third dressed state, located in-between the bare atomic ones, which as an transmission significantly smaller than the other dressed states due to the large Rabi frequency as explained when discussing the single cavity mode transmission spectrum.

The presence of the multiple transverse modes translates into the presence of many dressed states for $\delta_c < 0$. They correspond to the mixing of the two atomic modes with the ground cavity mode and the high order transverse mode families. Within a same mode family, we observe very different coupling strengths as pointed out when looking at the coupling matrix. Some of the dressed states are almost uncoupled until they reach the bare atomic states where we observe a small avoided crossings. Other dressed states of the same family start to show a larger coupling, thus showing a larger avoided crossing. The exact coupling of each mode within the same family is very sensitive to the cloud position with respect to the cavity mode center as we will discuss it later.

We consider the experimental transmission spectrum obtained for a spin-balanced unitary Fermi gas with a total atom number of 2×10^5 equally populating both spin states 5.11.a. The Fermi energy of the system is $E_F/\hbar = 53(5)$ kHz. In order to characterize its temperature we introduce a spin-imbalance following the procedure explained in Chapter 3, leading to two atomic densities in a single arm optical dipole as depicted in figure 5.7.c. The measurent of a temperature of $0.1\,T/T_F$ as well as the characteristic plateau in the integrated column density discussed in Chapter 4 confirms that the gas is in the superfluid regime [153, 158, 160, 161, 164, 192].

An example of a transmission trace acquired for a single realization at $\Delta_a = 0$ MHz is shown in figure 5.11.b. We can map out the entire transmission spectrum displayed in figure 5.11.c to compare it with the simulated spectrum presented in figure 5.10.

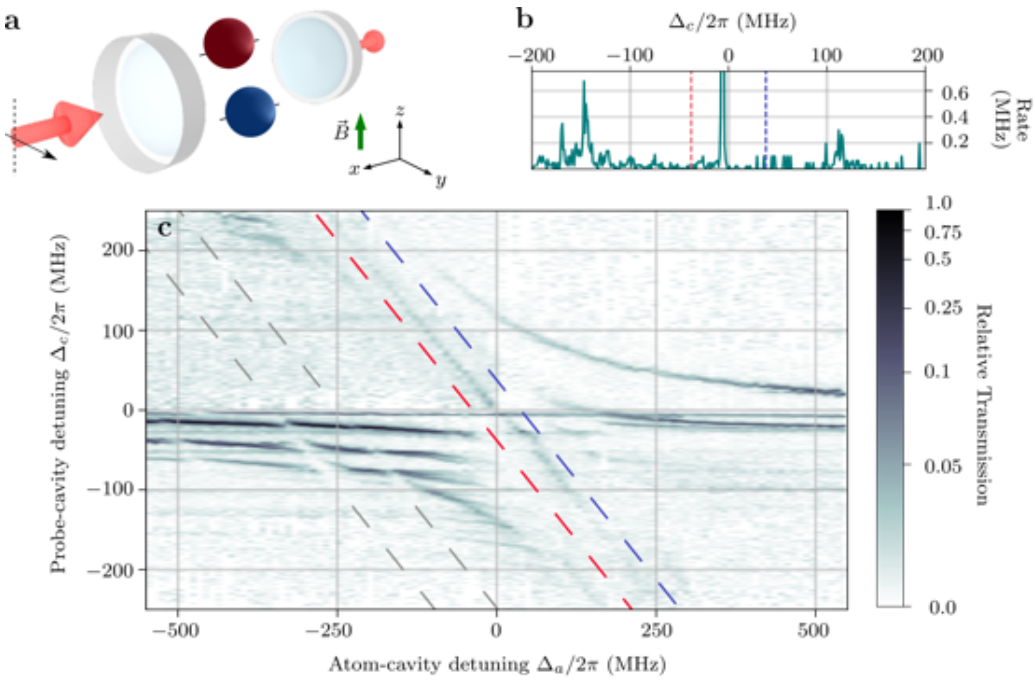

Figure 5.11: ***Transmission spectrum of a spin-balanced unitary Fermi gas.*** **a-b** Schematic view of the experiment, the three relevant energy levels and cavity transmission signal, averaged over three realizations, as a function of $\Delta_c/2\pi$, for $\Delta_a = 0$ for a spin-balanced Fermi gas of $2.0(1) \times 10^5$ atoms equally populating each spin state. **c** Coupled-system transmission spectrum as a function of $\Delta_c/2\pi$ and $\Delta_a/2\pi$spin-balanced Fermi gas **c**. The transmissions normalized by the maximum observed displayed in logarithmic scale. The bare atomic transitions for $|\uparrow\rangle$ and $|\downarrow\rangle$ are shown with red and blue dashed lines, respectively. The grey dashed lines indicate a weak contribution attributed to molecular states.

The main difference with the spectrum of the spin polarized gas consists in the existence of an extra dressed state in-between the two bare atomic states. Due to the large collective Rabi frequency of $2\pi \times 150$ MHz, its intensity is rather small as it is mostly of atomic nature for any values of Δ_a. The dressed states in the upper right and lower left quadrant show a large avoided-crossing when they approaches the bare atomic states. As the collective Rabi frequency is larger than the one of the spin-polarized case we

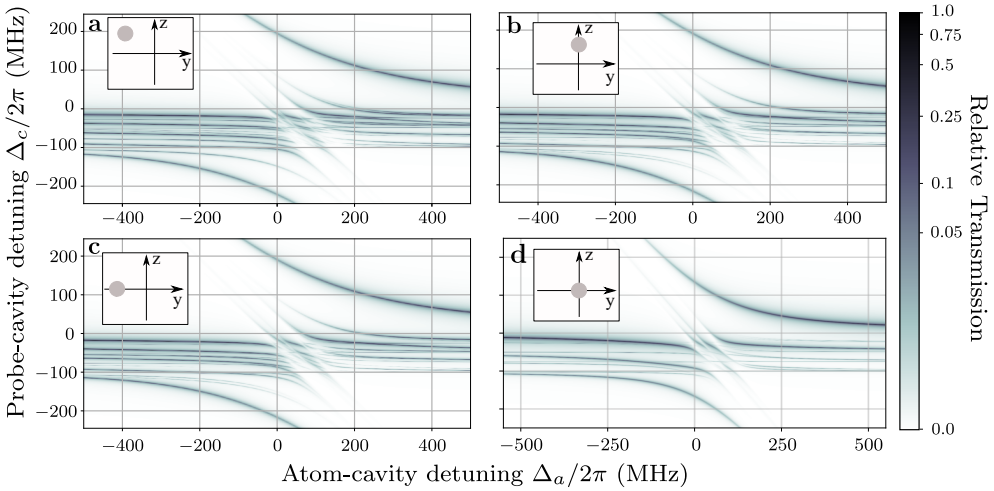

Figure 5.12: ***Effect of the cloud displacement on the trasmission spectrum of a spin-balanced unitary Fermi gas.*** The figure shows the simulation of the transmission spectrum for a spin-balanced unitary Fermi gas comprising $N_\uparrow = N_\downarrow = 1 \times 10^5$ atoms for different displacement from the center of the cavity mode. The intensity of the cavity transmission is normalized by its maximum value and displayed in logarithmic scale. textbfd Shows the spectrum in the case of a centred cloud. **b-c** show a displacement of 5 µm along the vertical and horizontal directions respectively. They show an identical transmission spectrum due to the symmetry of the TEM modes with these axes. **a** Shows the transmission spectrum when the cloud is displaced by 5 µm along both axis. We see that the main transmission branches are very weakly disturbed by any small displacement while the branches due to the high order modes, in the lower left quadrant, are qualitatively modified. We observe much more dressed states as the degeneracy between modes within the same family are lifted due to the symmetry breaking induced by the cloud displacement.

see a larger coupling to the transverse mode families of order 22, 33 and 44. The collective Rabi frequency $\Omega = 2\pi \times 150$ MHz leading to the large avoided-crossing validates that we are able to reach the strong collective coupling regime for the light-matter interaction.

We see that the ab-initio model reproduces well the main properties of the transmission spectrum obtained from the experiment. We will see in the next section that even at the quantitative level, the coupling to the ground mode is very well reproduced. However as it can be seen comparing the figure 5.11.c and 5.10, the exact locations of the dressed states mixing the high-order modes is only qualitatively reproduced. A quantitative comparison of the locations of these dressed states is not possible as they strongly depend on the exact location of the cloud on the transverse directions which we do not control at better than a few µm. Such a displacement would already lead to large quantitative modifications. In figure 5.12, we show how the spectrum is modified when the cloud is displaced by 5 µm along the two direction in the transverse plane. We see that the overall spectrum is very similar, but the details of which of the high order modes couple most is strongly affected. The optical dipole trap alignment is controlled up to a few µm as we can use the coupling to the fundamental mode to optimize it. However this shows very small variations for small displacements contrary to the behaviour of the high order transverse mode coupling, thus not guaranteeing a perfect alignment.

In figure 5.12 we observe that the main polaritons in the upper right and lower quadrant are almost not modified by introducing a small displacement of 5 µm along each axis. However, in the lower left quadrant we see that the coupling to the high-order modes for the displaced cloud (figure 5.12.a.b.c) is reduced compared with the cloud centered on the cavity mode (figure 5.12.d). Moreover we observe much more branches when the cloud is displaced, as a small displacement lift the degeneracy within a same mode family. At a qualitative level we see that a the simulated transmission spectra looks more similar to the experimental one, consistent with the fact that we do not control the cloud position at the few µm level.

5.4.4 *Coherent scaling with the number of atoms*

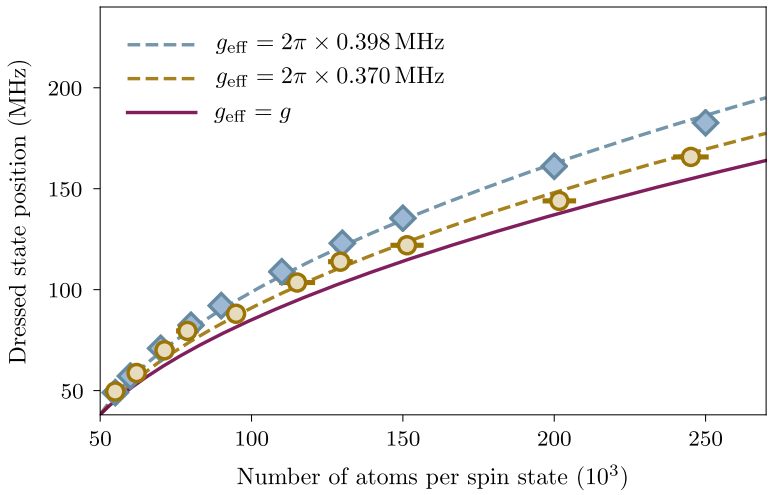

Figure 5.13: ***Scaling of the dressed state frequency with atom number.*** Position of the upper dressed state as a function of atom number in each spin state for a spin-balanced gas, with $\Delta_c > 0$ and $\Delta_a = 0$. Yellow circles show experimental data and light blue diamonds are obtained from the ab-initio theory calculation accounting for all the high-order cavity modes. The lines describe an analytical model with two atomic states and the TEM_{00} cavity mode only. The dashed lines are fits of both experimental data (yellow circles) and theory calculation (light blue diamonds) with g_{eff} as a free parameter (see text). The violet solid line is the expected scaling for $g_{\text{eff}} = g = 2\pi \times 0.339$ MHz. Error bars are given by the statistical fluctuations over 10 realizations.

In order to verify the coherent nature of the light-matter coupling we want to measure the scaling of the Rabi frequency of this coupling with the number of atoms. As all the atoms would get coherently coupled to the cavity field we expect to observe the square root scaling of g with the number of emitters, reminiscent of the Tavis-Cummings Hamiltonian. To do so we track the position of the upper dressed at $\Delta_a = 0$ MHz as a function of the total atom number for a spin-balanced gas. We present the scaling of the dressed state position in figure 5.13 together with the scaling obtained from the ab-initio model accounting for the presence of the high-order modes. In order to provide a comparison we also shows the scaling expected expected in the case of a single cavity mode, derived from the standard Tavis-Cummings model. Both the theory curves and the data are fitted with a square root law $\sqrt{g_{\text{eff}}^2 N + \frac{\Delta_{\text{HF}}^2}{4}}$ describing the two equally populated spin states uniformly

coupled to a single cavity mode with an effective coupling strength g_{eff} that is the free parameter of the fit procedure. We obtain $g_{eff}/2\pi = 0.370$ MHz and $g_{eff}/2\pi = 0.398$ MHz for the data and the ab-initio model respectively. They are 8% and 16% larger than g respectively, due to the coupling to the high order modes. This contribution is most likely overestimated from the model as it considers a perfectly centred cloud on the cavity mode. This would explain the slightly smaller value obtained from the measurement where the cloud is probably slightly shifted with respect to the cavity mode center.

We see that in addition of reproducing well the general features of the transmission spectrum, the model also is in quantitative agreement with the data concerning the effective light-matter coupling strength, which is modified by the presence of the higher-order mode compared with the one expected from a single mode Tavis-Cummings model. However, the presence of small avoided-crossings in the measured spectrum, indicated by the grey dashed lines in figure 5.11.c, is not explained by the ab-initio model.

5.5 CONCLUSIONS AND OUTLOOKS

We have seen that we can reach the strong coupling regime both for a spin-balanced unitary Fermi gas and a spin-polarized non-interacting Fermi gas. We have simulated the coupling to the high-order transverse mode families and reached a qualitative understanding of this coupling even if the limited knowledge of the location of the cloud limits any quantitative comparison. We have measured the square root scaling of the Rabi frequency with the total atom number, confirming the coherent coupling of the atoms of the gas with the cavity light field as predicted by the Tavis-Cummings model. We could compare the scaling between the experiment, the simulation and a single cavity mode model. We have extracted an effective coupling strength g_{eff} to the fundamental mode, accounting for the effect of the high-order transverse modes. It leads to a slightly larger coupling strength as predicted by the multimode model, in very good agreement with the experiment. The realization of a strongly interacting Fermi gas strongly coupled to light opens up a large variety perspectives such as engineering long-range interaction mediated by the cavity photons [180, 181], creating new phases of matter [177, 191, 193–198] , leveraging the cavity field to perform weakly destructive measurements [182, 199–203] and controlling atom-atom interactions with cavity photons [204–208]

However, we also observed smaller avoided-crossing for negative values of Δ_a where no atomic state exist (figure 5.11). This feature is only present in the case of a spin-balanced Fermi gas, and greatly suppressed for a single component non-interacting Fermi gas. This difference shows that these transitions are sensitive to the presence of two interacting spin states in the gas. We attribute this to the coupling to photoassociation transitions into a weakly bound-state of the $2S_{1/2} + 2P_{3/2}$ asymptotic potential. Even if the existence of this transitions is not particular to the presence of strong interaction nor to the fermionic nature of the atoms, the coupling to these transitions should be strongly influenced by the pre-existent pair-correlations in the unitary Fermi gas. The study of the coupling to photoassociation transitions and its intimate relation to the many-body nature of the unitary Fermi gas will be explored in the following chapter.

6

QUANTUM OPTICS WITH MANY BODY EXCITATIONS : FERMION-PAIRS POLARITON

In this chapter I will discuss how we address photoassociation (PA) transitions in a strongly correlated two-component Fermi gas with photons in a high-finesse cavity. Our experiment brings PA into the strong coupling regime, where the interaction between photons and atom pairs overcomes all dissipative processes. In such a regime, pairs, molecules and cavity photons coherently hybridize into composite quasiparticles: pair polaritons. These coherent excitations inherit from their photonic component the fast dynamics of the resonant light–matter interaction, much faster than that of the many-body physics in the gas, and a weak dissipation channel into the environment enabling direct optical detection. From their matter part, they inherit the universal properties of the short-distance pair correlations of the quantum gas, which get imprinted onto the optical spectrum.

CHAPTER CONTENTS

The results presented in this chapter closely follow the publication [1] :

H. Konishi*, K. Roux*, V. Helson ans J.-P. Brantut
Universal pair polaritons in a strongly interacting Fermi gas
Arxiv 2103.02459
to appear in *Nature*

6.1 MOTIVATION

One of the most striking successes of quantum science is the ability to engineer the interaction between light and matter, culminating with the strong

1 Parts of this chapter are directly taken from this publication

coupling regime in cavity quantum electrodynamics (QED) [171, 172]. Cavity QED is already a corner stone of quantum networks [36] and quantum information processing [209]. It is now emerging as a new tool for quantum simulation with quantum gases [1], where it provides unique features such as long-range, collective interactions [42, 45, 46, 210, 211], controlled dissipation enabling novel non-equilibrium dynamics [212] and real-time readout [213]. However, the light–matter interaction has been so far limited to the dipole coupling with single atoms, which dominates the energy scales of quantum gases by several orders of magnitudes. As a result, an interplay between many-body physics in a quantum gas and light–matter interactions could only be observed in the dispersive regime[1], effectively scaling down the light–matter interaction to match that of the motional degrees of freedom of atoms.

In a many-body system in free space, it is well known that photons can not only be absorbed and reemitted by individual atoms, but also exchanged between atoms, yielding a dipole-dipole interaction. Excited molecular states then form in the attractive branches of this interaction potential, yielding photo-association (PA) resonances in the optical spectrum [214]. When driving such a PA line, photons couple directly to pairs of free atoms separated by a distance R_C, the Condon length of the target molecular state, much shorter than typical inter-atomic distances in quantum gases. PA has been used for pair correlation measurements [72, 215–219], however only through losses in the incoherent regime. Coherent Rabi oscillations on ultra-narrow PA transitions have been observed in weakly interacting gases of two-electron atoms [220, 221].

6.2 PHOTOASSOCIATION OF ^{6}LI ATOMS AT LARGE MAGNETIC FIELD WITH A CAVITY

6.2.1 Introduction to photoassociation : simplest model

We first want to understand the interaction between two atoms sharing an optical excitation. As we have seen in Chapter 4, two atoms in their ground state interact via a Van der Waals potential $V(r) = C_6/r^6$ with $C^6 \propto (\Gamma/\omega)(\Gamma/k^2)$ with Γ the linewidth of the excited state, ω the reduced frequency of the atomic transition and k the wavenumber. In this section we will follow the same reasoning to derive the interaction potential for two atoms sharing one optical excitation [139].

We consider two atoms A, B with a ground state of angular momentum $L = 0$. The excited state is defined by $L = 1$, thus three-fold degenerate for the three possible projections of the orbital angular momentum along the quantization axis z, $m_L = -1, 0, 1$. We consider one of the two atom in its excited state leading to a Hilbert space of dimension 6 describing the system $\{|g; e_\alpha\rangle, |e_\alpha, g\rangle\}$ with $\alpha = x, y, z$ the space dimensions. In the absence of perturbation these states are degenerate. For this calculation, we take the inteparticle axis to be aligned with the quantization axis along z. We consider the electric dipole-dipole potential between the two-atoms described in the same basis

$$\hat{U}_{dip} = \frac{e^2}{r^3}\left[\hat{x}_A\hat{x}_A + \hat{y}_A\hat{y}_A - 2\hat{z}_A\hat{z}_A\right] \tag{6.1}$$

with $\hat{x}_i$ the position operator for each atom.

Calculating the coupling matrix elements of these interaction potentials shows that for a given α the only non-zero terms of the first order perturbation are

$$\langle g; e_\alpha | \hat{U}_{dip} | e_\alpha; g \rangle \tag{6.2}$$

Diagonalizing this matrix, we find two sets of eigenenergies using the Born-Oppenheimer approximation. First, for $\alpha = x, y$, which are two-times degenerate due to the rotational invariance with respect to the quantization axis :

$$E = \pm \frac{3}{4} \frac{\hbar\Gamma}{(kr)^3} \tag{6.3}$$

associated to the eigenstates $\frac{1}{\sqrt{2}} \left(|e_{x/y}; g\rangle \pm |g; e_{x/y}\rangle \right)$.

Second along the quantization axis, for $\alpha = z$

$$E = \pm \frac{3}{2} \frac{\hbar\Gamma}{(kr)^3} \tag{6.4}$$

associated to the eigenstates $\frac{1}{\sqrt{2}} (|e_z; g\rangle \mp |g; e_z\rangle)$.

We can rewrite the eigenstates of the two atoms using the standard molecular spectroscopy notation for states of the from $|L, m_L, S, m_s\rangle$. Regarding the electronic spin for the triplet state, the total spin is $S = 1$ with projections $m_s = -1, 0, 1$. As the excited state has an orbital angular momentum $L = 1$, the possible projections are $m_L = -1, 0, 1$. States with $m_L = 0$ are labelled Σ while states with $m_L = \pm 1$ will denoted Π. Moreover they will be labelled by their total spin S and their symmetry denoted $\sigma = u, g$ for the gerade and ungerade symmetries in such a way that the states reads

$$|1, \pm 1, S, m_s\rangle \longrightarrow^{2S+1} \Pi_\sigma \tag{6.5}$$

and

$$|1, 0, S, m_s\rangle \longrightarrow^{2S+1} \Sigma_\sigma \tag{6.6}$$

With this notation, we attribute the eigenenergies to the corresponding eigenstates

$$\begin{cases} +\frac{2C_3}{R^3} & \longrightarrow {}^1\Sigma_g, {}^3\Sigma_u \\ +\frac{C_3}{R^3} & \longrightarrow {}^1\Pi_u, {}^3\Pi_g \\ -\frac{C_3}{R^3} & \longrightarrow {}^1\Pi_g, {}^3\Pi_u \\ -\frac{2C_3}{R^3} & \longrightarrow {}^1\Sigma_u, {}^3\Sigma_g \end{cases}$$

The eigenenergies are displayed in figure 6.1 as a function of interatomic distance, with an additional term accounting for the hard-core repulsion between the two-atoms at short distances. As we observed for two ground state atoms, two atoms and one optical excitation create an interaction potential scaling with $1/r^3$, as expected for a dipole-dipole interaction. For this simple model we see that two potentials are repulsive while the two others are attractive, as they lower the energy of the atom-pair compared with the non-interacting case given by the large distance limit on figure 6.1. The two attractive potentials support bound states and have a non-zero coupling to the ground state $|g; g\rangle$ via the dipole potential, thus it is possible to create molecules in these potentials by shining a laser onto two free atoms. This process is called photoassociation.

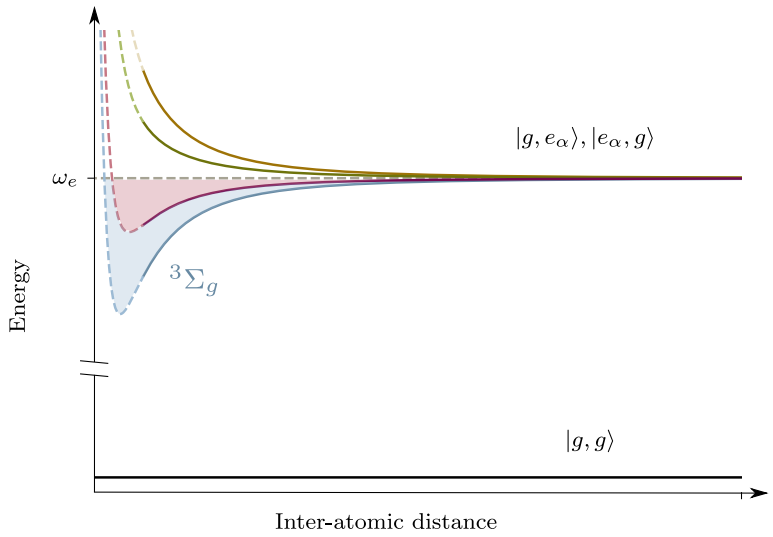

Figure 6.1: ***The simplest model for photoasociation : two-atoms and one optical excitation.*** The figure displays the interaction potential between two atoms sharing one optical excitation. The orbital angular momentum $L = 1$ of the excited state $|e_\alpha\rangle$ of both atoms leads to the presence of four states, degenerate in the absence of interactions. The solid lines represents the C_3/r^3 dipole-dipole interaction potentials combined with a hard core repulsion potential for short distances (dashed lines). Two potentials are repulsive while the two other are attractive and support bound states (shaded areas) where molecules composed of two atoms and one optical excitation can form.

Comparing this interaction potential with the Van der Waals potential derived for two ground state atoms, we see that the spatial dependence is different as the dipole-dipole interaction appears to the first order of perturbation while the Van der Waals interaction potential is a second order term. The dipole-dipole potential has a longer range as it scales with C_3/r^3 compared with the C_6/r^6 of the Van der Waals potential. Moreover, we can obtain a simple expressions in this model for the $C_6 \propto \frac{\Gamma}{\omega}\frac{\Gamma}{k^6}$ and $C_3 \propto \frac{\Gamma}{k^3}$ coefficient [139]. As $\frac{\Gamma}{\omega} \sim 10^{-7}$ for usual atomic transitions, the strength of the dipole-dipole interaction is stronger than the one of the Van der Waals interaction for the ground state atoms. This model gives a simple understanding of the concept of PA : two atoms sharing an optical excitation can form a molecule in one of the bound states of the attractive potential due to the dipole-dipole interaction. This technique is experimentally used in many laboratories to create ultracold gases of dipolar molecules [59, 222–228] and have been extensively studied over the last 30 years for many atomic species [214, 229–235]. In this work, we study this phenomenon in the regime of the BEC-BCS crossover of ^{6}Li, thus at large magnetic field, in the so called Pashen-Back regime [72, 215].

6.2.2 *Going further the simplest model*

The calculation of dipole-dipole interaction potentials between two atoms sharing an optical excitation represents a complex problem when it comes to account for the actual internal structure of the atom and to consider this problem in the regime of large magnetic fields [214]. In this section, I will

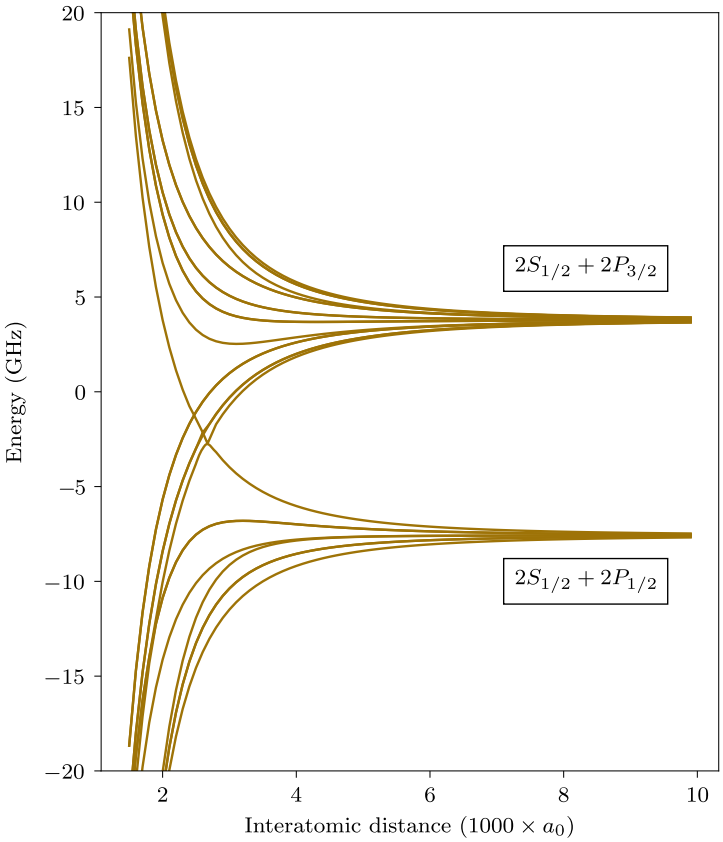

Figure 6.2: ***Interaction potential accounting for the spin-orbit interaction.*** The calculation of the interaction potential between two ^{6}Li atoms accounting for the fine structure leads to the presence of 16 interaction potentials (solid lines). Potentials emerge from both the asymptotic $2S_{1/2} + 2P_{3/2}$ and $2S_{1/2} + 2P_{1/2}$ potentials. Below the frequency of the bare $2S_{1/2} + 2P_{1/2}$ potential the attractive branches of both fine structure states mixes.

discuss the two problems to tackle, starting with the actual internal structure of ^{6}Li and zero bias magnetic field.

As it has been presented in Chapter 2, the ground state of ^{6}Li is a $2S_{1/2}$ state, thus $L = 0$ and $S = 1/2$ leading to $J = 1/2$. Concerning the excited state, the situation becomes more complex as we have to consider two excited states due to spin-orbit coupling. The first one, corresponding to the D_1 line, is the $2P_{1/2}$ state with $L = 1$ and $S = 1/2$ leading to $J = 1/2$. The second, corresponding to the D_2 line, is the $2P_{1/2}$ state with $L = 1$ and $S = 1/2$ leading to $J = 3/2$.

It is possible to derive the interaction considering the two PA cases with two atoms in the state $2S_{1/2} + 2P_{1/2}$ and $2S_{1/2} + 2P_{1/2}$. The spin-orbit coupling Hamiltonian for two atoms reads $\hat{H}_{SO} = C(\hat{\vec{l}}_A \cdot \hat{\vec{s}}_A) + C(\hat{\vec{l}}_B \cdot \hat{\vec{s}}_B)$ with:

$$C(\hat{\vec{l}} \cdot \hat{\vec{s}}) = C\left(\hat{l}_x\hat{s}_x + \hat{l}_y\hat{s}_y + \hat{l}_z\hat{s}_z\right) = C\left(\frac{1}{2}(\hat{l}_+\hat{s}_- + \hat{l}_-\hat{s}_+) + \hat{l}_z\hat{s}_z\right) \quad (6.7)$$

with $\Delta_{FS} = 3C/2$ defined with respect to the fine splitting Δ_{FS}. The operators $\hat{\vec{l}}_{A/B}$ act on the orbital angular momentum of atom A and B while

$\hat{\vec{s}}_{A/B}$) act on their respective electronic spin. $\hat{l}_\pm = \hat{l}_x \pm i\hat{l}_y$ and $\hat{s}_\pm = \hat{s}_x \pm i\hat{s}_y$ respectively increase or lower the value of the projection of the orbital angular momentum of the electronic spin.

We apply this Hamiltonian to the 24 states describing the two atomic excited states in the basis $|L, m_L, S, m_s\rangle$. Reorganising the 24 states by the projection of the total angular momentum J, denoted Θ, the matrix is diagonal by block

$$\begin{cases} \Theta = 2 \rightarrow \begin{cases} g \rightarrow |1111\rangle, |1-11-1\rangle \\ u \rightarrow |1111\rangle, |1-11-1\rangle \end{cases} \\ \Theta = 1 \rightarrow \begin{cases} g \rightarrow |1100\rangle, |1110\rangle, |1011g\rangle, |1-100\rangle, |1-110\rangle, |101-1\rangle \\ u \rightarrow |1100\rangle, |1110\rangle, |1011\rangle, |1-100\rangle, |1-110\rangle, |101-1\rangle \end{cases} \\ \Theta = 0 \rightarrow \begin{cases} g \rightarrow |1000\rangle, |1010\rangle, |1-111\rangle, |111-1\rangle \\ u \rightarrow |1000\rangle, |1010\rangle, |1-111\rangle, |111-1\rangle \end{cases} \end{cases}$$

The result of this calculation showing the interaction potential with the contribution from spin-orbit coupling is shown in figure 6.2. For $\Omega = 1, 2$ we observe that states come into pairs, since the projection onto the z axis can be either positive or negative. Since nothing breaks this symmetry, the potentials corresponding to these states are exactly degenerate. They will not be coupled by any term in the Hamiltonian. For $\Omega = 0$, the wavefunction of the molecular state is not enforced on the $|L, |m_L|, S\Sigma, m_s\rangle$ basis, so linear combinations of states within each of the $0_{g/u}$ manifolds have to be formed.

We observe 16 potentials, as some of them are degenerate due to the symmetries of the system. The calculation of these potentials already emphasizes a complicated situation, as all these potentials support bound states corresponding to the rotational and vibrational modes of the molecules. The good quantum number to describe these states depends on the binding energies compared with the other typical energy scales of the problem such as the fine splitting.

In the case of large magnetic fields it becomes even more complicated to obtain analytic expressions for the interaction potentials as the magnetic field couples to all angular momenta at different orders (dipolar, quadrupolar...). It is however possible to use numerical methods developed to calculate the interaction potentials between Rydgerg atoms [236] in order to obtain the potentials at 832 G as shown in figure 6.3

Among all potentials, we count 12 attractive ones, each of them supports bound states corresponding to different rotational and vibrational states of the molecules. The actual description of these bound states requires to account for the hybridization of the different dipole potentials at short distances. It becomes evident that having predictions on the position of the bound states is difficult. In this regime, the fine structure splitting, the Zeeman energy and the vibrational level spacings are comparable, thus preventing simple perturbative treatments.

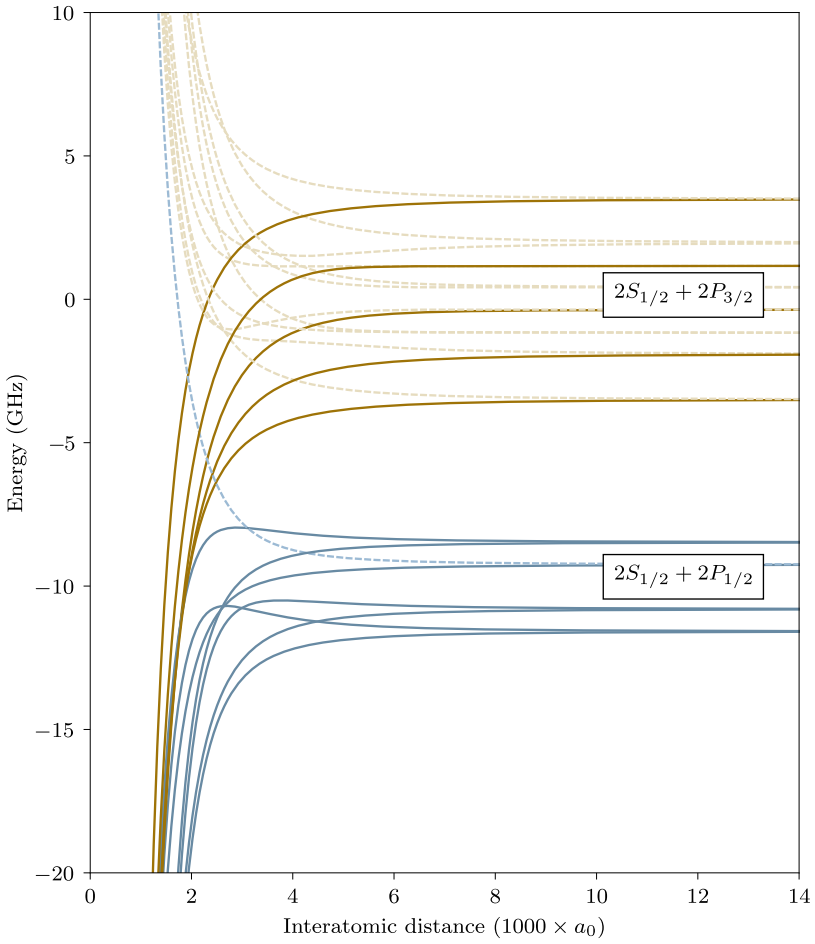

Figure 6.3: ***Numerical calculation of the interaction potentials at large magnetic field.*** Numerical simulation of the interaction potential between two ^{6}Li atoms at 832 G obtained from the Rydberg simulation code described in [236]. Blue and yellow solid lines corresponds to the asymptotic potentials $2S_{1/2} + 2P_{3/2}$ and $2S_{1/2} + 2P_{1/2}$ respectively. The solid lines show the attractive potentials while the dashed ones indicates the repulsive branches of the dipole-dipole interaction. Above the $2P_{1/2}$ we can easily attribute the potential to the $2S_{1/2} + 2P_{3/2}$ asymptotic potential while for red detunings with respect to the $2P_{1/2}$ state, they all overlap with each other making any experimental conclusion difficult when performing spectroscopic measurement in this region of detunings.

6.3 STRONG LIGHT-MATTER COUPLING TO PHOTOASSOCIATION TRANSITIONS

6.3.1 *Observing strong coupling regime on PA transitions with cavity transmission spectroscopy*

Probing method

We probe the PA states using the same transmission spectroscopy technique as presented in Chapter 5. We mode match the probe laser with the TEM_{00} mode of the cavity. As PA transitions correspond to bound states of the interaction potential, the laser frequency to address them, ω_{PA}, is smaller than the frequency of the bare atomic transition ω_0. We vary the detuning

between the cavity resonance frequency and the atomic bare frequency transition Δ_a, as well as the detuning between the cavity resonance frequency and the probe laser frequency Δ_c.

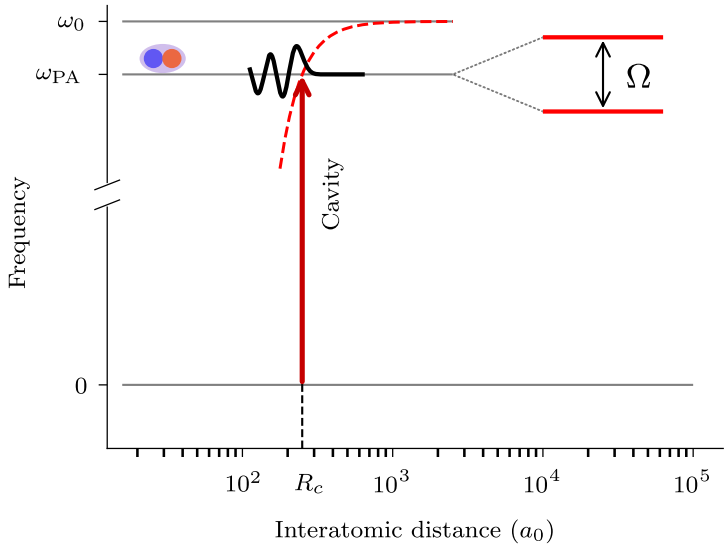

Figure 6.4: ***Dressing the PA bare transitions with cavity photons.*** Sketch of the cavity assisted PA process. The figure shows the wavefunction of a molecular state (solid black line) at the frequency ω_{PA} bound in a molecular potential (red dashed line) asymptotically reaching the single atom transition frequency ω_0. The cavity photons at frequency ω_{PA} induce transitions between free atoms and molecular states at the Condon point R_C. The collective Rabi frequency Ω of the process exceeds the rate of dissipation yielding a pair of resolved dressed states in the spectrum.

As presented in figure 6.4, we expect the PA transitions to be dressed by the cavity field. If the collective Rabi frequency between the PA transition and the cavity field Ω is large enough, meaning that it is larger than both the cavity decay rate κ and the linewidth of the excited molecular state Γ_m, we expect to observe avoided crossings in the spectrum. This would confirm that we reach the strong coupling regime on these molecular transitions as the small avoided crossings already observed in Chapter 5. As the targeted molecular states correspond to high vibrational states, the corresponding wavefunctions are described with an Airy function, centred on the classical turning point of the interaction potential. This specific point is the Condon radius R_C. Outside the potential, the wavefunction vanishes exponentially while the high vibrational states leads to fast oscillations at short distance in the potential. The structure of the wavefunction relates directly to the Franck-Condon principle: the transition matrix element to one of these excited molecular states is most sensitive to the value of the molecular wavefunction at distance R_C that depends on the C_3 coefficient of the potential and on the binding energy of the targeted molecular state. Thus, as a first approximation, we can linearise the dipole potential in the vicinity of the Condon radius in order to calculate the width L of the central lobe of the Airy function.

A journey in the jungle of PA transitions

We measure the transmission spectra for a spin-balanced unitary Fermi gas, spanning Δ_a between -15 GHz and $+4.5$ GHz around the atomic transition

$|2S_{1/2}, m_j = -1/2\rangle \rightarrow |2P_{3/2}, m_j = -3/2\rangle$ that is located at $\Delta_a = 0$. The probe laser is linearly polarized perpendicularly to the quantization axis, set by the large magnetic field. Hence, we mainly address atomic transitions driven by circularly polarized light. However, due to imperfect polarization alignment, a small fraction of the light also couples to atomic transitions driven by linearly polarized light along the quantization axis. The measured spectrum for a balanced unitary Fermi gas comprising $N = 10^5$ atoms is displayed in figure 6.14.

We observe large avoided crossings due to the coupling of the different transitions both on the D_1 and D_2 lines. The blue dashed lines indicate the transitions driven by circularly polarized light, while the red ones indicate the transition driven by the weak component of the probe linearly polarized along quantization axis. For negative values of Δ_c, close to the atomic resonance, we observe several transmission branches due to the multimode structure of the cavity, as explained in Chapter 5. The very interesting feature here is that we observe about 22 smaller avoided crossing or absorption line in regions of the spectrum where no atomic transitions are present (figure 6.14). All these lines are bound states in the attractive dipole-dipole potentials, each of them being an excited molecular bound state.

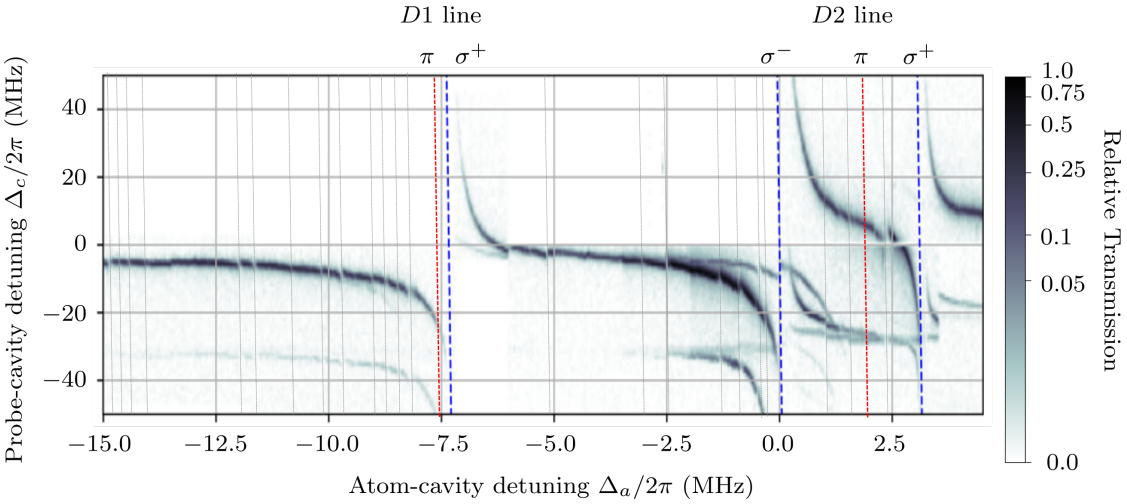

Figure 6.5: ***Cavity transmission spectroscopy of PA transitions around the D2 and D1 line of ^{6}Li.*** The figure shows the transmission spectrum spanning −15 and +4.5 GHz around the $|2S_{1/2}, m_j = -1/2\rangle \rightarrow |2P_{3/2}, m_j = -3/2\rangle$ transition (denoted σ^-). As the probe beam is horizontally polarized in the perpendicular plane with respect to the quantization axis, it mainly addresses the atomic transition driven by circularly polarized light ($\sigma^\pm$) with a weak polarization component of the probe addressing the atomic transition driven with linearly polarized light (π). The transmission is normalized by its maximum and displayed in logarithmic scale. The atomic transitions on the D1 and D2 lines dominate the spectrum with large avoided crossings. Multiple small avoided crossing can be observed, corresponding to molecular bound states addressed by PA (grey dashed lines).

As expected, we observe no coupling to PA transitions on the blue side of the $|2S_{1/2}, m_j = -1/2\rangle \rightarrow |2P_{3/2}, m_j = 1/2\rangle$ driven by the σ^+ polarization component of the probe beam. As each of the PA states are bound states in the interaction potential, their transition frequencies are smaller than the bare atomic transition. For the other atomic transitions, some of

these PA lines are located on the red side of the $|2S_{1/2}, m_j = -1/2\rangle \rightarrow |2P_{3/2}, m_j = 1/2\rangle$ and on the blue side of the other atomic transitions. This makes it complicated to identify which PA transitions correspond to which interaction potential, as they all mix when going from frequencies Δ_a far on the red side of all atomic transitions.

It is noticeable that the coupling to the high-order transverse modes (here located at $\Delta_c = -25$ MHz) decreases when going far on the dispersive regime. This can be understood by considering the collective coupling in the dispersive regime given by Ng_0^2/Δ_a. For large values of Δ_a, the coupling to the fundamental mode is reduced, as well as the coupling to the high-order transverse modes. Hence, the scattering from the ground mode to these higher order ones is reduced by about 2 order of magnitude when going at about 2 GHz from the atomic transition. As the coupling to the PA lines is smaller than the frequency separation between the transverse modes, they can be ruled out, thus only considering the atomic coupling to the fundamental mode of the cavity.

Detailed study of some PA lines

We now study in particular four PA transitions. For these we use a probe beam polarized linearly along the quantization axis (figure 6.6.a). In this configuration we only couple to two atomic transitions, one on the D_2 line $|2S_{1/2}, m_j = -1/2\rangle \rightarrow |2P_{3/2}, m_j = -1/2\rangle$ and one on the D_1 line, $|2S_{1/2}, m_j = -1/2\rangle \rightarrow |2P_{1/2}, m_j = -1/2\rangle$. We measure the transmission spectrum of a balanced-unitary Fermi gas comprising $N = 4.6 \times 10^5$ atoms at $T/T_{TF} = 0.08(2)$. The frequency of the probe beam is swept over 40 MHz in 500 µs. This sweep rate is fast enough compared with the dynamical timescale of the gas that we can consider the cloud fixed during the measurement, light being present in the resonator for about 12.5 µs. The decay rate of the cavity field $\kappa/2\pi = 77$ kHz while the coupling strengths to the two atomic transitions are $(g_{D1\pi}, g_{D2\pi})/2\pi = (276, 390)$ kHz.

The four PA transtions are denoted PA1,2,3 and 4 respectively (figure 6.6.a). PA transitions 1, 2 and 3 are located between the D1 and D2 lines at $\Delta_a/2\pi = -2.03, -3.21, -4.99$ GHz from the continuum (figure 6.6.a.b). The fourth transition PA4 is located further on the red side of the D1 line, at $\Delta_a/2\pi = -25.998$ GHz (figure 6.6.a) and corresponds to bound states in the $1^3\Sigma_g^+$ potential [237], for the vibrational level $\nu = 81$.

We first take a close look at the transmission spectrum of the first three PA transitions spanning 6 GHz on the red side of the $|2S_{1/2}, m_j = -1/2\rangle \rightarrow |2P_{3/2}, m_j = -1/2\rangle$ transition (figure 6.6.a). A zoom on each transition is shown in figure 6.6.c.d.e respectively. These bound states belong to the asymptotic potential $2S_{1/2} + 2P_{3/2}$, thus we can deduce the Condon radius of each bound state from their detuning from the continuum using the Leroy-Bernstein formula. We obtain $R_C = 244a_0, 210a_0, 181a_0, 164a_0$ for PA1-PA4, respectively.

For PA1-PA3 shown in figure 6.6.b.c.d.e, we clearly observe the characteristic avoided crossing we expect when the system is in the strong coupling regime. We will see now how we can extract from such spectra the Rabi frequency Ω giving the coupling between the cavity field and the different PA transitions.

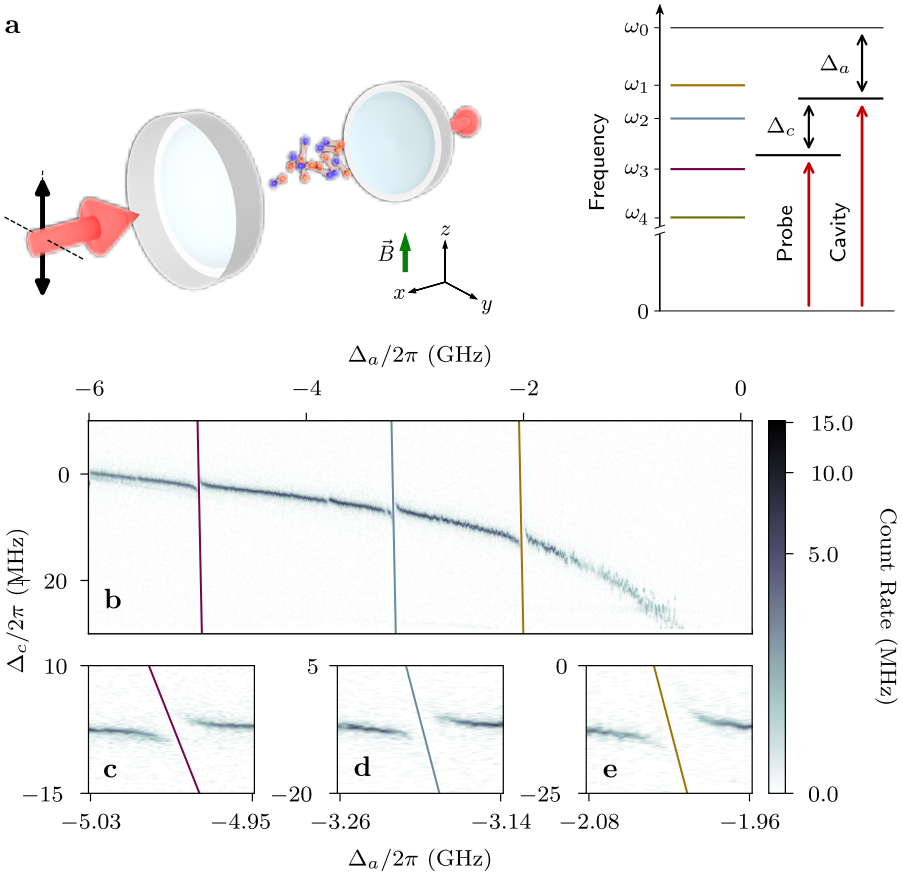

Figure 6.6: ***Cavity transmission spectroscopy : revealing the strong coupling regime between PA transitions and light.*** **a** A degenerate, strongly interacting two-component Fermi gas is placed inside a cavity. A beam linearly polarized along the bias magnetic field $\vec{B}$ measures the transmission through the cavity. **b** Frequency diagram relevant for the experiment. We address four PA transitions at ω_1, ω_2, ω_3 and ω_4 below the single atom D2 π-transition at ω_0. The cavity–atom and probe–cavity detunings Δ_a and Δ_c are independently controlled by tuning the cavity resonance and the probe frequency. **c** Cavity transmission spectrum of a unitary Fermi gas below the D2 π-transition. The solid lines indicate three PA transitions labeled as 1, 2 and 3 as in panel b. A few narrower PA signals can also be seen, which we attribute to PA into other interaction potentials. **c–e** Close up view in the vicinity of the three PA lines showing avoided crossing patterns.

Extracting the Rabi frequency from the spectra

To extract the value of the Rabi frequency from the spectra we need to fit a theoretical model to the data. Thus, we have to find the proper way to treat the coupling to the atomic transitions and the coupling to the molecular ones. Each of the avoided crossing appears on top of the atomic signal that shifts the transmission peaks to negative values of Δ_c compared with the bare cavity located at $\Delta_c = 0$. The purely atomic contribution is then just an offset of the polariton due to the dispersive coupling to the atomic transitions. The slope of the polariton over the typical extent of the PA avoided crossing, which is about 100 MHz (figure 6.6.c.d.e), can be written as $\frac{N g_{D2\pi}^2}{2}(1/100\text{MHz})$. For our experimental parameters, this represents a shift of the polariton over the avoided crossing of $\sim$ 200 kHz. Thus, in

this regime where the coupling to PA transition in almost resonant and the atomic coupling is purely dispersive, we treat this avoided crossings similarly to a standard two-level system with an offset and slope term to account for the dispersive contribution of the atomic transitions.

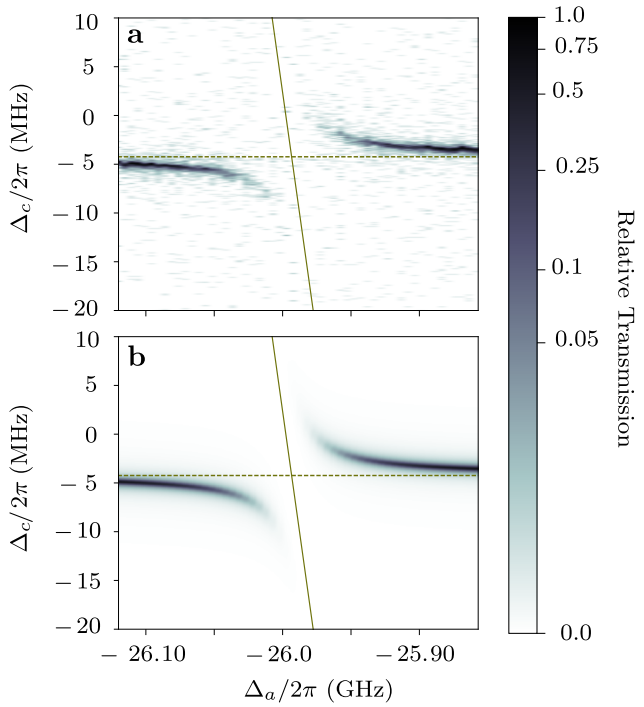

Figure 6.7: ***Measuring the Rabi frequency from experimental spectra : the fit method.*** **a** Spectrum of PA_4 at 832 G averaged over three realizations. **b** Spectrum reconstructed by equation 6.8 using the fit results. The solid and dashed lines indicate the fitted positions of the PA resonance and the dispersively shifted cavity resonance. The transmission is displayed in logarithmic scale, normalized by its maximum value.

We thus treat the coupling to PA transition as a collection of two-level systems distributed in the cavity. A purely classical model gives the transmission of light through a cavity [172]

$$T = \frac{1}{\left(1 + \frac{\Omega^2}{\kappa\Gamma}\mathcal{L}_a(\delta)\right)^2 + \left(\frac{2\Delta_c}{\kappa} + \frac{\Omega^2}{\kappa\Gamma}\mathcal{L}_d(\delta)\right)^2},$$

with the probe–atom detuning δ, the probe–cavity detuning Δ_c, the cavity field intensity decay rate κ, the atomic decay rate Γ and the collective Rabi frequency Ω. The absorption and dispersion parts of the scattering $\mathcal{L}_a(\delta)$ and $\mathcal{L}_d(\delta)$ are given by

$$\mathcal{L}_a(\delta) = \frac{1}{1+4(\delta/\Gamma)^2} \quad \text{and} \quad \mathcal{L}_d(\delta) = \frac{-2\delta/\Gamma}{1+4(\delta/\Gamma)^2}.$$

With the definition of given in figure 6.6.a, we have $\delta = \Delta_c + \Delta_a$.

The observed avoided crossings arise from the coupling between the atom–photon dressed-state and the molecular bound states. So far, the model only represents the coupling to the PA transitions. We introduce the linear slope

coefficient α to account for the detuning dependence of the dispersive shift due to the dispersive coupling to the atomic transition over the spectrum window. This leads to a fit function with an amplitude parameter q:

$$T_{fit} = \frac{q}{\left(1 + \frac{\Omega^2}{\kappa\Gamma}\mathcal{L}_a(\Delta_c + \Delta_a)\right)^2 + \left(\frac{2(\Delta_c - \alpha\Delta_a)}{\kappa} + \frac{\Omega^2}{\kappa\Gamma}\mathcal{L}_d(\Delta_c + \Delta_a)\right)^2}. \quad (6.8)$$

We apply this formula to fit the spectra obtained for the four PA transitions we consider. Figure 6.7.a show the transmission spectrum for the PA_4 transition and in figure 6.7.b the fitted spectrum using equation 6.8. The transmission spectra are plotted in logarithmic scale, with the value of the transmission normalized by its maximum. We see that the calculated spectrum from the fitting procedure reproduces well the one obtained on the experiment. Offsets in Δ_c and Δ_a (omitted in equation 6.8) are used to determine the PA position and the overall dispersive shift δ_{at}. Far detuned from atomic transitions, the dispersive shift is given by $\delta_{at} = \tilde{N}g_0^2/\Delta_a$ with $\tilde{N}$ the atom number coupled to the cavity field and the single-atom–single-photon coupling strength g_0 [172]. As most PA transitions used in our experiment are located between the D_1 and D_2 π transitions which are 10 GHz apart, we take contributions from the both transitions into account to infer the total atom number N as

$$N = \frac{2\delta_{at}/\zeta}{g_{D1\pi}^2/\Delta_{D1\pi} + g_{D2\pi}^2/\Delta_{D2\pi}}.$$

Here $\Delta_{D1\pi}$ and $\Delta_{D2\pi}$ are the detunings from each transition at the location of the resonance. The factor two accounts for the standing wave structure of the cavity field and $\zeta \sim 0.95$ is a factor for the mode overlap between the cloud and the cavity field in the transverse direction.

To extract error bars for the parameters fitted over the maps of figures 6.6.c.d.e and 6.7.a, we repeat each measurement on three different samples. We first construct a spectrum by randomly choosing one scan among the three realizations for each Δ_a and fit it with equation (6.8). We then repeat this procedure 100 times using randomly sampled data sets. We apply this fit procedure to the spectrum around each PA transition, allowing us to extract the Rabi frequencies and the atomic dispersive shift providing the purely atomic contribution linking to the total number of atoms N for each measurement. The Rabi frequencies extracted for PA1–4 are respectively $2\pi \times 14.6(10)$, 11.0(4), 8.0(1) and 18.9(1) MHz. These collective Rabi frequencies exceed both the atomic and the cavity decay rates, validating that the strong-coupling regime on these four PA transitions.

The ability to reach the strong coupling regime between pairs of free atoms forming a molecule and the cavity field represents a new type of dressed-state, where a two-atom optical transition is dressed. The corresponding dressed state, the pair polariton, mixes cavity photons and pairs of atom of the strongly interacting Fermi gas 5.

6.3.2 *Magnetic field dependence of the cavity transmission spectrum*

The pair polariton is a new type of dressed-state that we can create by dressing molecular transitions with cavity photons, reaching the strong coupling regime. A question is to wonder what happens to the transmission spectrum when changing the magnetic field. In the case of a purely atomic transition

we expect a displacement of the transition frequency, but no change in the Rabi frequency 5. We first measure the evolution of the avoided crossing when changing the bias magnetic field.

Magnetic field dependence of the PA lines position

We first measure the change in location of the four PA transitions with respect to the atomic transition when changing the bias magnetic field from 730 to 920 G. We perform the same cavity transmission spectrum measurement as presented in the previous section, record the spectrum and fit it with the procedure explained above. The results of the dependence on the binding energies of the four molecular states with the magnetic field are shown in figure 6.8. The PA lines positions linearly depend on magnetic fields by 0.31, 0.67, 0.89 and −0.83 MHz/G for PA1–4, respectively.

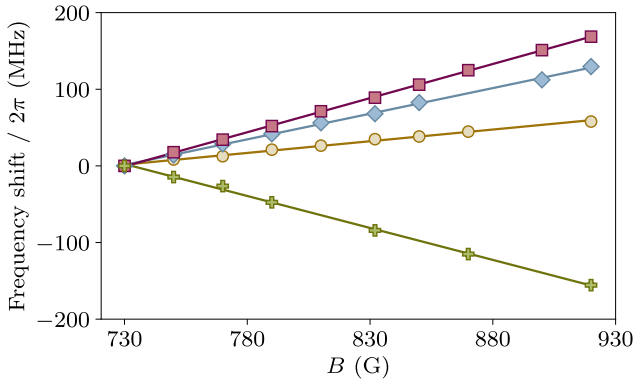

Figure 6.8: ***Location of the PA transitions across the BEC-BCS crossover.*** Positions of PA1–4 (yellow circles, blue diamonds, violet squares and green crosses, respectively) as a function of magnetic fields. The value at 730 G is subtracted for clarity. Linear fits presented by the solid lines yield 0.31, 0.67, 0.89 and −0.83 MHz/G for the four PA resonances respectively.

The magnetic dipole moments of the four molecular states we have probed are all different and do not correspond to the magnetic dipole moment of the atomic ground state. The molecular states couple different states of the free atoms, due to the coupling between the ro-vibrationnal, the angular orbital momemtum and the different hyperfine states.

Magnetic field dependence of the PA Rabi frequency

In addition of the displacement of the PA lines, we also observed a large variation of the Rabi frequencies of the four PA transitions. We show three spectra for the PA2 transition, one on the BEC side of the Feshbach resonance at 730 G, one at unitarity and one on the BCS side at 920 G (figure 6.9.a).

Qualitatively, we see that the strong coupling regime survives all over the BEC-BCS crossover range that we have explored. The Rabi frequency is larger on the BEC side and decreases smoothly towards the BCS side. We repeated this measurement for various magnetic fields across the BEC-BCS crossover for the four PA transitions and measured the corresponding Rabi frequencies. These results are displayed in figure 6.9.b. We see that, even if the change in the internal energy of the Fermi gas is of the order of the Fermi

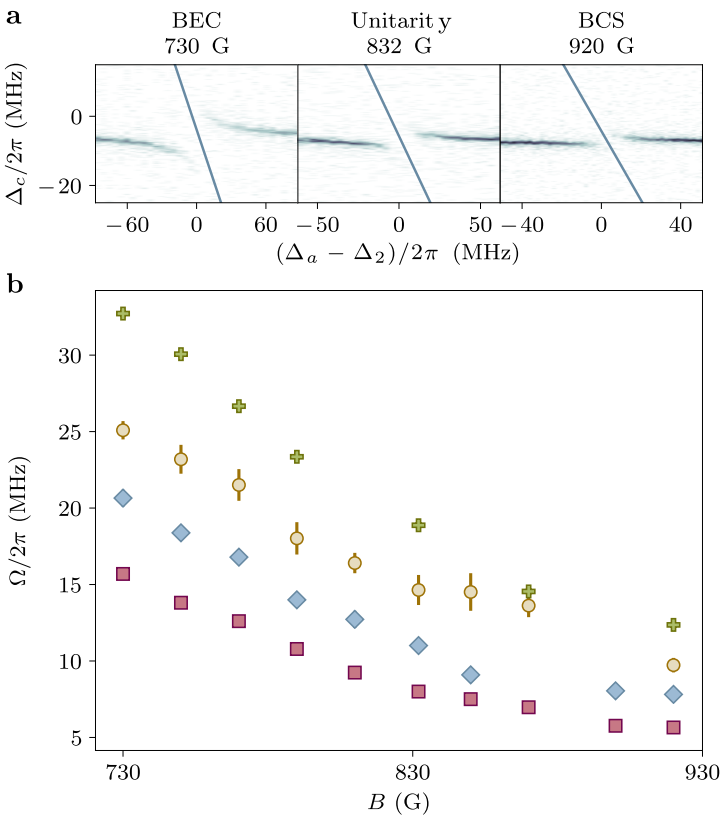

Figure 6.9: ***Evolution of the Rabi frequency across the BEC-BCS crossover.*** **a** Transmission spectra around PA2 in the BEC, unitarity and BCS regimes. Horizontal axis is shifted by $\Delta_2/2\pi = -3.27, -3.20$ and -3.14 GHz, respectively, for visibility. The solid lines indicate the fitted location of the PA line. The color scale is identical to figure 6.6. **b** Magnetic field dependence of the collective Rabi frequencies Ω.

energy (a few tens of kHz), the change in Rabi frequency is of the order of 20 MHz, thus about 100 times larger than the change in internal energy due to the change of the inter-atomic interactions. Despite the different molecular characteristics (Condon radii, vibrational state) of the molecular states probed with photoassociation, we see a similar interaction dependence. This dependence connects to the nature of the pair correlations in the ground state and is not a property of the excited molecular state. In the next section, we will investigate the interaction dependence of the Rabi frequency on PA transitions. We will see that the physics of pairs in the ground state due to the strong interactions in the gas modifies the pair polaritons that captures very interesting properties of the ground state of the strongly interacting Fermi gas.

6.4 UNIVERSALITY OF THE FERMION-PAIR POLARITONS

In this section we study how the Rabi frequency connects to the pairs emerging in the ground state of a strongly interacting Fermi gas. We look first at the light-matter interaction Hamiltonian and show the explicit connection between PA transitions and the pair correlation wavefunction. We will then compare this theoretical description with the actual dependence of the Rabi frequency on the interaction between atoms in the ground state.

6.4.1 Theoretical description of the pair polariton

The Hamiltonian

We start with the full Hamiltonian of the system

$$\hat{H} = \hat{H}_c + \hat{H}_e + \hat{H}_m + \hat{H}_{int} + \hat{H}_{at} \tag{6.9}$$

with $\hat{H}_c = \omega_c \hat{a}\hat{a}^\dagger$ corresponding to the cavity field, $\hat{H}_e = \omega_e \int d\mathbf{r}\hat{\psi}_e^\dagger(\mathbf{r})\hat{\psi}_e(\mathbf{r})$ describing the atoms in the excited state, $\hat{H}_m = \omega_m \int d\mathbf{r}\hat{\psi}_m^\dagger(\mathbf{r})\hat{\psi}_m(\mathbf{r})$ describing the molecules in the $2S+2P$ interaction potential. Here $\hat{a}$ describes the photons of the cavity field and $\hat{\psi}_e(\mathbf{r})$ and $\hat{\psi}_e(\mathbf{r})$ are the fermionic and bosonic field operators describing the atom and molecules in the excited state respectively. As the cloud is defined by two ground states equally populated, we introduce the fermionic field operators $\hat{\psi}_\sigma(\mathbf{r})$ with $\sigma = 1, 2$ representing the two ground states. $\hat{H}_{at}$ represents the atomic ground state Hamiltonian accounting for the kinetic and potential energies. Last, the interaction Hamiltonian that describes the PA process is

$$\hat{H}_{int} = \frac{i\Omega_0}{2}\left(\int d\mathbf{R}d\mathbf{r}g(\mathbf{R})f(\mathbf{r})\hat{\psi}_m^\dagger(\mathbf{R})\hat{\psi}_1(\mathbf{R}-\frac{\mathbf{r}}{2})\hat{\psi}_2(\mathbf{R}+\frac{\mathbf{r}}{2})\hat{a} - hc\right)$$

with $f(\mathbf{r})$ the molecular orbitals describing the relative motion of the two atoms in the target molecular state and $g(\mathbf{R})$ the cavity mode function. The interaction Hamiltonian describes how a pair of ground states atoms in state $|1\rangle$ and $|2\rangle$, of center of mass coordinate $\mathbf{R}$ and relative coordinate $\mathbf{r}$ is annihilated together with a cavity photon to form a molecule in a bound state of the dipole-dipole interaction potential. Ω_0 is the single-pair Rabi frequency. We denote the creation operator $\hat{F}^\dagger$ acting on the molecular and atomic Hilbert spaces by

$$\hat{F}^\dagger = \int d\mathbf{R}d\mathbf{r}g(\mathbf{R})f(\mathbf{r})\hat{\psi}_m^\dagger(\mathbf{R})\hat{\psi}_1(\mathbf{R}-\frac{\mathbf{r}}{2})\hat{\psi}_2(\mathbf{R}+\frac{\mathbf{r}}{2})$$

in such a way that the interaction Hamiltonian becomes $\hat{H}_{int} = \frac{i\Omega_0}{2}\left(\hat{F}^\dagger\hat{a} - \hat{F}\hat{a}^\dagger\right)$.

We can simplify the Hamiltonian in several ways :

- First, as the PA transitions we study are located far away from the bare atomic resonance, the population in the excited atomic state is negligible. In this regime it means that we can treat this part of the Hamiltonian as a perturbation to the second order.
- We can move to the interaction picture for the molecular et atomic fields and perform the rotating wave approximation to transform the Hamiltonian in a frame rotating at the molecular frequency.

Within these approximations the Hamiltonian becomes

$$\hat{H} = \delta\hat{a}^\dagger\hat{a} + \frac{i\Omega_0}{2}\left(\hat{F}^\dagger\hat{a} - \hat{F}\hat{a}^\dagger\right) \tag{6.10}$$

where δ is the detuning between the cavity and atomic transition.

The Rabi frequency

From this Hamiltonian that describes the coupling of cavity photons to PA transitions, we extract the expression of the Rabi frequency. As $\hat{F}$ depends on the ground state properties of the strongly interacting Fermi gas, Ω will depend on the many-body properties of the gas. For this, we write the Heisenberg equation $i\dot{\hat{a}} = \left[\hat{a}, \hat{H}\right]$ for the cavity field using the Hamiltonian described in equation 6.10

$$\dot{\hat{a}} = -i\delta\hat{a} - \frac{\Omega_0}{2}\hat{F} \tag{6.11}$$

Applying the same formula connecting the first and second derivative of the cavity field operator $i\ddot{\hat{a}} = \left[\dot{\hat{a}}, \hat{H}\right]$ we obtain a differential equation linking the cavity field to the operator $\hat{F}$

$$\left(\frac{\partial^2}{\partial t^2} + \delta^2 + \frac{\Omega_0^2}{4}\left[\hat{F}, \hat{F}^\dagger\right]\right)\hat{a} = i\delta\frac{\Omega_0}{2}\hat{F}$$

This equation is central to connect the Rabi frequency to the physics of the strongly interacting Fermi gas. We take the expectation value of the differential equation at $\delta = 0$ and use mean-field decoupling of both the atomic and cavity field components. Considering the cavity field classically we thus obtain the normal-mode splitting

$$\Omega^2 = \Omega_0^2\left\langle\left[\hat{F}, \hat{F}^\dagger\right]\right\rangle. \tag{6.12}$$

In order to connect the Rabi frequency to the properties of the strongly interacting Fermi gas, we need to express the expectation value of the commutator $\langle[\hat{F}, \hat{F}^\dagger]\rangle$. In the low saturation limit, where linear response theory applies, $\langle\hat{\psi}_m^\dagger(\mathbf{R})\hat{\psi}_m(\mathbf{R}\rangle = 0$. Hence the expression of the expectation value of the commutator simplifies into

$$\left\langle\left[\hat{F}, \hat{F}^\dagger\right]\right\rangle = \int d\mathbf{R}|g(\mathbf{R})|^2 \int d\mathbf{r}d\mathbf{r}' f(\mathbf{r})f^*(\mathbf{r}')\left\langle\hat{\psi}_2^\dagger(\mathbf{R}+\frac{\mathbf{r}'}{2})\hat{\psi}_1^\dagger(\mathbf{R}-\frac{\mathbf{r}'}{2})\hat{\psi}_1(\mathbf{R}-\frac{\mathbf{r}}{2})\hat{\psi}_2(\mathbf{R}+\frac{\mathbf{r}}{2})\right\rangle \tag{6.13}$$

leading to the expression for the Rabi frequency

$$\Omega^2 = \Omega_0^2\int d\mathbf{R}|g(\mathbf{R})|^2 \int d\mathbf{r}d\mathbf{r}' f(\mathbf{r})f^*(\mathbf{r}') \left\langle\hat{\psi}_1^\dagger(\mathbf{R}+\frac{\mathbf{r}'}{2})\hat{\psi}_2^\dagger(\mathbf{R}-\frac{\mathbf{r}'}{2})\hat{\psi}_2(\mathbf{R}-\frac{\mathbf{r}}{2})\hat{\psi}_1(\mathbf{R}+\frac{\mathbf{r}}{2})\right\rangle \tag{6.14}$$

This expression connects a quantity measurable on the transmission spectra, Ω^2 with the function describing pair-correlations in the strongly interacting Fermi gas. This function contains the many-body physics of the strongly interacting Fermi gas, the formation of pairs in the ground state being the direct consequence of the large contact interaction between the two spin component of the gas. This correlation is imprinted onto the Rabi frequency as the pair polariton inherits the properties of the ground state pairs. We recast the Hamiltonian in equation 6.10 in terms of creation and annihilation of pair polaritons $\hat{p}^\dagger, \hat{p}$ through a Holstein-Primakoff transformation (Chapter 5)

$$\hat{p} = \frac{\hat{F}}{\sqrt{\langle[\hat{F}, \hat{F}^\dagger]\rangle}}, \tag{6.15}$$

transforming the Hamiltonian into

$$\hat{H} = \delta \hat{a}^\dagger \hat{a} + \frac{i\Omega_0 \sqrt{\langle [\hat{F}, \hat{F}^\dagger] \rangle}}{2} \left(\hat{p}^\dagger \hat{a} - \hat{p} \hat{a}^\dagger \right), \tag{6.16}$$

describing coupled harmonic oscillators. In the mean field limit, this model should be equivalent to the one used to fit the transmission spectra 6.8.

The molecular orbitals

The molecular states we target are bound states in the $2S + 2P$ asymptotic potential. In our regime of experimental parameters, the binding energies of PA1, 2 and 3 are much smaller than the fine structure splitting of ^{6}Li, and of the order of the Zeeman shift. Therefore, for these states we use a minimal model of the molecular potential originating from the D2 π-transition only, with transition dipole moments computed from the Breit–Rabi formula. The Leroy-Bernstein formula suggests that they correspond to vibrational levels $-12, -13$ and -14 below the continuum, in the molecular potential resulting from the exchange of π-polarized photons between atoms.

The validity of this model can be tested using the Leroy–Bernstein formula connecting the C_3 coefficient to the location of the highly excited vibrational bound states. For the three photo-association lines PA1–3 used in the main text, a fit leaving as single free parameter the location of the continuum describes the binding energies better than 5%. Note however that for most of the transitions we observed, in particular closer to the D_1 line or with other polarization, we could not reproduce the spectrum with such a simple model. For PA4, the vibrational level $\nu = 81$ in the $1^3\Sigma_g^+$ orbital, we directly use the documented C_3 coefficient to calculate the Condon radius [237].

6.4.2 *The two-body correlation function in the short distance limit: Tan's contact*

We have described on general grounds the Rabi frequency of PA transition coupled to cavity photon, connecting to the ground state pair-correlation function $\left\langle \hat{\psi}_1^\dagger(\mathbf{R} + \frac{\mathbf{r}'}{2}) \hat{\psi}_2^\dagger(\mathbf{R} - \frac{\mathbf{r}'}{2}) \hat{\psi}_2(\mathbf{R} - \frac{\mathbf{r}}{2}) \hat{\psi}_1(\mathbf{R} + \frac{\mathbf{r}}{2}) \right\rangle$. In the case of the four PA lines we address, the extent of the molecular wavefunction $f(\mathbf{r})$ is given by the Condon Radii for each transitions, $R_C = 244a_0, 210a_0, 181a_0, 164a_0$ respectively for PA1-PA4. The extent of these Airy functions is then small compared with the typical interparticle distance given by $1/k_F$ which for us is about 100 nm when $200a_0 \sim 10$ nm. For large distances, the Airy function goes to zero while at very short distance, the fast oscillation make the integral in equation 6.14 goes to zero.

This is explained in a pictorial manner in figure 6.10 where both the molecular and the ground state wave functions are plotted at scale. Mathematically the overlap integral between the ground and excited pairs wavefunctions only takes significant values at distances close to R_C for all the four bound states, short compared with the extent of the pair-correlation function in the ground state, corresponding to the Franck-Condon principle. The wavefunction overlap integral leads to an important simplification of the two-body correlation function as PA processes are only sensitive to the short-range part of the two-body correlation function. The physics of interacting atoms at short distances is governed by a universal parameter: the Tan's contact.

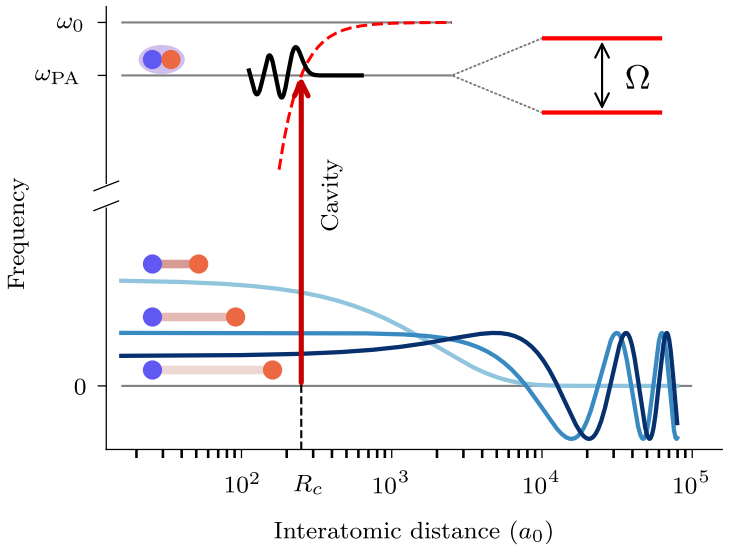

Figure 6.10: ***Dressing the PA bare transition with cavity photons.*** Sketch of the two-atom ground state wavefunctions for the BEC, unitary and BCS situations (light blue, blue and dark blue solid lines, respectively), and wavefunction of a molecular state (solid black line) at the frequency ω_{PA} bound in a molecular potential (red dashed line) asymptotically reaching the single atom transition frequency ω_0. The cavity photons at frequency ω_{PA} induce transitions between free atoms and molecular states at the Condon point R_C. The collective Rabi frequency Ω of the process exceeds the rate of dissipation yielding a pair of resolved dressed states in the spectrum.

Tan's contact

For strongly interacting gases, with short range interactions, the large interaction strength gives rise to strong atom-atom correlations. The complete structure of the correlation function can be complicated to calculate, and depends on the details of the system. However, as the quantum gases are dilute systems, we can consider two different length scales : the long distance for $r >> 1/k_F$ and the short distance limit when $r << 1/k_F$. In the short-distance limit, the complicated form of the two-body correlation function is fully governed by the Bethe-Peierls boundary conditions, assuming that all typical lengths of the system are large such as the De Broglie wavelength of the atoms or the harmonic oscillator length scale associated to the trapping harmonic potential. Under these conditions, the short range part of the two body correlation function is described by the contact.

We make the explicit connection between the two-body correlation function and the contact as the coupling to PA transitions probes the short-range part of the two-body correlation function. Following the reasoning made in [238], we write the pair-correlation function as

$$\left\langle \hat{\psi}_1^\dagger(r_1)\hat{\psi}_2^\dagger(r_2)\hat{\psi}_2(r_2)\hat{\psi}_1(r_1)\right\rangle = \sum_i n_i \phi^{(i)*}(r_1,r_2)\phi^{(i)}(r_1,r_2),$$

with n_i real positive coefficients and $\phi^{(i)}(r_1,r_2)$ a set of short range, normalized two-body orbitals.

This expansion onto the Hilbert space constructed from the two-body orbitals is a general mathematical property. These functions can be explicitly

simplified in our case as discussed extensively in Chapter 4. As the ground state atoms interact via a contact interaction and that we are interested only by the short-range part of the two-body correlation function due to the overlap with the molecular orbitals, we use the Bethe-Peierls boundary conditions. Each two-body orbitals become

$$\phi^{(i)}(r_1, r_2) \xrightarrow[|r_1-r_2|\to 0]{} A^{(i)} \left(\frac{1}{|r_1 - r_2|} - \frac{1}{a} \right),$$

where $A^{(i)}$ is a normalization coefficient and a is the scattering length. Therefore, we get

$$\left\langle \hat{\psi}_2^\dagger(\mathbf{R} + \frac{\mathbf{r}'}{2}) \hat{\psi}_1^\dagger(\mathbf{R} - \frac{\mathbf{r}'}{2}) \hat{\psi}_1(\mathbf{R} - \frac{\mathbf{r}}{2}) \hat{\psi}_2(\mathbf{R} + \frac{\mathbf{r}}{2}) \right\rangle = \sum_i n_i(\mathbf{R}) |A^{(i)}(\mathbf{R})|^2 \left(\frac{1}{|r|} - \frac{1}{a} \right) \left(\frac{1}{|r'|} - \frac{1}{a} \right),$$

in the relevant range of relative distances.

We introduce the contact as

$$\mathcal{C}(\mathbf{R}) = 16\pi^2 \sum_i n_i(\mathbf{R}) |A^{(i)}(\mathbf{R})|^2,$$

It has been demonstrated over the last decade that the contact governs many properties of the strongly interacting gases through universal relations known as the Tan's relations. They link the contact to the tail of the momentum distribution, to the kinetic energy or to the density-density correlator [239]. Additional Tan's relations making the connection between the contact and the total energy of the strongly interacting gas as a function of interactions [240] or with the pressure of the gas [241]. This shows that the entire thermodynamics of a strongly interacting Fermi gas is governed by the short range properties of the two-body correlation function. These universal relations have been extensively tested experimentally. The Tan's relation connecting to the virial theorem [242] was measured in the group of John Thomas as the first experimental confirmation of a Tan's relation. More experiments have been carried out in the group of Deborah Jin [243], confirming the universal behaviour of the thermodynamics properties of the gas. The connection between the contact and the high energy tail of RF spectra [244–246], the static structure factor [247–249] or the number of closed channel molecules [72, 250] were also verified experimentally. The last one mentioned was measured driving photoassociation transitions to directly address Feshbach molecules in the closed-channel of the Feshbach resonance [72, 218].

Intuitively, we can connect the value of the total contact to the number of pairs in a given volume of the strongly interacting Fermi gas. By virtue of Tan's relations [251], for a distance s much smaller than other many-body length scales, the number of pairs dN_p with a volume d^3R centred around point $\mathbf{R}$ is,

$$dN_p(\mathbf{R}, s) = \frac{\mathcal{C}(\mathbf{R}) s}{4\pi} d^3R$$

Integrating over the whole trapped cloud, we deduce the total number of pairs at distance s in terms of the trap-averaged contact $\mathcal{I}$,

$$N_p(s) = \frac{\mathcal{I} s}{4\pi} = \tilde{\mathcal{I}} \frac{N k_F s}{4\pi}$$

with $\mathcal{I} = \widetilde{\mathcal{I}} N k_F$, $\widetilde{\mathcal{I}}$ the trap-averaged contact per particle and N the total atom number.

Expression of the Rabi frequency

The commutator in equation (6.13) thus reads:

$$\left\langle \left[\hat{F}, \hat{F}^\dagger\right] \right\rangle = \int d\mathbf{R} |g(\mathbf{R})|^2 \mathcal{C}(\mathbf{R}, a) \left| \int_0^\infty dr \chi(r) \left(1 - \frac{r}{a}\right) \right|^2,$$

where we have explicitly written the scattering-length dependence of the contact. We have also specialized to s-wave molecular states and introduced $\chi(r) = rf(r)$. The molecular state is independent of interaction strength in the ground state. In the strongly interacting regime where the Condon radius R_C is much smaller than the scattering length, the dependence of the Rabi frequency on scattering length is thus fully universal, captured by the contact.

6.4.3 *Universality of the pair polariton*

In order to account for the finite value of R_C in the theory–experiment comparison that will follow, we apply the reasoning made in [252] and model the target molecular orbital as a square box of width L centred around R_C, such that the integral can be evaluated explicitly

$$\left\langle \left[\hat{F}, \hat{F}^\dagger\right] \right\rangle = \frac{L}{4\pi} \left| 1 - \frac{R_C}{a} \right|^2 \int d\mathbf{R} |g(\mathbf{R})|^2 \mathcal{C}(\mathbf{R}). \tag{6.17}$$

Therefore, we expect the evolution of the Rabi splitting with scattering length, compared with the value measured at unitarity to obey

$$\frac{\Omega^2(a)}{\Omega^2(\infty)} = \frac{\int d\mathbf{R} |g(\mathbf{R})|^2 \mathcal{C}(\mathbf{R}, a)}{\int d\mathbf{R} |g(\mathbf{R})|^2 \mathcal{C}(\mathbf{R}, \infty)} \cdot \left| 1 - \frac{R_C}{a} \right|^2. \tag{6.18}$$

We thus take the raw value for the Rabi frequencies over the BEC-BCS crossover (figure 6.9.b), and display them as a function of the interaction parameter $1/k_F a$ with a the scattering length. In figure 6.11, we show $\widetilde{\Omega}^2 = \frac{\Omega^2}{N k_F} |1 - \frac{R_C}{a}|^{-2}$, normalized by its value at unitarity $\widetilde{\Omega}_\infty$, for the different PA lines as a function of the interaction parameter. A first result is that all the four PA transitions show the exact same relative variations, even if they correspond to different molecular states from different interaction potentials.

Second, as presented in the calculation in the previous section, we expect the Rabi frequency to scale with the Tan's contact [239]. In order to connect to the actual experimental condition we introduce the dimensionless, trap-averaged contact per particle $\tilde{\mathcal{I}}$. From the calculation we thus expect $\Omega^2 \propto \widetilde{\mathcal{I}} N k_F |1 - \frac{R_C}{a}|^2$. In figure 6.11, we show the interaction dependence of the trap averaged contact at zero temperature obtained from [249, 253] without any fit parameter. The collapse of all the data for each PA line on the theory curves is the striking manifestation of the universal dependence of the pair polaritons on interactions. For data in the far BEC regime, the term accounting for the finite size of the molecule contributes by about 15–20% to the scaling.

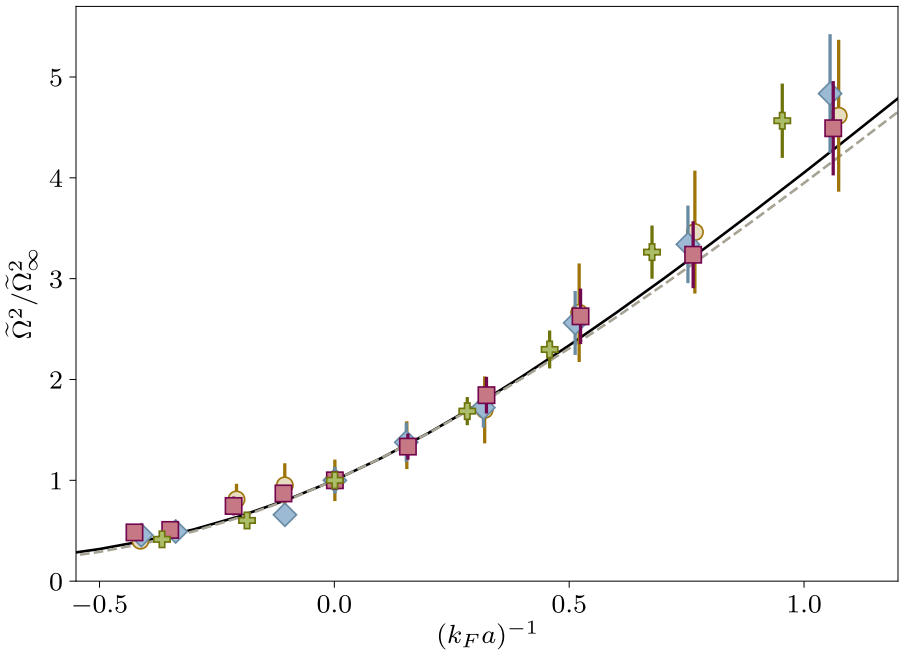

Figure 6.11: ***Universality of the Rabi frequency of the coupling to PA : Tan's contact.*** **a** Evolution of $\tilde{\Omega}^2$, normalized by its value at unitarity $\tilde{\Omega}^2_\infty$ for PA1 (yellow circles), 2 (blue diamonds), 3 (violet squares) and 4 (green crosses) as a function of $1/k_F a$. The black solid and red dashed lines represent the trap averaged contact calculated by Gaussian pair fluctuations and quantum Monte-Carlo, respectively, normalized by the value at unitarity.

We can now come back to the raw variation of Ω in light of equation 6.14 and on the universal scaling of the Rabi frequency in figure 6.11. The change due to interactions only affects

$$\left\langle \hat{\psi}_1^\dagger(\mathbf{R}+\frac{\mathbf{r}'}{2})\hat{\psi}_2^\dagger(\mathbf{R}-\frac{\mathbf{r}'}{2})\hat{\psi}_2(\mathbf{R}-\frac{\mathbf{r}}{2})\hat{\psi}_1(\mathbf{R}+\frac{\mathbf{r}}{2})\right\rangle$$

in the integral of equation 6.14, inducing a change of the internal energy of the gas comparable with the scale of the Fermi energy, meaning a few tens of kHz. Reaching the strong light matter coupling onto PA transitions acts as a magnifier for the small changes of internal energy, in our case by a factor ~ 100. This magnification can be arbitrarily strong as Ω_0 can be made arbitrarily large by reducing the cavity mode volume, for example. This is permitted because any change of the pair-correlation function is magnified by the atomic light-matter Rabi frequency $\Omega_0^2 \int d\mathbf{R}|g(\mathbf{R})|^2$, translating small changes on the energy of the gas into large changes in the optical signal from which we extract the Rabi frequency.

6.5 CAVITY QED WITH MANY-BODY EXCITATION

In this section we will explore two different aspects of the pair polaritons:

- First, we will make an analogy between the coherent coupling to fermion-pairs in a strongly interacting Fermi gas and the coherent coupling of multiple emitters as described by the Tavis-Cummings model (see Chapter 5). We will see that we can observe the expected square root

scaling of the Rabi frequency with the number of pairs in the ground state of the strongly interacting Fermi gas.

- Second, we will show how we can use the pair polaritons to perform weakly destructive measurement of the short range two-body correlation function over a single measurement. We will describe the technique we use to disentangle the atomic and molecular contributions with a single interrogation of the cloud, corresponding to one frequency sweep of the probe laser through the pair-polariton resonance.

6.5.1 *Quantum optics with many body excitations*

Counting fermion pairs

As we have shown, the contact connects directly to the number of pairs in the gas and the square of the Rabi frequency is proportionnal to the contact, therefore to the number of pairs at distance s in the strongly interacting Fermi gas. Thus, in the expression 6.12, the commutator relates directly to the number of pairs and the Rabi frequency reads

$$\Omega = \Omega_0 \sqrt{\frac{N_p}{2}}. \tag{6.19}$$

The overall coupling to the field is modulated by the mode function, such that on average, only half the pairs contribute. This is the expected behaviour of the set $N_p/2$ of identical emitters coherently coupled to one mode of the field. Our experiment thus represents the photo-association counterpart of the celebrated Tavis–Cummings model.

The PA transitions we probe in this work and the large interactions make the Condon radius R_C to be much smaller than the scattering length. The typical length scale $L = \left|\int_0^\infty dr \chi(r)\right|^2$ represents the width of the outer lobe of the molecular orbital close to the Condon point. This is where the overlap integral with the ground state pair correlation function take significant values.

We estimate the number of pairs in the gas addressed by the PA. To this end, we evaluate the length L by supposing that the molecular potential close to R is approximately linear with the position r as

$$V(r) = -E_b \left(1 - \frac{3r}{R_C}\right),$$

where we have expressed the C_3 coefficient in terms of the binding energy E_b.

Therefore the molecular orbital is approximately an Airy function, with a width $L = \left(\frac{\hbar^2 R_C}{3mE_b}\right)^{1/3}$, where m is the atomic mass and $\hbar$ is the Planck constant divided by 2π. We obtain thus $L = 28.9\,a_0$, $23.6\,a_0$, $19.4\,a_0$ and $12.6\,a_0$ for PA1–4, respectively. We introduce a normalized Rabi frequency $\overline{\Omega} = \Omega/\sqrt{N k_F L}$ and compare its scaling with the values of the contact, thus showing the scaling of $\overline{\Omega}$ with the number of pairs in the gas at distance R_C.

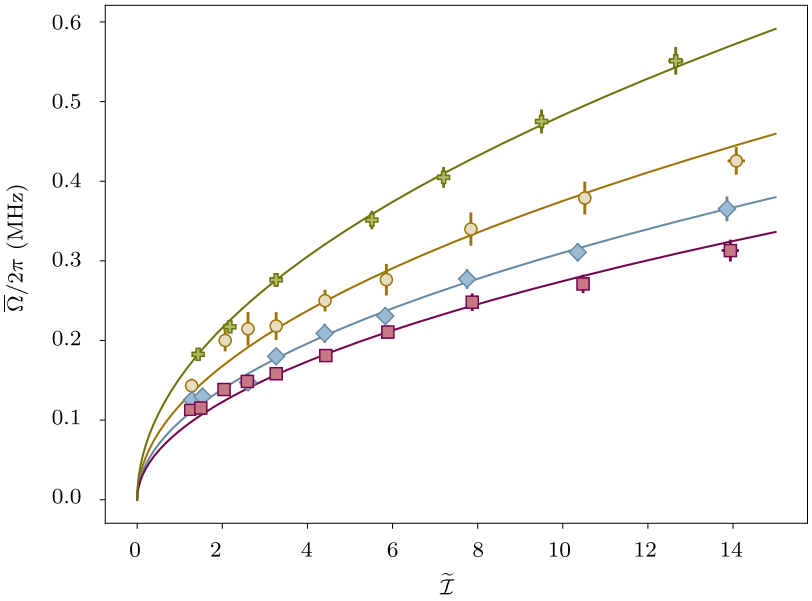

Figure 6.12: ***Collective coherent coupling to many-body excitations : quantum optics with fermion-pairs.*** Scaling of $\overline{\Omega}$ as a function of the trap averaged contact $\widetilde{\mathcal{I}}$ inferred from Gaussian pair fluctuations. The solid lines are square root fit to the data

Coherent collective coupling of photons with excitation of the many-body Hamiltonian

In figure 6.12, we display the scaling of $\overline{\Omega}$ for the four different PA transitions, where L is the estimated width of the molecular wavefunction lobe around R_C, as a function of the corresponding values of the trap-averaged contact per particle obtained from figure 6.11.a and thus as a function of the number of pairs in a box of volume L^3. We observe the square-root scaling of the Rabi frequency with the number of pairs in the strongly interacting Fermi gas, reminiscent of the coherent coupling of multiple identical emitters in the Tavis-Cummings model.

The fit of the Rabi frequency scaling (solid line in figure 6.12) provides an order-of-magnitude estimate for the single-photon–single-pair Rabi frequency Ω_0. We obtain $\Omega_0/2\pi = 595(11)$, $492(5)$, $435(7)$ and $765(5)$ kHz for the four PA lines respectively, comparable to the single-atom–single-photon Rabi frequency of $2\pi \times 780$ kHz for the D2 π-transition in the system. these values are lower bounds for the single-pair Rabi frequency as we assume a $\mathcal{S}$ symmetry of the molecular wavefunction. This approximation might be wrong as there is no fixed direction between the inter-atomic axis of the pairs and the quantization axis. This effect most likely leads to a different symmetry that would reduce the value of the wavefunction overlap and thus induce large Rabi frequencyin order to describe the collective coupling strength measured experimentally. While pairs in the unitary gas are inherently a many-body effect, and cannot be isolated individually, we nevertheless conclude that our cavity has a cooperativity for single pairs and single photons approaching one. This suggests that all the quantum optics protocols designed in the context of single atom–photon interactions could be directly generalized to fermion pairs in strongly interacting gases.

6.5.2 *Single-shot and weakly-destructive measurement of the short-range pair correlation function*

We have shown that we can retrieve the value of the short-range two body correlation function, Tan's contact, from a PA avoided crossing spectrum as well as the atomic contribution that leads to an offset in Δ_c on the position of the dressed-state.

What do we need to obtain a single-shot measurement of the pair-correlation function ?

In contrast with other existing methods [244, 246, 248, 254–256], the combination of cavity QED with pairs through PA offers an avenue to measure the short range pair correlations dispersively with a single interrogation, allowing for time-resolved, repeated measurements on a single atomic sample. The challenge is to be able, from a single interrogation, to obtain the atomic and pair contribution to the dispersive shift. These two contributions leading to the same effect, a shift of the polariton, knowing the position of the polariton at one detuning from the PA transition is not enough to disentangle both contribution.

To solve this challenge, we adapt our transmission spectroscopy technique to independently extract from a single interrogation of the system both the overall dispersive shift, originating from the coupling to single atoms, and the extra contribution due to the coupling to the PA transition. We rotate the probe polarization by 26° with respect to the magnetic field direction, such that the probe acquires a finite σ^+-polarization component. We probe the system close to PA4, the large detuning with respect to the atomic transitions mitigating spurious heating effects. There, the π and σ polarized photons couple to different excited molecular states as shown by the two avoided crossings displayed in figure 6.13.a taken for a unitary gas. Each vertical line of the spectrum corresponds to a single sweep of the probe frequency on one cloud, corresponding to one single interrogation.

Measuring the PA and atomic contribution on a single measurement

An example of raw photon counts obtained for a single interrogation is shown in figure 6.13.b at $\Delta_a/2\pi = -26.056\,\mathrm{GHz}$. We fit the positions of the two resonances corresponding to the π and σ^+ components using a double Lorentzian model. A typical spectrum corresponds to 16 intracavity photons on the transmission resonance, and of the order of one spontaneous emission event over the entire cloud.

The positions of the resonances at a given $\Delta_a/2\pi$ allows us to retrieve both the atomic dispersive shift δ and the collective Rabi frequency of the molecular transition Ω. The pair-polariton spectrum extrapolated from this single interrogation is presented on figure 6.13.a showing excellent agreement with a full data set covering all detunings taken for clouds prepared in similar experimental conditions.

A non-destructive probe of the pair correlations

Such a single interrogation can be repeated 50 consecutive times on the same atomic ensemble, separated by 10 ms, allowing for equilibration of the cloud between each interrogation. Figure 6.14.a shows δ and Ω, extracted

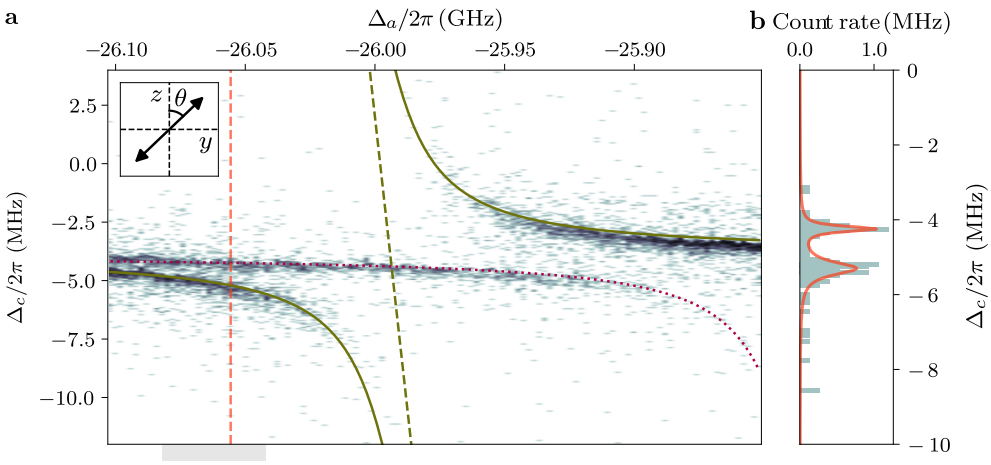

Figure 6.13: ***Extracting the Rabi frequency to PA transitions from a single shot measurement.*** **a** Transmission spectrum around PA4, for a balanced Fermi gas composed of $8.0(2) \times 10^5$ atoms at 832 G with a probe polarization tilted by $\theta = 26°$ (inset). The two resonances located around $\Delta_a/2\pi = -25.998$ and -25.842 GHz correspond to the π- and σ^+-polarization components, respectively. The dashed blue line indicates the position of the PA resonance coupled to π-polarized photons. **b** Raw photon counts at $\Delta_a/2\pi = -26.056$ GHz (orange dashed line on panel a). The solid line is a double-Lorentzian fit to the histogram. Two transmission peaks located at $\Delta_c/2\pi = -5.2$ and -4.3 MHz correspond to π and σ polarized photons, respectively. The blue solid and the red dotted lines on panel **a** represent the π- and σ^+-polariton branches, respectively, inferred from the measured polariton positions.

from each of these single consecutive interrogations. The retrieved values of Ω reflect the time-evolution of two-body correlations for one single atomic ensemble. We observe a decrease of $\Omega/2\pi$ from 18 to 15 MHz after the 50 consecutive interrogations, and a decrease of δ by 27% reflecting atom losses. About half of these losses can be attributed to the finite lifetime of the gas[75] due to the strong interactions. The remaining measurement-induced atom losses are thus $1.9(1) \times 10^3$ atoms per interrogation, 0.2% of the initial atom number per interrogation.

To confirm that the many-body physics is preserved in spite of the repeated measurements on a single atomic ensemble, we evaluate $\widetilde{\Omega}^2 = \Omega^2/Nk_F$ at each point in time. The result is shown in figure 6.14.b, normalized by its initial value, showing no discernible decay, where the noise originates predominantly from photon shot noise. An average of 20 traces of $\widetilde{\Omega}^2$ taken on different clouds and at different values of detuning in the dispersive regime of the PA4 resonance is shown in figure 6.14.d. This quantity is directly proportional to the trap averaged contact $\widetilde{\mathcal{I}}$, and remains constant demonstrating the weakness of the heating originating from the measurements. Independent temperature measurements indicate an initial temperature of $0.083(2)\,T_F$ and a final one of $0.10(2)\,T_F$ after the 50 interrogations, for which we would expect a decrease of the trap-averaged contact by about 4% [257].

6.6 PERSPECTIVES

The ability to observe pair-correlations in time while preserving the many-body physics is an ideal starting point for future theoretical and experimen-

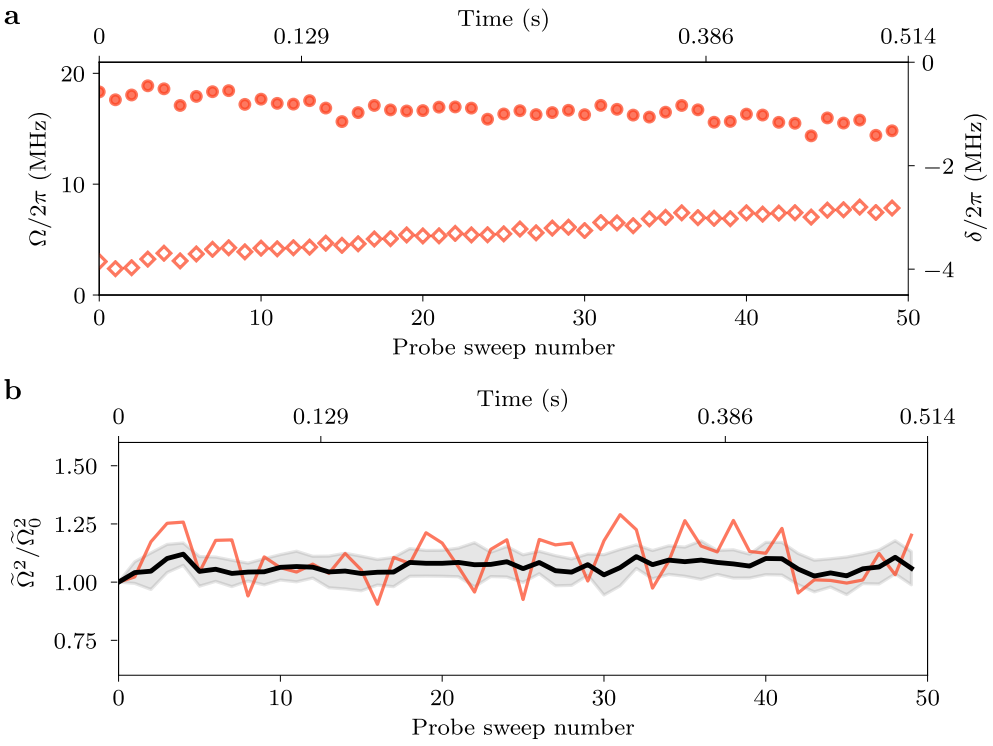

Figure 6.14: ***Weakly-destructive repeated measurement of the short-range two body correlation function.*** **a** Extracted Rabi frequency (filled circles) and atomic dispersive shift (open diamonds) from 50 consecutive interrogations on a single atomic ensemble at $\Delta_a/2\pi = -26.056\,\mathrm{GHz}$. **b** Evolution of $\widetilde{\Omega}^2$ normalized by its initial value $\widetilde{\Omega}_0^2$ evaluated from successive measurements for a single cloud (orange line) and averaged over 20 different clouds (black solid line) for detunings ranging from $\Delta_a/2\pi = -26.042$ to $-26.082\,\mathrm{GHz}$ (shaded area on figure 6.13.a). The grey area represents the standard deviation.

tal investigations of quantum noise and back-action mechanisms for correlation measurements in many-body systems. This will require a detailed understanding of technical and fundamental sources of noise including noise originating from the background coupling to atomic density [182].

Eventually, we then expect the quantum noise spectra to carry fundamental information on higher order correlations, opening the fascinating perspective of combining quantum-limited sensing with strongly correlated fermions. In our work, optomechanical effects originating from the motion of atoms triggered by the probe are absent, due to the short interrogation time. For slower probe sweeps, we will enter a regime where optomechanical non linearities or even dynamical back-action will emerge [187].

Coupling directly the cavity field to the pair correlation function in the dispersive regime suggests the possibility to engineer photon mediated pair–pair long range interactions [42], or pairing with a momentum space structure [258], opening an uncharted territory to quantum simulation of strongly correlated materials. Beyond these fundamental questions, the weakly destructive and time-resolved character of the cavity-assisted measurement will be of immediate, practical interest in the study of correlations after quenches, such as spin diffusion [259], repulsively interacting Fermi gases where pairing competes with ferromagnetism [260], or during slow trans-

port processes [261, 262], complementing other high-efficiency methods [263]. Finally, the addition of exquisite control over photons of a high finesse cavity to the existing cold molecules toolbox [58], opens the way to dissipation engineering of cold chemistry [55–57, 264].

Part III

DISPERSIVELY COUPLED STRONGLY INTERACTING FERMI GAS

7 OUTLOOKS

In this chapter, I present an outlook to the exploration of the coupling to the strongly interacting Fermi gas in the dispersive regime. We will show that in this regime, similarly to the measurement performed on the dispersive regime of the PA transitions (Chapter 6), fast sweeps enable weakly destructive measurements of the atom number. This technique, with some technical improvements, would be beneficial for transport measurements with increased sensitivity [182, 262].

In the same regime, we perform much slower probe laser frequency sweeps through the polariton transmission peak, in such a way that the atoms can now dynamically respond to the change of the intracavity field while the probe frequency is varied. This phenomenon leads to a strong optical non-linearity that connects to a fundamental quantity of the strongly interacting Fermi gas, the susceptibility.

Last, I will discuss the first results obtained when probing the cloud with a pump beam tilted with respect to the cavity axis. This pump beam is retroreflected forming a 1D lattice that can interfere with the photons scattered by the cloud in the cavity. This potential induces long-range interactions in the cloud, mediated by the cavity photons. We observe the qualitative experimental proof of such interactions, a superradiant phase due to the self-organization of the cloud when the optical power of the 1D lattice is large enough. This new type of Fermi gas with large short- and long-range interactions will be very interesting to study due to the competition between the two type of interactions.

CHAPTER CONTENTS

Part of this chapter closely follows our publication[1]:

K. Roux, V. Helson , H. Konishi and J.-P. Brantut
Cavity-assisted preparation and detection of a unitary Fermi gas
New Journal of Physics **23**, 043029 (2021)

7.1 LIGHT-MATTER INTERACTION IN THE DISPERSIVE REGIME

In the regime where the cavity resonance is far-detuned from the atomic one i.e. when Δ_a, the detuning between the cavity resonance and the atomic transition, is larger than the collective coupling strength, the cavity field

1 Parts of this chapter are directly taken from this publication

couples dispersively to the atoms [171, 172]. The dispersive Hamiltonian reads

$$\hat{H} = \int dr\hat{\Psi}^\dagger(\vec{r}) \left(-\frac{\nabla^2}{2m} + V_{ext}(\vec{r}) + \frac{g_0^2}{\Delta_a} g_c(\vec{r}) \hat{a}^\dagger \hat{a} \right) \hat{\Psi}(\vec{r}) + \Delta_c \hat{a}^\dagger \hat{a} + \kappa(\hat{a} + \hat{a}^\dagger) \tag{7.1}$$

with $\hat{\Psi}^\dagger(\vec{r})$ the field fermionic field operators for the atoms, $\hat{a}^\dagger$ the jump operator for the cavity field, $V_{ext}(\vec{r})$ the external trapping potential, Δ_a the detuning between the atomic transition and the cavity resonance and Δ_c the detuning between the cavity resonance and the pump frequency. The light-matter coupling strength is given by g_0. The first two terms correspond to the kinetic and potential energies. The last two terms account for the energy of the cavity field and the driving field of the pump. The dispersive coupling in this Hamiltonian is $\int dr\hat{\Psi}^\dagger(\vec{r}) \left(\frac{g_0^2}{\Delta_a} \hat{a}^\dagger \hat{a} \right) \hat{\Psi}(\vec{r})$. This term can have two different interpretations: the first one is that the atoms act as a collective dispersive medium that shifts the bare cavity frequency by a quantity proportional to $\frac{g_0^2}{\Delta_a}$ multiplied by the overlap integral between the atomic density $n(\vec{r})$ and $g_c(\vec{r})$ the spatial mode function of the cavity. The second interpretation is that the cavity field creates a lattice potential with a depth given by $\langle \hat{a}^\dagger \hat{a} \rangle$ that exerts a force onto the atoms. For negative values of Δ_a this force pushes the atoms towards the regions of larger coupling, meaning at the antinodes of the cavity field.

In this spirit we can rewrite the light-matter interaction term of the Hamiltonian as

$$\hat{H}_{lm} = \Omega \hat{a}^\dagger \hat{a} \int d^3r \hat{n}(\mathbf{r}) \cos^2(2\vec{k}_c \vec{r}) = \Omega \hat{a}^\dagger \hat{a} \left(\frac{N}{2} + \hat{M} \right) \tag{7.2}$$

where $\Omega = \frac{g_0^2}{\Delta_a}$ is the dispersive coupling strength, the cavity with a mode function $\cos^2(2\vec{k}_c \vec{r})$, $\hat{n}$ is the atomic density operator and N the total atom number. The transverse size of the cloud is much smaller than the cavity waist for our experimental parameters. Due to the longitudinal overlap between the cavity mode function and the atomic density, only half of the atoms dispersively couple to the cavity, explaining the factor 1/2. The first part represents the average dispersive shift of the cavity, and the second describes both a shift the cavity resonance frequency originating from a collective displacement $\hat{M}$, and an optical lattice with spacing $\pi/|\vec{k}_c|$ and depth $\Omega \hat{a}^\dagger \hat{a}$ imprinted onto the atoms.

In the experiment we use light linearly polarized along the magnetic field direction, which couples to the π-transition, for dispersive measurements. To calculate the effective light-matter coupling strength we have to account for the D_2 and D_1 transitions $|2S_{1/2}, m_J = -1/2\rangle \longrightarrow |2P_{3/2}, m_J = -1/2\rangle$ and $|2S_{1/2}, m_J = -1/2\rangle \longrightarrow |2P_{1/2}, m_J = -1/2\rangle$, and their respective detunings $\Delta_{D2\pi}$ and $\Delta_{D1\pi}$ and light matter coupling strengths $g_{D2\pi}$ and $g_{D1\pi}$, such that

$$\Omega = \frac{g_{D1\pi}^2}{\Delta_{D1\pi}} + \frac{g_{D2\pi}^2}{\Delta_{D2\pi}}. \tag{7.3}$$

At large magnetic fields, where all the dispersive measurements of this Chapter are performed, we have $g_{D1\pi} = 0.576 \cdot g_0$ and $g_{D2\pi} = 0.816 \cdot g_0$

with $g_0 = 2\pi \times 479$ kHz the coupling strength for a single atom located at the field maximum, for the closed D_2 σ_- transition $|2S_{1/2}, m_J = -1/2\rangle \longrightarrow |2P_{3/2}, m_J = -3/2\rangle$.

From equation 7.4 we can distinguish two cases :

- For fast probe frequency sweeps, the cavity light field does not couple to the center of mass motion of the atoms, hence $\langle \hat{M} \rangle = 0$. In this regime the dispersive light-matter interaction Hamiltonian reads

$$\hat{H}_{lm} = \Omega \hat{a}^\dagger \hat{a} \left(\frac{N}{2} \right) \tag{7.4}$$

  where we introduce the collective dispersive shift of the bare cavity resonance $\delta = \Omega \left(\frac{N}{2} \right)$. Fast probe frequency sweeps permit to measure δ, hence giving us access to the measurement of the atom number.

- For slow probe frequency sweeps compared with the characteristic timescale of the atomic dynamics, the atoms are displaced due to the presence of the lattice potential created by the pump, thus $\langle \hat{M} \rangle \neq 0$. For large enough power, the force exerted on the atoms localizes them at the antinodes of the fields, thus increasing the collective coupling to the cavity. This dynamical effect leads to an optical non-linearity and is the subject of the second part of this chapter

I will now present experimental results obtained in these two regimes.

7.2 PROBING A STRONGLY INTERACTING FERMI GAS IN THE DISPERSIVE REGIME

7.2.1 Weakly destructive measurement of atom number

To illustrate the potential of the cavity as a detection tool for Fermi gases, we perform repeated, weakly destructive measurements of the time evolution of the number of atoms in an individual cloud. We demonstrate that hundred measurements repeated over one second can be performed on a single cloud while maintaining the temperature below the superfluid transition, with limited atom losses. This represents a key milestone towards quantum-limited transport measurements, for example in a two-terminal configurations [79].

The measurement of dispersive shift with fast probe frequency sweeps probes atom number while limiting resonant light scattering: as the cooperativitiy of the cavity is larger than one, a majority of the light is channelled into the cavity mode, contributing coherently to the measurement signal, as opposed to scattering into free space which amounts to incoherent losses. In addition, this technique is free of saturation and Doppler effects that hinder absorption imaging for light species [265].

We measure $\delta/2\pi$ using transmission spectroscopy of the cavity at fixed $\Delta_a/2\pi = 20$ GHz below the D_2 transition, leading to a dispersive coupling strength $\Omega = 18.5$ Hz. To this end we send a probe beam matched to the TEM_{00} mode of the cavity, sweep its frequency by 20 MHz within 2 ms and record the transmitted photons on a single photon counting module. As for the measurements presented in Chapter 5 and 6, the probe frequency sweep rate is faster than the dynamical timescale of the atomic density.

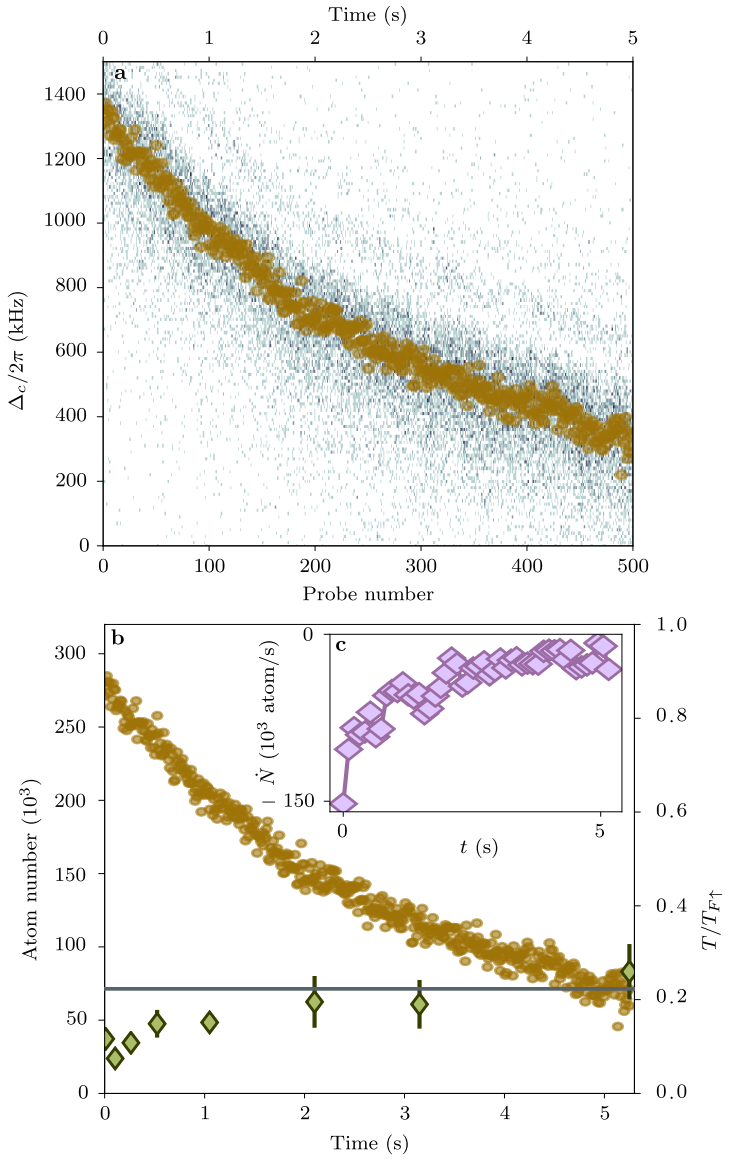

Figure 7.1: ***Weakly destructive measurment of atom number in the dispersive regime.*** **a** Stacked raw histograms of photon counts for 500 consecutive dispersive measurements realized on the same cloud with $\Delta_a/2\pi = 20$ GHz. The gas comprises $1.7(1)\cdot10^5$ and $0.9(1)\cdot10^5$ atoms in the majority and minority spin component, respectively. Brown circles indicate the fitted location of the cavity resonance, with respect to the empty cavity resonance (see text for details). **b** Inferred atom number (brown circles) as a function of time. Green diamonds indicate the temperature measured separately after 1, 10, 25, 50, 100, 200, 300 and 500 consecutive measurements. The grey line indicates the critical temperature $T_c = 0.223\,T_F$ [154] for a spin balanced Fermi gas. **c** Atomic losses calculated from the atom number variations averaged over three clouds. Each value of the derivative is fitted over 30 consecutive dispersive probe measurements.

This cavity-based detection offers the opportunity to monitor atom number variations on one single quantum degenerate Fermi gas over time. In order to later infer temperature increases, we use spin imbalanced gases comprising $1.7(1)\cdot10^5$ and $9(1)\cdot10^4$ atoms in $|\uparrow\rangle$ and $|\downarrow\rangle$ spin states. We then repeatedly send light on the cavity and sweep its frequency across the cavity

resonance, following the protocol described above, and record the transmitted signal. We performed up to 500 measurements in total, separated by 10 ms. Figure 7.1.a presents the raw photon detection histograms obtained for all the successive sweeps over one single realization of the Fermi gas, for $\Delta_{D2\pi}/2\pi = 20$ GHz. The presence of a clear resonance is obvious for each scan, with noise originating from the finite photon count. A weak ringing can be observed due to the sweep rate being comparable with the cavity linewidth. For each sweep, we determine the most likely location of the resonance using a Lorentzian fit, shown with brown circles in figure 7.1.a.

These measurements directly translate into variations of atom number, as shown in figure 7.1.b. This slow decay of atom number is primarily due to the combined effects of the dipole trap spontaneous emission and intensity noise, and background gas collisions. We also repeated these measurements, stopping after a variable number of probe pulses to evaluate the heating, using the method described above. After a ten scans we observe no detectable atom losses and a temperature of $T/T_{F\uparrow} = 0.07(1)$ compatible with the one measured without any cavity probe. Remarkably, after 100 measurements, we measure a temperature increase to $T/T_{F\uparrow} = 0.15(1)$, still well below the superfluid critical temperature. This demonstrates that tens of repeated probes preserve the many-body physics of the Fermi gas for as long as one second, which is compatible both with slow transport processes as well as dynamics after quenches.

The evolution of atom number in time represents particles escaping the trap, such that this measurement can be interpreted as an in-situ probe of atomic losses. To substantiate this, we use a linear fit of the atom number evolution over 30 consecutive shots to extract the total loss rate. The result is shown in figure 7.1.c, averaged over three realizations of the gas.

To assess the role of measurements in the loss processes, we performed similar measurements with a reduced probe rate but keeping the total observation duration at 5 s. We observed that increasing the number of measurements from 10 to 500 leads to an increase by 7% of the observed atomic losses (figure 7.2). Comparing the losses with different probe numbers, we estimate that a single probe pulse induces a loss of about 30 atoms. By comparison, the standard deviation in the determination of the most likely population in the cloud represents about 3000 atoms for the data of figure 7.1. Depending on the requirements, future experiments may use larger probe power at the cost of an increased destructivity. The overall timescale for the loss process extracted from 7.1.b is 4.2 s, comparable with that of the slow transport processes in single-mode point contacts [261].

Probing a dressed-cavity in the dispersive regime might allow for a QND measurement of atom number [266]. In the low temperature regime, a fortiori for our quantum degenerate gases, the recoil associated with measurement back-action breaks the QND character of the measurement, which can nevertheless approach the non destructive regime in the narrow cavity limit [182, 267], opening interesting perspectives for the study of transport processes in mesoscopic devices [261].

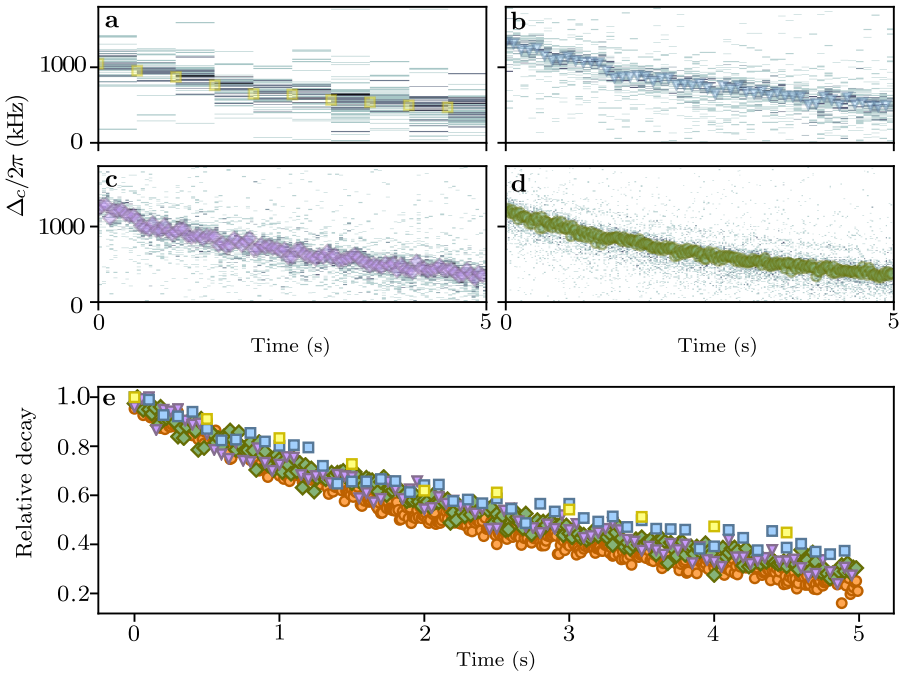

Figure 7.2: ***Estimation of the destructivity of the cavity-based atom number measurement.*** **(a)-(d)** Evolution of the dispersive shift position over 5 s for respectively 10, 50, 100 and 250 consecutive measurements. Transmission spectra are aligned in time for different number of consecutive probe sweeps. The markers are the fitted position of the transmission peak using a lorentzian fit on the spectrums with a binning of 10 kHz and an average photon count per sweep of 55. **(e)** Normalized time evolution of the transmission peak position for 10, 50, 100, 250 and 500 consecutive measurement. We observe a small additional decay of peak position of 7% in the case of 500 measurement compared with the other cases.

7.2.2 Probing the many-body physics through optical non-linearity

We now change an important parameter of our probing schematic: the sweep rate of the probe frequency. So far, all measurements presented were performed with fast frequency sweeps, allowing us to rule out any coupling to the motionnal degree of freedom of the atoms as the variations of the intracavity field were too fast to modulate the atomic density. Making this sweep rate slower so that the cloud can now adapt to it make us enter the regime of cavity opto-mechanics, where the cavity light couples to the motional degree of freedom of the cloud.

The framework of optomechanics naturally describes collective displacements of atoms within a cloud placed in a high finesse cavity: the mode of the cavity singles out a particular collective mode of the atomic medium, which amplitude directly controls the effective cavity length due to the dispersive coupling between atoms and light. The sensitivity to small displacements leads to strong non-linear effects upon probing the coupled atom-cavity system [268, 269]. The probe light inside the cavity exerts a force on the atoms, imprinting an atomic density modulation matched with the cavity mode. As a result, the effective cavity length changes, yielding a Kerr-type non-linearity, visible in particular as a deformation of the transmission profile of the cavity, and eventually leading to instabilities [270–274]. This

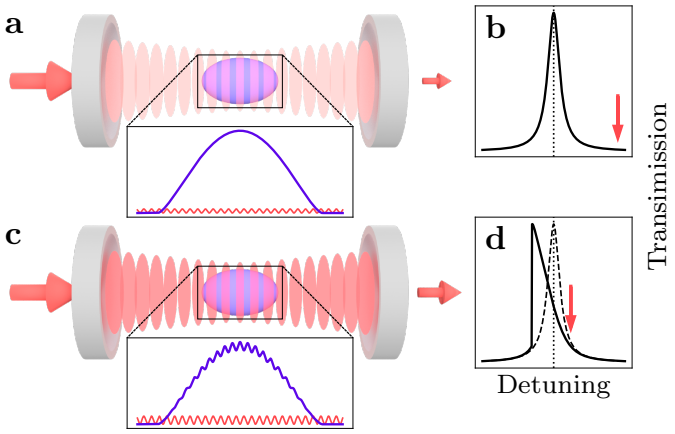

Figure 7.3: ***Cavity optomechanics with a strongly interacting Fermi gas: concept*** A weak laser beam dispersively probes an atomic ensemble trapped within the mode of a high-finesse optical cavity. **a** When the probe intensity is weak, the force exerted by the resulting intracavity lattice on the gas is negligible, and the atomic density is left unperturbed. **b** In that case, the cavity spectrum features a typical lorentzian shape when measured by means of transmission spectroscopy. **c** For a larger probe intensity, the lattice depth increases and imposes a weak static spatial modulation at wavevector $2\vec{k}_c$ on the density. The latter then experiences a higher spatial overlap with the cavity mode, which modifies the coupling strength and induces a shift of the atom-cavity resonance frequency. **d** The observed lineshape then reflects this shift and features a bistable profile with a distinctive sharp edge on the red side of the resonance.

non-linear effect is a hallmark of cavity optomechanics, observed in the cold atoms context on both tightly confined, thermal atoms [3, 41, 187, 275–278] and homogeneous BECs [270, 279, 280]. There, the system is in one-to-one correspondence with mechanical, harmonic oscillators with a frequency set either by the external trap or by the recoil frequency of atoms.

We study the optomechanical Kerr non-linearity in a degenerate, strongly interacting Fermi gas coupled dispersively to light in a high finesse cavity. In contrast to weakly interacting systems, the optical non-linearity of a strongly interacting Fermi gas depends strongly on the inter-atomic interaction strength, connecting the many-body physics to the optical spectrum of the atomic-cavity system. In our regime, where the optical wavevector k_c is much larger than the Fermi wavevector k_F, we hope to observe that the optical non-linearity captures the short-range physics of the strongly interacting Fermi gas, given by the contact (see Chapter 6). I present the first steps towards this goals.

For an empty cavity and equilibrated atoms, $\langle\hat{M}\rangle = 0$ (equation 7.4), so that probing the cavity with vanishingly small probe power yields a symmetric, Lorentzian lineshape with width κ, the inverse photon lifetime, as illustrated in figure 7.3.a. Upon increasing probe power, the finite intracavity photon number $\bar{n} = \langle\hat{a}^\dagger\hat{a}\rangle$ yields to first order a displacement

$$\langle\hat{M}\rangle = \frac{\Omega N}{8}\bar{n}\chi^R(2\vec{k}_c\vec{r}), 0), \tag{7.5}$$

where $\chi^R(\vec{k},\omega)$ is the retarded density response function per atom of the gas at frequency ω and wavevector $\vec{k}$. For $\omega > 0$, the imaginary part of the density response, the structure factor, has been measured with high precision [249, 256]. However, the real part, which is non-zero for $\omega = 0$, has never been measured, due to the impossibility to observe weak, short wavelength density perturbations in a strongly interacting system.

In the strong dispersive coupling regime $\Omega N \gg \kappa$, the cavity converts the weak, perturbative displacement into a dispersive shift with a large gain, modifying significantly the transmission of the atom-cavity system, as illustrated in figure 7.3.d. This cavity-mediated feedback thus imprints directly the density response function, a many-body property of the quantum gas, onto the optical spectrum, where it is read-out by transmission spectroscopy.

Accounting for the displacement induced by the probe, described by equation 7.5, in the equations of motion for the intracavity field yields a Kerr optical non-linearity. In the steady state, the frequency dependence of the cavity photon number reads

$$\bar{n} = \frac{\bar{n}_0}{1 + \frac{4}{\kappa^2}(\delta_{pr} + \eta\bar{n})^2} \tag{7.6}$$

where $\bar{n}_0$ is the maximum photon number, δ_{pr} the detuning of the probe with respect to the dispersively shifted cavity resonance and $\eta = \frac{\Omega^2}{8}\chi^R(2\vec{k}_c, 0)$ measures the strength of the Kerr non-linearity.

The experiments are performed on degenerate, balanced two-component, Fermi gases of ^{6}Li comprising 9×10^5 atoms, held in a crossed dipole trap at the center of the cavity mode. A homogeneous magnetic field $\vec{B}$ is tuned in the vicinity of the Feshbach resonance at 832 G, where the gas explores the BEC–BCS crossover. The gas has a temperature of $T = 0.1\,T_F$. We probe the system using light linearly polarized along the quantization axis, matched to the TEM_{00} mode of the cavity. The cavity resonance frequency is detuned by $-2\pi \times 16\,\text{GHz}$ from the D_1 π-transition of ^{6}Li at 832 G, yielding $\Omega = 10.75$ Hz. With $\Omega N/\kappa = 125$, the system operates deeply in the strong dispersive coupling regime. The probe frequency is dynamically swept across the cavity resonance over a range of $-2\pi \times 3\,\text{MHz}$ in 3 ms during a single experimental run, and the photons arrival times are recorded with a single photon counting module. The sweep rate is chosen fast enough to minimize atomic losses during the probe process, but slow enough compared with the typical dynamical time scales of the system to ensure that we probe its steady state.

For large enough intracavity photon number, the Kerr non-linearity originating from atomic displacements distorts the profiles (figure 7.4.a). We observe distinctive sharp edge towards the red side of the cavity resonance, due to the onset of bistability, predicted by equations 7.6. To quantify the Kerr non-linearity, we fit these profiles to equation 7.6. To achieve a high signal-to-noise ratio, necessary for an accurate determination of η, we aggregate multiple traces taken in similar experimental conditions and average them. The Kerr non-linearity measures the ability of atoms to redistribute due the force exerted by the cavity light, quantified by $\chi^R(\vec{k},\omega)$. Repeating the measurement procedure for different magnetic fields and same probe power provides a measurement of the variations of $\chi^R(\vec{k},\omega)$ with the scat-

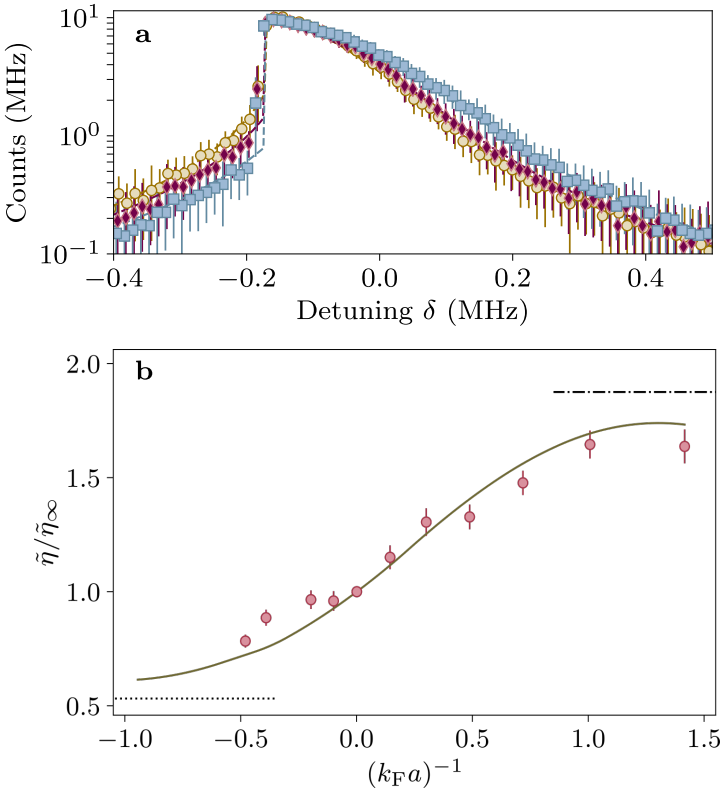

Figure 7.4: ***Scaling of the optical non-linearity across the BEC-BCS crossover.*** **a** Averaged transmission spectra and their fit using equation 7.6, taken for $1/k_F a = (-0.48, 0, 1.42)$, and depicted by yellow circles, violet diamonds and blue squares respectively. The observed nonlinearity increases with $1/k_F a$. **b** Fit values of η (red circles) from data acquired accross the BEC-BCS crossover. The error bars on the data represent statistical fluctuations of the measurement and fitting uncertainties. The theoretical prediction of the non-linearity obtained from the OPE of the susceptibility (yellow solid line) shows a good quantitative agreement with the experiment. The horizontal dashed (dotted) line shows the limit value of the non-linearity based on the expression of the susceptibility for a non-interacting Fermi gas (non-interacting BEC), respectively.

tering length a. Typical observations are presented in figure 7.4.a for different interaction parameters $1/k_F a = (-0.48, 0, 1.42)$, together with the fit to equation 7.6, showing a large increase of the response as the gas crosses over from the BCS to the BEC regime.

We now systematically explore the scaling of the Kerr-non linearity with interactions by measuring $\tilde{\eta} = \eta/\Omega^2 N$ as a function of B. We normalize the results by the value of the non-linearity observed at unitarity $\tilde{\eta}_\infty$, allowing for the observations of the relative variations of the response function in the BEC-BCS crossover. The variations are presented in figure 7.4.b, showing a smooth increase by factor of two from the BCS to the BEC regime.

In our regime $2k_c \sim 3 \times k_F$, thus the response function $\chi^R(2\vec{k}_c, 0)$ depends on the short-range physics, as the modulation of the density happens at short distances compared with the typical pair size. In collaboration with Shun Uchino, we have shown that in our regime of parameter we can develop asymptotically (Operator Product Expensaion) the susceptibility that

is expressed as a function of the contact and the internal energy of the strongly interacting Fermi gas. Even though the details of this theoretical development are beyond the scope of this manuscript, figure 7.4.b shows the theoretical prediction together with the experimental data, showing a good quantitative agreement. It is remarkable that the Kerr non-linearity in the optomechanics context probes the same short-range physics as the coupling to PA transitions does (Chapter 6). In the optomechanics case, this universal physics is captured by the density modulation at $2k_c$, thus by the susceptibility. The steady-state response of the density should give us access to the contact. For the PA, the contact is captured by the wavefunction overlap of the ground state wavefunction of the pairs and the one of the molecular states. These two approach are completely different but relate to the same universal short-range physics.

7.3 TOWARDS CAVITY-MEDIATED LONG-RANGE INTERACTION

Cavity QED with quantum gases has opened up the possibility to create long-range interactions, mediated by the exchange of cavity photons [1, 42]. To create this interaction the quantum gas placed in the cavity is pumped transversally to the cavity axis leading to the scattering of the pump photons into the cavity mode [1, 45, 47, 186]. This process leads to the virtual exchange of cavity photons between the atoms of the cloud, thus creating a potential seen by all the atoms of the cloud. This potential provides the cavity-mediated long-range interaction. For large enough pump power the cloud self-organize such that all atoms scatter the pump photon in phase leading to a super-radiant phase. This cavity-mediated interaction has been used over the last years in combination with a bosonic Mott insulator to study the competition between short- and long-range interaction in the extended Bose-Hubbard model [33, 34].

The study of long-range cavity mediated interaction has been limited so far to bosonic quantum gases and thermal gases while studying this effect with Fermi gases was so far not possible despite strong theoretical interest [175–177, 179, 181, 193–196, 198, 208, 281–283]. As we have developed the first experiment combining both strong light-matter coupling and strong atom-atom interactions in a Fermi gas, I will present in this section the first steps towards the realization of long-range, cavity-mediated interactions in a strongly interacting Fermi gas. I will explain the specificity of our experiment compared with the ones realized so far, where the pump was perpendicular to the cavity axis. In our experiment we use a pump tilted with respect to the cavity axis by a small angle. I will discuss the first experimental results where we observe the presence of superradiance above a critical pump power due to the self-organization of the cloud. This phase diagram shows that we can implement long-range interactions in our strongly interacting Fermi gas with contact interactions.

7.3.1 Tilted transverse pump setup

The cloud is placed at the center of the cavity mode. We typically prepare cloud comprising 8×10^5 atoms populating the two lowest hyperfine states. The large bias field is oriented vertically. A beam is aligned onto the atomic cloud with an angle of 18° with respect to the cavity axis. The pump beam, linearly polarized along the vertical axis, is retroreflected, creating a 1D lat-

tice potential with a wavevector $\vec{k}_p$ (figure 7.5.a). Both the cavity resonance and the pump frequencies are detuned with respect to the D_1 line of ^{6}Li by $\Delta_a/2\pi = -60$ GHz. The frequency of the pump beam is detuned with respect to the dressed cavity by a detuning $\Delta_c = 6\delta_{at}$.

During the experiment, the power of the pump beam is ramped up linearly over a duration of typically 5 ms to mitigate the heating effects while being slow enough to probe the steady state of the gas. At low power, no photons from the pump field are scattered into the cavity mode, thus no light is observed at the cavity output (figure 7.5.a). The pump power is then increased linearly. When it reaches the critical threshold power, light is scattered from the pump to the cavity mode by the cloud. The pump and scattered fields interfere, creating a 2D lattice potential and light is observed at the cavity output (figure 7.5.b). The interference potential is characterized by the two wavevectors $\vec{k}_+$ and $\vec{k}_-$, corresponding to the sum and difference of the pump $\vec{k}_p$ and cavity $\vec{k}_c$ field wavevectors.

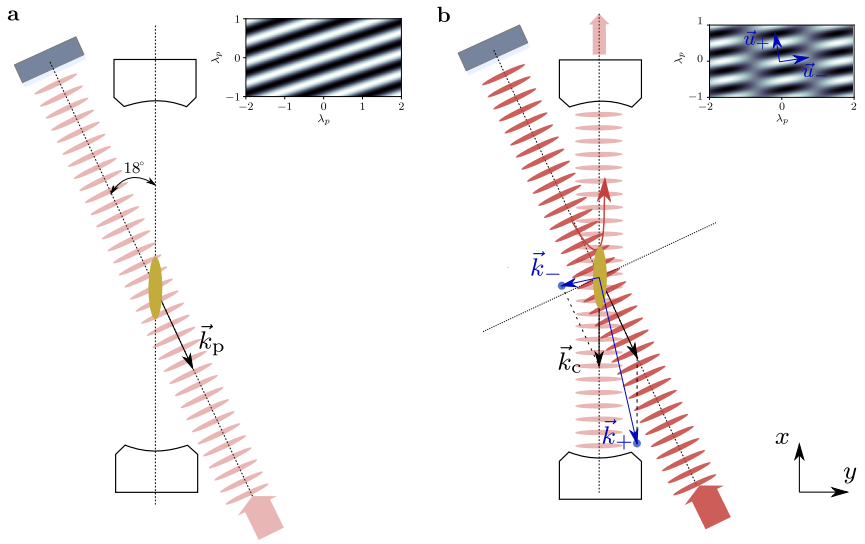

Figure 7.5: ***Self-organization and tilted-pump: concept.*** **a** The transverse pump consist of a retroreflected beam tilted by 18° with respect to the cavity axis. The pump laser frequency and the cavity resonance are detuned with respect to the atomic transition by $\Delta_a/2\pi = -60$ GHz. The transverse pump frequency is detuned with respect to the dispersively shifted cavity transmission by $\Delta_c/2\pi = -10\delta$ MHz, with $\delta_{at} = 1$ MHz the cavity dispersive shift. The cloud (in yellow) is trapped at the cavity mode center sees a 1D lattice potential (inset panel **a**). For low pump power no light is scattered in the cavity from the atomic density. **b** When increasing the pump power above a critical value, the cloud starts to scatter photons from the transverse pump field to the cavity mode. The scatted photons interferes with the 1D lattice of the transverse pump, forming a 2D lattice (inset panel **b**) with unit vector $\vec{u}_+$ and $\vec{u}_-$ corresponding to the sum and difference of the cavity $\vec{k}_c$ and pump wavevector $\vec{k}_p$, $\vec{k}_+$ and $\vec{k}_-$ respectively.

In the next section we will discuss the light-matter interaction Hamiltonian, showing the emergence of a potential due to the interference between the pump field and the scattered one in the cavity by the atomic cloud. This will give us the characteristics of the long range interactions mediated by the cavity that we will compare with the first experimental results observed on the experiment.

7.3.2 Observation of self-organization across the BEC-BCS crossover

Light-matter interaction Hamiltonian in the dispersive regime with a tilted pump

On a similar way as we defined the light-matter interaction Hamiltonian in the dispersive coupling regime in equation 7.4 we now introduce the Hamiltonian in the presence of a tilted pump

$$\hat{H} = \hat{H}_{at} + \omega_c \hat{a}^\dagger \hat{a} + \Omega \int d^3\mathbf{r} \hat{n}(\mathbf{r}) \hat{\phi}^\dagger \hat{\phi}(\mathbf{r}) \tag{7.7}$$

with a total electromagnetic field $\hat{\phi}(\mathbf{r}) = \hat{a} g_c(\mathbf{r}) + \alpha g_p(\mathbf{r}) e^{i\omega_p t}$, where we have the cavity mode function g_c, the pump mode mode function g_p and the pump frequency ω_{tp}. $\hat{H}_{at}$ is the atomic Hamiltonian describing the strongly correlated Fermi gas.

We expand the product $\hat{\phi}^\dagger \hat{\phi}(\mathbf{r})$ and integrate the dispersive shift in an effective tilted pump cavity resonance detuning Δ_c. The tilted pump potential is included in the atomic Hamiltonian. We can introduce the atomic mode

$$\hat{M} = \int d^3\mathbf{r} \hat{n}(\mathbf{r}) g_c(\mathbf{r}) g_p(\mathbf{r}) = \frac{1}{4} \left(\hat{n}_{\mathbf{k}_+} + \hat{n}_{-\mathbf{k}_+} + \hat{n}_{\mathbf{k}_-} + \hat{n}_{-\mathbf{k}_-} \right)$$

with $\hat{n}_{\mathbf{q}} = \int d^3\mathbf{r} \hat{n}(\mathbf{r}) e^{i\mathbf{q}\mathbf{r}}$ the Fourrier components of the density distribution at the spatial frequency q. The atomic mode $\hat{M}$ corresponds to the density modulation due to the interference between the tilted pump field and the light scattered in the cavity, thus inducing a density modulation at $\pm\vec{k}_+ = \pm\left(\vec{k}_c + \vec{k}_{tp}\right)$ and $\pm\vec{k}_- = \pm\left(\vec{k}_c - \vec{k}_{tp}\right)$. In our system $k_- = 0.31 \times k_c$ and $k_+ = 1.98 \times k_c$. We can also compare these wavevectors to the Fermi wavevector k_F leading to $k_-/k_F = 0.39$ and $k_+/k_F = 2.4$ with $E_F/2\pi = \hbar^2 k_F^2/2m = 47$ kHz. This shows that the density modulation building up at k_- is at much lower energy than k_+.

Performing the adiabatic elimination of the cavity field the effective interaction Hamiltonian reads

$$\hat{H}_{lm} = 2\frac{\Omega^2 |\alpha|^2}{\Delta_c} \hat{M}^2 \tag{7.8}$$

with $|\alpha|^2$ the intensity of the tilted pump field and Ω the dispersive coupling strength. This interaction term has a spatial dependency coming from $\hat{M}^2$ that will be $\propto \cos(k_- u) = \cos((\vec{k}_c - \vec{k}_{tp})u)$ and $\propto \cos(k_+ v) = \cos((\vec{k}_c + \vec{k}_{tp})v)$, u, v corresponding to the spatial coordinates in the $\vec{u}_-, \vec{u}_+$ basis (figure 7.5.b). This interaction only has this cosine modulation but no spatial decay over the cavity mode. This constitutes the cavity-mediated long range interaction term that depends linearly on the tilted-pump power $|\alpha|^2$ and is inversely proportional to the detuning of the tilted pump frequency with respect to the dressed cavity Δ_c.

First experimental results

We measured the phase diagram for a strongly interacting Fermi gase for various magnetic fields across the BEC-BCS crossover as a function of the detuning between the dressed-cavity and the tilted-pump frequency δ_{at} and of the tilted lattice depth s in unit of the ^{6}Li recoil $E_r/2\pi = \hbar \times 73.6$ kHz. The result are presented in figure 7.6.a-d.

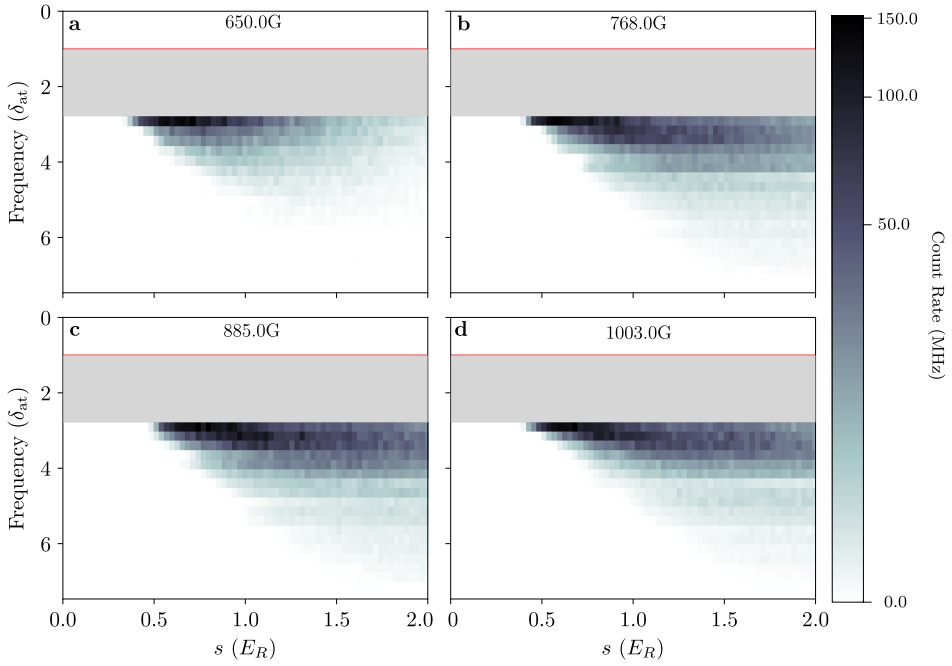

Figure 7.6: ***Self-organization of a strongly interacting Fermi gas across the BEC-BCS crossover: phase diagrams.*** **a-d** Phase diagrams as a function of the lattice depth s (in units of the ^{6}Li recoil) and of the detuning between the pump frequency and the dressed cavity (red line) in units of the dispersive shift δ_{at} for magnetic fields 650, 768, 885 and 1003 G. For detunings smaller that $2.6\delta_{at}$ the photon counter saturates due to large count rates, thus this points are excluded (grey region). The count rates are displayed in logarithmic scale. We see clear lattice depth threshold above which light is scattered in the cavity. This threshold depends linearly on the frequency detuning.

We observe for all magnetic fields the phase transition to a superradiant phase due to the self-organization of the strongly interacting cloud. For larger detunings between the pump and the dispersively shifted cavity, the power threshold increases. Comparing the evolution of the critical power threshold with equation 7.8, we observe a linear dependence of the threshold with the tilted-pump power as a function of Δ_c. The observation of superradiance across the BEC-BCS crossover validates that we can realize a strongly interacting Fermi gas with long-range interactions, opening an uncharted territory for quantum simulation. A short term perspective is the study of the influence of the short range atom-atom interaction on the location of the phase transition.

With this new system, combining both strong short and long range interactions, we can envision to measure all the characteristic physical quantities across the BEC-BCS crossover. Looking at the evolution of the critical temperature or of the pairing gap for varying strength of long-range interactions would provide interesting insights on the competition between the pairing and the long range interaction. As previously demonstrated for BECs [45], it is possible to perform a cavity-assisted Bragg spectroscopy measurement to probe the excitation spectrum of the gas. Experimentally it consists in injecting a beam along the cavity axis with a fixed frequency difference δ_{tp} with respect to the pump frequency 7.7.

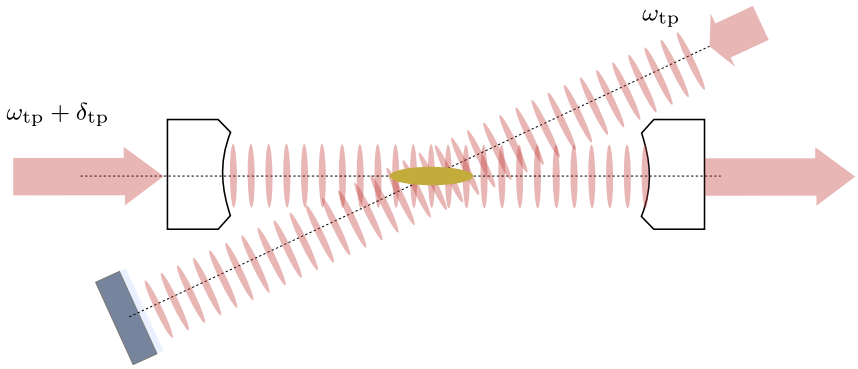

Figure 7.7: ***Cavity-assited bragg spectroscopy: concept.*** Cavity-assisted Bragg spectroscopy setup: in addition of the transverse pump a weak beam is coupled on the cavity axis at a fixed frequency difference with respect to the transverse pump frequency δ_{tp}. As we vary δ_{tp} we can map out the excitation spectrum onto the cavity transmission as a function of δ_{tp} [45].

The presence of the two beams onto the cloud can drive two-photon transitions, mapping the excitation spectrum at the frequency δ_{tp}. This method has been used to show the presence of a roton-mode softening in the BEC dispersion relation due to the presence of long-range interactions. The measurement of the cavity transmission as a function of the detuning δ_{tp} allows to map out the excitation spectrum [45]. We have implemented this capability onto the experiment where both the tilted-pump and the on-axis can be detuned by a fixed frequency. We hope to be able to connect the cavity field to the excitations of a strongly interaction Fermi gas [284, 285]. This would open up the possibility to study the excitation spectrum of a strongly interacting Fermi gas in the presence of long-range interactions, offering an uncharted territory for quantum simulation.

8

CONCLUSION

In this work, we have for the first time coupled a strongly interacting Fermi gas to cavity photon,, reaching the strong coupling regime. This has been made possible by the design of the experimental apparatus where we combine the production of deeply degenerate, strongly correlated Fermi gases and a high finesse optical cavity. The use of the cavity as an optical dipole trap has proven to be an interesting technique to efficiently capture atoms and perform efficient evaporative cooling once its lattice structure has been cancelled.

We also proved that reaching the strong light-matter coupling regime on molecular transitions was experimentally possible, by dressing PA transitions with the cavity photons. We demonstrated that the emerging dressed-states, the pair-polaritons, capture the universal short-range physics of the strongly correlated Fermi gas. We could confirm that our experiment reached the strong coupling regime for a single excitation of the ground state of the many-body Hamiltonian, paving the way to apply all quantum optics protocols to the many-body excitations of the gas. We also showed our ability to measure the pair-polaritons spectrum without destroying its many-body character. This result in very encouraging as pair-polaritons can be used to probe the short-range pair correlation function of a single system over time due to the weak destructivity of the cavity QED measurement. The pair-polariton will be an interesting tool to study the dynamics of strongly interacting Fermi gases in the future. The possibility to track the short-range correlation function in time after a quench is a very promising perspective and so is the measurement of the noise on the pair-correlation function that would give access to higher order correlation functions.

We also demonstrated that the same short-range physics of the many-body Hamiltonian should be imprinted onto the optomechanical non-linearity observed when probing the steady state of cavity-atom system far in the dispersive regime. This measurement and the pair-polaritons are the two sides of a same coin: the many-body physics is imprinted onto the optical spectrum which we can coherently access using our cavity QED apparatus.

In the last part of the manuscript I have shown the first results we obtained on the implementation of long-range interactions in the strongly correlated Fermi gas, making use of the standard self-organization framework used for BECs. Our observation of a self-organized, superradiant phase shows the existence of cavity-mediated long-range interactions in the gas. This new system opens up an uncharted territory for quantum simulation that cannot be explored by any other platform such as Rydberg atoms, quantum gases in optical lattices or dipolar quantum gases.

In the future we should be able to obtain a system with full and independent control on the short-range and long-range interaction between atoms for a degenerate Fermi gas. Besides the possibility of exploring all the changes due to the long-range interactions on the pairing gap or the critical temperature, this system offers the possibility to explore more fundamental

questions in the quest of understanding strongly correlated materials. With our system, where we know the microscopic Hamiltonian we will be able to study the competition between the pairing and the charge density wave due to long-range atom-atom interactions. Similarly we could implement long-range interactions between pairs using the dispersive coupling to PA transitions. This would allow to study the competition between pairing, the charge density and the pair density waves for a fermionic gas. This very rich system, with three possible types of interactions, would be extremely useful as only quantum simulation could make it possible to study this Hamiltonian.

Part IV

APPENDIX

A

TRANSFER CAVITY

This table summarize the properties of the transfer cavity discussed in Chapter 2 and 3

Table A.1: Transfer cavity optical properties.

	671 nm	532 nm	1064 nm
Cavity length	16 cm		
Free spectral range (ν_{FSR})	0.937(1) GHz		
Transverse Mode Spacing (ν_{TEM})	0.660(2) GHz		
Finesse	30000	3000	3000
Linewidth $\kappa/2\pi$	$3.1 \cdot 10^3$ kHz	$300 \cdot 10^3$ kHz	

The cavity mirrors are fixed onto a piezoelectric actuator itself glue onto a piece of Teflon in order to provide damping of mechanical vibrations A.1 and A.2. The two mirrors are then glued on a tube in carbon fiber that provides a high rigidity, thus high frequency mechanical vibration modes. The cavity in its carbon fiber tube lies onto a brass bar that is itself mounted onto Viton rods for vibration damping. The complete assembly is positioned in a standard CF40 cross with two large optical access along the cavity axis and one CF electrical feed through.

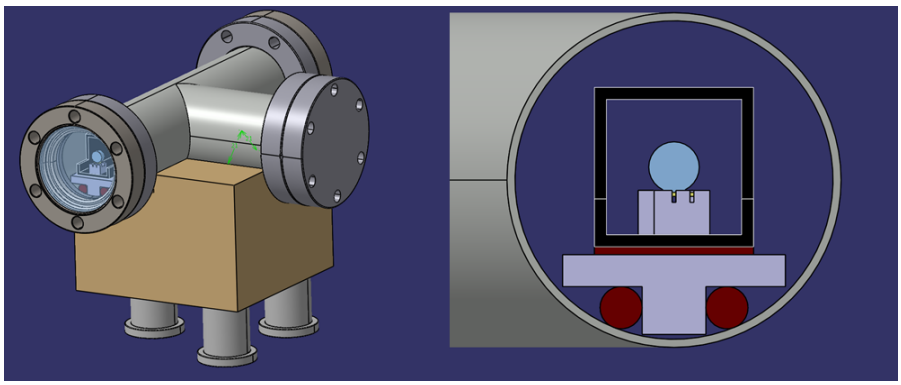

Figure A.1: *CAD view of the transfer cavity.*

The cross is mounted on a heavy mount made out of a massive brass cube that will have low frequency mechanical vibration mode, thus allowing to decouple the cavity from the acoustic environment. Three post fix it to the optical table. The mount is not fixed onto the post as three Sorbothane dampers are positioned in between the posts and the brass mount, providing an additional damping of vibrations.

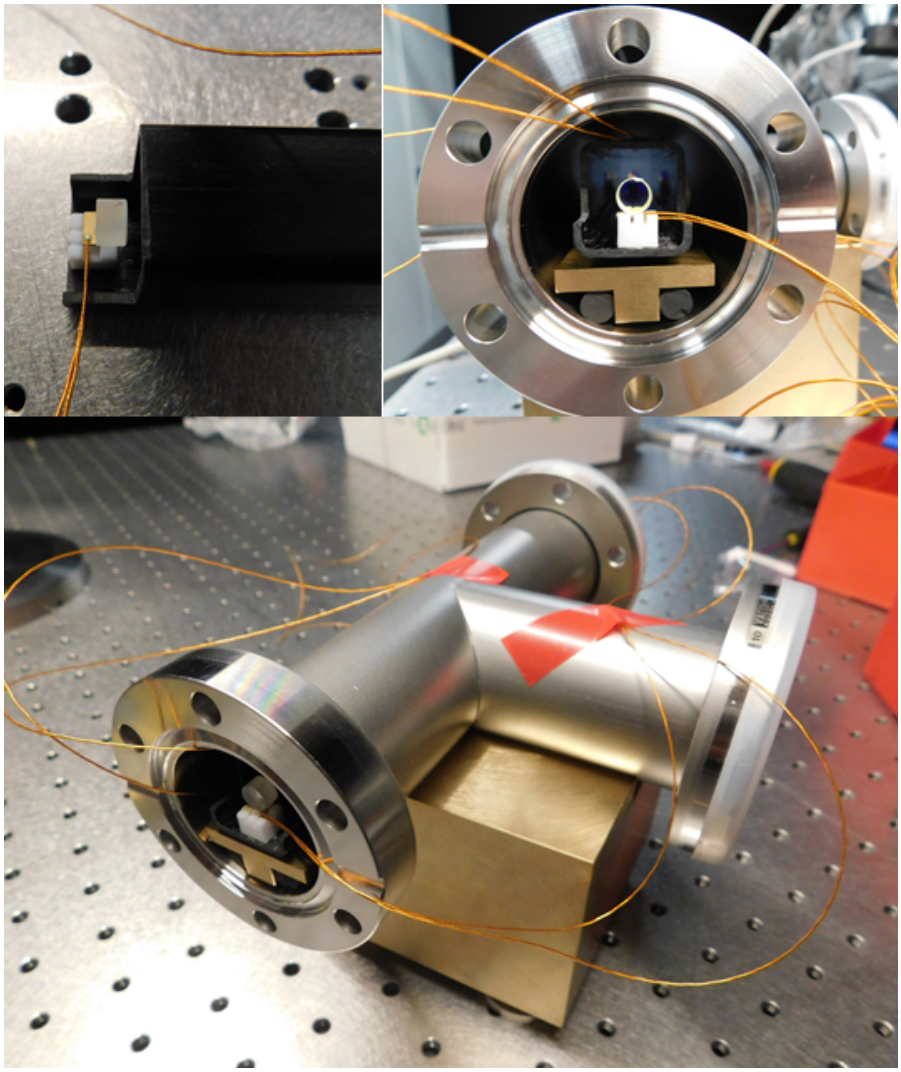

Figure A.2: *Picture of the transfer cavity.*

LIST OF FIGURES

LIST OF TABLES

BIBLIOGRAPHY

1. Mivehvar, F., Piazza, F., Donner, T. & Ritsch, H. Cavity QED with Quantum Gases: New Paradigms in Many-Body Physics. *arXiv:2102.04473 [cond-mat, physics:physics, physics:quant-ph].* arXiv: 2102.04473. http://arxiv.org/abs/2102.04473 (2021) (Feb. 2021) (cit. on pp. 1, 150, 188).
2. Imamoglu, A., Awschalom, D. D., Burkard, G., DiVincenzo, D. P., Loss, D., Sherwin, M. & Small, A. Quantum Information Processing Using Quantum Dot Spins and Cavity QED. *Physical Review Letters* **83.** Publisher: American Physical Society, 4204–4207. https://link.aps.org/doi/10.1103/PhysRevLett.83.4204 (2021) (Nov. 1999) (cit. on p. 1).
3. Spethmann, N., Kohler, J., Schreppler, S., Buchmann, L. & Stamper-Kurn, D. M. Cavity-mediated coupling of mechanical oscillators limited by quantum back-action. *Nature Physics* **12,** 27–31. https://www.nature.com/articles/nphys3515 (2021) (Jan. 2016) (cit. on pp. 1, 185).
4. LIGO Scientific Collaboration and Virgo Collaboration *et al.* Observation of Gravitational Waves from a Binary Black Hole Merger. *Physical Review Letters* **116.** Publisher: American Physical Society, 061102. https://link.aps.org/doi/10.1103/PhysRevLett.116.061102 (2021) (Feb. 2016) (cit. on p. 1).
5. Whittle, C. *et al.* Approaching the motional ground state of a 10-kg object. *Science* **372.** Publisher: American Association for the Advancement of Science Section: Report, 1333–1336. https://science.sciencemag.org/content/372/6548/1333 (2021) (June 2021) (cit. on p. 1).
6. Haroche, S., Brune, M. & Raimond, J. M. From cavity to circuit quantum electrodynamics. *Nature Physics* **16.** Publisher: Nature Publishing Group, 243–246. https://www.nature.com/articles/s41567-020-0812-1 (2021) (Mar. 2020) (cit. on p. 1).
7. Blais, A., Grimsmo, A. L., Girvin, S. & Wallraff, A. Circuit quantum electrodynamics. *Reviews of Modern Physics* **93.** Publisher: American Physical Society, 025005. https://link.aps.org/doi/10.1103/RevModPhys.93.025005 (2021) (May 2021) (cit. on p. 1).
8. Martinis, J. M., Devoret, M. H. & Clarke, J. Quantum Josephson junction circuits and the dawn of artificial atoms. *Nature Physics* **16.** Publisher: Nature Publishing Group, 234–237. https://www.nature.com/articles/s41567-020-0829-5 (2021) (Mar. 2020) (cit. on p. 1).
9. Chiorescu, I., Nakamura, Y., Harmans, C. J. P. M. & Mooij, J. E. Coherent Quantum Dynamics of a Superconducting Flux Qubit. *Science* **299.** Publisher: American Association for the Advancement of Science Section: Report, 1869–1871. https://science.sciencemag.org/content/299/5614/1869 (2021) (Mar. 2003) (cit. on p. 1).

10. Vion, D., Aassime, A., Cottet, A., Joyez, P., Pothier, H., Urbina, C., Esteve, D. & Devoret, M. H. Manipulating the Quantum State of an Electrical Circuit. *Science* **296.** Publisher: American Association for the Advancement of Science Section: Report, 886–889. https://science.sciencemag.org/content/296/5569/886 (2021) (May 2002) (cit. on p. 1).

11. Nakamura, Y., Pashkin, Y. A. & Tsai, J. S. Coherent control of macroscopic quantum states in a single-Cooper-pair box. *Nature* **398.** Publisher: Nature Publishing Group, 786–788. https://www.nature.com/articles/19718 (2021) (Apr. 1999) (cit. on p. 1).

12. Vučković, J. in *Quantum Optics and Nanophotonics* (Oxford University Press, Oxford, 2017). https://oxford.universitypressscholarship.com/10.1093/oso/9780198768609.001.0001/oso-9780198768609-chapter-8 (2021) (cit. on p. 1).

13. Burkard, G., Gullans, M. J., Mi, X. & Petta, J. R. Superconductor–semiconductor hybrid-circuit quantum electrodynamics. *Nature Reviews Physics* **2.** Publisher: Nature Publishing Group, 129–140. https://www.nature.com/articles/s42254-019-0135-2 (2021) (Mar. 2020) (cit. on p. 1).

14. Najer, D. *et al.* A gated quantum dot strongly coupled to an optical microcavity. *Nature* **575.** Publisher: Nature Publishing Group, 622–627. https://www.nature.com/articles/s41586-019-1709-y (2021) (Nov. 2019) (cit. on p. 1).

15. Scarlino, P. *et al.* Coherent microwave-photon-mediated coupling between a semiconductor and a superconducting qubit. *Nature Communications* **10.** Publisher: Nature Publishing Group, 3011. https://www.nature.com/articles/s41467-019-10798-6 (2021) (July 2019) (cit. on p. 1).

16. Landig, A. J., Koski, J. V., Scarlino, P., Mendes, U. C., Blais, A., Reichl, C., Wegscheider, W., Wallraff, A., Ensslin, K. & Ihn, T. Coherent spin–photon coupling using a resonant exchange qubit. *Nature* **560,** 179–184. https://www.nature.com/articles/s41586-018-0365-y (2021) (Aug. 2018) (cit. on p. 1).

17. Kawakami, E., Scarlino, P., Ward, D. R., Braakman, F. R., Savage, D. E., Lagally, M. G., Friesen, M., Coppersmith, S. N., Eriksson, M. A. & Vandersypen, L. M. K. Electrical control of a long-lived spin qubit in a Si/SiGe quantum dot. *Nature Nanotechnology* **9.** Publisher: Nature Publishing Group, 666–670. https://www.nature.com/articles/nnano.2014.153 (2021) (Sept. 2014) (cit. on p. 1).

18. Wallraff, A., Schuster, D. I., Blais, A., Frunzio, L., Huang, R.-S., Majer, J., Kumar, S., Girvin, S. M. & Schoelkopf, R. J. Strong coupling of a single photon to a superconducting qubit using circuit quantum electrodynamics. *Nature* **431.** Publisher: Nature Publishing Group, 162–167. https://www.nature.com/articles/nature02851 (2021) (Sept. 2004) (cit. on p. 1).

19. Blais, A., Huang, R.-S., Wallraff, A., Girvin, S. M. & Schoelkopf, R. J. Cavity quantum electrodynamics for superconducting electrical circuits: An architecture for quantum computation. *Physical Review A* **69.** Publisher: American Physical Society, 062320. https://link.aps.org/doi/10.1103/PhysRevA.69.062320 (2021) (June 2004) (cit. on p. 1).

20. Blais, A., Girvin, S. M. & Oliver, W. D. Quantum information processing and quantum optics with circuit quantum electrodynamics. *Nature Physics* **16.** Publisher: Nature Publishing Group, 247–256. https://www.nature.com/articles/s41567-020-0806-z (2021) (Mar. 2020) (cit. on p. 1).

21. Arute, F. *et al.* Quantum supremacy using a programmable superconducting processor. *Nature* **574.** Publisher: Nature Publishing Group, 505–510. https://www.nature.com/articles/s41586-019-1666-5 (2021) (Oct. 2019) (cit. on p. 1).

22. Watson, T. F. *et al.* A programmable two-qubit quantum processor in silicon. *Nature* **555.** Publisher: Nature Publishing Group, 633–637. https://www.nature.com/articles/nature25766 (2021) (Mar. 2018) (cit. on p. 1).

23. Capone, M., Fabrizio, M., Castellani, C. & Tosatti, E. Strongly Correlated Superconductivity. *Science* **296.** Publisher: American Association for the Advancement of Science Section: Report, 2364–2366. https://science.sciencemag.org/content/296/5577/2364 (2021) (June 2002) (cit. on p. 1).

24. Tokura, Y., Kawasaki, M. & Nagaosa, N. Emergent functions of quantum materials. *Nature Physics* **13.** Number: 11 Publisher: Nature Publishing Group, 1056–1068. https://www.nature.com/articles/nphys4274 (2021) (Nov. 2017) (cit. on p. 1).

25. Basov, D. N., Averitt, R. D. & Hsieh, D. Towards properties on demand in quantum materials. *Nature Materials* **16.** Number: 11 Publisher: Nature Publishing Group, 1077–1088. https://www.nature.com/articles/nmat5017 (2021) (Nov. 2017) (cit. on p. 1).

26. Fausti, D., Tobey, R. I., Dean, N., Kaiser, S., Dienst, A., Hoffmann, M. C., Pyon, S., Takayama, T., Takagi, H. & Cavalleri, A. Light-Induced Superconductivity in a Stripe-Ordered Cuprate. *Science* **331.** Publisher: American Association for the Advancement of Science Section: Report, 189–191. https://science.sciencemag.org/content/331/6014/189 (2021) (Jan. 2011) (cit. on p. 1).

27. Hu, W., Kaiser, S., Nicoletti, D., Hunt, C. R., Gierz, I., Hoffmann, M. C., Le Tacon, M., Loew, T., Keimer, B. & Cavalleri, A. Optically enhanced coherent transport in YBa2Cu3O6.5 by ultrafast redistribution of interlayer coupling. *Nature Materials* **13.** Publisher: Nature Publishing Group, 705–711. https://www.nature.com/articles/nmat3963 (2021) (July 2014) (cit. on p. 1).

28. Thomas, A. *et al.* Exploring Superconductivity under Strong Coupling with the Vacuum Electromagnetic Field. *arXiv:1911.01459 [cond-mat, physics:quant-ph].* arXiv: 1911.01459. http://arxiv.org/abs/1911.01459 (2021) (Dec. 2019) (cit. on p. 1).

29. Mitrano, M. *et al.* Possible light-induced superconductivity in K3C60 at high temperature. *Nature* **530.** Publisher: Nature Publishing Group, 461–464. https://www.nature.com/articles/nature16522 (2021) (Feb. 2016) (cit. on p. 1).

30. Raimond, J. M., Brune, M. & Haroche, S. Manipulating quantum entanglement with atoms and photons in a cavity. *Reviews of Modern Physics* **73.** Publisher: American Physical Society, 565–582. https://link.aps.org/doi/10.1103/RevModPhys.73.565 (2021) (Aug. 2001) (cit. on p. 1).

31. Gleyzes, S., Kuhr, S., Guerlin, C., Bernu, J., Deléglise, S., Busk Hoff, U., Brune, M., Raimond, J.-M. & Haroche, S. Quantum jumps of light recording the birth and death of a photon in a cavity. *Nature* **446.** Publisher: Nature Publishing Group, 297–300. https://www.nature.com/articles/nature05589 (2021) (Mar. 2007) (cit. on p. 1).

32. Deléglise, S., Dotsenko, I., Sayrin, C., Bernu, J., Brune, M., Raimond, J.-M. & Haroche, S. Reconstruction of non-classical cavity field states with snapshots of their decoherence. *Nature* **455.** Publisher: Nature Publishing Group, 510–514. https://www.nature.com/articles/nature07288 (2021) (Sept. 2008) (cit. on p. 1).

33. Landig, R., Hruby, L., Dogra, N., Landini, M., Mottl, R., Donner, T. & Esslinger, T. Quantum phases from competing short- and long-range interactions in an optical lattice. *Nature* **532.** Publisher: Nature Publishing Group, 476–479. https://www.nature.com/articles/nature17409 (2021) (Apr. 2016) (cit. on pp. 1, 122, 188).

34. Klinder, J., Keßler, H., Bakhtiari, M. R., Thorwart, M. & Hemmerich, A. Observation of a Superradiant Mott Insulator in the Dicke-Hubbard Model. *Physical Review Letters* **115.** Publisher: American Physical Society, 230403. https://link.aps.org/doi/10.1103/PhysRevLett.115.230403 (2021) (Dec. 2015) (cit. on pp. 1, 122, 188).

35. Léonard, J., Morales, A., Zupancic, P., Esslinger, T. & Donner, T. Supersolid formation in a quantum gas breaking a continuous translational symmetry. *Nature* **543,** 87–90. https://www.nature.com/articles/nature21067 (2019) (Mar. 2017) (cit. on p. 1).

36. Reiserer, A. & Rempe, G. Cavity-based quantum networks with single atoms and optical photons. *Reviews of Modern Physics* **87.** Publisher: American Physical Society, 1379–1418. https://link.aps.org/doi/10.1103/RevModPhys.87.1379 (2021) (Dec. 2015) (cit. on pp. 1, 122, 150).

37. Specht, H. P., Nölleke, C., Reiserer, A., Uphoff, M., Figueroa, E., Ritter, S. & Rempe, G. A single-atom quantum memory. *Nature* **473.** Publisher: Nature Publishing Group, 190–193. https://www.nature.com/articles/nature09997 (2021) (May 2011) (cit. on pp. 1, 126).

38. Leroux, I. D., Schleier-Smith, M. H. & Vuletić, V. Implementation of Cavity Squeezing of a Collective Atomic Spin. *Physical Review Letters* **104.** Publisher: American Physical Society, 073602. https://link.aps.org/doi/10.1103/PhysRevLett.104.073602 (2021) (Feb. 2010) (cit. on p. 1).

39. Braverman, B. *et al.* Near-Unitary Spin Squeezing in ^{171}Yb. *Physical Review Letters* **122.** Publisher: American Physical Society, 223203. https://link.aps.org/doi/10.1103/PhysRevLett.122.223203 (2021) (June 2019) (cit. on pp. 1, 122).

40. Sayrin, C. *et al.* Real-time quantum feedback prepares and stabilizes photon number states. *Nature* **477.** Publisher: Nature Publishing Group, 73–77. https://www.nature.com/articles/nature10376 (2021) (Sept. 2011) (cit. on p. 1).

41. Brooks, D. W. C., Botter, T., Schreppler, S., Purdy, T. P., Brahms, N. & Stamper-Kurn, D. M. Non-classical light generated by quantum-noise-driven cavity optomechanics. *Nature* **488.** Publisher: Nature Publishing Group, 476–480. https://www.nature.com/articles/nature11325 (2021) (Aug. 2012) (cit. on pp. 1, 185).

42. Ritsch, H., Domokos, P., Brennecke, F. & Esslinger, T. Cold atoms in cavity-generated dynamical optical potentials. *Reviews of Modern Physics* **85.** Publisher: American Physical Society, 553–601. https://link.aps.org/doi/10.1103/RevModPhys.85.553 (2021) (Apr. 2013) (cit. on pp. 1, 122, 150, 175, 188).

43. Brennecke, F., Donner, T., Ritter, S., Bourdel, T., Köhl, M. & Esslinger, T. Cavity QED with a Bose–Einstein condensate. *Nature* **450.** Publisher: Nature Publishing Group, 268–271. https://www.nature.com/articles/nature06120 (2021) (Nov. 2007) (cit. on pp. 1, 122).

44. Colombe, Y., Steinmetz, T., Dubois, G., Linke, F., Hunger, D. & Reichel, J. Strong atom–field coupling for Bose–Einstein condensates in an optical cavity on a chip. *Nature* **450.** Publisher: Nature Publishing Group, 272–276. https://www.nature.com/articles/nature06331 (2021) (Nov. 2007) (cit. on pp. 1, 122).

45. Mottl, R., Brennecke, F., Baumann, K., Landig, R., Donner, T. & Esslinger, T. Roton-Type Mode Softening in a Quantum Gas with Cavity-Mediated Long-Range Interactions. *Science* **336.** Publisher: American Association for the Advancement of Science Section: Report, 1570–1573. https://science.sciencemag.org/content/336/6088/1570 (2021) (June 2012) (cit. on pp. 1, 68, 150, 188, 191, 192).

46. Norcia, M. A., Lewis-Swan, R. J., Cline, J. R. K., Zhu, B., Rey, A. M. & Thompson, J. K. Cavity-mediated collective spin-exchange interactions in a strontium superradiant laser. *Science* **361.** Publisher: American Association for the Advancement of Science Section: Report, 259–262. https://science.sciencemag.org/content/361/6399/259 (2021) (July 2018) (cit. on pp. 1, 150).

47. Baumann, K., Mottl, R., Brennecke, F. & Esslinger, T. Exploring Symmetry Breaking at the Dicke Quantum Phase Transition. *Physical Review Letters* **107.** Publisher: American Physical Society, 140402. https://link.aps.org/doi/10.1103/PhysRevLett.107.140402 (2021) (Sept. 2011) (cit. on pp. 1, 188).

48. Pedrozo-Peñafiel, E. *et al.* Entanglement on an optical atomic-clock transition. *Nature* **588.** Publisher: Nature Publishing Group, 414–418. https://www.nature.com/articles/s41586-020-3006-1 (2021) (Dec. 2020) (cit. on p. 1).

49. Kroeze, R. M., Guo, Y. & Lev, B. L. Dynamical Spin-Orbit Coupling of a Quantum Gas. *Physical Review Letters* **123.** Publisher: American Physical Society, 160404. https://link.aps.org/doi/10.1103/PhysRevLett.123.160404 (2021) (Oct. 2019) (cit. on p. 1).

50. Rylands, C., Guo, Y., Lev, B. L., Keeling, J. & Galitski, V. Photon-Mediated Peierls Transition of a 1D Gas in a Multimode Optical Cavity. *Physical Review Letters* **125.** Publisher: American Physical Society, 010404. https://link.aps.org/doi/10.1103/PhysRevLett.125.010404 (2021) (July 2020) (cit. on p. 1).

51. Ostermann, S., Piazza, F. & Ritsch, H. Spontaneous Crystallization of Light and Ultracold Atoms. *Physical Review X* **6.** Publisher: American Physical Society, 021026. https://link.aps.org/doi/10.1103/PhysRevX.6.021026 (2021) (May 2016) (cit. on p. 1).

52. Gopalakrishnan, S., Lev, B. L. & Goldbart, P. M. Emergent crystallinity and frustration with Bose–Einstein condensates in multimode cavities. *Nature Physics* **5.** Publisher: Nature Publishing Group, 845–850. https://www.nature.com/articles/nphys1403 (2021) (Nov. 2009) (cit. on p. 1).

53. Schuster, S., Wolf, P., Ostermann, S., Slama, S. & Zimmermann, C. Supersolid Properties of a Bose-Einstein Condensate in a Ring Resonator. *Physical Review Letters* **124.** Publisher: American Physical Society, 143602. https://link.aps.org/doi/10.1103/PhysRevLett.124.143602 (2021) (Apr. 2020) (cit. on p. 1).

54. Shalabney, A., George, J., Hutchison, J., Pupillo, G., Genet, C. & Ebbesen, T. W. Coherent coupling of molecular resonators with a microcavity mode. *Nature Communications* **6.** Publisher: Nature Publishing Group, 5981. https://www.nature.com/articles/ncomms6981 (2021) (Jan. 2015) (cit. on p. 1).

55. Wellnitz, D., Schütz, S., Whitlock, S., Schachenmayer, J. & Pupillo, G. Collective Dissipative Molecule Formation in a Cavity. *Physical Review Letters* **125.** Publisher: American Physical Society, 193201. https://link.aps.org/doi/10.1103/PhysRevLett.125.193201 (2021) (Nov. 2020) (cit. on pp. 1, 176).

56. Flick, J., Ruggenthaler, M., Appel, H. & Rubio, A. Atoms and molecules in cavities, from weak to strong coupling in quantum-electrodynamics (QED) chemistry. *Proceedings of the National Academy of Sciences* **114.** Publisher: National Academy of Sciences Section: Physical Sciences, 3026–3034. https://www.pnas.org/content/114/12/3026 (2021) (Mar. 2017) (cit. on pp. 1, 176).

57. Kampschulte, T. & Denschlag, J. H. Cavity-controlled formation of ultracold molecules. *New Journal of Physics* **20.** Publisher: IOP Publishing, 123015. https://doi.org/10.1088/1367-2630/aaf5f5 (2021) (Dec. 2018) (cit. on pp. 1, 176).

58. Bohn, J. L., Rey, A. M. & Ye, J. Cold molecules: Progress in quantum engineering of chemistry and quantum matter. *Science* **357.** Publisher: American Association for the Advancement of Science Section: Review, 1002–1010. https://science.sciencemag.org/content/357/6355/1002 (2021) (Sept. 2017) (cit. on pp. 1, 2, 176).

59. Ni, K.-K., Ospelkaus, S., Miranda, M. H. G. d., Pe'er, A., Neyenhuis, B., Zirbel, J. J., Kotochigova, S., Julienne, P. S., Jin, D. S. & Ye, J. A High Phase-Space-Density Gas of Polar Molecules. *Science* **322.** Publisher: American Association for the Advancement of Science Section: Research Article, 231–235. https://science.sciencemag.org/content/322/5899/231 (2021) (Oct. 2008) (cit. on pp. 1, 152).

60. Valtolina, G., Matsuda, K., Tobias, W. G., Li, J.-R., De Marco, L. & Ye, J. Dipolar evaporation of reactive molecules to below the Fermi temperature. *Nature* **588.** Publisher: Nature Publishing Group, 239–243. https://www.nature.com/articles/s41586-020-2980-7 (2021) (Dec. 2020) (cit. on p. 1).

61. Marco, L. D., Valtolina, G., Matsuda, K., Tobias, W. G., Covey, J. P. & Ye, J. A degenerate Fermi gas of polar molecules. *Science* **363.** Publisher: American Association for the Advancement of Science Section: Report, 853–856. https://science.sciencemag.org/content/363/6429/853 (2021) (Feb. 2019) (cit. on p. 1).

62. Liu, Y., Hu, M.-G., Nichols, M. A., Yang, D., Xie, D., Guo, H. & Ni, K.-K. Precision test of statistical dynamics with state-to-state ultracold chemistry. *Nature* **593.** Publisher: Nature Publishing Group, 379–384. https://www.nature.com/articles/s41586-021-03459-6 (2021) (May 2021) (cit. on p. 1).

63. Hu, M.-G., Liu, Y., Nichols, M. A., Zhu, L., Quéméner, G., Dulieu, O. & Ni, K.-K. Nuclear spin conservation enables state-to-state control of ultracold molecular reactions. *Nature Chemistry* **13.** Publisher: Nature Publishing Group, 435–440. https://www.nature.com/articles/s41557-020-00610-0 (2021) (May 2021) (cit. on p. 1).

64. Liu, Y., Hu, M.-G., Nichols, M. A., Grimes, D. D., Karman, T., Guo, H. & Ni, K.-K. Photo-excitation of long-lived transient intermediates in ultracold reactions. *Nature Physics* **16.** Publisher: Nature Publishing Group, 1132–1136. https://www.nature.com/articles/s41567-020-0968-8 (2021) (Nov. 2020) (cit. on p. 1).

65. Hu, M.-G., Liu, Y., Grimes, D. D., Lin, Y.-W., Gheorghe, A. H., Vexiau, R., Bouloufa-Maafa, N., Dulieu, O., Rosenband, T. & Ni, K.-K. Direct observation of bimolecular reactions of ultracold KRb molecules. *Science* **366.** Publisher: American Association for the Advancement of Science Section: Report, 1111–1115. https://science.sciencemag.org/content/366/6469/1111 (2021) (Nov. 2019) (cit. on p. 1).

66. Anderegg, L., Cheuk, L. W., Bao, Y., Burchesky, S., Ketterle, W., Ni, K.-K. & Doyle, J. M. An optical tweezer array of ultracold molecules. *Science* **365.** Publisher: American Association for the Advancement of Science Section: Report, 1156–1158. https://science.sciencemag.org/content/365/6458/1156 (2021) (Sept. 2019) (cit. on p. 1).

67. Anderegg, L., Burchesky, S., Bao, Y., Yu, S. S., Karman, T., Chae, E., Ni, K.-K., Ketterle, W. & Doyle, J. M. Observation of Microwave Shielding of Ultracold Molecules. *arXiv:2102.04365 [cond-mat, physics:physics].* arXiv: 2102.04365. http://arxiv.org/abs/2102.04365 (2021) (Feb. 2021) (cit. on p. 1).

68. Roux, K., Konishi, H., Helson, V. & Brantut, J.-P. Strongly correlated Fermions strongly coupled to light. *Nature Communications* **11.** Publisher: Nature Publishing Group, 2974. https://www.nature.com/articles/s41467-020-16767-8 (2021) (June 2020) (cit. on p. 1).

69. *The BCS-BEC Crossover and the Unitary Fermi Gas* (ed Zwerger, W.) https://www.springer.com/gp/book/9783642219771 (2021) (Springer-Verlag, Berlin Heidelberg, 2012) (cit. on pp. 2, 106, 108).

70. Making, probing and understanding ultracold Fermi gases. *La Rivista del Nuovo Cimento* **31,** 247–422. https://doi.org/10.1393/ncr/i2008-10033-1 (2021) (July 2008) (cit. on pp. 2, 96, 103, 109).

71. Chin, C., Grimm, R., Julienne, P. & Tiesinga, E. Feshbach resonances in ultracold gases. *Reviews of Modern Physics* **82.** Publisher: American Physical Society, 1225–1286. https://link.aps.org/doi/10.1103/RevModPhys.82.1225 (2021) (Apr. 2010) (cit. on pp. 2, 35, 55, 72, 81, 96, 100, 101, 103).

72. Partridge, G. B., Strecker, K. E., Kamar, R. I., Jack, M. W. & Hulet, R. G. Molecular Probe of Pairing in the BEC-BCS Crossover. *Physical Review Letters* **95.** Publisher: American Physical Society, 020404. https://link.aps.org/doi/10.1103/PhysRevLett.95.020404 (2021) (July 2005) (cit. on pp. 2, 102, 150, 152, 168).

73. Konishi, H., Roux, K., Helson, V. & Brantut, J.-P. Universal pair-polaritons in a strongly interacting Fermi gas. *arXiv:2103.02459 [cond-mat, physics:physics, physics:quant-ph]*. arXiv: 2103.02459. http://arxiv.org/abs/2103.02459 (2021) (Mar. 2021) (cit. on p. 2).

74. Cirac, J. I. & Zoller, P. Goals and opportunities in quantum simulation. *Nature Physics* **8.** Number: 4 Publisher: Nature Publishing Group, 264–266. https://www.nature.com/articles/nphys2275 (2021) (Apr. 2012) (cit. on pp. 2, 122).

75. Roux, K., Helson, V., Konishi, H. & Brantut, J. P. Cavity-assisted preparation and detection of a unitary Fermi gas. *New Journal of Physics* **23.** Publisher: IOP Publishing, 043029. https://doi.org/10.1088/1367-2630/abeb91 (2021) (Apr. 2021) (cit. on pp. 2, 174).

76. *A User's Guide to Vacuum Technology, 3rd Edition | Wiley* https://www.wiley.com/en-us/A+User%27s+Guide+to+Vacuum+Technology%2C+3rd+Edition-p-9780471270522 (2021) (cit. on p. 10).

77. Gehm, M. E. *Preparation of an optically-trapped degenerate Fermi gas of 6Li: Finding the route to degeneracy* Publication Title: Ph.D. Thesis ADS Bibcode: 2003PhDT.....61G. PhD thesis (Jan. 2003). https://ui.adsabs.harvard.edu/abs/2003PhDT.....61G (2021) (cit. on pp. 16, 17, 20).

78. Brog, K. C., Eck, T. G. & Wieder, H. Fine and Hyperfine Structure of the 2^2P Term of Li^6 and Li^7. *Physical Review* **153.** Publisher: American Physical Society, 91–103. https://link.aps.org/doi/10.1103/PhysRev.153.91 (2021) (Jan. 1967) (cit. on p. 17).

79. Krinner, S. J. *Quantum Transport of Ultracold Atoms* Accepted: 2017-12-05T13:20:14Z. Doctoral Thesis (ETH Zurich, 2015). https://www.research-collection.ethz.ch/handle/20.500.11850/106754 (2021) (cit. on pp. 19, 181).

80. Kogelnik, H. & Li, T. Laser Beams and Resonators. *Applied Optics* **5.** Publisher: Optical Society of America, 1550–1567. https://www.osapublishing.org/ao/abstract.cfm?uri=ao-5-10-1550 (2021) (Oct. 1966) (cit. on p. 24).

81. Siegman, A. E. *Lasers* (University Science Books, 1986) (cit. on pp. 24, 26).

82. Poirson, J., Bretenaker, F., Vallet, M. & Floch, A. L. Analytical and experimental study of ringing effects in a Fabry–Perot cavity. Application to the measurement of high finesses. *JOSA B* **14.** Publisher: Optical Society of America, 2811–2817. https://www.osapublishing.org/josab/abstract.cfm?uri=josab-14-11-2811 (2021) (Nov. 1997) (cit. on p. 29).

83. Chubar, O., Elleaume, P. & Chavanne, J. A three-dimensional magnetostatics computer code for insertion devices. *Journal of Synchrotron Radiation* **5,** 481–484 (May 1998) (cit. on p. 31).

84. Roux, K., Cilenti, B., Helson, V., Konishi, H. & Brantut, J.-P. Compact bulk-machined electromagnets for quantum gas experiments. *SciPost Physics* **6,** 048. https://scipost.org/SciPostPhys.6.4.048 (2021) (Apr. 2019) (cit. on p. 34).

85. Metcalf, H. J. & Straten, P. v. d. Laser cooling and trapping of atoms. *JOSA B* **20.** Publisher: Optical Society of America, 887–908. https://www.osapublishing.org/josab/abstract.cfm?uri=josab-20-5-887 (2021) (May 2003) (cit. on p. 35).

86. Bell, S. C., Junker, M., Jasperse, M., Turner, L. D., Lin, Y.-J., Spielman, I. B. & Scholten, R. E. A slow atom source using a collimated effusive oven and a single-layer variable pitch coil Zeeman slower. *Review of Scientific Instruments* **81.** Publisher: American Institute of Physics, 013105. https://aip.scitation.org/doi/10.1063/1.3276712 (2021) (Jan. 2010) (cit. on p. 35).

87. Cheiney, P., Carraz, O., Bartoszek-Bober, D., Faure, S., Vermersch, F., Fabre, C. M., Gattobigio, G. L., Lahaye, T., Guéry-Odelin, D. & Mathevet, R. A Zeeman slower design with permanent magnets in a Halbach configuration. *Review of Scientific Instruments* **82.** Publisher: American Institute of Physics, 063115. https://aip.scitation.org/doi/10.1063/1.3600897 (2021) (June 2011) (cit. on p. 35).

88. Bitter, F. The Design of Powerful Electromagnets Part II. The Magnetizing Coil. *Review of Scientific Instruments* **7.** Publisher: American Institute of Physics, 482–488. https://aip.scitation.org/doi/10.1063/1.1752068 (2021) (Dec. 1936) (cit. on pp. 35, 36).

89. Bitter, F. Water Cooled Magnets. *Review of Scientific Instruments* **33.** Publisher: American Institute of Physics, 342–349. https://aip.scitation.org/doi/10.1063/1.1717838 (2021) (Mar. 1962) (cit. on pp. 35, 36).

90. Sabulsky, D. O., Parker, C. V., Gemelke, N. D. & Chin, C. Efficient continuous-duty Bitter-type electromagnets for cold atom experiments. *Review of Scientific Instruments* **84.** Publisher: American Institute of Physics, 104706. https://aip.scitation.org/doi/10.1063/1.4826498 (2021) (Oct. 2013) (cit. on pp. 35, 36).

91. Wang, R., Liu, M., Minardi, F. & Kasevich, M. Reaching ^{7}Li quantum degeneracy with a minitrap. *Physical Review A* **75.** Publisher: American Physical Society, 013610. https://link.aps.org/doi/10.1103/PhysRevA.75.013610 (2021) (Jan. 2007) (cit. on p. 35).

92. Saint, R. *et al.* 3D-printed components for quantum devices. *Scientific Reports* **8.** Number: 1 Publisher: Nature Publishing Group, 8368. https://www.nature.com/articles/s41598-018-26455-9 (2021) (May 2018) (cit. on p. 35).

93. Zhou, Y., Welch, N., Crawford, R., Oručević, F., Wang, F., Krüger, P., Wildman, R., Tuck, C. & Fromhold, T. M. Design of Magneto-Optical Traps for Additive Manufacture by 3D Printing. *arXiv:1704.00430 [physics, physics:quant-ph].* arXiv: 1704.00430. http://arxiv.org/abs/1704.00430 (2021) (Apr. 2017) (cit. on p. 35).

94. Folman, R., Kruger, P., Schmiedmayer, J., Denschlag, J. & Henkel, C. Microscopic atom optics: from wires to an atom chip. *arXiv:0805.2613 [quant-ph].* arXiv: 0805.2613. http://arxiv.org/abs/0805.2613 (2021) (May 2008) (cit. on p. 35).

95. Reichel, J. Microchip traps and Bose–Einstein condensation. *Applied Physics B* **74,** 469–487. https://doi.org/10.1007/s003400200861 (2021) (Apr. 2002) (cit. on p. 35).

96. Ricci, L., Martini, L. M., Franchi, M. & Bertoldi, A. A current-carrying coil design with improved liquid cooling arrangement. *Review of Scientific Instruments* **84.** Publisher: American Institute of Physics, 065115. https://aip.scitation.org/doi/10.1063/1.4811666 (2021) (June 2013) (cit. on pp. 35, 36).

97. Long, Y., Xiong, F., Gaire, V., Caligan, C. & Parker, C. V. All-optical production of ^{6}Li molecular Bose-Einstein condensates in excited hyperfine levels. *Physical Review A* **98.** Publisher: American Physical Society, 043626. https://link.aps.org/doi/10.1103/PhysRevA.98.043626 (2021) (Oct. 2018) (cit. on pp. 36, 72).

98. Gänger, B., Phieler, J., Nagler, B. & Widera, A. A versatile apparatus for fermionic lithium quantum gases based on an interference-filter laser system. *Review of Scientific Instruments* **89.** Publisher: American Institute of Physics, 093105. https://aip.scitation.org/doi/full/10.1063/1.5045827 (2021) (Sept. 2018) (cit. on p. 36).

99. Starkey, P. T., Billington, C. J., Johnstone, S. P., Jasperse, M., Helmerson, K., Turner, L. D. & Anderson, R. P. A scripted control system for autonomous hardware-timed experiments. *Review of Scientific Instruments* **84.** Publisher: American Institute of Physics, 085111. https://aip.scitation.org/doi/10.1063/1.4817213 (2021) (Aug. 2013) (cit. on pp. 47, 48).

100. Metcalf, H. J. & Straten, P. v. d. Laser cooling and trapping of atoms. *JOSA B* **20.** Publisher: Optical Society of America, 887–908. https://www.osapublishing.org/josab/abstract.cfm?uri=josab-20-5-887 (2021) (May 2003) (cit. on p. 52).

101. Lett, P. D., Watts, R. N., Westbrook, C. I., Phillips, W. D., Gould, P. L. & Metcalf, H. J. Observation of Atoms Laser Cooled below the Doppler Limit. *Physical Review Letters* **61.** Publisher: American Physical Society, 169–172. https://link.aps.org/doi/10.1103/PhysRevLett.61.169 (2021) (July 1988) (cit. on pp. 52, 60).

102. Lu, Z. T., Corwin, K. L., Renn, M. J., Anderson, M. H., Cornell, E. A. & Wieman, C. E. Low-Velocity Intense Source of Atoms from a Magneto-optical Trap. *Physical Review Letters* **77.** Publisher: American Physical Society, 3331–3334. https://link.aps.org/doi/10.1103/PhysRevLett.77.3331 (2021) (Oct. 1996) (cit. on p. 52).

103. Phillips, W. D. Laser cooling and trapping of neutral atoms. *Rev. Mod. Phys.* **70,** 21 (1998) (cit. on p. 52).

104. Ketterle, W. & Druten, N. J. V. in *Advances In Atomic, Molecular, and Optical Physics* (eds Bederson, B. & Walther, H.) 181–236 (Academic Press, Jan. 1996). https://www.sciencedirect.com/science/article/pii/S1049250X08601019 (2021) (cit. on p. 52).

105. Dalibard, J. Une brève histoire des atomes froids, 126 (cit. on p. 52).

106. Grimm, R., Weidemüller, M. & Ovchinnikov, Y. B. in *Advances In Atomic, Molecular, and Optical Physics* (eds Bederson, B. & Walther, H.) 95–170 (Academic Press, Jan. 2000). https://www.sciencedirect.com/science/article/pii/S1049250X0860186X (2021) (cit. on p. 53).

107. Granade, S. R., Gehm, M. E., O'Hara, K. M. & Thomas, J. E. All-Optical Production of a Degenerate Fermi Gas. *Physical Review Letters* **88.** Publisher: American Physical Society, 120405. https://link.aps.org/doi/10.1103/PhysRevLett.88.120405 (2021) (Mar. 2002) (cit. on pp. 53, 72).

108. Luo, L., Clancy, B., Joseph, J., Kinast, J., Turlapov, A. & Thomas, J. E. Evaporative cooling of unitary Fermi gas mixtures in optical traps. *New Journal of Physics* **8.** Publisher: IOP Publishing, 213–213. https://doi.org/10.1088/1367-2630/8/9/213 (2021) (Sept. 2006) (cit. on pp. 55, 79).

109. Phelps, G. A., Hébert, A., Krahn, A., Dickerson, S., Öztürk, F., Ebadi, S., Su, L. & Greiner, M. Sub-second production of a quantum degenerate gas. *arXiv:2007.10807 [cond-mat, physics:physics].* arXiv: 2007.10807. http://arxiv.org/abs/2007.10807 (2021) (July 2020) (cit. on p. 55).

110. Phillips, W. D. & Metcalf, H. Laser Deceleration of an Atomic Beam. *Physical Review Letters* **48.** Publisher: American Physical Society, 596–599. https://link.aps.org/doi/10.1103/PhysRevLett.48.596 (2021) (Mar. 1982) (cit. on p. 56).

111. Metcalf, H. J., Straten, P. v. d. & Straten, P. v. d. *Laser Cooling and Trapping* https://www.springer.com/gp/book/9780387987286 (2021) (Springer-Verlag, New York, 1999) (cit. on p. 57).

112. Wieman, C. E. & Hollberg, L. Using diode lasers for atomic physics. *Review of Scientific Instruments* **62.** Publisher: American Institute of Physics, 1–20. https://aip.scitation.org/doi/10.1063/1.1142305 (2021) (Jan. 1991) (cit. on p. 57).

113. Preston, D. W. Doppler-free saturated absorption. *Laser spectroscopy.Am. J. Phys,* 1432—1436. (2021) (1996) (cit. on p. 57).

114. Dalibard, J. & Cohen-Tannoudji, C. Laser cooling below the Doppler limit by polarization gradients: simple theoretical models. *JOSA B* **6.** Publisher: Optical Society of America, 2023–2045. https://www.osapublishing.org/josab/abstract.cfm?uri=josab-6-11-2023 (2021) (Nov. 1989) (cit. on p. 60).

115. Duarte, P. M., Hart, R. A., Hitchcock, J. M., Corcovilos, T. A., Yang, T.-L., Reed, A. & Hulet, R. G. All-optical production of a lithium quantum gas using narrow-line laser cooling. *Physical Review A* **84.** Publisher: American Physical Society, 061406. https://link.aps.org/doi/10.1103/PhysRevA.84.061406 (2021) (Dec. 2011) (cit. on p. 60).

116. Burchianti, A., Valtolina, G., Seman, J. A., Pace, E., De Pas, M., Inguscio, M., Zaccanti, M. & Roati, G. Efficient all-optical production of large ^{6}Li quantum gases using D_1 gray-molasses cooling. *Physical Review A* **90.** Publisher: American Physical Society, 043408. https://link.aps.org/doi/10.1103/PhysRevA.90.043408 (2021) (Oct. 2014) (cit. on pp. 60, 72).

117. Grier, A. T., Ferrier-Barbut, I., Rem, B. S., Delehaye, M., Khaykovich, L., Chevy, F. & Salomon, C. Λ-enhanced sub-Doppler cooling of lithium atoms in D_1 gray molasses. *Physical Review A* **87.** Publisher: American Physical Society, 063411. https://link.aps.org/doi/10.1103/PhysRevA.87.063411 (2021) (June 2013) (cit. on p. 60).

118. Long, Y., Xiong, F., Gaire, V., Caligan, C. & Parker, C. V. All-optical production of ^{6}Li molecular Bose-Einstein condensates in excited hyperfine levels. *Physical Review A* **98.** Publisher: American Physical Society, 043626. https://link.aps.org/doi/10.1103/PhysRevA.98.043626 (2021) (Oct. 2018) (cit. on p. 60).

119. Mosk, A., Jochim, S., Moritz, H., Elsässer, T., Weidemüller, M. & Grimm, R. Resonator-enhanced optical dipole trap for fermionic lithium atoms. *Optics Letters* **26.** Publisher: Optical Society of America, 1837–1839. https://www.osapublishing.org/ol/abstract.cfm?uri=ol-26-23-1837 (2021) (Dec. 2001) (cit. on pp. 60, 74).

120. Naik, D. S., Kuyumjyan, G., Pandey, D., Bouyer, P. & Bertoldi, A. Bose–Einstein condensate array in a malleable optical trap formed in a traveling wave cavity. *Quantum Science and Technology* **3.** Publisher: IOP Publishing, 045009. https://doi.org/10.1088/2058-9565/aad48e (2021) (Aug. 2018) (cit. on pp. 60, 73).

121. Cox, K. C., Greve, G. P., Wu, B. & Thompson, J. K. Spatially homogeneous entanglement for matter-wave interferometry created with time-averaged measurements. *Physical Review A* **94.** Publisher: American Physical Society, 061601. https://link.aps.org/doi/10.1103/PhysRevA.94.061601 (2021) (Dec. 2016) (cit. on pp. 60, 69, 75).

122. Black, E. D. An introduction to Pound–Drever–Hall laser frequency stabilization. *American Journal of Physics* **69.** Publisher: American Association of Physics Teachers, 79–87. https://aapt.scitation.org/doi/10.1119/1.1286663 (2021) (Dec. 2000) (cit. on p. 62).

123. Whittaker, E. A., Gehrtz, M. & Bjorklund, G. C. Residual amplitude modulation in laser electro-optic phase modulation. *JOSA B* **2.** Publisher: Optical Society of America, 1320–1326. https://www.osapublishing.org/josab/abstract.cfm?uri=josab-2-8-1320 (2021) (Aug. 1985) (cit. on p. 64).

124. Jaatinen, E. & Hopper, D. J. Compensating for frequency shifts in modulation transfer spectroscopy caused by residual amplitude modulation. *Optics and Lasers in Engineering* **46,** 69–74. https://www.sciencedirect.com/science/article/pii/S0143816607001224 (2021) (Jan. 2008) (cit. on p. 64).

125. Fuchs, J., Duffy, G. J., Veeravalli, G., Dyke, P., Bartenstein, M., Vale, C. J., Hannaford, P. & Rowlands, W. J. Molecular Bose–Einstein condensation in a versatile low power crossed dipole trap. *Journal of Physics B: Atomic, Molecular and Optical Physics* **40.** Publisher: IOP Publishing, 4109–4118. https://doi.org/10.1088/0953-4075/40/20/011 (2021) (Oct. 2007) (cit. on p. 70).

126. Burchianti, A., Seman, J. A., Valtolina, G., Morales, A., Inguscio, M., Zaccanti, M. & Roati, G. All-optical production of ^{6}Li quantum gases. *Journal of Physics: Conference Series* **594.** Publisher: IOP Publishing, 012042. https://doi.org/10.1088/1742-6596/594/1/012042 (2021) (Mar. 2015) (cit. on p. 72).

127. Dieckmann, K., Stan, C. A., Gupta, S., Hadzibabic, Z., Schunck, C. H. & Ketterle, W. Decay of an Ultracold Fermionic Lithium Gas near a Feshbach Resonance. *Physical Review Letters* **89.** Publisher: American Physical Society, 203201. https://link.aps.org/doi/10.1103/PhysRevLett.89.203201 (2021) (Oct. 2002) (cit. on p. 81).

128. Schunck, C. H., Zwierlein, M. W., Stan, C. A., Raupach, S. M. F., Ketterle, W., Simoni, A., Tiesinga, E., Williams, C. J. & Julienne, P. S. Feshbach resonances in fermionic ^{6}Li. *Physical Review A* **71.** Publisher: American Physical Society, 045601. https://link.aps.org/doi/10.1103/PhysRevA.71.045601 (2021) (Apr. 2005) (cit. on p. 81).

129. Gerken, M., Tran, B., Häfner, S., Tiemann, E., Zhu, B. & Weidemüller, M. Observation of dipolar splittings in high-resolution atom-loss spectroscopy of $^{6}\mathrm{Li}$ p-wave Feshbach resonances. *Physical Review A* **100.** Publisher: American Physical Society, 050701. https://link.aps.org/doi/10.1103/PhysRevA.100.050701 (2021) (Nov. 2019) (cit. on p. 81).

130. Guajardo, E. R. S., Tey, M. K., Sidorenkov, L. A. & Grimm, R. Higher-nodal collective modes in a resonantly interacting Fermi gas. *Physical Review A* **87,** 063601. https://link.aps.org/doi/10.1103/PhysRevA.87.063601 (2019) (June 2013) (cit. on p. 82).

131. Gadway, B., Pertot, D., Reimann, R., Cohen, M. G. & Schneble, D. Analysis of Kapitza-Dirac diffraction patterns beyond the Raman-Nath regime. *Optics Express* **17.** Publisher: Optical Society of America, 19173–19180. https://www.osapublishing.org/oe/abstract.cfm?uri=oe-17-21-19173 (2021) (Oct. 2009) (cit. on p. 88).

132. Urban, E., Johnson, T. A., Henage, T., Isenhower, L., Yavuz, D. D., Walker, T. G. & Saffman, M. Observation of Rydberg blockade between two atoms. *Nature Physics* **5.** Publisher: Nature Publishing Group, 110–114. https://www.nature.com/articles/nphys1178 (2021) (Feb. 2009) (cit. on p. 92).

133. Wilk, T., Gaëtan, A., Evellin, C., Wolters, J., Miroshnychenko, Y., Grangier, P. & Browaeys, A. Entanglement of Two Individual Neutral Atoms Using Rydberg Blockade. *Physical Review Letters* **104.** Publisher: American Physical Society, 010502. https://link.aps.org/doi/10.1103/PhysRevLett.104.010502 (2021) (Jan. 2010) (cit. on p. 92).

134. Gadway, B. & Yan, B. Strongly interacting ultracold polar molecules. *Journal of Physics B: Atomic, Molecular and Optical Physics* **49.** Publisher: IOP Publishing, 152002. https://doi.org/10.1088/0953-4075/49/15/152002 (2021) (June 2016) (cit. on p. 92).

135. *Cold Molecules: Theory, Experiment, Applications* (eds Krems, R., Friedrich, B. & Stwalley, W. C.) (CRC Press, Boca Raton, June 2009) (cit. on p. 92).

136. Ni, K.-K., Ospelkaus, S., Wang, D., Quéméner, G., Neyenhuis, B., de Miranda, M. H. G., Bohn, J. L., Ye, J. & Jin, D. S. Dipolar collisions of polar molecules in the quantum regime. *Nature* **464.** Publisher: Nature Publishing Group, 1324–1328. https://www.nature.com/articles/nature08953 (2021) (Apr. 2010) (cit. on p. 92).

137. Lahaye, T., Menotti, C., Santos, L., Lewenstein, M. & Pfau, T. The physics of dipolar bosonic quantum gases. *Reports on Progress in Physics* **72.** Publisher: IOP Publishing, 126401. https://doi.org/10.1088/0034-4885/72/12/126401 (2021) (Nov. 2009) (cit. on p. 92).

138. Stuhler, J., Griesmaier, A., Koch, T., Fattori, M., Pfau, T., Giovanazzi, S., Pedri, P. & Santos, L. Observation of Dipole-Dipole Interaction in a Degenerate Quantum Gas. *Physical Review Letters* **95.** Publisher: American Physical Society, 150406. https://link.aps.org/doi/10.1103/PhysRevLett.95.150406 (2021) (Oct. 2005) (cit. on p. 92).

139. Dalibard, J. Les interactions entre atomes dans les gaz quantiques, 135 (cit. on pp. 92, 150, 152).

140. Yu, Z., Thywissen, J. H. & Zhang, S. Universal Relations for a Fermi Gas Close to a p-Wave Interaction Resonance. *Physical Review Letters* **115.** Publisher: American Physical Society, 135304. https://link.aps.org/doi/10.1103/PhysRevLett.115.135304 (2021) (Sept. 2015) (cit. on p. 96).

141. Giorgini, S., Pitaevskii, L. P. & Stringari, S. Theory of ultracold atomic Fermi gases. *Reviews of Modern Physics* **80.** Publisher: American Physical Society, 1215–1274. https://link.aps.org/doi/10.1103/RevModPhys.80.1215 (2021) (Oct. 2008) (cit. on p. 96).

142. Söding, J., Guéry-Odelin, D., Desbiolles, P., Ferrari, G. & Dalibard, J. Giant Spin Relaxation of an Ultracold Cesium Gas. *Physical Review Letters* **80.** Publisher: American Physical Society, 1869–1872. https://link.aps.org/doi/10.1103/PhysRevLett.80.1869 (2021) (Mar. 1998) (cit. on p. 100).

143. Feshbach, H. Unified theory of nuclear reactions. *Annals of Physics* **5,** 357–390. https://www.sciencedirect.com/science/article/pii/0003491658900071 (2021) (Dec. 1958) (cit. on p. 100).

144. Castin, Y. Basic theory tools for degenerate Fermi gases. *arXiv:cond-mat/0612613*. arXiv: cond-mat/0612613. http://arxiv.org/abs/cond-mat/0612613 (2021) (Apr. 2007) (cit. on pp. 101, 106, 108).

145. Zürn, G., Lompe, T., Wenz, A. N., Jochim, S., Julienne, P. S. & Hutson, J. M. Precise Characterization of ^{6}Li Feshbach Resonances Using Trap-Sideband-Resolved RF Spectroscopy of Weakly Bound Molecules. *Physical Review Letters* **110.** Publisher: American Physical Society, 135301. https://link.aps.org/doi/10.1103/PhysRevLett.110.135301 (2021) (Mar. 2013) (cit. on pp. 102, 107, 137).

146. Castin, Y. & Pricoupenko, L. One particle in a box: The simplest model for a Fermi gas in the unitary limit. *Physical Review A* **69.** Publisher: American Physical Society, 051601. https://link.aps.org/doi/10.1103/PhysRevA.69.051601 (2021) (May 2004) (cit. on p. 103).

147. Lee, Y.-R., Heo, M.-S., Choi, J.-H., Wang, T. T., Christensen, C. A., Rvachov, T. M. & Ketterle, W. Compressibility of an ultracold Fermi gas with repulsive interactions. *Physical Review A* **85.** Publisher: American Physical Society, 063615. https://link.aps.org/doi/10.1103/PhysRevA.85.063615 (2021) (June 2012) (cit. on p. 106).

148. Sanner, C., Su, E. J., Huang, W., Keshet, A., Gillen, J. & Ketterle, W. Correlations and Pair Formation in a Repulsively Interacting Fermi Gas. *Physical Review Letters* **108.** Publisher: American Physical Society, 240404. https://link.aps.org/doi/10.1103/PhysRevLett.108.240404 (2021) (June 2012) (cit. on p. 106).

149. Valtolina, G., Scazza, F., Amico, A., Burchianti, A., Recati, A., Enss, T., Inguscio, M., Zaccanti, M. & Roati, G. Exploring the ferromagnetic behaviour of a repulsive Fermi gas through spin dynamics. *Nature Physics* **13.** Publisher: Nature Publishing Group, 704–709. https://www.nature.com/articles/nphys4108 (2021) (July 2017) (cit. on p. 106).

150. Randeria, M. & Taylor, E. BCS-BEC Crossover and the Unitary Fermi Gas. *Annual Review of Condensed Matter Physics* **5.** arXiv: 1306.5785, 209–232. http://arxiv.org/abs/1306.5785 (2021) (Mar. 2014) (cit. on p. 106).

151. Petrov, D. S., Salomon, C. & Shlyapnikov, G. V. Scattering properties of weakly bound dimers of fermionic atoms. *Physical Review A* **71.** Publisher: American Physical Society, 012708. https://link.aps.org/doi/10.1103/PhysRevA.71.012708 (2021) (Jan. 2005) (cit. on p. 107).

152. Giorgini, S., Pitaevskii, L. P. & Stringari, S. Theory of ultracold atomic Fermi gases. *Reviews of Modern Physics* **80.** Publisher: American Physical Society, 1215–1274. https://link.aps.org/doi/10.1103/RevModPhys.80.1215 (2021) (Oct. 2008) (cit. on p. 107).

153. Zwierlein, M. W., Abo-Shaeer, J. R., Schirotzek, A., Schunck, C. H. & Ketterle, W. Vortices and superfluidity in a strongly interacting Fermi gas. *Nature* **435.** Publisher: Nature Publishing Group, 1047–1051. https://www.nature.com/articles/nature03858 (2021) (June 2005) (cit. on pp. 107, 145).

154. Tey, M. K., Sidorenkov, L. A., Guajardo, E. R. S., Grimm, R., Ku, M. J. H., Zwierlein, M. W., Hou, Y.-H., Pitaevskii, L. & Stringari, S. Collective Modes in a Unitary Fermi Gas across the Superfluid Phase Transition. *Physical Review Letters* **110.** Publisher: American Physical Society, 055303. https://link.aps.org/doi/10.1103/PhysRevLett.110.055303 (2021) (Jan. 2013) (cit. on pp. 107, 182).

155. Schirotzek, A., Shin, Y.-i., Schunck, C. H. & Ketterle, W. Determination of the Superfluid Gap in Atomic Fermi Gases by Quasiparticle Spectroscopy. *Physical Review Letters* **101.** Publisher: American Physical Society, 140403. https://link.aps.org/doi/10.1103/PhysRevLett.101.140403 (2021) (Oct. 2008) (cit. on p. 107).

156. O'Hara, K. M., Hemmer, S. L., Gehm, M. E., Granade, S. R. & Thomas, J. E. Observation of a Strongly Interacting Degenerate Fermi Gas of Atoms. *Science* **298.** Publisher: American Association for the Advancement of Science Section: Report, 2179–2182. https://science.sciencemag.org/content/298/5601/2179 (2021) (Dec. 2002) (cit. on p. 109).

157. Ku, M. J. H., Sommer, A. T., Cheuk, L. W. & Zwierlein, M. W. Revealing the Superfluid Lambda Transition in the Universal Thermodynamics of a Unitary Fermi Gas. *Science* **335.** Publisher: American Association for the Advancement of Science Section: Report, 563–567. https://science.sciencemag.org/content/335/6068/563 (2021) (Feb. 2012) (cit. on pp. 109, 113).

158. Nascimbène, S., Navon, N., Jiang, K. J., Chevy, F. & Salomon, C. Exploring the thermodynamics of a universal Fermi gas. *Nature* **463.** Publisher: Nature Publishing Group, 1057–1060. https://www.nature.com/articles/nature08814 (2021) (Feb. 2010) (cit. on pp. 109, 113, 145).

159. Sidorenkov, L. A., Tey, M. K., Grimm, R., Hou, Y.-H., Pitaevskii, L. & Stringari, S. Second sound and the superfluid fraction in a Fermi gas with resonant interactions. *Nature* **498.** Publisher: Nature Publishing Group, 78–81. https://www.nature.com/articles/nature12136 (2021) (June 2013) (cit. on p. 110).

160. Zwierlein, M. W., Schunck, C. H., Schirotzek, A. & Ketterle, W. Direct observation of the superfluid phase transition in ultracold Fermi gases. *Nature* **442.** Publisher: Nature Publishing Group, 54–58. https://www.nature.com/articles/nature04936 (2021) (July 2006) (cit. on pp. 110, 113, 145).

161. Partridge, G. B., Li, W., Kamar, R. I., Liao, Y.-a. & Hulet, R. G. Pairing and Phase Separation in a Polarized Fermi Gas. *Science* **311.** Publisher: American Association for the Advancement of Science Section: Report, 503–505. https://science.sciencemag.org/content/311/5760/503 (2021) (Jan. 2006) (cit. on pp. 110, 111, 145).

162. Nascimbène, S. *Thermodynamics of ultracold Fermi gases* PhD thesis (Université Pierre et Marie Curie - Paris VI, June 2010). https://tel.archives-ouvertes.fr/tel-00491711 (2021) (cit. on p. 111).

163. De Silva, T. N. & Mueller, E. J. Surface Tension in Unitary Fermi Gases with Population Imbalance. *Physical Review Letters* **97.** Publisher: American Physical Society, 070402. https://link.aps.org/doi/10.1103/PhysRevLett.97.070402 (2021) (Aug. 2006) (cit. on pp. 111, 113).

164. Shin, Y., Zwierlein, M. W., Schunck, C. H., Schirotzek, A. & Ketterle, W. Observation of Phase Separation in a Strongly Interacting Imbalanced Fermi Gas. *Physical Review Letters* **97.** Publisher: American Physical Society, 030401. https://link.aps.org/doi/10.1103/PhysRevLett.97.030401 (2021) (July 2006) (cit. on pp. 111, 113, 145).

165. Ferrier-Barbut, I., Delehaye, M., Laurent, S., Grier, A. T., Pierce, M., Rem, B. S., Chevy, F. & Salomon, C. A mixture of Bose and Fermi superfluids. *Science* **345.** Publisher: American Association for the Advancement of Science Section: Report, 1035–1038. https://science.sciencemag.org/content/345/6200/1035 (2021) (Aug. 2014) (cit. on p. 113).

166. Chin, C., Bartenstein, M., Altmeyer, A., Riedl, S., Jochim, S., Denschlag, J. H. & Grimm, R. Observation of the Pairing Gap in a Strongly Interacting Fermi Gas. *Science* **305.** Publisher: American Association for the Advancement of Science Section: Report, 1128–1130. https://science.sciencemag.org/content/305/5687/1128 (2021) (Aug. 2004) (cit. on p. 116).

167. Schunck, C. H., Shin, Y.-i., Schirotzek, A. & Ketterle, W. Determination of the fermion pair size in a resonantly interacting superfluid. *Nature* **454.** Publisher: Nature Publishing Group, 739–743. https://www.nature.com/articles/nature07176 (2021) (Aug. 2008) (cit. on pp. 116, 117).

168. Yan, Z., Patel, P. B., Mukherjee, B., Fletcher, R. J., Struck, J. & Zwierlein, M. W. Boiling a Unitary Fermi Liquid. *Physical Review Letters* **122.** Publisher: American Physical Society, 093401. https://link.aps.org/doi/10.1103/PhysRevLett.122.093401 (2021) (Mar. 2019) (cit. on p. 116).

169. Mukherjee, B., Patel, P. B., Yan, Z., Fletcher, R. J., Struck, J. & Zwierlein, M. W. Spectral Response and Contact of the Unitary Fermi Gas. *Physical Review Letters* **122.** Publisher: American Physical Society, 203402. https://link.aps.org/doi/10.1103/PhysRevLett.122.203402 (2021) (May 2019) (cit. on p. 116).

170. Gupta, S., Hadzibabic, Z., Zwierlein, M. W., Stan, C. A., Dieckmann, K., Schunck, C. H., Kempen, E. G. M. v., Verhaar, B. J. & Ketterle, W. Radio-Frequency Spectroscopy of Ultracold Fermions. *Science* **300.** Publisher: American Association for the Advancement of Science Section: Report, 1723–1726. https://science.sciencemag.org/content/300/5626/1723 (2021) (June 2003) (cit. on p. 116).

171. Haroche, S. & Raimond, J.-M. *Exploring the Quantum: Atoms, Cavities, and Photons* https://oxford.universitypressscholarship.com/10.1093/acprof:oso/9780198509141.001.0001/acprof-9780198509141 (2021) (Oxford University Press, Oxford, 2006) (cit. on pp. 122, 150, 180).

172. Tanji-Suzuki, H., Leroux, I. D., Schleier-Smith, M. H., Cetina, M., Grier, A. T., Simon, J. & Vuletić, V. in *Advances In Atomic, Molecular, and Optical Physics* (eds Arimondo, E., Berman, P. R. & Lin, C. C.) 201–237 (Academic Press, Jan. 2011). https://www.sciencedirect.com/science/article/pii/B9780123855084000048 (2021) (cit. on pp. 122, 124, 125, 150, 160, 161, 180).

173. Kollath, C., Sheikhan, A., Wolff, S. & Brennecke, F. Ultracold Fermions in a Cavity-Induced Artificial Magnetic Field. *Physical Review Letters* **116.** Publisher: American Physical Society, 060401. https://link.aps.org/doi/10.1103/PhysRevLett.116.060401 (2021) (Feb. 2016) (cit. on p. 122).

174. Mivehvar, F., Ritsch, H. & Piazza, F. Superradiant Topological Peierls Insulator inside an Optical Cavity. *Physical Review Letters* **118.** Publisher: American Physical Society, 073602. https://link.aps.org/doi/10.1103/PhysRevLett.118.073602 (2021) (Feb. 2017) (cit. on p. 122).

175. Colella, E., Citro, R., Barsanti, M., Rossini, D. & Chiofalo, M.-L. Quantum phases of spinful Fermi gases in optical cavities. *Physical Review B* **97.** Publisher: American Physical Society, 134502. https://link.aps.org/doi/10.1103/PhysRevB.97.134502 (2021) (Apr. 2018) (cit. on pp. 122, 188).

176. Sheikhan, A. & Kollath, C. Cavity-induced superconducting and $4k_F$ charge-density-wave states. *Physical Review A* **99.** Publisher: American Physical Society, 053611. https://link.aps.org/doi/10.1103/PhysRevA.99.053611 (2021) (May 2019) (cit. on pp. 122, 188).

177. Schlawin, F., Cavalleri, A. & Jaksch, D. Cavity-Mediated Electron-Photon Superconductivity. *Physical Review Letters* **122.** Publisher: American Physical Society, 133602. https://link.aps.org/doi/10.1103/PhysRevLett.122.133602 (2021) (Apr. 2019) (cit. on pp. 122, 148, 188).

178. Schlawin, F. & Jaksch, D. Cavity-Mediated Unconventional Pairing in Ultracold Fermionic Atoms. *Physical Review Letters* **123.** Publisher: American Physical Society, 133601. https://link.aps.org/doi/10.1103/PhysRevLett.123.133601 (2021) (Sept. 2019) (cit. on p. 122).

179. Curtis, J. B., Raines, Z. M., Allocca, A. A., Hafezi, M. & Galitski, V. M. Cavity Quantum Eliashberg Enhancement of Superconductivity. *Physical Review Letters* **122.** Publisher: American Physical Society, 167002. https://link.aps.org/doi/10.1103/PhysRevLett.122.167002 (2021) (Apr. 2019) (cit. on pp. 122, 188).

180. Mazza, G. & Georges, A. Superradiant Quantum Materials. *Physical Review Letters* **122.** Publisher: American Physical Society, 017401. https://link.aps.org/doi/10.1103/PhysRevLett.122.017401 (2021) (Jan. 2019) (cit. on pp. 122, 148).

181. Colella, E., Ostermann, S., Niedenzu, W., Mivehvar, F. & Ritsch, H. Antiferromagnetic self-ordering of a Fermi gas in a ring cavity. *New Journal of Physics* **21.** Publisher: IOP Publishing, 043019. https://doi.org/10.1088/1367-2630/ab151e (2021) (Apr. 2019) (cit. on pp. 122, 148, 188).

182. Uchino, S., Ueda, M. & Brantut, J.-P. Universal noise in continuous transport measurements of interacting fermions. *Physical Review A* **98.** Publisher: American Physical Society, 063619. https://link.aps.org/doi/10.1103/PhysRevA.98.063619 (2021) (Dec. 2018) (cit. on pp. 122, 148, 175, 179, 183).

183. Khitrova, G., Gibbs, H. M., Kira, M., Koch, S. W. & Scherer, A. Vacuum Rabi splitting in semiconductors. *Nature Physics* **2.** Publisher: Nature Publishing Group, 81–90. https://www.nature.com/articles/nphys227 (2021) (Feb. 2006) (cit. on p. 122).

184. Basov, D. N., Fogler, M. M. & Abajo, F. J. G. d. Polaritons in van der Waals materials. *Science* **354.** Publisher: American Association for the Advancement of Science Section: Review. https://science.sciencemag.org/content/354/6309/aag1992 (2021) (Oct. 2016) (cit. on p. 122).

185. Miller, R., Northup, T. E., Birnbaum, K. M., Boca, A., Boozer, A. D. & Kimble, H. J. Trapped atoms in cavity QED: coupling quantized light and matter. *Journal of Physics B: Atomic, Molecular and Optical Physics* **38.** Publisher: IOP Publishing, S551–S565. https://doi.org/10.1088/0953-4075/38/9/007 (2021) (Apr. 2005) (cit. on p. 122).

186. Slama, S., Bux, S., Krenz, G., Zimmermann, C. & Courteille, P. W. Superradiant Rayleigh Scattering and Collective Atomic Recoil Lasing in a Ring Cavity. *Physical Review Letters* **98.** Publisher: American Physical Society, 053603. https://link.aps.org/doi/10.1103/PhysRevLett.98.053603 (2021) (Feb. 2007) (cit. on pp. 122, 188).

187. Gupta, S., Moore, K. L., Murch, K. W. & Stamper-Kurn, D. M. Cavity Nonlinear Optics at Low Photon Numbers from Collective Atomic Motion. *Physical Review Letters* **99.** Publisher: American Physical Society, 213601. https://link.aps.org/doi/10.1103/PhysRevLett.99.213601 (2021) (Nov. 2007) (cit. on pp. 122, 175, 185).

188. Daiss, S., Langenfeld, S., Welte, S., Distante, E., Thomas, P., Hartung, L., Morin, O. & Rempe, G. A quantum-logic gate between distant quantum-network modules. *Science* **371.** Publisher: American Association for the Advancement of Science Section: Report, 614–617. https://science.sciencemag.org/content/371/6529/614 (2021) (Feb. 2021) (cit. on p. 126).

189. Gardiner, C. & Zoller, P. *The Quantum World of Ultra-Cold Atoms and Light Book I: Foundations of Quantum Optics* https://www.worldscientific.com/worldscibooks/10.1142/p941 (2021) (Imperial College Press, May 2014) (cit. on p. 135).

190. Wickenbrock, A., Hemmerling, M., Robb, G. R. M., Emary, C. & Renzoni, F. Collective strong coupling in multimode cavity QED. *Physical Review A* **87.** Publisher: American Physical Society, 043817. https://link.aps.org/doi/10.1103/PhysRevA.87.043817 (2021) (Apr. 2013) (cit. on p. 136).

191. Kollár, A. J., Papageorge, A. T., Vaidya, V. D., Guo, Y., Keeling, J. & Lev, B. L. Supermode-density-wave-polariton condensation with a Bose–Einstein condensate in a multimode cavity. *Nature Communications* **8.** Publisher: Nature Publishing Group, 14386. https://www.nature.com/articles/ncomms14386 (2021) (Feb. 2017) (cit. on pp. 136, 148).

192. Shin, Y.-i., Schunck, C. H., Schirotzek, A. & Ketterle, W. Phase diagram of a two-component Fermi gas with resonant interactions. *Nature* **451.** Publisher: Nature Publishing Group, 689–693. https://www.nature.com/articles/nature06473 (2021) (Feb. 2008) (cit. on p. 145).

193. Piazza, F. & Strack, P. Umklapp Superradiance with a Collisionless Quantum Degenerate Fermi Gas. *Physical Review Letters* **112.** Publisher: American Physical Society, 143003. https://link.aps.org/doi/10.1103/PhysRevLett.112.143003 (2021) (Apr. 2014) (cit. on pp. 148, 188).

194. Chen, Y., Yu, Z. & Zhai, H. Superradiance of Degenerate Fermi Gases in a Cavity. *Physical Review Letters* **112.** Publisher: American Physical Society, 143004. https://link.aps.org/doi/10.1103/PhysRevLett.112.143004 (2021) (Apr. 2014) (cit. on pp. 148, 188).

195. Keeling, J., Bhaseen, M. & Simons, B. Fermionic Superradiance in a Transversely Pumped Optical Cavity. *Physical Review Letters* **112.** Publisher: American Physical Society, 143002. https://link.aps.org/doi/10.1103/PhysRevLett.112.143002 (2021) (Apr. 2014) (cit. on pp. 148, 188).

196. Chen, Y., Zhai, H. & Yu, Z. Superradiant phase transition of Fermi gases in a cavity across a Feshbach resonance. *Physical Review A* **91.** Publisher: American Physical Society, 021602. https://link.aps.org/doi/10.1103/PhysRevA.91.021602 (2021) (Feb. 2015) (cit. on pp. 148, 188).

197. Ashida, Y., Furukawa, S. & Ueda, M. Quantum critical behavior influenced by measurement backaction in ultracold gases. *Physical Review A* **94.** Publisher: American Physical Society, 053615. https://link.aps.org/doi/10.1103/PhysRevA.94.053615 (2021) (Nov. 2016) (cit. on p. 148).

198. Pan, J.-S., Liu, X.-J., Zhang, W., Yi, W. & Guo, G.-C. Topological Superradiant States in a Degenerate Fermi Gas. *Physical Review Letters* **115.** Publisher: American Physical Society, 045303. https://link.aps.org/doi/10.1103/PhysRevLett.115.045303 (2021) (July 2015) (cit. on pp. 148, 188).

199. Mazzucchi, G., Caballero-Benitez, S. F., Ivanov, D. A. & Mekhov, I. B. Quantum optical feedback control for creating strong correlations in many-body systems. *Optica* **3.** Publisher: Optical Society of America, 1213–1219. https://www.osapublishing.org/optica/abstract.cfm?uri=optica-3-11-1213 (2021) (Nov. 2016) (cit. on p. 148).

200. Mazzucchi, G., Kozlowski, W., Caballero-Benitez, S. F., Elliott, T. J. & Mekhov, I. B. Quantum measurement-induced dynamics of many-body ultracold bosonic and fermionic systems in optical lattices. *Physical Review A* **93.** Publisher: American Physical Society, 023632. https://link.aps.org/doi/10.1103/PhysRevA.93.023632 (2021) (Feb. 2016) (cit. on p. 148).

201. Lye, J. E., Hope, J. J. & Close, J. D. Nondestructive dynamic detectors for Bose-Einstein condensates. *Physical Review A* **67.** Publisher: American Physical Society, 043609. https://link.aps.org/doi/10.1103/PhysRevA.67.043609 (2021) (Apr. 2003) (cit. on p. 148).

202. Hope, J. J. & Close, J. D. Limit to Minimally Destructive Optical Detection of Atoms. *Physical Review Letters* **93.** Publisher: American Physical Society, 180402. https://link.aps.org/doi/10.1103/PhysRevLett.93.180402 (2021) (Oct. 2004) (cit. on p. 148).

203. Eckert, K., Romero-Isart, O., Rodriguez, M., Lewenstein, M., Polzik, E. S. & Sanpera, A. Quantum non-demolition detection of strongly correlated systems. *Nature Physics* **4.** Publisher: Nature Publishing Group, 50–54. https://www.nature.com/articles/nphys776 (2021) (Jan. 2008) (cit. on p. 148).

204. Bauer, D. M., Lettner, M., Vo, C., Rempe, G. & Dürr, S. Control of a magnetic Feshbach resonance with laser light. *Nature Physics* **5.** Publisher: Nature Publishing Group, 339–342. https://www.nature.com/articles/nphys1232 (2021) (May 2009) (cit. on p. 148).

205. Bernier, J.-S., Barmettler, P., Poletti, D. & Kollath, C. Emergence of spatially extended pair coherence through incoherent local environmental coupling. *Physical Review A* **87.** Publisher: American Physical Society, 063608. https://link.aps.org/doi/10.1103/PhysRevA.87.063608 (2021) (June 2013) (cit. on p. 148).

206. Theis, M., Thalhammer, G., Winkler, K., Hellwig, M., Ruff, G., Grimm, R. & Denschlag, J. H. Tuning the Scattering Length with an Optically Induced Feshbach Resonance. *Physical Review Letters* **93,** 123001. https://link.aps.org/doi/10.1103/PhysRevLett.93.123001 (2020) (Sept. 2004) (cit. on p. 148).

207. Vallet, G., Bookjans, E., Eismann, U., Bilicki, S., Targat, R. L. & Lodewyck, J. A noise-immune cavity-assisted non-destructive detection for an optical lattice clock in the quantum regime. *New Journal of Physics* **19.** Publisher: IOP Publishing, 083002. https://doi.org/10.1088/1367-2630/aa7c84 (2021) (Aug. 2017) (cit. on p. 148).

208. Laflamme, C., Yang, D. & Zoller, P. Continuous measurement of an atomic current. *Physical Review A* **95.** Publisher: American Physical Society, 043843. https://link.aps.org/doi/10.1103/PhysRevA.95.043843 (2021) (Apr. 2017) (cit. on pp. 148, 188).

209. Krantz, P., Kjaergaard, M., Yan, F., Orlando, T. P., Gustavsson, S. & Oliver, W. D. A quantum engineer's guide to superconducting qubits. *Applied Physics Reviews* **6.** Publisher: American Institute of Physics, 021318. https://aip.scitation.org/doi/10.1063/1.5089550 (2021) (June 2019) (cit. on p. 150).

210. Münstermann, P., Fischer, T., Maunz, P., Pinkse, P. W. H. & Rempe, G. Observation of Cavity-Mediated Long-Range Light Forces between Strongly Coupled Atoms. *Physical Review Letters* **84.** Publisher: American Physical Society, 4068–4071. https://link.aps.org/doi/10.1103/PhysRevLett.84.4068 (2021) (May 2000) (cit. on p. 150).

211. Vaidya, V. D., Guo, Y., Kroeze, R. M., Ballantine, K. E., Kollár, A. J., Keeling, J. & Lev, B. L. Tunable-Range, Photon-Mediated Atomic Interactions in Multimode Cavity QED. *Physical Review X* **8.** Publisher: American Physical Society, 011002. https://link.aps.org/doi/10.1103/PhysRevX.8.011002 (2021) (Jan. 2018) (cit. on p. 150).

212. Dogra, N., Landini, M., Kroeger, K., Hruby, L., Donner, T. & Esslinger, T. Dissipation-induced structural instability and chiral dynamics in a quantum gas. *Science* **366.** Publisher: American Association for the Advancement of Science Section: Report, 1496–1499. https://science.sciencemag.org/content/366/6472/1496 (2021) (Dec. 2019) (cit. on p. 150).

213. Mekhov, I. B., Maschler, C. & Ritsch, H. Probing quantum phases of ultracold atoms in optical lattices by transmission spectra in cavity quantum electrodynamics. *Nature Physics* **3.** Publisher: Nature Publishing Group, 319–323. https://www.nature.com/articles/nphys571 (2021) (May 2007) (cit. on p. 150).

214. Jones, K. M., Tiesinga, E., Lett, P. D. & Julienne, P. S. Ultracold photoassociation spectroscopy: Long-range molecules and atomic scattering. *Reviews of Modern Physics* **78.** Publisher: American Physical Society, 483–535. https://link.aps.org/doi/10.1103/RevModPhys.78.483 (2021) (May 2006) (cit. on pp. 150, 152).

215. Junker, M., Dries, D., Welford, C., Hitchcock, J., Chen, Y. P. & Hulet, R. G. Photoassociation of a Bose-Einstein Condensate near a Feshbach Resonance. *Physical Review Letters* **101.** Publisher: American Physical Society, 060406. https://link.aps.org/doi/10.1103/PhysRevLett.101.060406 (2021) (Aug. 2008) (cit. on pp. 150, 152).

216. Kinoshita, T., Wenger, T. & Weiss, D. S. Local Pair Correlations in One-Dimensional Bose Gases. *Physical Review Letters* **95.** Publisher: American Physical Society, 190406. https://link.aps.org/doi/10.1103/PhysRevLett.95.190406 (2021) (Nov. 2005) (cit. on p. 150).

217. Semczuk, M., Gunton, W., Bowden, W. & Madison, K. W. Anomalous Behavior of Dark States in Quantum Gases of ^{6}Li. *Physical Review Letters* **113.** Publisher: American Physical Society, 055302. https://link.aps.org/doi/10.1103/PhysRevLett.113.055302 (2021) (July 2014) (cit. on p. 150).

218. Liu, X.-P., Yao, X.-C., Chen, H.-Z., Wang, X.-Q., Wang, Y.-X., Chen, Y.-A., Chen, Q., Levin, K. & Pan, J.-W. Observation of the density effect on the closed-channel fraction in a ^{6}Li superfluid. *arXiv:1903.12321 [cond-mat].* arXiv: 1903.12321. http://arxiv.org/abs/1903.12321 (2021) (Oct. 2019) (cit. on pp. 150, 168).

219. Paintner, T. *et al.* Pair fraction in a finite-temperature Fermi gas on the BEC side of the BCS-BEC crossover. *Physical Review A* **99.** Publisher: American Physical Society, 053617. https://link.aps.org/doi/10.1103/PhysRevA.99.053617 (2021) (May 2019) (cit. on p. 150).

220. Yan, M., DeSalvo, B. J., Huang, Y., Naidon, P. & Killian, T. C. Rabi Oscillations between Atomic and Molecular Condensates Driven with Coherent One-Color Photoassociation. *Physical Review Letters* **111.** Publisher: American Physical Society, 150402. https://link.aps.org/doi/10.1103/PhysRevLett.111.150402 (2021) (Oct. 2013) (cit. on p. 150).

221. Taie, S., Watanabe, S., Ichinose, T. & Takahashi, Y. Feshbach-Resonance-Enhanced Coherent Atom-Molecule Conversion with Ultranarrow Photoassociation Resonance. *Physical Review Letters* **116.** Publisher: American Physical Society, 043202. https://link.aps.org/doi/10.1103/PhysRevLett.116.043202 (2021) (Jan. 2016) (cit. on p. 150).

222. Ospelkaus, S., Ni, K.-K., Wang, D., Miranda, M. H. G. d., Neyenhuis, B., Quéméner, G., Julienne, P. S., Bohn, J. L., Jin, D. S. & Ye, J. Quantum-State Controlled Chemical Reactions of Ultracold Potassium-Rubidium Molecules. *Science* **327.** Publisher: American Association for the Advancement of Science Section: Report, 853–857. https://science.sciencemag.org/content/327/5967/853 (2021) (Feb. 2010) (cit. on p. 152).

223. Ni, K.-K., Ospelkaus, S., Wang, D., Quéméner, G., Neyenhuis, B., de Miranda, M. H. G., Bohn, J. L., Ye, J. & Jin, D. S. Dipolar collisions of polar molecules in the quantum regime. *Nature* **464.** Publisher: Nature Publishing Group, 1324–1328. https://www.nature.com/articles/nature08953 (2021) (Apr. 2010) (cit. on p. 152).

224. Danzl, J. G., Mark, M. J., Haller, E., Gustavsson, M., Hart, R., Aldegunde, J., Hutson, J. M. & Nägerl, H.-C. An ultracold high-density sample of rovibronic ground-state molecules in an optical lattice. *Nature Physics* **6.** Publisher: Nature Publishing Group, 265–270. https://www.nature.com/articles/nphys1533 (2021) (Apr. 2010) (cit. on p. 152).

225. Molony, P. K., Gregory, P. D., Ji, Z., Lu, B., Köppinger, M. P., Le Sueur, C. R., Blackley, C. L., Hutson, J. M. & Cornish, S. L. Creation of Ultracold $^{87}Rb^{133}Cs$ Molecules in the Rovibrational Ground State. *Physical Review Letters* **113.** Publisher: American Physical Society, 255301. https://link.aps.org/doi/10.1103/PhysRevLett.113.255301 (2021) (Dec. 2014) (cit. on p. 152).

226. Park, J. W., Will, S. A. & Zwierlein, M. W. Ultracold Dipolar Gas of Fermionic $^{23}Na^{40}K$ Molecules in Their Absolute Ground State. *Physical Review Letters* **114.** Publisher: American Physical Society, 205302. https://link.aps.org/doi/10.1103/PhysRevLett.114.205302 (2021) (May 2015) (cit. on p. 152).

227. Guo, M., Zhu, B., Lu, B., Ye, X., Wang, F., Vexiau, R., Bouloufa-Maafa, N., Quéméner, G., Dulieu, O. & Wang, D. Creation of an Ultracold Gas of Ground-State Dipolar $^{23}Na^{87}Rb$ Molecules. *Physical Review Letters* **116.** Publisher: American Physical Society, 205303. https://link.aps.org/doi/10.1103/PhysRevLett.116.205303 (2021) (May 2016) (cit. on p. 152).

228. Guttridge, A., Hopkins, S. A., Frye, M. D., McFerran, J. J., Hutson, J. M. & Cornish, S. L. Production of ultracold Cs^*Yb molecules by photoassociation. *Physical Review A* **97.** Publisher: American Physical Society, 063414. https://link.aps.org/doi/10.1103/PhysRevA.97.063414 (2021) (June 2018) (cit. on p. 152).

229. Tojo, S., Kitagawa, M., Enomoto, K., Kato, Y., Takasu, Y., Kumakura, M. & Takahashi, Y. High-Resolution Photoassociation Spectroscopy of Ultracold Ytterbium Atoms by Using the Intercombination Transition. *Physical Review Letters* **96.** Publisher: American Physical Society, 153201. https://link.aps.org/doi/10.1103/PhysRevLett.96.153201 (2021) (Apr. 2006) (cit. on p. 152).

230. Herschbach, N., Tol, P. J. J., Vassen, W., Hogervorst, W., Woestenenk, G., Thomsen, J. W., van der Straten, P. & Niehaus, A. Photoassociation Spectroscopy of Cold $He(2^3S)$ Atoms. *Physical Review Letters* **84.** Publisher: American Physical Society, 1874–1877. https://link.aps.

org/doi/10.1103/PhysRevLett.84.1874 (2021) (Feb. 2000) (cit. on p. 152).

231. Kim, J., Moal, S., Portier, M., Dugué, J., Leduc, M. & Cohen-Tannoudji, C. Frequency shifts of photoassociative spectra of ultracold metastable helium atoms: A new measurement of the -wave scattering length. *Europhysics Letters* **72.** Publisher: EDP Sciences, 548–554. https://epljournal.edpsciences.org/articles/epl/abs/2005/22/epl9024/epl9024.html (2021) (Nov. 2005) (cit. on p. 152).

232. Vogt, F., Grain, C., Nazarova, T., Sterr, U., Riehle, F., Lisdat, C. & Tiemann, E. Determination of the calcium ground state scattering length by photoassociation spectroscopy at large detunings. *The European Physical Journal D* **44,** 73–79. https://doi.org/10.1140/epjd/e2007-00175-8 (2021) (July 2007) (cit. on p. 152).

233. Mickelson, P. G., Martinez, Y. N., Saenz, A. D., Nagel, S. B., Chen, Y. C., Killian, T. C., Pellegrini, P. & Côté, R. Spectroscopic Determination of the s-Wave Scattering Lengths of ^{86}Sr and ^{88}Sr. *Physical Review Letters* **95.** Publisher: American Physical Society, 223002. https://link.aps.org/doi/10.1103/PhysRevLett.95.223002 (2021) (Nov. 2005) (cit. on p. 152).

234. Yasuda, M., Kishimoto, T., Takamoto, M. & Katori, H. Photoassociation spectroscopy of ^{88}Sr: Reconstruction of the wave function near the last node. *Physical Review A* **73.** Publisher: American Physical Society, 011403. https://link.aps.org/doi/10.1103/PhysRevA.73.011403 (2021) (Jan. 2006) (cit. on p. 152).

235. Takasu, Y., Komori, K., Honda, K., Kumakura, M., Yabuzaki, T. & Takahashi, Y. Photoassociation Spectroscopy of Laser-Cooled Ytterbium Atoms. *Physical Review Letters* **93.** Publisher: American Physical Society, 123202. https://link.aps.org/doi/10.1103/PhysRevLett.93.123202 (2021) (Sept. 2004) (cit. on p. 152).

236. Weber, S., Tresp, C., Menke, H., Urvoy, A., Firstenberg, O., Büchler, H. P. & Hofferberth, S. Calculation of Rydberg interaction potentials. *Journal of Physics B: Atomic, Molecular and Optical Physics* **50.** Publisher: IOP Publishing, 133001. https://doi.org/10.1088/1361-6455/aa743a (2021) (June 2017) (cit. on pp. 154, 155).

237. Abraham, E. R. I., Ritchie, N. W. M., McAlexander, W. I. & Hulet, R. G. Photoassociative spectroscopy of long-range states of ultracold $^6Li_2$ and $^7Li_2$. *The Journal of Chemical Physics* **103.** Publisher: American Institute of Physics, 7773–7778. https://aip.scitation.org/doi/abs/10.1063/1.470296 (2021) (Nov. 1995) (cit. on pp. 158, 166).

238. Leggett, A. J. & Zhang, S. in *The BCS-BEC Crossover and the Unitary Fermi Gas* (ed Zwerger, W.) 33–47 (Springer, Berlin, Heidelberg, 2012). https://doi.org/10.1007/978-3-642-21978-8_2 (2021) (cit. on p. 167).

239. Tan, S. Energetics of a strongly correlated Fermi gas. *Annals of Physics* **323,** 2952–2970. https://www.sciencedirect.com/science/article/pii/S0003491608000456 (2021) (Dec. 2008) (cit. on pp. 168, 169).

240. Tan, S. Large momentum part of a strongly correlated Fermi gas. *Annals of Physics* **323,** 2971–2986. https://www.sciencedirect.com/science/article/pii/S0003491608000432 (2021) (Dec. 2008) (cit. on p. 168).

241. Tan, S. Generalized virial theorem and pressure relation for a strongly correlated Fermi gas. *Annals of Physics* **323,** 2987–2990. https://www.sciencedirect.com/science/article/pii/S0003491608000420 (2021) (Dec. 2008) (cit. on p. 168).

242. Thomas, J. E., Kinast, J. & Turlapov, A. Virial Theorem and Universality in a Unitary Fermi Gas. *Physical Review Letters* **95.** Publisher: American Physical Society, 120402. https://link.aps.org/doi/10.1103/PhysRevLett.95.120402 (2021) (Sept. 2005) (cit. on p. 168).

243. Stewart, J. T., Gaebler, J. P., Drake, T. E. & Jin, D. S. Verification of Universal Relations in a Strongly Interacting Fermi Gas. *Physical Review Letters* **104.** Publisher: American Physical Society, 235301. https://link.aps.org/doi/10.1103/PhysRevLett.104.235301 (2021) (June 2010) (cit. on p. 168).

244. Sagi, Y., Drake, T. E., Paudel, R. & Jin, D. S. Measurement of the Homogeneous Contact of a Unitary Fermi Gas. *Physical Review Letters* **109.** Publisher: American Physical Society, 220402. https://link.aps.org/doi/10.1103/PhysRevLett.109.220402 (2021) (Nov. 2012) (cit. on pp. 168, 173).

245. Bardon, A. B. *et al.* Transverse Demagnetization Dynamics of a Unitary Fermi Gas. *Science* **344.** Publisher: American Association for the Advancement of Science Section: Report, 722–724. https://science.sciencemag.org/content/344/6185/722 (2021) (May 2014) (cit. on p. 168).

246. Mukherjee, B., Patel, P. B., Yan, Z., Fletcher, R. J., Struck, J. & Zwierlein, M. W. Spectral Response and Contact of the Unitary Fermi Gas. *Physical Review Letters* **122.** Publisher: American Physical Society, 203402. https://link.aps.org/doi/10.1103/PhysRevLett.122.203402 (2021) (May 2019) (cit. on pp. 168, 173).

247. Veeravalli, G., Kuhnle, E., Dyke, P. & Vale, C. J. Bragg Spectroscopy of a Strongly Interacting Fermi Gas. *Physical Review Letters* **101.** Publisher: American Physical Society, 250403. https://link.aps.org/doi/10.1103/PhysRevLett.101.250403 (2021) (Dec. 2008) (cit. on p. 168).

248. Kuhnle, E. D., Hu, H., Liu, X.-J., Dyke, P., Mark, M., Drummond, P. D., Hannaford, P. & Vale, C. J. Universal Behavior of Pair Correlations in a Strongly Interacting Fermi Gas. *Physical Review Letters* **105.** Publisher: American Physical Society, 070402. https://link.aps.org/doi/10.1103/PhysRevLett.105.070402 (2021) (Aug. 2010) (cit. on pp. 168, 173).

249. Hoinka, S., Lingham, M., Fenech, K., Hu, H., Vale, C. J., Drut, J. E. & Gandolfi, S. Precise Determination of the Structure Factor and Contact in a Unitary Fermi Gas. *Physical Review Letters* **110.** Publisher: American Physical Society, 055305. https://link.aps.org/doi/10.1103/PhysRevLett.110.055305 (2021) (Jan. 2013) (cit. on pp. 168, 169, 186).

250. Werner, F., Tarruell, L. & Castin, Y. Number of closed-channel molecules in the BEC-BCS crossover. *The European Physical Journal B* **68,** 401–415. https://doi.org/10.1140/epjb/e2009-00040-8 (2021) (Apr. 2009) (cit. on p. 168).

251. Braaten, E. Universal Relations for Fermions with Large Scattering Length. *arXiv:1008.2922 [cond-mat, physics:hep-ph, physics:nucl-th].* arXiv: 1008.2922. http://arxiv.org/abs/1008.2922 (2021) (Aug. 2010) (cit. on p. 168).

252. Côté, R., Dalgarno, A., Sun, Y. & Hulet, R. G. Photoabsorption by Ultracold Atoms and the Scattering Length. *Physical Review Letters* **74.** Publisher: American Physical Society, 3581–3584. https://link.aps.org/doi/10.1103/PhysRevLett.74.3581 (2021) (May 1995) (cit. on p. 169).

253. Hu, H., Liu, X.-J. & Drummond, P. D. Universal contact of strongly interacting fermions at finite temperatures. *New Journal of Physics* **13.** Publisher: IOP Publishing, 035007. https://doi.org/10.1088/1367-2630/13/3/035007 (2021) (Mar. 2011) (cit. on p. 169).

254. Chang, R., Bouton, Q., Cayla, H., Qu, C., Aspect, A., Westbrook, C. & Clément, D. Momentum-Resolved Observation of Thermal and Quantum Depletion in a Bose Gas. *Physical Review Letters* **117.** Publisher: American Physical Society, 235303. https://link.aps.org/doi/10.1103/PhysRevLett.117.235303 (2021) (Dec. 2016) (cit. on p. 173).

255. Laurent, S., Pierce, M., Delehaye, M., Yefsah, T., Chevy, F. & Salomon, C. Connecting Few-Body Inelastic Decay to Quantum Correlations in a Many-Body System: A Weakly Coupled Impurity in a Resonant Fermi Gas. *Physical Review Letters* **118.** Publisher: American Physical Society, 103403. https://link.aps.org/doi/10.1103/PhysRevLett.118.103403 (2021) (Mar. 2017) (cit. on p. 173).

256. Carcy, C., Hoinka, S., Lingham, M., Dyke, P., Kuhn, C., Hu, H. & Vale, C. Contact and Sum Rules in a Near-Uniform Fermi Gas at Unitarity. *Physical Review Letters* **122.** Publisher: American Physical Society, 203401. https://link.aps.org/doi/10.1103/PhysRevLett.122.203401 (2021) (May 2019) (cit. on pp. 173, 186).

257. Kuhnle, E. D., Hoinka, S., Dyke, P., Hu, H., Hannaford, P. & Vale, C. J. Temperature Dependence of the Universal Contact Parameter in a Unitary Fermi Gas. *Physical Review Letters* **106.** Publisher: American Physical Society, 170402. https://link.aps.org/doi/10.1103/PhysRevLett.106.170402 (2021) (Apr. 2011) (cit. on p. 174).

258. Yamazaki, R., Taie, S., Sugawa, S. & Takahashi, Y. Submicron Spatial Modulation of an Interatomic Interaction in a Bose-Einstein Condensate. *Physical Review Letters* **105.** Publisher: American Physical Society, 050405. https://link.aps.org/doi/10.1103/PhysRevLett.105.050405 (2021) (July 2010) (cit. on p. 175).

259. Enss, T. & Thywissen, J. H. Universal Spin Transport and Quantum Bounds for Unitary Fermions. *Annual Review of Condensed Matter Physics* **10.** Publisher: Annual Reviews, 85–106. https://www.annualreviews.org/doi/10.1146/annurev-conmatphys-031218-013732 (2021) (Mar. 2019) (cit. on p. 175).

260. Amico, A., Scazza, F., Valtolina, G., Tavares, P., Ketterle, W., Inguscio, M., Roati, G. & Zaccanti, M. Time-Resolved Observation of Competing Attractive and Repulsive Short-Range Correlations in Strongly Interacting Fermi Gases. *Physical Review Letters* **121.** Publisher: American Physical Society, 253602. https://link.aps.org/doi/10.1103/PhysRevLett.121.253602 (2021) (Dec. 2018) (cit. on p. 175).

261. Krinner, S., Esslinger, T. & Brantut, J.-P. Two-terminal transport measurements with cold atoms. *Journal of Physics: Condensed Matter* **29.** Publisher: IOP Publishing, 343003. https://doi.org/10.1088/1361-648x/aa74a1 (2021) (July 2017) (cit. on pp. 176, 183).

262. Zeiher, J., Wolf, J., Isaacs, J. A., Kohler, J. & Stamper-Kurn, D. M. Tracking evaporative cooling of a mesoscopic atomic quantum gas in real time. *arXiv:2012.01280 [cond-mat, physics:physics].* arXiv: 2012.01280. http://arxiv.org/abs/2012.01280 (2021) (Dec. 2020) (cit. on pp. 176, 179).

263. Eisele, M., Maier, R. & Zimmermann, C. Fast In Situ Observation of Atomic Feshbach Resonances by Photoassociative Ionization. *Physical Review Letters* **124.** Publisher: American Physical Society, 123401. https://link.aps.org/doi/10.1103/PhysRevLett.124.123401 (2021) (Mar. 2020) (cit. on p. 176).

264. Pérez-Ríos, J., Kim, M. E. & Hung, C.-L. Ultracold molecule assembly with photonic crystals. *New Journal of Physics* **19.** Publisher: IOP Publishing, 123035. https://doi.org/10.1088/1367-2630/aa9b49 (2021) (Dec. 2017) (cit. on p. 176).

265. Horikoshi, M., Ito, A., Ikemachi, T., Aratake, Y., Kuwata-Gonokami, M. & Koashi, M. Appropriate Probe Condition for Absorption Imaging of Ultracold 6Li Atoms. *Journal of the Physical Society of Japan* **86.** Publisher: The Physical Society of Japan, 104301. https://journals.jps.jp/doi/10.7566/JPSJ.86.104301 (2021) (Sept. 2017) (cit. on p. 181).

266. Zhang, H., McConnell, R., Ćuk, S., Lin, Q., Schleier-Smith, M. H., Leroux, I. D. & Vuletić, V. Collective State Measurement of Mesoscopic Ensembles with Single-Atom Resolution. *Physical Review Letters* **109.** Publisher: American Physical Society, 133603. https://link.aps.org/doi/10.1103/PhysRevLett.109.133603 (2021) (Sept. 2012) (cit. on p. 183).

267. Yang, D., Vasilyev, D. V., Laflamme, C., Baranov, M. A. & Zoller, P. Quantum scanning microscope for cold atoms. *Physical Review A* **98.** Publisher: American Physical Society, 023852. https://link.aps.org/doi/10.1103/PhysRevA.98.023852 (2021) (Aug. 2018) (cit. on p. 183).

268. Aspelmeyer, M., Kippenberg, T. J. & Marquardt, F. Cavity optomechanics. *Reviews of Modern Physics* **86.** Publisher: American Physical Society, 1391–1452. https://link.aps.org/doi/10.1103/RevModPhys.86.1391 (2021) (Dec. 2014) (cit. on p. 184).

269. Stamper-Kurn, D. M. Cavity optomechanics with cold atoms. *arXiv:1204.4351 [cond-mat, physics:physics, physics:quant-ph].* arXiv: 1204.4351. http://arxiv.org/abs/1204.4351 (2021) (Apr. 2012) (cit. on p. 184).

270. Brennecke, F., Ritter, S., Donner, T. & Esslinger, T. Cavity Optomechanics with a Bose-Einstein Condensate. *Science* **322.** Publisher: American Association for the Advancement of Science Section: Report, 235–238. https://science.sciencemag.org/content/322/5899/235 (2021) (Oct. 2008) (cit. on pp. 184, 185).

271. Purdy, T. P., Brooks, D. W. C., Botter, T., Brahms, N., Ma, Z.-Y. & Stamper-Kurn, D. M. Tunable Cavity Optomechanics with Ultracold Atoms. *Physical Review Letters* **105.** Publisher: American Physical Society, 133602. https://link.aps.org/doi/10.1103/PhysRevLett.105.133602 (2021) (Sept. 2010) (cit. on p. 184).

272. Brahms, N. & Stamper-Kurn, D. M. Spin optodynamics analog of cavity optomechanics. *Physical Review A* **82.** Publisher: American Physical Society, 041804. https://link.aps.org/doi/10.1103/PhysRevA.82.041804 (2021) (Oct. 2010) (cit. on p. 184).

273. Brahms, N., Botter, T., Schreppler, S., Brooks, D. W. C. & Stamper-Kurn, D. M. Optical Detection of the Quantization of Collective Atomic Motion. *Physical Review Letters* **108.** Publisher: American Physical Society, 133601. https://link.aps.org/doi/10.1103/PhysRevLett.108.133601 (2021) (Mar. 2012) (cit. on p. 184).

274. Botter, T., Brooks, D. W. C., Schreppler, S., Brahms, N. & Stamper-Kurn, D. M. Optical Readout of the Quantum Collective Motion of an Array of Atomic Ensembles. *Physical Review Letters* **110.** Publisher: American Physical Society, 153001. https://link.aps.org/doi/10.1103/PhysRevLett.110.153001 (2021) (Apr. 2013) (cit. on p. 184).

275. Schreppler, S., Spethmann, N., Brahms, N., Botter, T., Barrios, M. & Stamper-Kurn, D. M. Optically measuring force near the standard quantum limit. *Science* **344,** 1486–1489. https://science.sciencemag.org/content/344/6191/1486 (2021) (June 2014) (cit. on p. 185).

276. Kohler, J., Spethmann, N., Schreppler, S. & Stamper-Kurn, D. M. Cavity-Assisted Measurement and Coherent Control of Collective Atomic Spin Oscillators. *Physical Review Letters* **118.** Publisher: American Physical Society, 063604. https://link.aps.org/doi/10.1103/PhysRevLett.118.063604 (2021) (Feb. 2017) (cit. on p. 185).

277. Kohler, J., Gerber, J. A., Dowd, E. & Stamper-Kurn, D. M. Negative-Mass Instability of the Spin and Motion of an Atomic Gas Driven by Optical Cavity Backaction. *Physical Review Letters* **120.** Publisher: American Physical Society, 013601. https://link.aps.org/doi/10.1103/PhysRevLett.120.013601 (2021) (Jan. 2018) (cit. on p. 185).

278. Botter, T., Brooks, D. W. C., Brahms, N., Schreppler, S. & Stamper-Kurn, D. M. Linear amplifier model for optomechanical systems. *Physical Review A* **85.** Publisher: American Physical Society, 013812. https://link.aps.org/doi/10.1103/PhysRevA.85.013812 (2021) (Jan. 2012) (cit. on p. 185).

279. Keßler, H., Klinder, J., Wolke, M. & Hemmerich, A. Optomechanical atom-cavity interaction in the sub-recoil regime. *New Journal of Physics* **16.** Publisher: IOP Publishing, 053008. https://doi.org/10.1088/1367-2630/16/5/053008 (2021) (May 2014) (cit. on p. 185).

280. Keßler, H., Klinder, J., Wolke, M. & Hemmerich, A. Steering Matter Wave Superradiance with an Ultranarrow-Band Optical Cavity. *Physical Review Letters* **113.** Publisher: American Physical Society, 070404. https://link.aps.org/doi/10.1103/PhysRevLett.113.070404 (2021) (Aug. 2014) (cit. on p. 185).

281. Colella, E., Mivehvar, F., Piazza, F. & Ritsch, H. Hofstadter butterfly in a cavity-induced dynamic synthetic magnetic field. *Physical Review B* **100.** Publisher: American Physical Society, 224306. https://link.aps.org/doi/10.1103/PhysRevB.100.224306 (2021) (Dec. 2019) (cit. on p. 188).

282. Sheikhan, A., Brennecke, F. & Kollath, C. Cavity-induced generation of nontrivial topological states in a two-dimensional Fermi gas. *Physical Review A* **94.** Publisher: American Physical Society, 061603. https://link.aps.org/doi/10.1103/PhysRevA.94.061603 (2021) (Dec. 2016) (cit. on p. 188).

283. Zheng, W. & Cooper, N. Superradiance Induced Particle Flow via Dynamical Gauge Coupling. *Physical Review Letters* **117.** Publisher: American Physical Society, 175302. https://link.aps.org/doi/10.1103/PhysRevLett.117.175302 (2021) (Oct. 2016) (cit. on p. 188).

284. Hoinka, S., Dyke, P., Lingham, M. G., Kinnunen, J. J., Bruun, G. M. & Vale, C. J. Goldstone mode and pair-breaking excitations in atomic Fermi superfluids. *Nature Physics* **13.** Publisher: Nature Publishing Group, 943–946. https://www.nature.com/articles/nphys4187 (2021) (Oct. 2017) (cit. on p. 192).

285. Biss, H., Sobirey, L., Luick, N., Bohlen, M., Kinnunen, J. J., Bruun, G. M., Lompe, T. & Moritz, H. Excitation Spectrum and Superfluid Gap of an Ultracold Fermi Gas. *arXiv:2105.09820 [cond-mat].* arXiv: 2105.09820. http://arxiv.org/abs/2105.09820 (2021) (May 2021) (cit. on p. 192).

ACKNOWLEDGEMENTS

To conclude this manuscript I would like to start by thanking all the people that contributed to the project since 2016 : Barbara, Oscar, Victor, Hideki and Timo. I would also like to thank the members of the jury, who kindly accepted to review my PhD work: Joseph Thywissen, Jakob Reichel, Guido Pupilllo and Pasquale Scarlino, as well as Frédéric mila the president of my jury. I want to thank especially the mechanical workshop team : Gilles, Olivier, Philippe, Luc, Adrien, David, Léo, Dylan and Claude. I have spent countless hours in the workshop discussing, asking many questions during the first three years of this PhD. You all have been of great help, always trying to find a solution and it was a pleasure to work with all of you. The clean room team with whom we shared the corridor also helped us a lot in the early time of the experiment so thanks to all of you : Nicolas, Damien, Yoan. I would like now to move to more personal acknowledgements.

This PhD thesis represented an important part of my life so far. When taking a look back at it, many conflicting feelings arise, mixing pride, nostalgia but also relief. As probably any experimental physicist knows, getting an experiment such as a quantum gases machine running is a permanent fight against the machine and yourself. In this combat, having allies, people that have your back in the lab but also outside is pretty much the only way to go through the PhD in a single piece. Now that I am finishing to write my dissertation, what I want to remember are all these persons without whom I could have never accomplished what is presented in this manuscript. This section of the manuscript is small by its size but made the rest of this manuscript possible.

I spent the last five years of my life at EPFL but it all started when Jean-Philippe offered me to join this project back at ETHZ, when I was feeling too stupid among many great scientists in the Esslinger group. Besides a great scientific project, working aside Jean-Philippe has been a chance where I learnt a lot. I have learned how to start a lab and an experiment from scratch and your supervision in this phase taught me a very important lesson: better start with something simple that works, than a Ferrari that does not start. You have been able to guide me but also hold me back when I was losing myself in technical upgrades. Your pragmatism made it possible for me to have enough time to accomplish all the nice physics we did and to learn a lot from strongly interacting fermions to molecular physics passing by quantum optics. Seeing how fast you can come up with ideas, jump from one field to another as always been a great source of motivation for me to be able, one day, to have the same ability that makes you an impressive physicist. For all of that thanks a lot.

Many people have been part of this project from Barbara that started the project and the lab with me, to Hideki that joined a year later. Both of you have participated to make the experiment what it has become and we can be proud of the pretty cool result. Among all people, I would like to give special thanks to Victor. I remember you coming in the office, five years ago looking for a master thesis, coming from solar panels and plastic lenses. Spending four month with me as you master thesis supervisor did not make you leave the lab, and better, you decided to sign in for five more years! When I was talking about allies that have your back in the lab I could not

have hoped for a better one than you (and not only because of your python skills). You came with almost no hands-on experience in an optics lab but with your calm, your steadiness and your curiosity it did not take you long to become an awesome team-mate, never dodging technical problems when we had to dig deep in the experiment. Your state of mind made you a great experimentalist (more that what you think) and any results in this thesis are also yours. The time we spent in the lab will stay in my memories for long and I am proud to say that I introduced you to french 80's music. I have no doubt that the experiment is in good hands with you and that you will keep doing nice science. The new lab members will have a lot of luck to have you on their side. And more than a lab ally, I am happy to call you my friend, despite your strong opinions on pickles, and being together made it easier to overcome the struggle coming from boundary conditions. I am sure that even if we are not in the same lab anymore I have one more friend. For all of these last four years thank you for everything: the gin sessions, the post-day sushis, the cat parties, the coffee breaks, the curry lunches... and proof reading this manuscript (yes I owe you one).

With the arrival of a second experiment, a batch of new people joined the lab in 2018. Besides making the group meeting more lively, it made me met Tigrane, the new postdoc. This new friendship arrived in the middle, and not the best, part of my PhD. Besides his expertise in Rydberg, broken cryostats, coffee and good wine and whiskey, Tigrane became a very good friend. You joined the coffee break team, and actually brought it to another level. Your chillness and kindness brought me so much. Thank you for the multiple home parties, board games, card games, where you have hosted me more than I can count. You made me step up my "Les aventuriers du rail" game, which unfortunately still cannot fight against your insolent luck. I am extremely happy to have you now in Grenoble, to keep having these good moments.

A Victor et toi merci beaucoup, je ne serais pas là si je ne vous avais pas rencontré pendant cette thèse. Nos pauses cafés vont me manquer mais je ne doute pas que nous trouverons le moyen de continuer le coffee break club sous un autre format !

Together with Victor and Tigrane I had the chance to meet Lauranne and Alex. Lauranne participated with Victor to get me out of the lab after a couple of years. I am so thankful that I got invited to her birthday/crémaillère/Victor's candidacy exam. That was the start of a nice friendship with a climax when I got to host Orion for a weekend. Alex made her entrance in this story in 2018, soon after Tigrane. You are probably the person with the more strong opinions I have met so far, excluding myself ! While people are usually afraid of someone direct and passionate, I spent countless nights with you discussing, arguing and sometimes having quite heated debates. But you are also one of the nicest and kindest person I have ever met. You have changed my vision of the world I am living in on many ways, and not only about coffee. I am glad to be able to call you my friend even if you are the worse winner at any game I have ever seen <3<3. You have been one the best support I have had during my thesis, in the worse and also the best moments. I hope I will prove myself worthy of that friendship. Thank you for being there and for being who you are.

Among the different persons I have met during this thesis, one is particularly important. I met you Chloé two years and a half ago and since then you have been my friend, my rage partner and my love. I would have never

made it through all of that without you. You have brought so much in my life for the last years and I wish it will stay like that wherever we go next. We make a nice team in the good and the bad moments and you are probably the best discovery of this PhD (yes even if pair polaritons are extremely cool). Thank you for being here, for listening to me about lab problems, quantum gases and many other things. I love you and I look forward that we build our team of cats and dogs.

I have met a bunch of nice people that made the life outside the lab sweeter, and even if I cannot give them all the credit they deserve I want to thank all of them. The "La bossette" team (mes voisins !) : Hannah, Mickey and Ludo who have hosted many of our evenings where we could release stress form work in this very nice environment. The Geneva team that I met thanks to Chloé : Mireia, Laura, Ilaria, Audrey, Arielle and Nick. I discovered Geneva thanks to you and you are all so different but you make such a nice group of friend. I was happy to share some of your parties/weekends. Geneva became my second swiss home and you made it extremely nice. To Hugo, ten years since the first time we met in Gibert, and you are still here ! I am happy to meet you every time I come to Paris to discuss physics and many other things. I do not know where your postdoc will bring you but I hope we will resume our ski holidays now that we have a basecamp in Grenoble.

Pour finir je voudrais remercier ma famille, qui me supporte depuis 27 ans. Mes parents, Lionel et Véronique, pour m'avoir fourni votre soutien depuis si longtemps ainsi que ma petite soeur, Katia. Vous avez toujours cru en moi et m'avez laissé entreprendre toute mes aventures de Houston à Lausanne en passant par Zurich. Je ne serais pas là si vous ne m'aviez fourni cette curiosité qui fait de moi le physicien que je suis aujourd'hui. À mon oncle Stéphane (le barbu) pour les voyages Marseille-Gap pendant ces "belles" années de classe prépa, tes tutos bricolages, tes prêts de livres et tes conseils de voyage à Patmos. À mon oncle Stéphane (de Paris) et Lydie pour votre soutien pendant mes années d'écoles d'ingénieur, à la fois moral et matériel (les repas le dimanche et les lessives). Merci d'avoir été là pour moi et d'avoir été convaincu que je réussirai même quand j'en doutais. À Christian et Françoise pour toutes ces escales grenobloises où, non content de trouver un lit, j'ai toujours passé de très bonnes soirées (et de merveilleux repas). À ma grand-mère Jeanine pour se tenir au courant régulièrement de l'avancée de ma thèse (et de ce manuscrit). À mes grand-parents Antoinette et Etienne qui j'espère sont fiers de moi. Enfin à toi pépé, j'aurais aimé que tu puisses voir l'aboutissement de ce travail dont on discutait toutes les semaines depuis longtemps, je te dédis cette thèse et je peux finalement te le dire : je me suis défendu, ton petit-fils est docteur !

And now as Freddie would say : the show must go on !

CURRICULUM VITÆ

PERSONAL

born December 21st, 1991, in Tremblay-en-France, France
citizen of France

E-mail: kevin.roux@epfl.ch

EDUCATION

2016 – 2021	Ph. D. thesis under the supervision of J.P. Brantut: *Cavity Quantum Electro Dynamics with strongly correlated fermions*. EPFL, Switzerland
2016	Master thesis under the supervision of T. Esslinger. ETHZ, Switzerland
2015	Project under the supervision of R. Hulet, Rice University, USA.
2015-2016	Master of Science at Université Paris Saclay, France.
2014	Summer project under the supervision of A. Browaeys, Laboratoire Charles Fabry, Palaiseau, France.
2013 – 2016	Graduate studies at Institut d'Optique, Palaiseau, France
2011 – 2013	*Classes préparatoires* at Lycée Thiers, Marseille, France
2011	*Baccalauréat* at Lycée Dominique Villars, Gap, France

PUBLICATIONS

1. K. Roux, B. Cilenti, V. Helson, H. Konishi, J.P. Brantut
   Compact bulk-machined electromagnets for quantum gas experiments
   Scipost Phys **6**, 048 (2019)

2. K. Roux, H. Konishi , V. Helson, J.P. Brantut
   Strongly correlated Fermions strongly coupled to light
   Nature Comm. **11**, 2974 (2020)

3. K. Roux, V. Helson, H. Konishi, J.P. Brantut
   Cavity-assisted preparation and detection of a unitary Fermi gas
   New Journal of Physics **23**, 043029 (2020)

4. H. Konishi*, K. Roux*, V. Helson, J.P. Brantut
   Universal pair-polaritons in a strongly interacting Fermi gas
   Nature **596**, 509-513 (2021)

COLOPHON

The design of this thesis is largely inspired by Robert Bringhurst's seminal book on typography *"The Elements of Typographic Style"*. It was typeset in XeLaTeX with a style that is partly based on `classicthesis.sty` by André Miede, `arsclassica.sty` by Lorenzo Pantieri and the dissertation of Thomas Uehlinger.